Universidad Autónoma de Madrid

Departamento de Física de Materiales

Luminescence plasmon enhancement and laser at the nanoscale in a Nd^{3+} based solid state gain medium

Eduardo Yraola Crespo

December 2015

Universidad Autónoma de Madrid

Departamento de Física de Materiales

Luminescence plasmon enhancement and laser at the nanoscale in a Nd^{3+} based solid state gain medium

by

Eduardo Yraola Crespo

PhD in Physics of Light and Matter

Supervisors

Luisa E. Bausá & Pablo Molina

December 2015

Contents

1 Introducción general (Español).....1

1.1 Justificación de la temática.....1
1.2 Objetivos y aportación original.....3
1.3 Trabajos compendiados.....5
1.4 Estructura de la tesis.....6

1 General introduction (English).....7

1.1 Motivation.....7
1.2 Main goals and original contribution.....8
1.3 List of publications.....10
1.4 Thesis structure.....11

Section I Ferroelectric materials.....13
Section II Nd^{3+} activated $LiNbO_3$ crystals.....27
Section III Localized surface plasmons.....41
Section IV Experimental methods.....57

2 Resumen global (Español).....69

2 Overall summary (English).....77

3 Publications.....83

4 Conclusiones (Español).....147

4 Conclusions (English).....151

5 References.....153

Español

1 Introducción general

1.1 Justificación de la temática

Una de las principales áreas de investigación dentro del campo de la fotónica se centra en el estudio y desarrollo de nuevos dispositivos láser ya que estos constituyen las fuentes de radiación electromagnética con mayor grado de coherencia, densidad espectral de energía y posibilidad de manipulación y control.

Desde sus inicios hace ya más 50 años, la ciencia del láser ha experimentado enormes avances que han dado lugar a láseres en configuraciones extremas como los láseres de alta intensidad diseñados para experimentos en fusión nuclear, los láseres ultra-rápidos usados para investigar reacciones químicas y procesos atómicos, o los micro-láseres compactos que pueden implementarse en grandes redes de datos [Jackson 2012, Perry 1994, Zayhowski 1989].

De entre las diferentes clases de láseres que podemos encontrar hoy en día, los láseres de estado sólido (en adelante SSL del inglés *Solid State laser)* destacan por sus excelentes y versátiles propiedades, siendo una herramienta fundamental en una gran variedad de áreas científicas y tecnológicas. En este tipo de láseres el medio de ganancia está constituido por iones de tierras raras (RE^{3+}), iones de metales de transición o incluso centros de color, incorporados como impurezas o defectos ópticamente activos en matrices aislantes tales como cristales, vidrios o cerámicas. En estos sistemas la transición láser tiene lugar entre los niveles de energía de estos dopantes ópticos.

Desde la primera demostración experimental del láser de rubí en 1960 [Maiman 1960] el desarrollo de los SSLs ha dado lugar a una enorme y sorprendente diversidad de sistemas y dispositivos. Esto se debe principalmente a la amplia variedad de

combinaciones de matriz cristalina-ion activo que constituyen el medio de ganancia laser. Por ello, el rango espectral que cubren estos sistemas es muy amplio, abarcando desde el visible hasta el infrarrojo medio. Además, estos láseres pueden operar en régimen continuo o pulsado, con pulsos que van desde los nanosegundos a los femtosegundos [Kaminskii 1990, Keller 2003, Sennaroglu 2006]. Estas características, junto con la compacidad y estabilidad, han hecho posible la utilización de los SSLs en campos que abarcan desde grandes instalaciones que requieren potencias de Teravatios, hasta diseños en fibra o en guías de onda micrométricas.

En la actualidad el interés científico por estudiar y comprender procesos fundamentales a escalas cada vez más pequeñas ha hecho que sean necesarias fuentes de luz coherente de tamaños sub-micrométricos. Las limitaciones que sufren los sistemas ópticos convencionales a estas escalas, debido principalmente a difracción óptica, hacen que el desarrollo de láseres a escala nanométrica constituya un objetivo altamente buscado. Alcanzar esta meta posibilitaría el desarrollo de nuevas herramientas para investigar los límites de la física más allá del límite de difracción de la luz. Considerando las prestaciones y ventajas anteriormente descritas, sería de especial interés obtener un SSL activado con RE^{3+} en tamaño nanométrico, manteniendo sus características de estabilidad física y química, estabilidad en frecuencia y calidad espectral de línea características de los SSLs.

En este contexto Bergman y Stockman predijeron de manera teórica en 2003 una nueva clase de acción láser mediada por ondas de densidad de carga electrónica en metales a escalas nanométricas [Bergman 2003]. Son los llamados láseres plasmónicos. En contraste con los láseres clásicos, los láseres plasmónicos amplifican luz acoplada a las oscilaciones electrónicas que soportan determinadas estructuras metálicas permitiendo que el tamaño físico y el volumen modal del dispositivo se reduzcan por debajo del límite de difracción. Como consecuencia estos sistemas pueden presentar nuevas e interesantes ventajas que, dependiendo de las configuraciones, pueden traducirse en una reducción del umbral de bombeo, en modificaciones de la direccionalidad de la radiación emitida, una drástica reducción del volumen modal, mayor eficiencia...

Desde la predicción teórica en 2003 solamente algunas configuraciones particulares de láseres plasmónicos han sido demostradas. En 2009 se publicaron los primeros trabajos experimentales donde se emplearon semiconductores (InGaAs y CdS) o moléculas de colorante orgánico (OG 488) como medios de ganancia [Hill 2009, Noginov 2009, Oulton 2009]. Aunque la temática ha avanzado, hasta la fecha del presente trabajo no se ha demostrado la influencia de los plasmones de superficie en la respuesta óptica de un SSL.

1.2 Objetivos y aportación original

El objetivo principal de esta tesis se ha centrado en conseguir por primera vez acción láser en la nanoescala en un SSL. Para ello se asoció un SSL activado con RE^{3+} con nanoestructuras metálicas con el fin de explotar el fenómeno de localización e intensificación de radiación electromagnética, asociado con las resonancias plasmónicas, en las cercanías de los iones RE^{3+}. Bajo este enfoque la investigación realizada puede resumirse en tres puntos: i) fabricación de nanoestructuras metálicas con respuesta plasmónica sobre el medio de ganancia óptica consistente en un sustrato ferroeléctrico dopado con RE^{3+}; ii) el estudio de la espectroscopia óptica de este nuevo sistema híbrido plasmón-RE^{3+} y iii) obtención de acción laser en la nanoescala mediante la acción de las nanoestructuras plasmónicas en el medio de ganancia constituido por un SSL.

i) Para conseguir nanoestructuras de respuesta plasmónica sobre nuestro material laser nos hemos basado en un proceso de deposición foto-inducida, llamada *litografía ferroeléctrica,* en el que las superficies polares de los materiales ferroeléctricos se aprovechan como plataformas funcionales para el ensamblado de nanopartículas (NPs). En concreto se utilizaron las estructuras monodimensionales de dominios ferroeléctricos, presentes en un cristal de $LiNbO_3$ dopado con iones Nd^{3+}, como plantillas para el ensamblado de NPs de plata. La aportación original de este primer bloque ha sido obtener por vez primera alineamientos de NPs de Ag sobre un sustrato ferroeléctrico dopado con iones de RE^{3+}. Además, estas nanoestructuras se obtuvieron tanto sobre superficies polares en corte Z como sobre superficies en corte Y del $LiNbO_3$:Nd^{3+}, demostrando en este último caso la validez de la técnica de litografía ferroeléctrica en superficies no polares. Los resultados obtenidos relativos a la fabricación de nanoestructuras metálicas muestran el valor añadido de los materiales ferroeléctricos para ofrecer una alternativa simple y de bajo coste frente a técnicas de fabricación más complejas y costosas actualmente empleadas para la deposición de nanoestructuras metálicas. En el marco de la tesis, la deposición de NPs metálicas sobre un cristal ferroeléctrico dopado con iones de Nd^{3+} supuso el punto de partida de este trabajo y constituyó la pieza clave en el estudio de las interacciones ópticas entre plasmones localizados y las propiedades ópticas de los iones Nd^{3+}.

ii) De entre las diferentes impurezas de RE^{3+} elegimos el ion Nd^{3+}, siendo en este trabajo la primera vez que se estudia la interacción de este ión con resonancias plasmónicas localizadas. El ion Nd^{3+} constituye uno de los iones láser más utilizados ya que presenta excelentes propiedades pudiendo funcionar como láser de cuatro niveles, en modo continuo o pulsado y presentando un nivel metaestable de alta eficiencia cuántica. Gracias a su configuración electrónica $4f^3$, este ión cuenta con

numerosas bandas de absorción en el espectro visible e infrarrojo cercano, haciendo que su bombeo óptico sea fácilmente accesible y eficiente. Para analizar la espectroscopia del sistema en presencia de las NPs de Ag se empleó principalmente la técnica de microscopia de fluorescencia. Se demostró por primera vez la emisión espontanea de los iones Nd^{3+} cercanos a las nanoestructuras plasmónicas, consiguiendo además intensificar de manera selectiva la emisión procedente de transiciones las Stark del Nd^{3+} con polarización específica aprovechando la simetría que presentaban estas nanoestructuras. Adicionalmente, se estudiaron los efectos de orden de los arreglos de NPs de plata sobre la emisión del Nd^{3+}, con el proposito de optimizar la respuesta del sistema Ag NPs/$LiNbO_3$: Nd^{3+}.

iii) Finalmente, mediante el diseño de una cavidad óptica apropiada se demostró acción láser en la nanoescala en el sistema $LiNbO_3$: Nd^{3+} gracias a la mediación de las estructuras plasmónicas. Este resultado constituye la primera demostración de oscilación láser con confinamiento espacial nanométrico en un medio de ganancia constituido por un SSL. La oscilación laser del sistema se consiguió a temperatura ambiente, y se obtuvo una reducción del umbral de bombeo y una mejora sustancial de la eficiencia láser con respecto a la operación del sistema en volumen. Todo esto permite considerar este trabajo como el punto de partida para extender los resultados a una amplia lista de medios de ganancia de estado sólido, constituidos por la gran cantidad de combinaciones entre iones RE^{3+} (por ejemplo Er^{3+}, Yb^{3+}, Cr^{3+}, Ti^{3+},…) y matrices aislantes. Esta nueva clase de láseres plasmónicos mejoraría y aportaría nuevas prestaciones de los sistemas SSLs actuales manteniendo las ventajas previamente descritas de los mismos.

La alta focalización e intensidad de campo cercano de láseres plasmónicos podría ser útil para técnicas de fotolitografía, que permitirán reducir el tamaño de los láseres convencionales más allá del límite de difracción de la luz. También podrían ser útiles para aumentar la capacidad de almacenamiento de información en soportes ópticos. Por otra parte, el fuerte confinamiento de campo eléctrico de los láseres plasmónicos podría utilizarse para amplificar procesos de poca intensidad. Por ejemplo, se podría aplicar en la detección de moléculas individuales, permitiendo el desarrollo en sistemas de bio-detección extremadamente sensibles o conseguir realizar mediciones in-situ y en la nanoescala en técnicas como la espectroscopia Raman o la espectroscopia de fluorescencia. Además, gracias a su pequeño tamaño y su potencial de operar a altas frecuencias, representan una fuente de luz prometedora para circuitos fotónicos ultra-compactos y ultra-rápidos. Por lo tanto los láseres plasmónicas ofrecen la posibilidad de explorar las interacciones extremas entre luz y materia, abriendo nuevos caminos en el campo de los circuitos fotónicos activos, bio-sensores y tecnologías basadas en información cuántica.

En esencia el trabajo presentado en esta tesis ha aportado las bases para entender y optimizar las propiedades fotónicas de este nuevo sistema híbrido Ag NPs/$LiNbO_3$**:**Nd^{3+}, y demostrar por primera vez la acción de un láser de estado sólido en la nanoescala.

1.3 Trabajos compendiados

Los resultados obtenidos durante la tesis doctoral han dado lugar a 5 publicaciones (una de ellas en proceso de revisión a la fecha de presentación de la documentación) en las siguientes revistas científicas: Advanced Materials, Nano Letters, Optics Express y Journal of Luminescence. A continuación se presenta la lista de publicaciones:

1. **Spontaneous emission and nonlinear response enhancement by silver nanoparticles in a Nd^{3+} doped periodically poled $LiNbO_3$ laser crystal**
   E. Yraola, P. Molina, J. L. Plaza, M. O Ramírez, L. E. Bausá
   Advanced Materials **25**, 910-915 (2013).
   Inside Front Cover - Advanced Materials. **25**, 794 (2013).

2. **Selective plasmon enhancement of the 1.08 μm Nd^{3+} laser Stark transition by tailoring Ag nanoparticles chains on a PPLN Y‑cut**
   P. Molina, E. Yraola, M. O Ramírez, J. L. Plaza, C. de las Heras, L. E. Bausá
   Nano Letters. **13**, 4931 (2013).

3. **Controlling solid state gain media by deposition of silver nanoparticles: from thermally-quenched to plasmon-enhanced Nd^{3+} luminescence**
   E. Yraola, L. Sánchez-García, C. Tserkezis, P. Molina, M. O Ramírez, J. L. Plaza, J. Aizpurua, L. E. Bausá
   Optics Express **23**, 15670 (2015).

4. **Polarization-selective enhancement of Nd^{3+} photoluminescence assisted by linear chains of silver nanoparticles**
   E. Yraola, L. Sánchez-García, C. Tserkezis, P. Molina, M. O Ramírez, J. Aizpurua, L. E. Bausá
   Journal of Luminescence (2015). doi:10.1016/j.jlumin.2014.12.053

5. **Plasmon assisted Nd^{3+} based solid-state nanolaser**
   P. Molina, E. Yraola, M. O. Ramírez, C. Tserkezis, J. L. Plaza, J.Aizpurua, J. Bravo-Abad, L.E. Bausá.
   Nano Letters (en proceso de revisión).

Además, este trabajo ha dado lugar a 15 comunicaciones en congresos internacionales y nacionales relacionados con el tema de tesis. 7 de las cuales han correspondido a charlas invitadas.

1.4 Estructura de la tesis

El manuscrito está estructurado como sigue. Después de una introducción que incluye la justificación y originalidad del trabajo se continúa con cuatro secciones útiles para una mejor comprensión de los artículos presentados. Las tres primeras sientan las bases de la temática tratada en esta tesis y el estado del arte de las mismas. En concreto, en la sección 1 abordamos los materiales ferroeléctricos desde el punto de vista de su uso en la técnica de litografía ferroeléctrica, en la sección 2 el cristal $LiNbO_3$**:**Nd^{3+} como sistema laser de estado sólido, y en la sección 3 los plasmones localizados de superficie enfocados en la intensificación de las propiedades ópticas de los iones RE^{3+} y su acción laser. Finalmente, la cuarta sección se presenta un resumen de las técnicas experimentales empleadas en la tesis. El manuscrito de tesis continúa con un resumen global, las publicaciones compendiadas y las conclusiones.

English

1 General introduction

1.1 Motivation

One of the main research areas in the field of photonics is focused on the study and development of new laser devices since they constitute the source of electromagnetic radiation with the highest degree of coherence, spectral density and possibility of manipulation and control.

Since the first demonstration of laser action more than 50 years ago, laser science has experienced great advances being available nowadays in extreme configurations such as high-power lasers designed for nuclear fusion experiments, ultra-fast lasers used to investigate chemical reactions and atomic processes, or compact micro-lasers which can be implemented in large data networks [Jackson 2012, Perry 1994, Zayhowski 1989].

Among all the different laser types that can be found nowadays, solid state lasers (SSL) stand out for their excellent and versatile properties, being an essential tools in a large variety of scientific and technological areas. In this type of lasers the gain medium is constituted by rare earth ions (RE^{3+}), transition metal ions or color centers, incorporated as impurities or optically active defects in insulating matrices such as crystals, glasses or ceramics. In these systems the laser transition occurs between the energy levels of these dopants.

Since the first experimental demonstration of the ruby laser in 1960 [Maiman 1960], the development of SSLs has led to an enormous and amazing variety of systems and devices. This is mainly due to the wide variety of crystal matrix-optical ion combinations that constitute the laser gain medium. Therefore, the spectral range covered by these systems is very large, going from the visible to the mid-infrared. In

addition, these lasers can operate in continuous or pulsed regimes with pulses ranging from nanoseconds to femtoseconds [Kaminskii 1990, Keller 2003, Sennaroglu 2006]. All these features, together with its compactness and stability, have enabled the use of SSLs in fields that range from large Terawatt installations, to fiber designs or micro-sized wave guides.

Today, the scientific interest to study and understand the fundamental processes at increasingly smaller scales has made necessary the development of coherent light sources of sub-micrometric sizes. The limitations experienced by conventional optical systems at these scales, mainly due to optical diffraction, have made the development of nanosized lasers a highly pursued objective. Achieving this goal would enable the development of new tools to investigate the limits of physics beyond the diffraction limit of light. Considering the benefits and advantages described above, it would be of particular interest to obtain SSLs in a nanometric size, maintaining their advantageous features such as physical, chemical and frequency stability and spectral line quality.

In this framework Bergman and Stockman theoretically proposed in 2003 a new type of laser action mediated by electronic charge density waves in nanoscaled metals [Bergman 2003]. These are the so-called plasmonic lasers. In contrast with classical lasers, plasmonic lasers amplify light coupled to the electronic oscillations supported by specific metallic structures allowing their physical size and modal volume to be reduced below the diffraction limit. As a result these systems can present new and interesting advantages that, depending on the configuration, may be referred to a reduction of the pump threshold, modifications in the directionality of the emitted radiation, a drastic reduction of the modal volume, a higher efficiency...

Since the theoretical prediction in 2003 only some particular plasmonic laser configurations have been demonstrated. In 2009 several experimental works were published, in which semiconductors (InGaAs and CdS) or organic dye molecules (OG 488) were used as gain media [Hill 2009, Noginov 2009, Oulton 2009] in association with metallic nanostructures. Though this topic has advanced, up to the date, the influence of surface plasmons on the optical response of a SSL has not been demonstrated.

1.2 Main goals and original contribution

The main objective of this thesis has been focused on achieving for the first time lasing action at the nanoscale from a SSL. For this purpose we have associated a RE^{3+} based SSL with metallic nanostructures to exploit the phenomenon of localization and

intensification of electromagnetic radiation near the RE^{3+} ions due to the plasmonic resonances. Under this approach the research can be summarized in three main points: i) fabrication of metallic nanostructures with plasmonic response on an optical gain medium consisting of a RE^{3+} doped ferroelectric substrate; ii) study the optical spectroscopy of this new hybrid plasmon-RE^{3+} system, and iii) obtaining laser action at the nanoscale through the action of plasmonic nanostructures in the gain medium based on a SSL.

i) In order to obtain nanostructures of plasmonic response on our laser material we employed a photo-induced deposition process, called ferroelectric lithography, in which the polar surfaces of the ferroelectric materials are used as functional platforms for the assembly of nanoparticles (NPs). Specifically, ferroelectric mono-domain structures, presented in a $LiNbO_3$ crystal doped with Nd^{3+} ions, were used as templates for assembling of silver NPs. The original contribution of this first block was to obtain for the first time alignments of Ag NPs on a RE^{3+} doped ferroelectric substrate. Furthermore, these nanostructures were obtained on both Z-cut (polar) and Y-cut (non-polar) surfaces of the $LiNbO_3$:Nd^{3+}, providing in the latter case the validity to use the ferroelectric lithography technique in non-polar surfaces. The obtained results relative to the metallic nanostructures show the value of such ferroelectric materials to offer a simple and low-cost method alternative to the more complicated and expensive techniques currently used for the deposition of metallic nanostructures. In the frame of this thesis, the deposition of metallic NPs on a Nd^{3+} doped ferroelectric crystal constituted the starting point of the work and constituted the key task for the study of optical interactions between localized surface plasmons and the optical properties of Nd^{3+} ions.

ii) Among the different RE^{3+} impurities Nd^{3+} ion was chosen. The Nd^{3+} ion is one of the most widely used laser ions since it presents excellent properties that allow it to operate as a four-level laser in continuous or pulsed regime, having a metastable level of high quantum efficiency. Due to its $4f^3$ electronic configuration, this ion has numerous absorption bands in the visible and near infrared range, making its optical pumping easily accessible and efficient. In our work the intensification of the spontaneous emission of Nd^{3+} ions near the plasmonic nanostructures was demonstrated. Furthermore, a selectively intensification of the Nd^{3+} Stark transitions of specific polarization was achieved, taking advantage of the linear symmetry presented by these nanostructures. Additionally, the effects of ordering of the silver NPs arrangements on the Nd^{3+} emission were studied, in order to optimize the response of Ag NPs/$LiNbO_3$:Nd^{3+} system.

iii) Finally, thanks to the appropriate designing of an optical cavity, laser action at the nanoscale was demonstrated in the $LiNbO_3$:Nd^{3+} system mediated by the

plasmonic nanostructures. This result is the first demonstration of laser oscillation presenting nanometric spatial confinement in a gain medium consisting of a SSL. The laser oscillation system was achieved at room temperature, obtaining a reduction in the pump threshold and a substantial improvement of the laser efficiency with respect to the bulk laser operation. This allows to consider this work as a starting point to extend the results to the vast list of solid state gain media comprising the large number of combinations between RE^{3+} ions (for instance Er^{3+}, Yb^{3+}, Cr^{3+}, Ti^{3+}, …) and insulating matrices. This new class of plasmonic lasers would provide new capabilities to the current SSLs, while preserving their advantages. The highly focused near field of plasmon lasers could be useful for photolithography, enabling feature sizes beyond the limits of conventional lasers. These systems could also be useful for packing more data onto optical storage media. Moreover, the strong electric field confinement in plasmon lasers could be utilized to amplify very weak effects. This could be employed for detecting single molecules, allowing for extremely sensitive bio-detection and in-situ nanoscale Raman and Fluorescence spectroscopy. Furthermore, owing to their small size and potentially high frequency operation, they are a promising light source for ultra-compact and fast photonic circuits. Plasmonic lasers thus offer the possibility of exploring extreme interactions between light and matter, opening up new avenues in the fields of active photonic circuits, bio-sensing and quantum information technology.

Summarizing, the work presented in this thesis constitutes the first work which aims to understand and optimize the photonic properties of this new hybrid system Ag NPs/$LiNbO_3$: Nd^{3+}, and demonstrate for the first time the laser action of a SSL at the nanoscale.

1.3 List of publications

The results obtained during this thesis have resulted in 5 publications (one still under review at the time of submission) in the following scientific journals: Advanced Materials, Nano Letters, Optics Express and Journal of Luminescence. The list of publications is presented below:

1. **Spontaneous emission and nonlinear response enhancement by silver nanoparticles in a Nd^{3+} doped periodically poled $LiNbO_3$ laser crystal**
   E. Yraola, P. Molina, J. L. Plaza, M. O Ramírez, L. E. Bausá
   Advanced Materials **25**, 910-915 (2013).
   Inside Front Cover - Advanced Materials. **25**, 794 (2013).

2. **Selective plasmon enhancement of the 1.08 μm Nd^{3+} laser Stark transition by tailoring Ag nanoparticles chains on a PPLN Y‑cut**
   P. Molina, E. Yraola, M. O Ramírez, J. L. Plaza, C. de las Heras, L. E. Bausá
   Nano Letters. **13**, 4931 (2013).

3. **Controlling solid state gain media by deposition of silver nanoparticles: from thermally-quenched to plasmon-enhanced Nd^{3+} luminescence**
   E. Yraola, L. Sánchez-García, C. Tserkezis, P. Molina, M. O Ramírez, J. L. Plaza, J. Aizpurua, L. E. Bausá
   Optics Express **23**, 15670 (2015).

4. **Polarization-selective enhancement of Nd^{3+} photoluminescence assisted by linear chains of silver nanoparticles**
   E. Yraola, L. Sánchez-García, C. Tserkezis, P. Molina, M. O Ramírez, J. Aizpurua, L. E. Bausá
   Journal of Luminescence. (2015).
   http://dx.doi.org/10.1016/j.jlumin.2014.12.053

5. **Plasmon assisted Nd^{3+} based solid-state nanolaser**
   P. Molina, E. Yraola, M. O. Ramírez, C. Tserkezis, J. L. Plaza, J.Aizpurua, J. Bravo-Abad, L.E. Bausá.
   Nano Letters (under revision).

The work has also given rise to 15 communications in national and international conferences related with the topic of the thesis. 7 of these were invited presentations.

1.4 Thesis structure

The manuscript is structured as follows. After the introduction containing the motivation and the originality of the work, we include four sections which are considered useful for a better understanding of the articles presented. The first three sections include the fundamentals of the subject and the state of art. Specifically, in the first one we begin focusing our attention on ferroelectric materials from the point of view of their properties suitable for the ferroelectric lithography technique. In the second and third one, we present some previous information on the $LiNbO_3$:Nd^{3+} crystal, and on localized surface plasmons, respectively. The fourth section summarizes the experimental techniques used in the thesis. The manuscript continues with an overall summary, the compiled publications and the conclusions.

Section I

Ferroelectric materials

In this work we have used an optical gain medium consisting of a ferroelectric crystal on which we deposited metallic NPs. Through a simple and low cost photochemical process, we used the periodic ferroelectric domains pattern presented in the crystal as a template for the selective assembly of Ag NPs. The novelty of this work is to use this technique, commonly called *ferroelectric lithography*, for the first time on a ferroelectric crystal doped with RE^{3+} impurities, specifically a $LiNbO_3$**:**Nd^{3+} crystal. In this way, we open the possibility of studying the interactions between metallic NPs and a RE^{3+} based laser substrate. The ferroelectric character associated with the spontaneous polarization of the crystal plays a significant role in the process used to obtain the selective deposition of Ag NPs. This section contains the most relevant characteristics of ferroelectric materials involved in the selective deposition process of metallic NPs.

1.1.1 Introduction

Ferroelectric materials are characterized by the presence of a spontaneous polarization (**P**) in the absence of an external electric field (**E**). This spontaneous polarization may present different orientations and can be inverted by external agents.

Figure 1.1 illustrates the classification of the 32 existing crystal classes according to their symmetry with respect to a point. Ferroelectric materials in the ferroelectric phase are also piezoelectric and pyroelectric. The reverse sense of this statement is not true. That is, not all pyroelectric and piezoelectric materials are ferroelectrics. Pyroelectricity is the property associated with materials that exhibit a spontaneous polarization **P** under the influence of a temperature variation. On the other hand, piezoelectricity arises when any charge movement, due to ionic displacement such as compression, is not compensated for, giving rise to a surface electric charge. Thus, piezoelectrics are non-polar, but present a surface charge. All these kinds of materials are contained in the non-centrosymmetric crystal classification due to their absence of inversion symmetry.

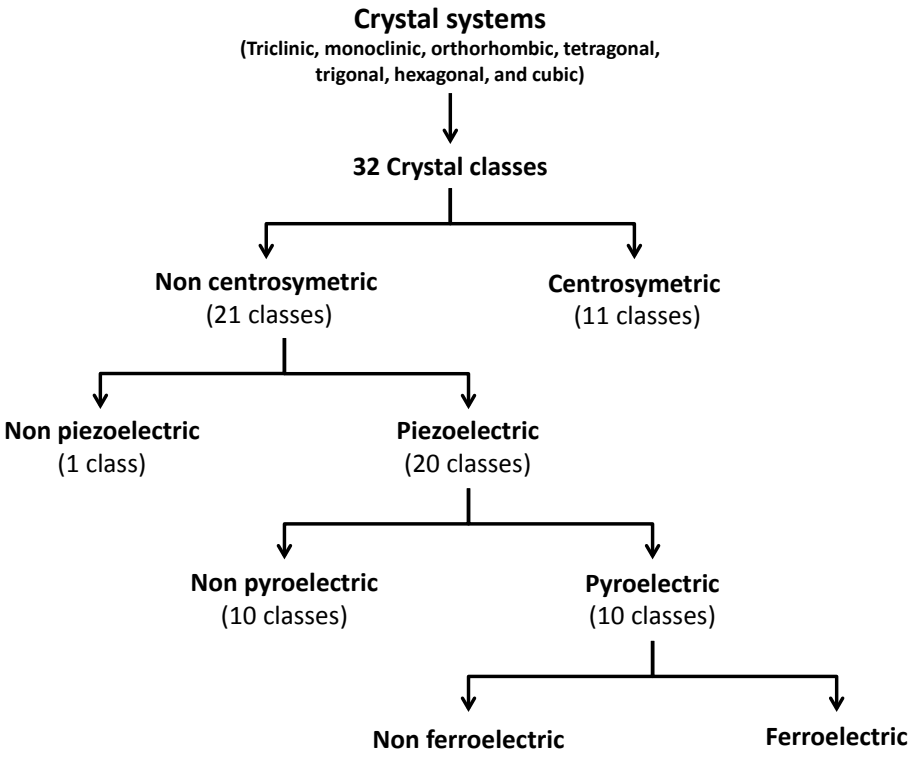

Figure 1.1: Classification of crystal systems according to their properties.

The lack of inversion symmetry is responsible for the nonlinear optical response of these materials, enabling the generation of nonlinear processes related with the even-order non-linear susceptibilities, specifically with the second order susceptibility $\chi^{(2)}$, which accounts, among others, for the sum and difference frequency generation.

The term "ferroelectric" was first introduced by E. Shrodinger in 1912, but it was not until 1920 when J. Valasek experimentally demonstrated that the direction of spontaneous polarization in a Rochelle salt ($NaKC_4H_4O_64H_2O$) could be reversed by applying a field external electric [Valasek 1921]. During the 40s many different ferroelectric materials, such as $BaTiO_3$, $KNbO_3$, $NaNbO_3$, $LiNbO_3$, $LiTaO_3$ and $PbTiO_3$, were discovered and investigated [Matthias 1948, Matthias 1949, Matthias 1951, Shirane 1950]. Since then, the interest in ferroelectric materials has increased due to their many applications [Auciello 1998, Dawber 2005, Scott 2007, Uchino 2000]. Nowadays, more than a thousand ferroelectric materials have been reported, including oxides, fluorides, organic materials, etc...

The origin of **P** in ferroelectrics arises from the specific arrangement of atoms or molecules that constitute the ferroelectric material, and the relative displacement between ions in the crystal lattice. Thus, ferroelectricity is understood as a cooperative phenomenon in which the spontaneous polarization of a single unit cell interacts with

its adjacent generating a permanent net dipole moment per unit volume [Xu 2013]. The key feature that characterizes ferroelectric materials is that the spontaneous polarization can be reoriented by means of an external agent such as an electric field (**E**). The electric field dependence of the polarization follows a hysteresis loop which presents well-defined saturated and concave regions [Scott 2008]. A typical hysteresis loop is shown in Figure 1.2.

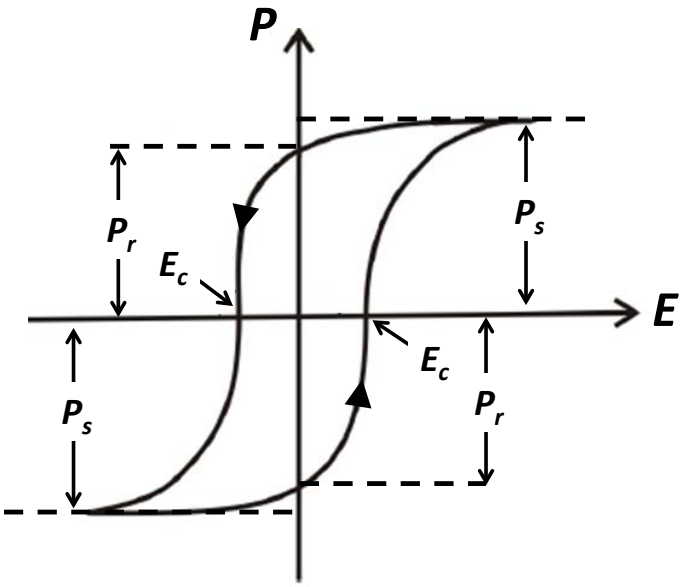

Figure 1.2: Hysteresis cycle for a ferroelectric representing the polarization of the material versus the electric field. E_c refers to the coercive field, whereas P_s and P_r stand for the saturation polarization and the remnant polarization, respectively.

When no electric field is applied **P** can take two stable values of opposite polarity ($\pm P_r$) which are called remnant polarization states, while for high values of **E**, **P** tends to saturate to $+P_s$ or $-P_s$, regarding the sign of **E**. The coercive field E_c is defined as the electric field that has to be applied so that the polarization presents a null value. Therefore, in order to reverse the spontaneous polarization in a given region, it is necessary to overcome this value. The value of the coercive field for a given material depends on the temperature, and is also sensitive to the presence of defects and impurities. For the case of congruent $LiNbO_3$ (see next Section), the coercive field is around 21 kV/mm, while for a stoichiometric composition this value is reduced to ~ 2 - 3 kV/mm [Gopalan 1998].

1.1.2 Ferroelectric domains and domain walls

Ferroelectrics typically exhibit regions called *domains*, which present a well defined value of **P**. Thus, the boundary between two adjacent domains constitutes a ferroelectric *domain wall*. Figure 1.3 shows different configurations of domain orientations and walls that can be found in different ferroelectrics.

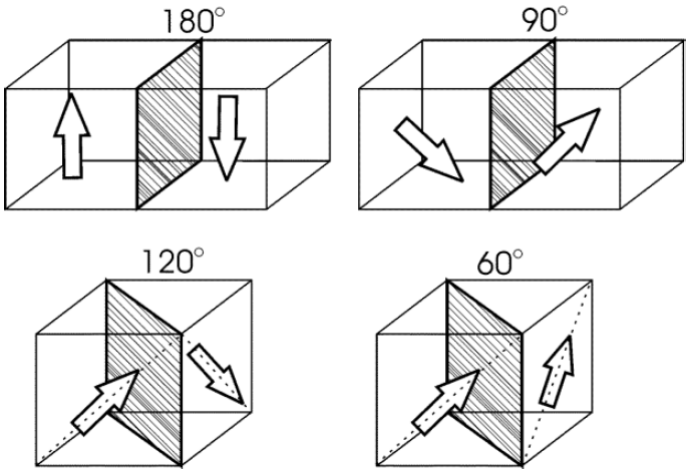

Figure 1.3: Configurations of domains and domain walls in ferroelectrics. The arrows indicate the orientations of the spontaneous polarization **P** [Gupta 2006].

The different orientations that **P** can take in a ferroelectric depend on the point group symmetry of the material. Similarly, the domain walls are restricted by the symmetry of the different crystal planes within the crystal.

All materials may present antiparallel ferroelectric domains (with an angle of 180^o between +**P** and -**P**). Regarding their specific crystal symmetry, ferroelectrics may also present other angles between domains. For the specific case of $LiNbO_3$ crystals its uniaxial trigonal symmetry leads, in the most common cases, to such 180^o domains. The formation of these ferroelectric domains can be understood from a classical point of view considering a monodomain film with the spontaneous polarization perpendicular to the faces of it. The ferroelectric surface is characterized by a polarization charge density given by:

$$\sigma_{pol} = \mathbf{P} \cdot \hat{n} \tag{1.1}$$

where **P** is the polarization vector and $\hat{n}$ is the unit normal to the surface. Therefore, the face pointed by **P** has a bound surface charge density of the same modulus and positive sign (σ = +P), whereas for the opposite face the surface charge has negative sign (σ = -P). The presence of these surface charge density, is related to an electric field at the surface E_d = - P·ε_0, which is called the depolarization field and has opposite direction to **P**. This E_d tends to destabilize the ferroelectric domain so that a mechanism to neutralize the surface charges and counteract the effect of E_d becomes necessary.

The natural alternative to neutralize E_d is the presence of a multidomain state in which the depolarization fields vanish in average. On the other hand, the formation of

domain walls requires a certain amount of energy (W_w). Thus, the balance between the decrease of depolarization energy W_d (associated with the E_d field) to form a multidomain and the increase of the domain wall energy W_w determines the final structure of ferroelectric domains in the crystal.

Calculations on the first principles have predicted that the domain walls in an ideal ferroelectric have a few unit cells thick (1 to 2), where the spontaneous polarization direction abruptly changes when crossing a wall [Meyer 2002, Padilla 1996, Poykko 1999]. On the other hand, studies conducted by Gopalan et al. [Gopalan 2007] have concluded that some elastic, optical and electrical properties may present variations that extend up to several microns in the surroundings of the domain walls.

Based on the surface properties afforded by the spontaneous polarization, assembled metallic NPs can be obtained on the ferroelectric surfaces by means of a recently developed photochemical method [Kalinin 2004]. The fundamentals of this process are described below.

1.1.3 Ferroelectric lithography

Ferroelectric lithography is a photo-chemical process which exploits the surface properties of a ferroelectric material to obtain a polarization mediated assembly of nanostructures of a given species (usually metals) on the polar surface. Its origin is mainly determined by the combination of two phenomena: the presence of a polarization dependent surface charge on ferroelectric materials and the photo-reduction of metallic cations nearby the polar surface of a ferroelectric crystal.

The polarization-dependent chemical reactivity of the ferroelectric surfaces was demonstrated shortly after the discovery of ferroelectricity [Jona 1962], but it was not until 2001 when Giocondi and Rohrer obtained for the first time domain-specific photo-deposition of metal cations on the surface of a $BaTiO_3$ crystal [Giocondi 2001]. Since then, several studies have combined ferroelectric domain patterning with domain-specific photo-deposition processes to produce a variety of metallic nanostructures on different kinds of ferroelectric substrates [Kalinin 2004, Rankin 2007, Xiaojun 2005]. Depending on the surface properties, namely on the surface defect concentration, we can obtain a domain-selective photo-deposition or an enhanced formation of nanostructures on the surface of the domain boundaries.

Experimentally, the ferroelectric lithography can be performed by illuminating the polar surface of a ferroelectric crystal with above band-gap light while it is placed in a solution containing metallic ions. The above band-gap light excitation produces

electron-hole pairs in the first layers of the surface. The electronic photocarriers can migrate to the surface under the influence of internal electric fields or under the influence of the bending of the energy bands at the surface of ferroelectrics. The electronic accumulation on the surface leads to the reduction of metallic cations from the solution. The resultant metallic deposition is selectively distributed on the surface of the ferroelectric following the underlying ferroelectric domain structure.

The formation and distribution of metallic nanostructures are deeply dependent on the surface properties of the crystal through mechanisms such as the screening of the bound charges, the bending of electronic bands at the surface of ferroelectrics, the electric field distribution on the surface, and the excitation of the charge carriers.

As previously pointed out, the ferroelectric surface is characterized by a polarization charge density (see equation 1.1). However, to have an energetically stable state this surface charge density is in most cases screened by adsorbates and/or surface states or free charges [Fridkin 1980]. Partially, completely or over-screened surfaces are likely to be the usual state of a ferroelectric surface in air. These screening charges are equivalent to have a surface charge density (σ_s) with opposite polarity to σ_{pol}. From this point of view two different scenarios have to be considered: ferroelectrics presenting mainly internal screening due to free carriers and surface-defect states, or ferroelectrics with mainly external screening arising from adsorbed charges from the environment. In Figure 1.4 both cases are schematically illustrated.

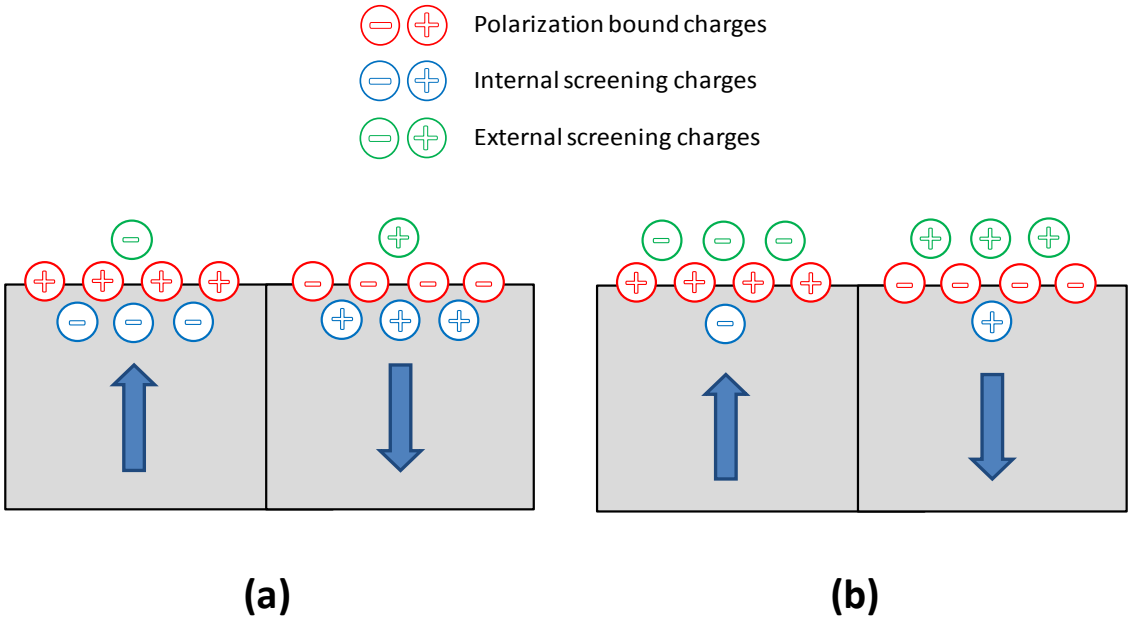

Figure 1.4: Schematic diagram of surface charges in a (a) mainly internally and (b) mainly externally screened ferroelectric crystal surface. The blue arrows indicate the orientation of the spontaneous polarization vector.

As a result of the screening charge the electronic structure of the surface is modified. The different screening processes lead to different bending of the electronic bands at the surface and to different electron affinity in the surface of positive and negative domains. The deposition rate of metallic species depends on these features.

1.1.3.1 Ferroelectric lithography in internally screened ferroelectrics

For ferroelectrics presenting a high number of charge defects (e.g. 10^{14} cm^{-2} for PZT) the screening mechanism is mainly internal [Sun 2011B]. The high concentration of surface defect states causes a strong bending of the conduction (E_c) and valence (E_v) bands in the surface proximities. This effect is schematically shown in Figure 1.5 for both positive and negative domains.

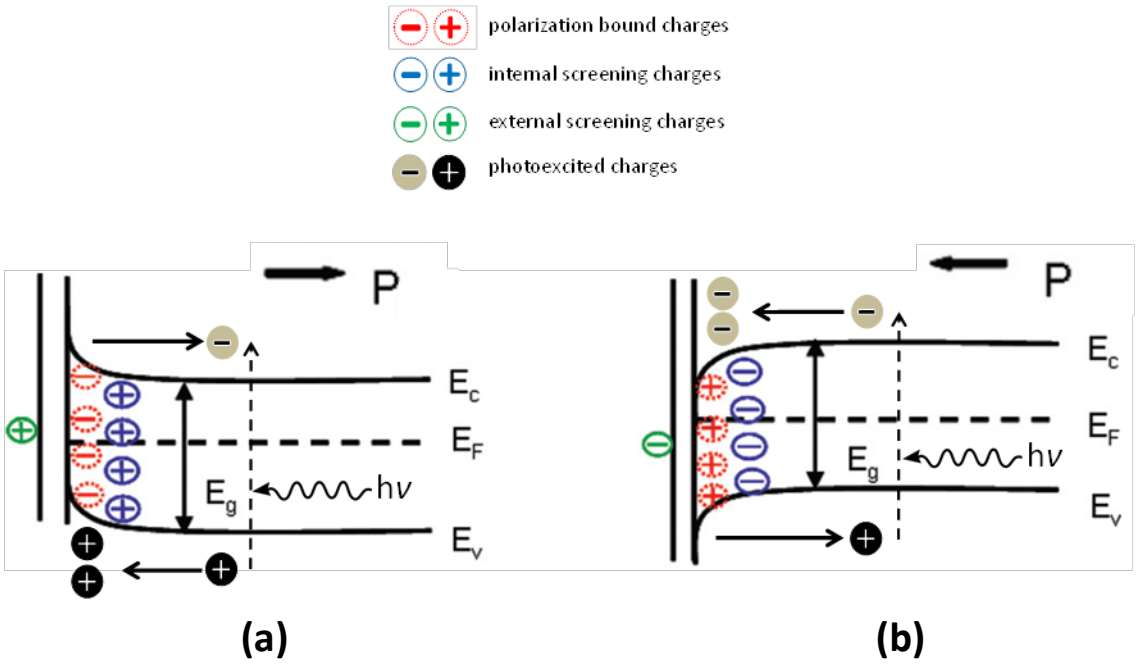

Figure 1.5: Energy band diagram for (a) negative and (b) positive domains in a ferroelectric material with internal screening. Photo-excited charge carriers are attracted towards or repealed from the surface due to the band bending.

In negative domain surfaces an upward band bending takes place inducing an accumulation of holes at the surface when charge carriers are photo-excited. On the contrary, a downward band bending occurs in positive domain surfaces inducing an accumulation of electrons at the surface. The photo-excited electrons and holes migrate to the most energetically favored state where they can accumulate, decay to the ground state, or take part in chemical reactions. On the surface of domains with specific polarization, surface reactions involving electrons or holes donation will selectively occur. Surface reactions involving electron donation (reduction) will occur

at a substantially high rate on positive domain surfaces, while reactions based on holes donation (oxidation) will preferentially occur on negative domain surfaces. Therefore, the formation of nanostructures on the surface of an internally screened ferroelectric occurs mainly on positive domain surfaces [Kalinin 2004].

If the internally screened ferroelectric is placed in solution containing metallic cations, a Stern layer is created on the surface due to the surface potential that forms when the internal charge compensation process is only partially screening the surface depolarizing field. For this case, the surface potential (*V)*, given by the Poisson equation (1.2), is determined by the surface charge (ρ) and the remnant polarization (P_r):

$$\nabla^2 V(x) = -\frac{1}{\varepsilon_0 \varepsilon_r}(\rho - \nabla P_r) \tag{1.2}$$

and the surface charge is in turn determined by the balance of positive and negative carriers and ionized atoms (1.3):

$$\rho = q(h^+ + N_A^+ - e^- - N_D^-) \tag{1.3}$$

where q denotes the elementary charge, h^+ and e^- the densities of holes and electrons respectively, and N_A^+ and N_D^- the densities of ionized defects in their respective charged states [Jones 2009]. When there is no illumination, and the surface is under equilibrium conditions, P_r is greater than ρ on the positive domains. From (1.2) it can be seen that this imbalance will give a positive value of V, leading to the attraction of negative ions. Consequently, the first plane of external charges will mainly consist of attracted anions.

Considering the case of photo-reduction of silver, Each photo-excited electron that reaches the surface can be trapped by a Ag^+ cation from the solution to be reduced to metallic Ag^0 following the next expression:

$$Ag^+ + e^- \rightarrow Ag^0 \tag{1.4}$$

For the case in which a silver nitrate ($AgNO_3$) solution is used as ionic reservoir, the first external screening layer formed on the positive domains of the crystal will consist of dissolved NO_3^- ions and polar H_2O molecules that will act as a barrier to the Ag^+ ions. On the contrary, the external layer in negative domains will be constituted of Ag^+ ions and polarized H_2O molecules [Jones 2009].

In order to generate Ag clusters on positive domains there must be a disturbance in the domain surface so that the screening molecules are driven away to let the Ag^+ ions reach the surface. If not, there would be a large barrier of negative charges that will inhibit the necessary reaction with electrons. This perturbation arises during the irradiation process when the photo-excited electrons are driven to the surface. V becomes negative, as ρ becomes greater than P_r, making the NO^{3-} ions and polarized H_2O molecules disassociate from the surface. This enables the transport of the Ag^+ ions from the solution to the surface, allowing the reduction with the available electrons.

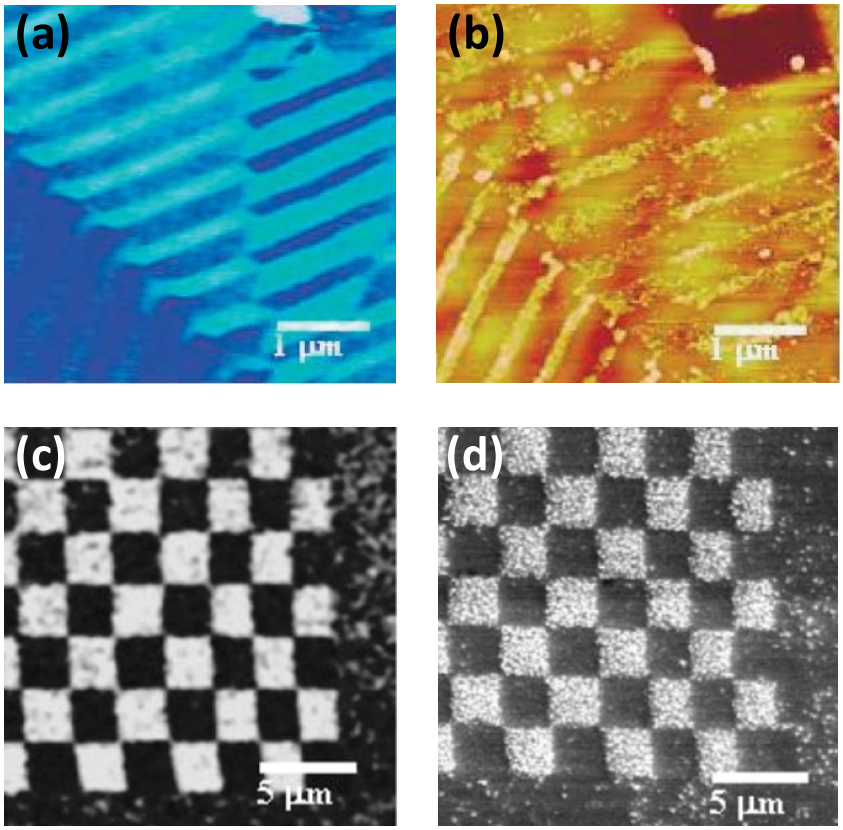

Figure 1.6: (a) PFM image of the surface of a $BaTiO_3$ crystal. The bright and dark areas indicate positive and negative domains, respectively. (b) AFM image after silver deposition. (c) Domain distributions on PZT crystal visualized through surface potential microscopy, and (d) the subsequent photo-induced deposition of Ag NPs [Kalinin 2004]. In both cases the metallic deposition is mainly distributed on positive domains.

On the other hand, in negative domains the negative bound charges repel the photo-excited electrons and inhibit the reaction. However, the generation of electron-hole pairs reduces the width of the electrons depletion region (i.e. region where photo-excited electrons diffuse and recombine) resulting in an increase of the band-bending near the surface. If the depletion region is sufficiently reduced the electrons can tunnel across the negative bound charges and react with the Ag^+ ions when they

meet [Dunn 2007]. In other words, the reduction mechanism is similar to that on the positive domains but the effective photo-current on the surface is decreased. Two examples of internally screened ferroelectric substrates are shown in Figure 1.6 before and after the photo-deposition of metallic species. They correspond to metallic species predominantly located in such a way that they are covering the domain surfaces of positive polarity.

1.1.3.2 Ferroelectric lithography in externally screened ferroelectrics

For ferroelectrics presenting smaller concentration of surface defects (e.g. 10^{12} cm^{-2} for $LiNbO_3$) the screening mechanism is mainly external [Yang 2004]. Figure 1.7 schematically shows the band-bending and photo-excitation of charge carriers for both positive and negative domains in this case.

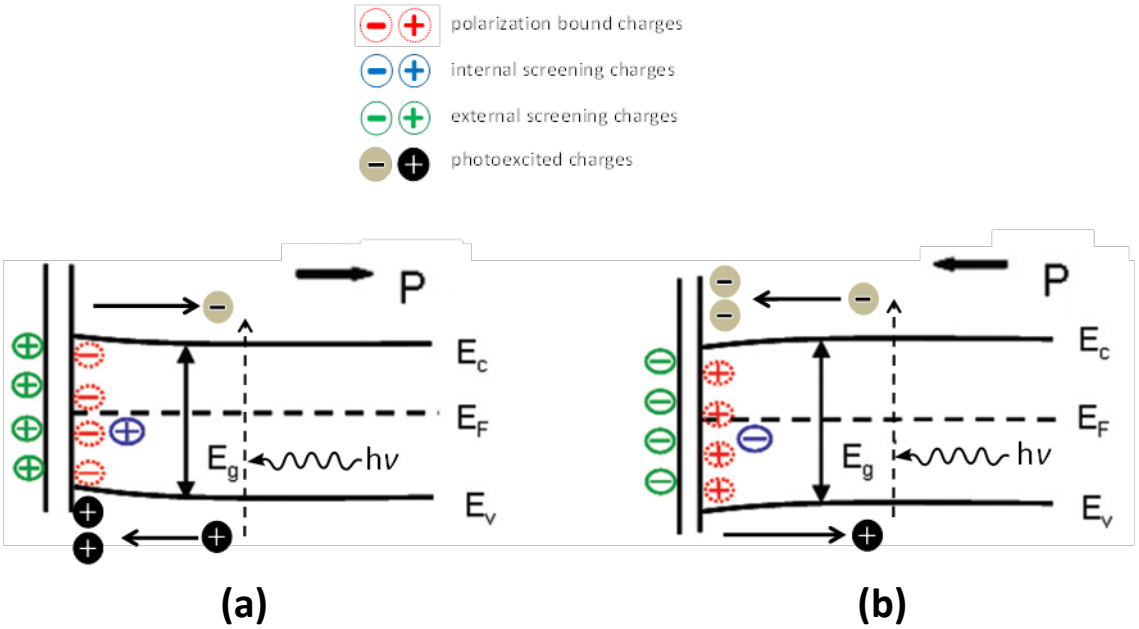

Figure 1.7: Energy band diagrams for (a) negative and (b) positive domains in an externally screened ferroelectric. Compared with the internal screening, the band bending is less pronounced but still, photo-excited charge carriers are attracted to or repealed from the polar surfaces, though at slower rates.

As observed the band bending presents the same behavior as in internally screened ferroelectrics, but less pronounced. Therefore, a similar but less remarked metallic decoration occurs preferentially on the positive domain surfaces.

In addition to the domain selective decoration of metallic NPs there is a different effect that causes the metallic NPs to grow at faster rates on the ferroelectric domain boundaries. In 2006 Hanson and co-workers performed for the first time a selective

deposition of Ag on a periodically poled $LiNbO_3$ crystal [Hanson 2006]. In contrast to previous works, metallic Ag was preferential located on the domain boundary surfaces forming Ag nanowires.

Figure 1.8 shows some images of the metallic nanowires obtained in various $LiNbO_3$ samples presenting different domain distributions. A selective photo-reduction of metallic silver is clearly observed on the domain walls. In this case, the decoration of the positive domain surfaces is practically undetectable, as a consequence of the weak band-bending. In other words, more electrons are available for the photo-reduction at the ferroelectric boundary walls than on the domain surfaces.

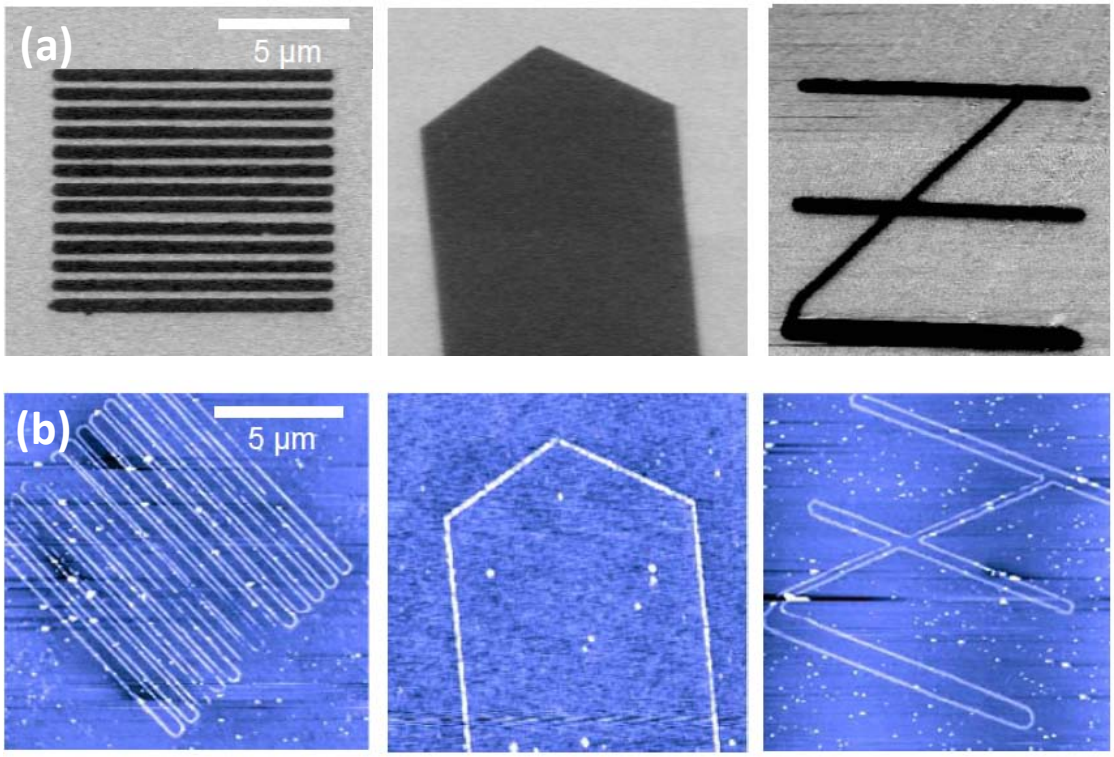

Figure 1.8: (a) PFM images of different domain patterns in different $LiNbO_3$ samples. (b) AFM images of silver nanowires formed on the corresponding domain walls after the photo-reduction [Hanson 2006].

Following the approaches made by Kalinin [Kalinin 2001], Hanson [Hanson 2006] attributed this process to the presence of an inhomogeneous electric field on the polar surface of the crystal. Figure 1.9 shows the calculations of the normal electric field component E_z (where *z* corresponds to the ferroelectric axis direction *c*) near the surface of 180^0 domain boundaries in a $LiNbO_3$ crystal, assuming external screening. As observed, a non-uniform electric field distribution with a strong E_z component (electric field perpendicular to the polar surface) is observed in the vicinity of the 180^o domain walls. Away from the boundaries the electric field decreases rapidly due to the polarization and screening charges. The E_z component near the domain boundary

surface is much larger than that in the domain surface. For this case, photo-excited electrons migrate to the surface under the influence of the electric field distribution resulting in an excess of electron charges accumulating in the surface of the ferroelectric domain boundaries.

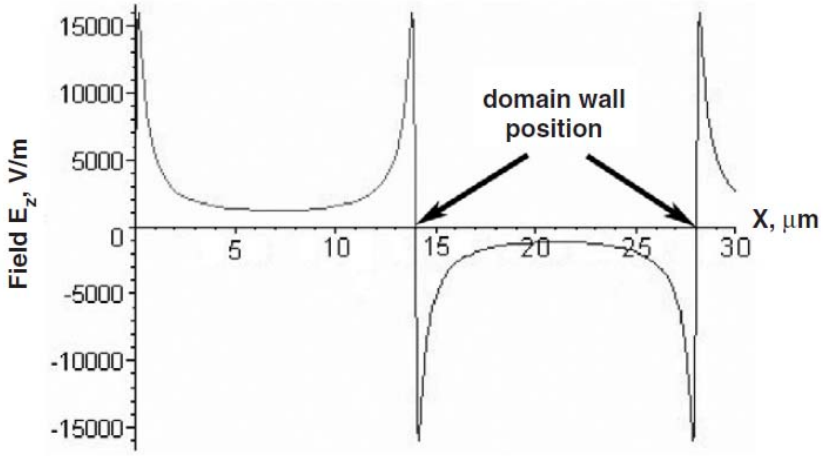

Figure 1.9: Distribution of the normal electric field component (E_z) for a $LiNbO_3$ crystal at a distance of 100 nm below the surface. Note the abrupt variations occurring at the domain boundary walls [Hanson 2006].

Since the photo-generated electrons mainly follow the magnitude of the electric field, the reduction of Ag NPs will be enhanced on the surface of the domain walls.

For the case of $LiNbO_3$, some studies have pointed out that the normal component of the electric field at the boundary is roughly 10–30 times larger than that at the domain surface, and thus, the electrons generated around the domain boundary region would migrate to the surface from a depth of several tens of nanometers, while on the domains the generated electrons would migrate to the surface only from a few nanometers [Sun 2011].

A schematic image of the photo-assisted excitation-reduction process in a $LiNbO_3$ crystal is presented in Figure 1.10, illustrating the formation of metallic Ag at a domain boundary as well as on the domain surfaces. The resulting distribution of Ag^0 atoms reflects the electric field distribution within the crystal surface

Based on these results the ferroelectric lithography technique was used during this thesis in Nd^{3+} doped $LiNbO_3$ crystals in order to obtain metallic nanostructures on an optically activated ferroelectric material. Z-cut Nd^{3+} doped (0.1 at.%) PPLN samples, grown by the off-centered Czochralski technique. The samples were immersed in a $AgNO_3$ solution of and illuminated with a UV Mercury lamp at 254 nm (see details in Section IV). Self-assembled sphere-like Ag NPs were obtained with the subsequent

observation of chain-like structures on the ferroelectric domain walls for the first time. Besides, a selective decoration with smaller NPs took place on the domain surfaces, being more pronounced on positive domain. Thus, the formation of Ag NPs on a Nd^{3+} doped $LiNbO_3$ crystal can be compared with previous works. Analogous average NPs sizes from boundaries and domain surfaces are obtained with similar preparation conditions.

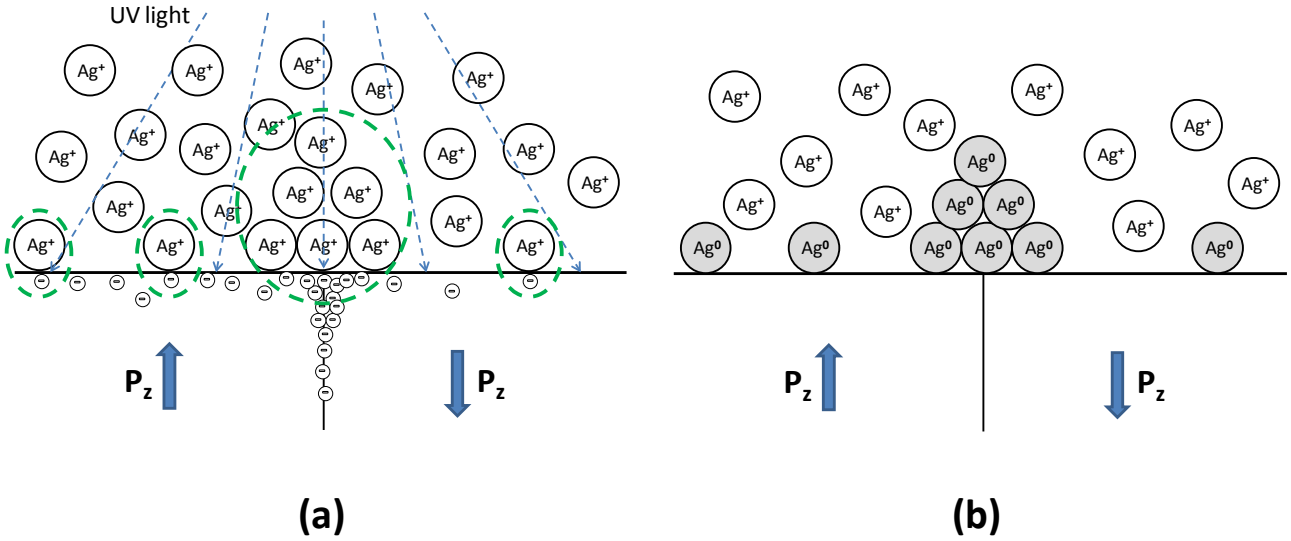

Figure 1.10: Schematics of the deposition process in a $LiNbO_3$ crystal. (a) Photo-excited electrons are driven by the internal electric fields to the surface where (b) they reduce the Ag^+ cations. [Sun 2011].

Section II

Nd^{3+} activated $LiNbO_3$ crystals

The crystal structure of $LiNbO_3$ plays a significant role in the formation and orientation of ferroelectric domains, required for the selective deposition of metallic NPs and provides a specific symmetry to the Nd^{3+} crystal environment that determines the Stark transitions of this ion. Taking this into account, in the introductory part of this section we provide the main features of $LiNbO_3$ as well as the properties associated with the presence of defects in the crystal. In order to achieve laser action in the proposed Ag NPs/$LiNbO_3$**:**Nd^{3+} hybrid system, one of the aims of this work was to study the interactions between the Ag nanostructures and the optical properties of Nd^{3+} ions embedded in the $LiNbO_3$ crystal. As starting point a presentation of the spectroscopy of Nd^{3+} in $LiNbO_3$ is needed as well as the previous results and the state of the art related with the laser action of $LiNbO_3$**:**Nd^{3+}. Accordingly, this section also contains the basics of the spectroscopy of the $LiNbO_3$**:**Nd^{3+} system, and some previous results on the laser action of this solid state gain medium.

1.2.1 Introduction

$LiNbO_3$ is a human-made dielectric material and one of the four oxides of the Li_2O-Nb_2O_5 binary system. It was first synthesized by Matthias and Remeika [Matthias 1949] in 1949 and grown, some years later, as a single-crystal by the Czochralski method by S.A. Fedulov [Fedulov 1965] and A.A. Ballman [Ballman 1965]. It presents a melting temperature of 1250° C and a hardness of 5.5 in the Mohs scale.

$LiNbO_3$ presents a exceptional combination of high electro-optic, acousto-optic, piezoelectric and nonlinear coefficients. This fact has made possible the use of this material for the development of a wide variety of optical devices such as high speed electro-optic and acousto-optic modulators, piezoelectric devices, multiplexers and self-frequency doubling generators converting the $LiNbO_3$ in the “silicon of photonics” [Arizmendi 2004].

$LiNbO_3$ shows a ferroelectric phase at room temperature [Matthias 1949.B] with a relatively large value of the spontaneous polarization (~80 $\mu C/cm^2$) [Ganesamoorthy 2005]. As previously stated, the surface properties associated with the spontaneous polarization of $LiNbO_3$ can be exploited to selectively assemble different kinds of nanostructures on its polar surfaces.

$LiNbO_3$ presents a paraelectric phase above the Curie temperature (T_c), which is located at around 1200 °C depending on the crystal composition and on the Li/Nb ratio [Bergman 1968, Bordui 1991]. The Li/Nb ratio of the crystal also determines other important features such as the density, the lattice parameter or the absorption edge. [Chow 1974, Foldvari 1984].

In its congruent composition (Li/Nb = 0.945), it presents structural defects due to the lack of Li^+ ions (Li^+ defects). The presence of these defects has important implications such as a decrease in the electro-optical coefficients and the increase in the coercive field E_c [Gopalan 1998, Tian 2004]. $LiNbO_3$ shows optical birefringence, so that it simultaneously exhibits an ordinary and an extraordinary refractive index (typical values for n_o = 2.34 and n_e = 2.25 at 488 nm [Kitaeva 1998]). As an optical system, it is transparent in the visible and NIR regions of the spectrum between 0.35 μm and 5.2 μm. In the context of this work it is worth noting the possibility to incorporate different ions as dopants in the $LiNbO_3$ matrix in order to increase or attenuate some of its properties as well as to obtain more functionalities from the system.

1.2.2 Crystal structure

In order to understand the origin of the spontaneous polarization in $LiNbO_3$ Figure 2.1 schematically shows the atomic arrangement for both paraelectric and ferroelectric phases.

Above the Curie temperature (T_c ~ 1210^{o}C) $LiNbO_3$ exhibits a paraelectric phase that corresponds to a rhombohedral structure, belonging to a symmetry point group D_{3d} and space group $R\bar{3}c$. The atomic arrangement consists of Li^+ and Nb^{5+} ions inserted between planar sheets of oxygen that form the faces of regular oxygen octahedra. The Nb^{5+} ions are centered inside the oxygen octahedra while the Li^+ ions are aligned with the oxygen sheets. Besides, the Li and Nb atoms are aligned inside the octahedra following the Li-Nb-vacancy sequence. This crystallographic system presents inversion symmetry making the paraelectric phase a non-polar structure due to the absence of a permanent dipole moment.

On the other hand, below T_c $LiNbO_3$ presents a ferroelectric phase with hexagonal symmetry, point group C_{3V} and space group R3c. In this phase Li^+ and Nb^{5+} ions are displaced in the same direction inside the oxygen octahedra. Besides, the Li^+ ions are further displaced than Nb^{5+} due to the difference in bond strengths (Li-O bonds are weaker than Nb-O bonds). The ionic displacement turns $LiNbO_3$ into a non-centrosymmetric system. Therefore, a permanent electric dipole moment and thus a spontaneous polarization **P** characterize this phase [Megaw 1954].

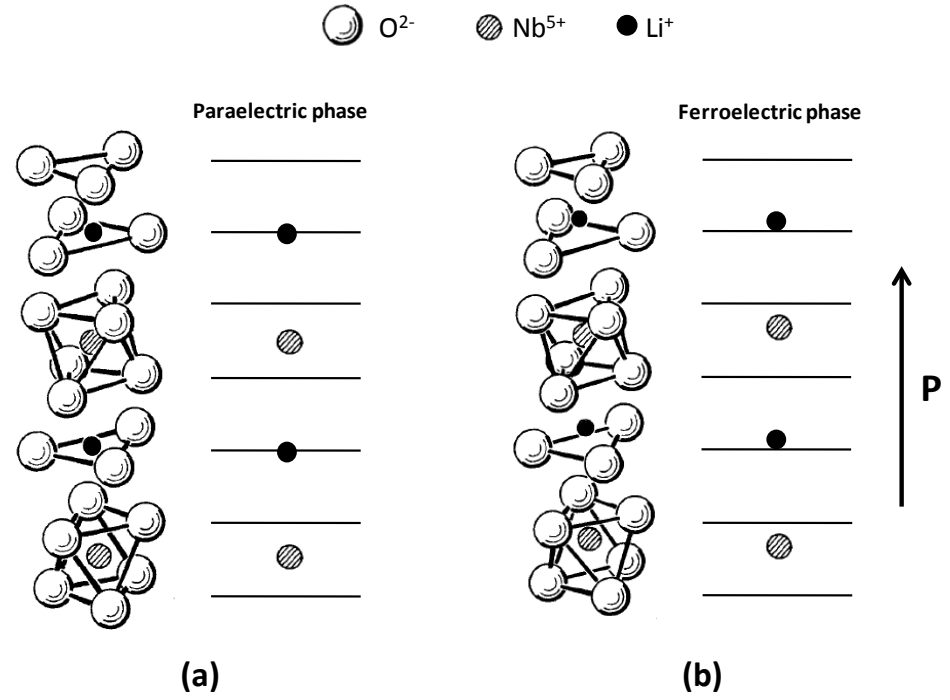

Figure 2.1: (a) Paraelectric and (b) ferroelectric structures along the c axis in $LiNbO_3$. The horizontal lines in both diagrams represent the oxygen layers. The positions of the Li^+ and Nb^{5+} ions in $LiNbO_3$ with respect to the Oxygen octahedra are shown.

In the ferroelectric phase the crystal presents a three-fold symmetry rotation axis (*z* or *c*-axis) defined by the Li^+ and Nb^{5+} ions, while two other axes (*x,y* or *a,b*-axes) are orthogonal to it. The *x*-axis is perpendicular to the mirror symmetry plane while the *y* axis is parallel to it [Weis 1985]. Since the motion of Li^+ and Nb^{5+} cations is restricted to the *z*-axis, in most cases anti-parallel ferroelectric domains (i.e. **P** switches 180° between adjacent domains) can be formed in $LiNbO_3$ crystals.

The oxygen octahedra have different sizes, since the octahedron with vacancies are greater in volume than the octahedron occupied by Li^+, and this in turn is greater than the octahedron occupied by the Nb^{5+}. In the ferroelectric phase the lattice constants for the congruent composition are a = b = 5.148 Å and c = 13.863 Å [Nassau 1966].

Figure 2.2(a) shows a real-space atomic arrangement in a *Z*-cut configuration with the corresponding *x* and *y* axes. Figure 2.2(b) schematically illustrates the orientation of the x, y and z axes in the *X*-cut, *Y*-cut and *Z*-cut, respectively. The signs of the surface in the Z-cut and Y-cut surfaces are also included.

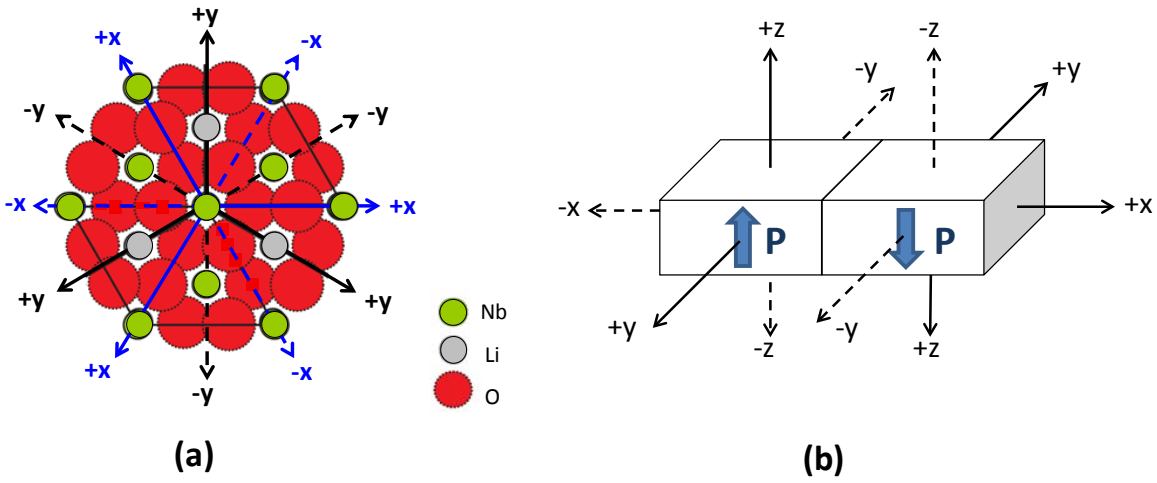

Figure 2.2: (a) Projection of the unit cell in the plane perpendicular to the z-axis. (b) Schematic picture of both *Z*-cut and *Y*-cut illustrating the orientation of the *x*, *y* and *z* axes (blue arrows correspond to the spontaneous polarization orientation).

The *y*-axis is nominally non-polar. However, piezoelectricity along this axis and the presence of a surface dipole leads to surface charge on the Y-cut. The magnitude of the surface charge on the Y-cut is approximately one-third of the one on the polar Z-cut surface [Sanna 2010]. This feature is going to play a relevant role in the formation of metallic NPs, obtained by ferroelectric lithography technique, on these non-polar Y-cut surfaces, on the frame of this work.

1.2.3 Crystal growth

At present, the Czochralski technique is the more extended method to grow bulk $LiNbO_3$. In this technique the growth is initiated by a small seed crystal that rotates, generally around the c-axis, as it is pulled from a melt in the form of a boule. The Czochralski method can be used to obtain periodically poled ferroelectric domain structures (PPLN). Specifically, using the *x*-axis as the rotation axis, and displacing it away from the temperature gradient axis of the melt, induces small temperature fluctuations that produce the appearance of periodically alternate ferroelectric domains. The width and period of the ferroelectric domains can be modulated by the rotation and pulling rates [Nai-Ben 1982]. RE^{3+} ions or other kinds of impurities seems to be needed to obtain PPLN crystals by this technique [Bermudez 1999]. In our work,

these type of structures were used as templates for selective deposition of metallic nanostructures.

1.2.4 Absorption edge in $LiNbO_3$

The absorption edge of $LiNbO_3$ is mainly determined by the transition energy (band gap energy) to promote electrons form the 2p orbitals of the Oxygen ions (valence band) to the 4d orbitals of the Niobium ions (conduction band) [Huignard 1989]. The absorption edge is located around 330-370 nm, depending on the stoichiometry and the presence of impurities. Illumination of $LiNbO_3$ within the absorption band-edge of the material induces the excitation of charge carriers in the surface, and the subsequent development of a photo-current [Lines 1977]. In the context of this work, the excitation of electronic charge carriers in the $LiNbO_3$:Nd^{3+} crystal was ensured since the illumination light source used in the ferroelectric lithography experiments had a main emission line at 254 nm.

1.2.5 Crystal defects

The presence of defects in $LiNbO_3$ plays a significant role in its physical and chemical properties. These defects can appear spontaneously during the crystal growth or arise when the crystal is doped with certain impurities. Regarding their nature, these defects are classified in two main groups: intrinsic and extrinsic defects. The presence or lack of defects can affect the value of the spontaneous polarization and therefore the deposition of metallic nanostructures.

1.2.5.1 Intrinsic Defects

$LiNbO_3$ in its congruent composition ([Li]/[Nb] = 0.945) presents a high concentration of intrinsic defects in order to compensate the deficit of Li^+ ions and ensure the charge neutrality of the crystal. These defects can cause modifications of internal local fields and modify the crystal environment, which in turn, influences the optical and dielectric properties of the crystal, and plays a crucial role in the reversal of the spontaneous polarization [Lines 1977].

Although several defect models have been proposed for congruent $LiNbO_3$ crystals, the most widely accepted is the one proposed by Iyi [Iyi 1992] and Zotov [Zotov 1994]. They proposed a structure of defects formed by Niobium antisites $(Nb_{Li})^{4+}$ surrounded by three Lithium vacancies $(V_{Li})^-$ in their nearest vicinity, plus a Lithium vacancy further separated along the *z*-axis direction. A scheme of this model is illustrated in Figure 2.3.

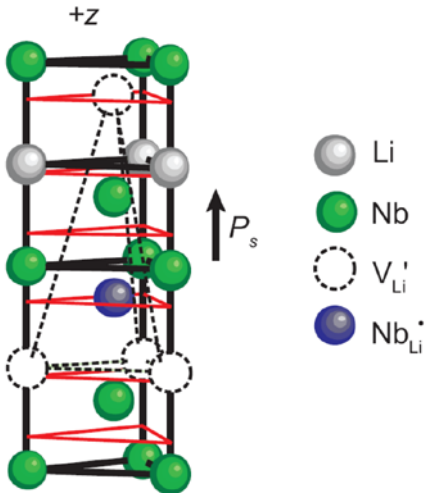

Figure 2.3: Diagram of the defect structure model in $LiNbO_3$ crystal presenting the Niobium anti-sites $(Nb_{Li})^{4+}$ and the Lithium vacancies $(V_{Li})^{-}$.

1.2.5.2 Extrinsic Defects

Extrinsic defects are generated when specific impurities are intentionally added into the crystal lattice to provide new functionalities or enhance a particular property. $LiNbO_3$ has been doped with a large variety of ions in order to perform fundamental studies and cover a wide variety of applications. Here, we present the most relevant ones:

- Optical damage inhibitors, such as Mg^{2+}, Zn^{2+} and Sc^{3+} ions, to improve the stability of laser devices [Volk 1996].

- Photorefractive enhancers, such as Fe^{2+}, for the development of optical memories [McMillen 1998].

- Optically active ions, such as transition metal ions like Cr^{3+} and Hf^{4+} or rare earth ions such as Nd^{3+}, Pr^{3+}, Eu^{3+}, Er^{3+}, Yb^{3+}, to provide absorption bands and luminescence to the crystal [Wong 2002]. Among their many applications we highlight the development of fiber amplifiers or solid-state lasers [Lallier 1992].

- Refractive index modifiers, such as Zr^{4+} ions and Ti^{4+}, to fabricate waveguides [Zhang 2015].

The position of these impurities in the crystal lattice depends mainly on the valence state of the ion and on the ionic radius. Additionally, the incorporation of these dopants depends on the composition as well as the defect structure of the

crystal. Specifically, some studies have revealed that most trivalent rare earth ions are preferentially occupying the Li^+ site in the $LiNbO_3$ lattice, with a slight shift along the ferroelectric axis [Lorenzo 1997]. Particularly, some studies have determined that Nd^{3+} occupy three off-centered Li^+ sites in $LiNbO_3$, giving place to three non-equivalent optical centers [Sole 1993].

1.2.6 The Nd^{3+} in $LiNbO_3$ system

Nd^{3+} doped $LiNbO_3$ crystal is a photonic material that combines the excellent ferroelectric and nonlinear properties of $LiNbO_3$ with the optical properties of the Nd^{3+} ion. This has allowed the design of interesting optical devices such as self-frequency-doubled lasers [Zhang 1996], self-Q-switched and self-modulated lasers [Chen 2012], and waveguide laser devices [Di Paolo 2001, Lallier 1990]. In the next section, the main spectroscopic properties of the Nd^{3+} ion in the $LiNbO_3$ crystal are presented.

1.2.6.1 The Nd^{3+} ion

Neodymium (Nd) is a rare-earth element (Z=60) that belongs to the lanthanide family. It was first discovered in 1885 by the Austrian chemist Carl Auer von Welsbach when he dissociated Didymium into Praseodymium and Neodymium. It has a melting point of 1021 °C, a boiling point of 3074 °C, a density of 7,01 g/cm^3 and atomic mass of 144,24 u. The electron configuration of the Nd atom in its neutral state is *[Xe] $4f^3$ $5d^1$ $6s^2$*. When incorporated into a solid it loses its three most energetic electrons ($5d^1$ and $6s^2$) to become Neodymium ion (Nd^{3+}) with electronic configuration *[Xe] $4f^3$*. This particular ionization provides the Nd^{3+} ion of specific and interesting optical properties. The 5s and 5p shells in the Xenon core screen the 4f shell from external perturbations. This screening effect protects the optically active electrons to some extent from the influence of the crystal field, providing the ion of sharp and well defined spectral lines [Dieke 1968].

Nd^{3+} exhibits excellent properties as an optically active ion since it presents the advantage to operate as a four-level solid-state laser when incorporated into a crystal host [Kaminskii 1990]. Nd^{3+} based lasers are widely used in a lot of industrial, technological and scientific applications, being one of the most studied rare earth ions [Guy 1998].

When Nd^{3+} is placed in a crystal environment the spherical symmetry is lost and each energy level splits under the influence of the crystal field. The corresponding Hamiltonian can be expressed as:

$$H = H_o + H_{ee} + H_{so} + H_{cc} \quad (2.1)$$

where H_o, H_{ee}, H_{so} and H_{cc} correspond to the Hamiltonians of the central field, the electron-electron interaction, the spin-orbit interaction, and the crystal field interaction, respectively. For rare earth ions the term H_{cc} is small compared with H_{so} and may be treated as a perturbation that originates a shifting and a splitting of the $^{2S+1}L_J$ states due to the presence of the external electric field (Stark effect) [Henderson 2006]. The maximum number of Stark levels of each $^{2S+1}L_J$ state depends on the quantum number of the total angular momentum (J) of the energy level, on the number of electrons of the considered ion, and on the crystal field symmetry. It can be determined by group theory as well as the selection rules that affect the electronic transitions of the ion [Heine 2007, Tinkham 2003].

Since the intra-configurational 4f→4f transitions occur between states of the same parity, in principle only magnetic dipole transitions are expected to occur. However, when the rare-earth ion is in a site which lacks inversion symmetry a mixing of opposite-parity states of the $4f^{(n-1)}5d$ configuration into the $4f^n$ states can occur. Even though the amount of this mixing is small and has a negligible effect on the energy values it may significantly change the intensity of transitions between levels allowing electric dipole components of the transition. Since the electric dipole process is in the order of five orders of magnitude stronger than the magnetic dipole it can significantly increase the transition intensity [Henderson 2006]. The resulting transitions are often called forced electric-dipole transitions.

1.2.6.2 Polarized transitions

By means of Group Theory, it is possible to identify the different Stark levels of an optical ion, as well as to obtain the selection rules to predict the polarization character of a given transition. As previously mentioned, Nd^{3+} ions preferentially occupy the Li^+ site in the $LiNbO_3$ lattice, with a C_3 symmetry. This symmetry breaks the degeneracy of the Nd^{3+} states so that each $^{2S+1}L_J$ state splits into (2J+1)/2 Stark levels. Specifically, the $^4F_{3/2}$ state splits into two Stark levels, the $^4I_{11/2}$ splits into six and the $^4I_{9/2}$ splits into five. The Stark levels are labeled through the crystal quantum number (μ) which, according to the C_3 symmetry, can only take the 1/2 and 3/2 values. Therefore, the Nd^{3+} ion levels belong to two distinct classes characterized by these two quantum numbers in $LiNbO_3$, $E_{1/2}$ and $E_{3/2}$.

$LiNbO_3$ is a uniaxial crystal, therefore, three possible configurations can be distinguished regarding the relative orientations of the electric field of light and the optical axis (c):

- π configuration: the electric field of light is parallel to the c axis of $LiNbO_3$.
- σ configuration: the electric field of light is perpendicular to the c axis of $LiNbO_3$.
- α configuration: the light beam is parallel to the c axis of $LiNbO_3$.

These three configurations are schematically illustrated in Figure 2.4.

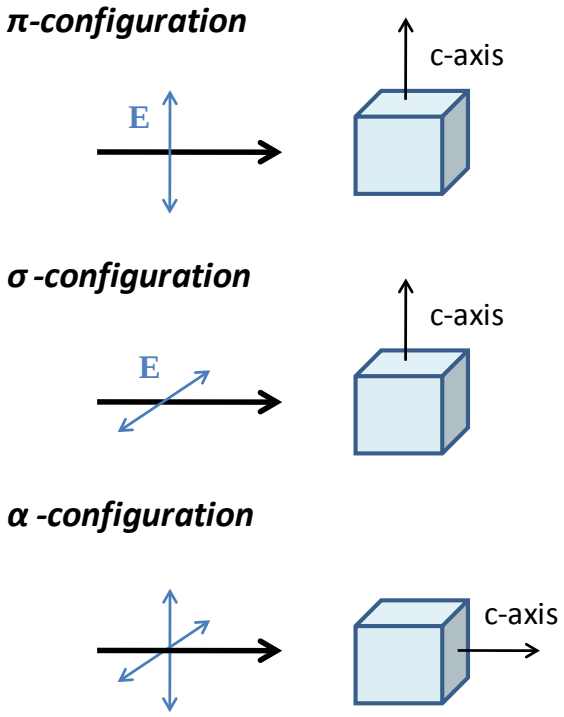

Figure 2.4: Schemes of the π, σ and α configurations in uniaxial crystals.

For the case of Nd^{3+}, in $LiNbO_3$ the σ spectrum is equal to the α spectrum in the $^4F_{3/2} \rightarrow {}^4I_{9/2}$ and $^4F_{3/2} \rightarrow {}^4I_{11/2}$ regions. This means that the relevant fact to determine the specific selection rules is the relative orientation of the electric field of light with respect to the c axis of the crystal. Thus, Nd^{3+} transitions are forced electric dipole transitions, and the polar character of the Stark levels is determined by the selection rules corresponding to the electric dipole order in the C_3 group.

The corresponding selection rules for electric dipole transitions in the C_3 symmetry are given by:

C_3	$E_{1/2}$	$E_{3/2}$
$E_{1/2}$	σ, π	σ
$E_{3/2}$	σ	π

Table 2.1: Selection rules for the transitions between $E_{1/2}$ and $E_{3/2}$ Stark levels, corresponding to the C_3 symmetry.

Therefore, the $E_{1/2} \rightarrow E_{1/2}$ transitions are allowed in π and σ configurations, the $E_{1/2} \leftrightarrow E_{3/2}$ transitions are only allowed in σ, and the $E_{3/2} \rightarrow E_{3/2}$ transitions are only allowed in π configuration.

Figure 2.5 shows an energy level scheme together with the corresponding spectra of the most relevant absorption transitions of Nd^{3+} in a $LiNbO_3$ crystal for both σ and π polarizations [Fan 1986].

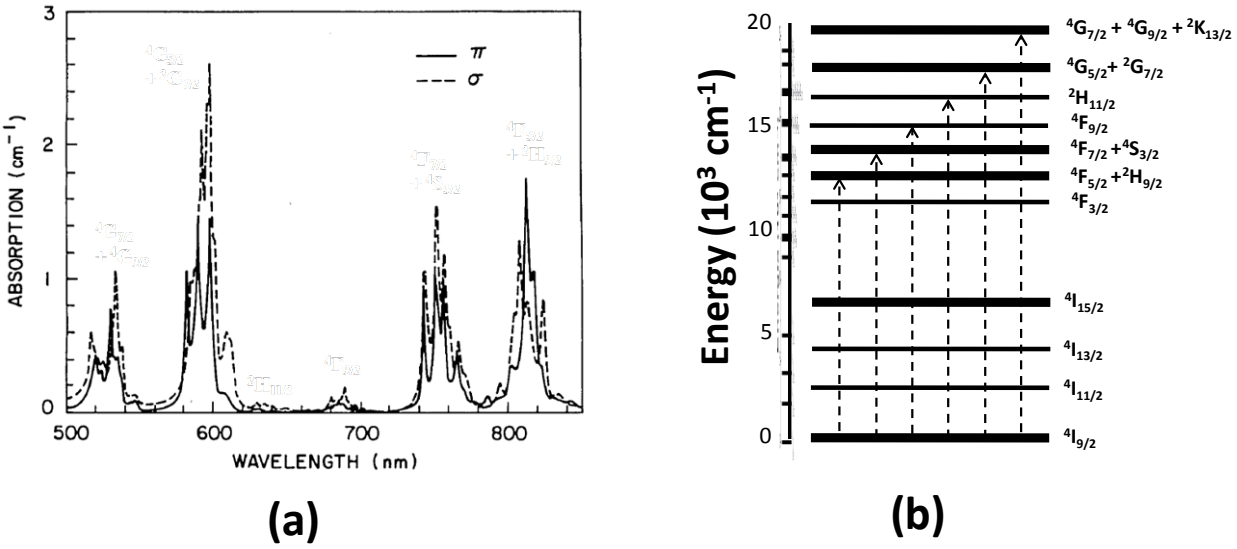

Figure 2.5: (a) Room temperature polarized absorption spectra of Nd^{3+} (0.1 at%) in $LiNbO_3$ [Fan 1986]; (b) partial energy level scheme of Nd^{3+} revealing the $^{2S+1}L_J$ states involved in each band of the spectra (dotted arrows). The width of each state indicates different magnitudes of the crystal field splitting [Dieke 1968].

Concerning the lifetime of Nd^{3+} levels, some studies have reported that the $^4F_{3/2}$ meta-stable level in $LiNbO_3$:Nd^{3+} presents a radiative lifetime value of around 170 μs and a quantum efficiency of 0.6 [Loro 1995]. In our samples the obtained value of the fluorescence lifetime of the $^4F_{3/2}$ state at room temperature was $\tau \sim 90$ μs.

In Figure 2.6 we show the polarized emission spectra (a,b) and the energy level diagram (c,d) corresponding to the $^4F_{3/2}\rightarrow{}^4I_{9/2}$ and $^4F_{3/2}\rightarrow{}^4I_{11/2}$ transitions centered at around 900 and 1085 nm respectively. These spectra have been obtained in the frame of this work. In the $^4F_{3/2}\rightarrow{}^4I_{11/2}$ spectrum the Stark transition at around 1085 nm, which dominates the π-polarized spectrum, corresponds to the main laser line ($R_1\rightarrow Y_2$) of $LiNbO_3$:Nd^{3+} [Fan 1986]. On the other hand, the main σ-polarized emission peaks at 1078 and 1093 nm provide an optical gain which is almost three times lower than the one for the π-polarized spectrum. Despite this fact, laser oscillation has also been demonstrated for these lines [Jaque 1999].

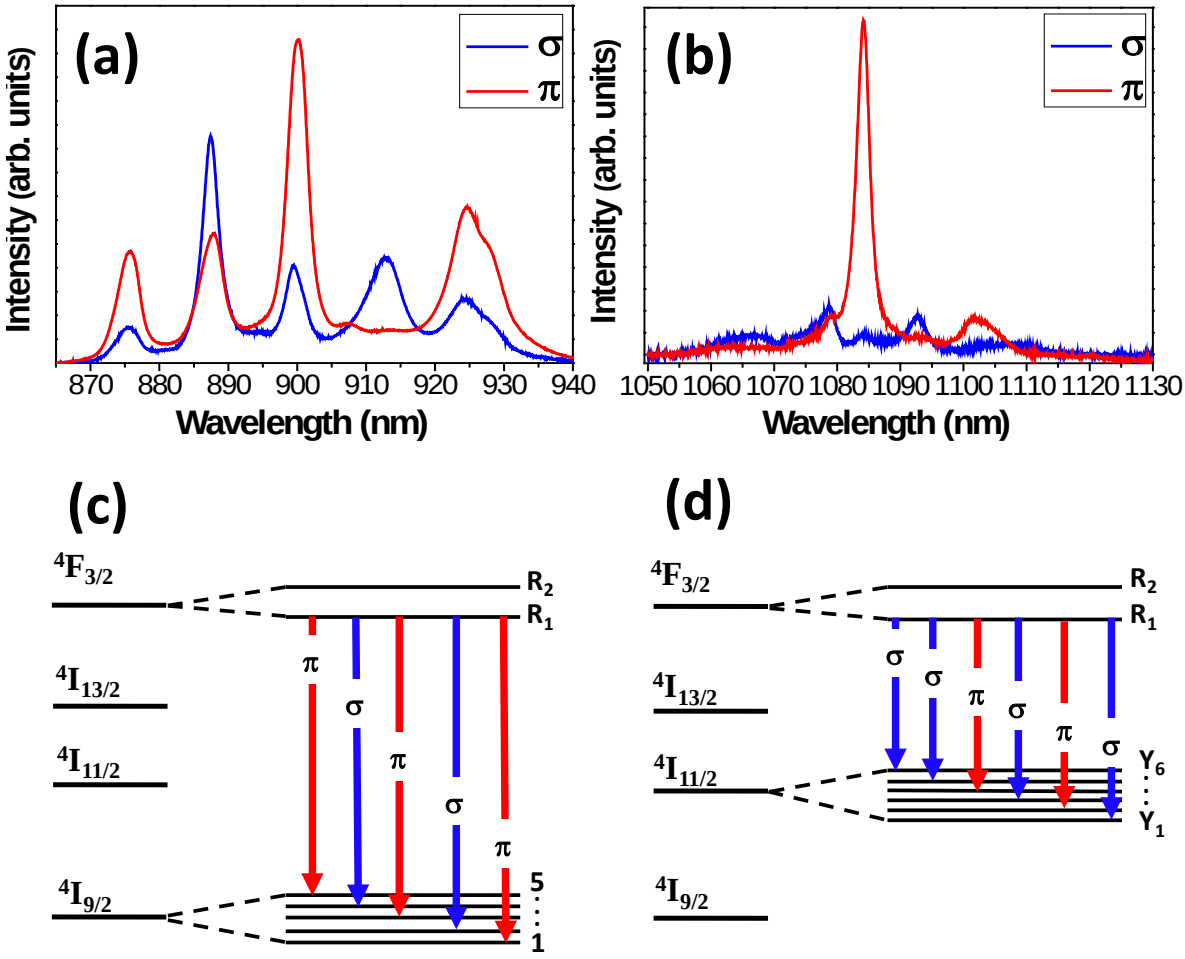

Figure 2.6: Polarized emission spectra corresponding to the (a) $^4F_{3/2}\rightarrow{}^4I_{9/2}$ and (b) $^4F_{3/2}\rightarrow{}^4I_{11/2}$ transitions of Nd^{3+}. (c,d) Energy level scheme showing the σ (blue lines) and π (red lines) polarization character of the Stark transition.

1.2.6.3 Laser oscillation

One of the most important characteristics of Nd^{3+} ions in $LiNbO_3$ is the possibility of obtaining laser oscillation. Laser emission in $LiNbO_3$:Nd^{3+} was first reported in 1967.

Since then, several groups have studied the optical spectroscopy and the energy levels of this material [Belabaev 1975, Burlot 1996, Evlanova 1967, Kaminskii 1968, Kaminskii 1972, Loro 1995].

Later, different studies have successfully improved the laser efficiency of $LiNbO_3:Nd^{3+}$ [Kaminow 1975] and $LiNbO_3:MgO:Nd^{3+}$ [Fan 1986, Jaque 1999] under diode pumping. This has enabled the design and fabrication of self-frequency doubling devices, in which it is possible to obtain infrared laser radiation and coherent visible radiation simultaneously, as well as self Q-switched devices based on $LiNbO_3:MgO:Nd^{3+}$ crystals [Cordovaplaza 1988].

In this system, the typical resonant pumping is usually performed from the $^4I_{9/2}$ ground level to the $^4F_{7/2}$, $^4F_{5/2}$ or $^4F_{3/2}$ levels. Laser oscillation in $LiNbO_3:Nd^{3+}$ crystal has being reported between the $^4F_{3/2}$ meta-stable state and the $^4I_{11/2}$ the state (1084 nm), since this specific transition presents the highest branching ratio (β = 0.52) [Munoz 1998]. However, laser action has also being demonstrated with other insulating matrices in the $^4F_{3/2} \rightarrow {}^4I_{13/2}$ and $^4F_{3/2} \rightarrow {}^4I_{9/2}$ channels.

Figure 2.7 shows a partial Nd^{3+} level scheme with the different absorption transitions that give rise to the different laser emission.

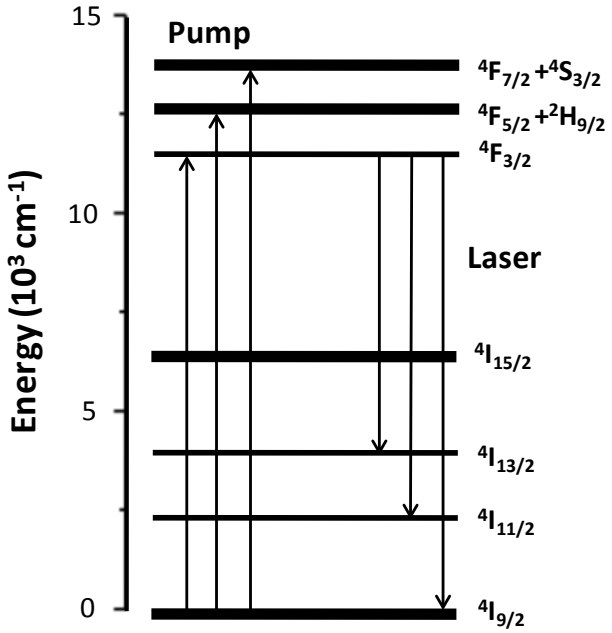

Figure 2.7: Energy levels and operational scheme of a Nd^{3+} based solid state laser.

In the last decades a diode-pump at around 810 nm, has being used as the optimal pump source for Nd^{3+} based lasers. This wavelength corresponds to the $^4I_{9/2} \rightarrow$

$^4F_{5/2}$ + $^2H_{9/2}$ transition. Figure 2.8 shows the absorption cross sections for both π and σ polarizations in $LiNbO_3$:MgO:Nd^{3+} at room temperature, corresponding to this spectral region. The π and σ polarized absorption spectra present maximum values at around 809.5 and 812.2 nm respectively.

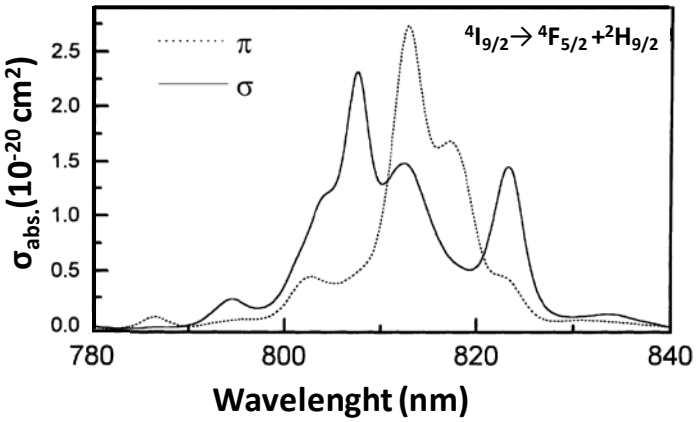

Figure 2.8: (a) Polarized absorption cross-section in the range 740-840 nm for a $LiNbO_3$:MgO:Nd^{3+} (0.2 at%.) crystal [Jaque 1999].

Typically, the absorption cross section of rare-earth ions (10^{-19} cm^2) is significantly smaller (and hence the optical gain) than that of other types of optical emitters, such as organic dyes (10^{-15} cm^2) or inorganic semiconductor quantum dots (10^{-14} cm^2) [Forget 2013]. The spectral dependence of the $^4F_{3/2} \rightarrow {}^4I_{11/2}$ emission cross sections at around 1080 nm, calculated from the measured emission spectra at RT is presented in Fig. 2.9. The 1084 nm line that dominates the π emission spectrum corresponds to the main laser line of $LiNbO_3$:Nd^{3+}.

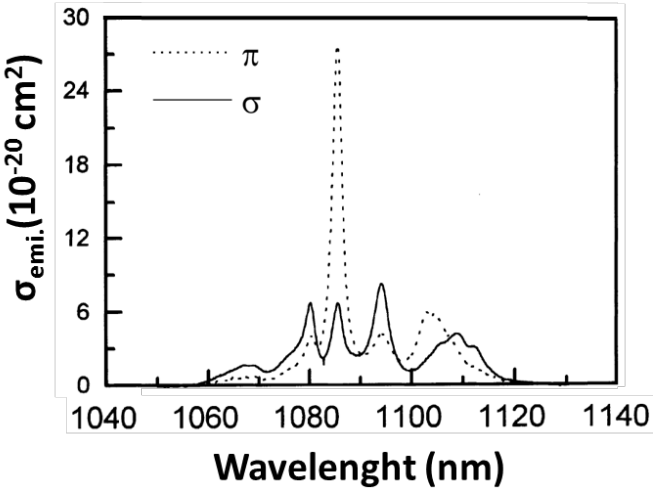

Figure 2.9: Polarized emission cross section spectra of the main laser channel $^4F_{3/2} \rightarrow {}^4I_{11/2}$ in the range of 1000-1150 nm for $LiNbO_3$:MgO:Nd^{3+} (0.2 at%.) [Jaque 1999].

Up to now Nd^{3+} has shown laser action in $LiNbO_3$ in different configurations. Bulk laser operation has been reported with pump power at thresholds of around 4 mW and efficiencies of a 10% in a 9 cm long quasi-spherical cavity. It has been also lased in waveguide configuration with threshold and efficiencies of 1.5 mW and 13%, respectively. Table 2.2 presents typical laser parameters from different reports concerning laser oscillation of $LiNbO_3$:Nd^{3+} in bulk and waveguide configurations. In most cases MgO has been incorporated to prevent the crystal photorefractive damage, which makes laser oscillation unstable. However, an alternative possibility to reduce the photorefractive damage is based on the fabrication of channel waveguides by Zn diffusion [Di Paolo 2001].

	Gain media	Cavity	Cavity length (mm)	Threshold (mW)	Efficiency (%)	Nd concentration (at.%)	Laser mode	Regime	Ref.
Bulk	$LiNbO_3$:MgO:Nd^{3+}	Quasi-hemispherical	4	0.83	4.1	0.2	TEM_{00}	quasi-CW (π-pol.)	[Ishibashi 1996]
	$LiNbO_3$:MgO:Nd^{3+}	Quasi-hemispherical	4	1.1	2.8	0.07	TEM_{00}	CW (π-pol.)	[Ishibashi 1996]
Waveguide	$LiNbO_3$:MgO:Nd^{3+}	Proton-exchange waveguide	11.3	1.5	13	0.22	---	CW (π-pol.)	[Lallier 1990]
	$LiNbO_3$:Nd^{3+}	Zn-diffused waveguide	10	1.25	20	0.1	---	CW (π-pol.)	[Di Paolo 2001]

Table 2.2: Typical laser parameters for different Nd^{3+} doped $LiNbO_3$ crystals.

Under these considerations we incorporated our Ag NPs/$LiNbO_3$:Nd^{3+}(0.1 at.%) gain system inside a planar Fabry-Perot cavity in order to achieve laser oscillation. The system exhibited sub-diffraction laser action, well below the spatial confinement obtained in other configurations, in the regions where the metallic nanostructures were located. Even so, the nano-lasing was achieved at room temperature and preserves the SSL characteristics. Besides, this new plasmon mediated SSL exhibited a pump threshold reduction of 50% and an 15-fold improvement of laser efficiency compared with the bulk laser oscillation of the naked $LiNbO_3$:Nd^{3+} crystal (see article 5).

Section III

Localized surface plasmons

In this work we have used metallic Ag nanostructures to enhance the spectroscopic properties of Nd^{3+} ions, exploiting their ability to strongly concentrate the optical fields in metal/dielectric boundaries. This phenomenon is known as localized surface plasmon resonance (LSPR). This section provides a brief description of the physical principles in this area. Since the main objective of this work was to generate laser radiation at the nanoscale using for the first time a solid state laser, the last block of this section contains the state of the art of laser action mediated by plasmon resonance in several configurations.

1.3.1 Introduction

When an electromagnetic wave is applied to a metal, it produces the displacement of conduction electrons, leading to surface charge oscillations. Both the electromagnetic and the surface charge waves can couple when a resonant condition is fulfilled at a preferential frequency. This phenomenon is known as *surface plasmon resonance* (SPR). SPR opens the possibility to concentrate, manipulate and enhance optical fields at the nanoscale, overcoming the diffraction limit of traditional optics. Nowadays, plasmonics are used in a wide variety of scientific fields such as biomedical [Hu 2006], localization and guiding [Maier 2003, Maier 2005], transport and storage of energy [Ozbay 2006], surface-enhanced Raman spectroscopy [Haynes 2005], as well as applications in information technology [Barnes 2003]. The fundamentals of SPRs are briefly presented below.

As a first step, we consider an interface between two media, characterized by their corresponding dielectric function $\varepsilon(\omega)$, and solve Maxwell's equations in order to determine the general conditions for surface electromagnetic modes to exist. We consider that one medium is characterized by a complex frequency-dependent dielectric function $\varepsilon_1(\omega)$, while the other medium $\varepsilon_2(\omega)$ is assumed to be real. This interface is schematically presented in Figure 3.1.

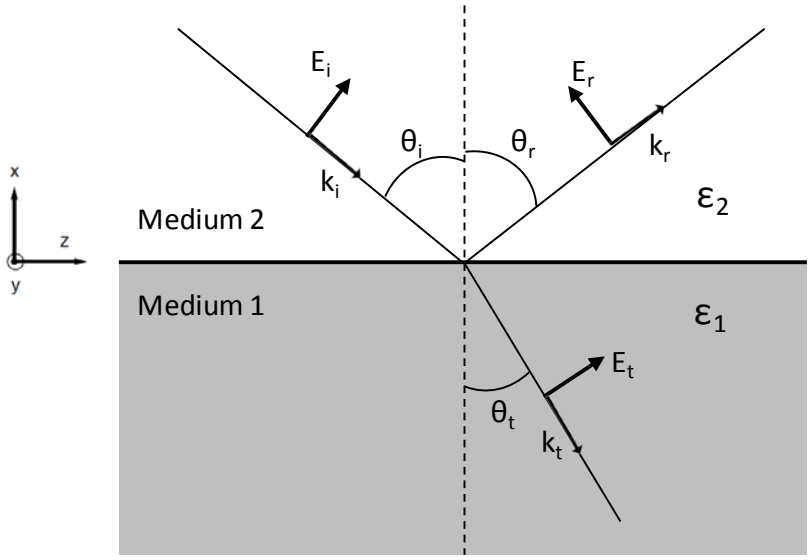

Figure 3.1: Interface between two media characterized by their dielectric functions ε_1 and ε_2. In each medium we consider only p-polarized waves.

The general conditions for the existence of a electromagnetic mode at the interface are [Novotny 2012]:

$$\varepsilon_1(\omega) \cdot \varepsilon_2(\omega) < 0 \tag{3.1}$$

$$\varepsilon_1(\omega) + \varepsilon_2(\omega) < 0 \tag{3.2}$$

Which means that one of the dielectric functions, for instance $\varepsilon_2(\omega)$, must be negative with an absolute value exceeding that of the other. This is the case for metals and especially noble metals, such as gold or silver, since they present a large negative real part of the dielectric constant together with a small imaginary part at visible frequencies. Thus, at an interface between a noble metal and a dielectric, such as glass or air, electromagnetic modes can exist.

The complex dielectric function of metals at a given frequency (ω) can be described by considering the Drude model for a free electron gas [Drude 1902]:

$$\varepsilon_{Drude}(\omega) = 1 - \frac{\omega_p^2}{\omega^2 + i\Gamma\omega} \tag{3.3}$$

being $\omega_p = \sqrt{ne^2/m_e\varepsilon_0}$ the plasma frequency, and n and m_e the density of valence electrons and the effective electron mass, respectively. The damping rate (Γ), determined by the electron-electron and electron-phonon scattering, is proportional

to $\Gamma = v_F/l$, where v_F is the Fermi velocity and l is the electron mean free path between scattering events.

However, the values of ω_p obtained with the Drude Model can disagree from those obtained experimentally, since the contributions from bond electrons or interband transitions are not considered. For instance, the Drude model predicts that the plasma frequency of silver is 9.2 eV [Bohren 1983], whereas the measured value is actually 3.9 eV (~320 nm) [Johnson 1972]. From this point, two different plasmonic systems may be distinguished: propagating electromagnetic modes traveling along a metal-dielectric interface which are called surface plasmon polaritons (SPP) (their designation as polaritons arises from the coupling of electromagnetic waves with the surface charge oscillations); and non-propagating electromagnetic modes, presented in metallic nanoparticles (NPs) and nanostructures, known as localized surface plasmons (LSP). Both cases are schematically illustrated in Figure 3.2.

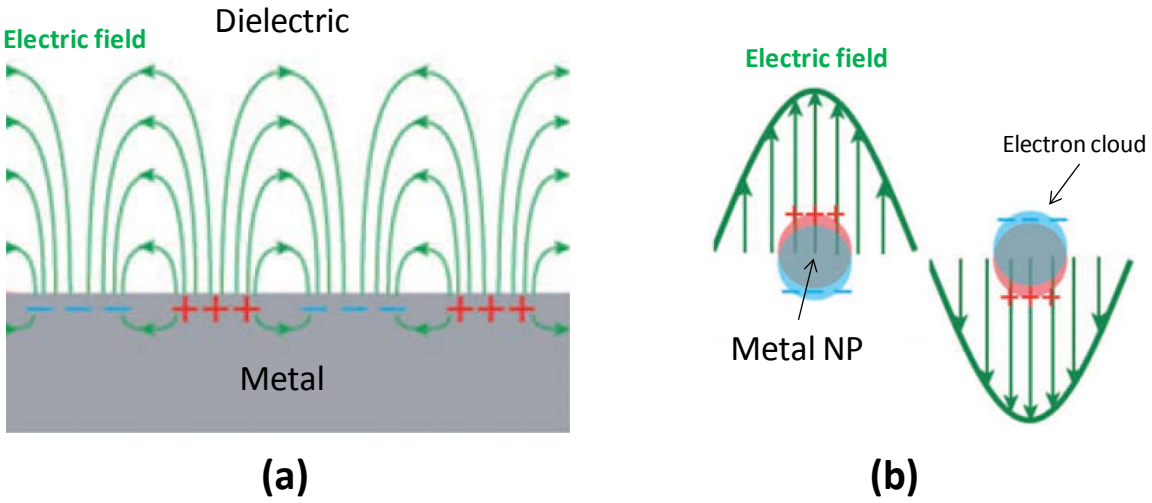

Figure 3.2: Schematics of (a) surface plasmon polariton (SPP) and (b) localized surface plasmon (LSP) modes at metal dielectric interfaces, showing both the charge density oscillations in the metal and the electric fields in the surrounding dielectric.

The surface charge density oscillations in SPPs give rise to strongly enhance optical near-fields which are spatially confined near the metal-dielectric interface. Similarly, if the conduction electron cloud is confined in three dimensions, as in the case of a sub-wavelength particle, extreme charge accumulations can occur accompanied by strongly localization and enhancement of optical fields. In the first case, a momentum mismatch between light and SPPs is required to excite a propagating SPP mode in a metal-dielectric interface. This is not the case for metallic NPs since their curved surfaces make the LSPR to be easily excited without having to fulfill any matching condition. Due to this advantage, we centered our studies only on this latter case.

1.3.2 Localized surface plasmons

Despite its rising interest during the last century in many scientific fields, the history of localized surface plasmons dates back to Roman times when metallic nanoparticles were used for glass coloring [Freestone 2007]. It was not until the beginning of the 20th century when Gustav Mie established the first mathematical basis which described the scattering of electromagnetic waves by homogeneous spherical particles [Mie 1908].

Based on the Drude model, we can start considering a metallic NP as a lattice of fixed ionic cores in which the conduction electrons can move almost freely inside the volume of the particle. Under the influence of an electromagnetic wave these electrons are forced to move in the opposite direction of the electric field vector. Consequently, the free carriers accumulate in one side of the NP surface leaving a positive charge in the opposite side, and thus creating an electric dipole (see Figure 3.3).

This dipole generates an electric field inside the NP opposite to that of the light, leading to a restoring force that makes the electrons return to its equilibrium position. Actually, the electron movement inside the NP is similar to a harmonic oscillator with some degree of damping caused by the collisions with the ionic cores.

The amplitude of the electronic oscillation will reach its maximum value when the frequency of light matches the natural resonance frequency of the oscillating electrons, known as the *plasmonic frequency*. This approximation is only valid if the NP size is much smaller than the wavelength of light so that the phase of the oscillating electromagnetic field can be considered as constant over the volume of the NP.

The excitation light will be partially extinguished since the electrons absorb and scatter its energy as they oscillate. The absorption of light is responsible for high ohmic losses and associated with the heating of the NP. Besides, the oscillating dipole induced by the electric charge displacement, can re-radiate electromagnetic energy leading to the *scattering* of the incident light wave. The sum of both absorption and scattering cross sections is defined as the *extinction cross section*, given by:

$$\sigma_{ext} = \sigma_{abs} + \sigma_{scatt} \tag{3.4}$$

It is found that for isolated plasmonic NPs the extinction cross section can be up to 10 times higher than its geometrical section [Garcia 2012].

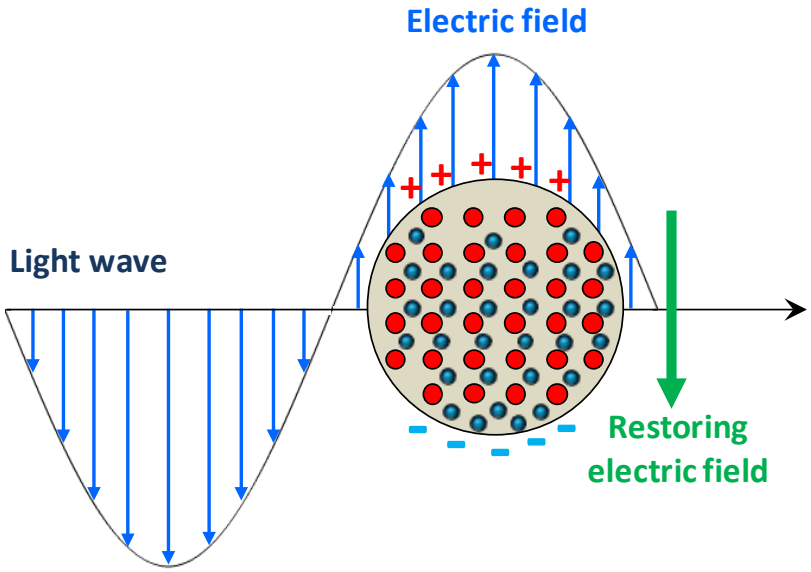

Figure 3.3: Scheme of a metallic NP interacting with a electromagnetic wave. The electric field of light induces the movement of conduction electrons (blue circles) through the stationary lattice ions (red circles). The electrons accumulate at the surface of the NP creating an electric dipole opposite to the electric field of the light wave.

1.3.2.1 LSP in Silver nanoparticles

Of the three metals (Ag, Au and Cu) that display plasmon resonances in the visible spectrum, Silver was chosen in this work since it presents the lowest ohmic damping at visible and infrared frequencies, and thus exhibits the highest efficiency of plasmon excitation [Kreibig 1995]. Moreover, a single Ag NP interacts with light more efficiently than a particle of the same dimension composed of any known organic or inorganic chromophore. The plasmonic resonance of a metallic NP is sensitive to its shape, size, and composition. It also depends on its surrounding medium. All these parameters may influence in the spectral position, width, and amplitude of the resonance. Table 3.1 presents values, extracted from different reports, of the LSP resonances of different isolated sphere-like Ag NPs configurations regarding their size and surrounding media.

Ag NPs configuration	NPs diameter (nm)	Plasmon resonance peak (nm)	Ref.
On $GeSe_4$ susbtrate	2	362	[Pinchuk 2004]
Aqueous suspension	30	420	[Evanoff 2004]
On glass substrate	60	490	[Hu 2010]
Embedded in $LiNbO_3$	20	519 (pol. in the ordinary direction) 509 (pol. In the extraordinary direction)	[Wolf 2014]
On 50nm Au film	60	640	[Hu 2010]

Table 3.1: LSP of different Ag NPs configuration parameters

In general, large metallic NPs support longer oscillation periods of the collective motion of electrons. Since the motion distance covered by the electrons is increased, the plasmonic resonance of the NP will be achieved for higher wavelengths. Therefore, increasing the diameter of a spherical nanoparticle leads to a red-shift in the plasmonic response. As the NP size changes, the nature of optical interaction also varies and the absorption and scattering spectra may significantly differ. Figure 3.4 shows the evolution of the plasmonic modes of three differently sized Ag NPs.

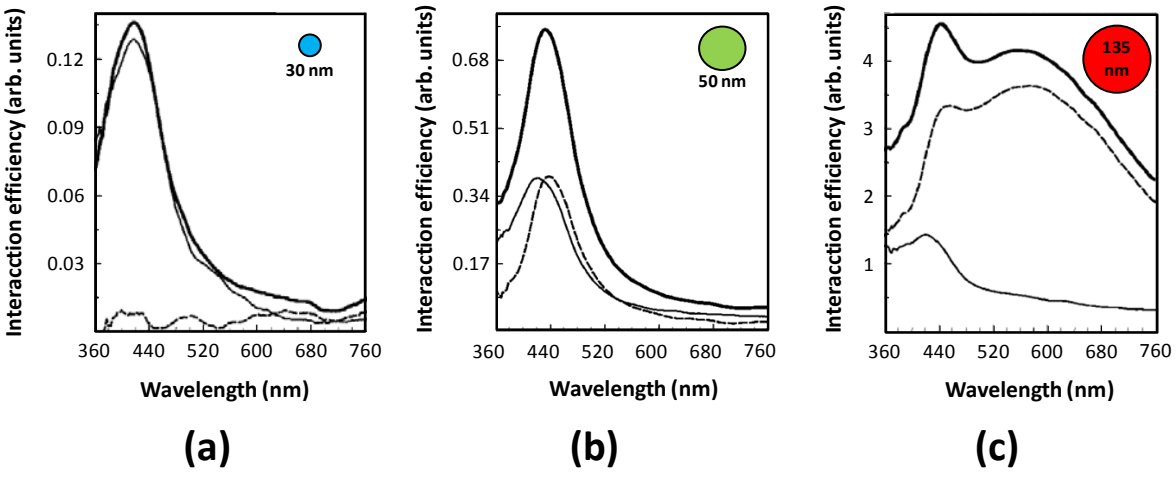

Figure 3.4: Measured extinction (thick solid line), absorption (thin solid line), and scattering (dashed line) spectra for suspensions of spherical Ag NPs with different sizes [Evanoff 2004].

For small metallic NPs (i.e. the particle is much smaller than the wavelength of light in the surrounding medium), extinction is dominated almost entirely by the

resonance of dipole absorption. However, for larger particles the scattering component becomes dominant and the shift between absorption-scattering maxima is much more pronounced. The peak in the absorption spectrum that remains at 420 nm in panel (c) is most likely due to the absorption contribution from the quadrupole component of the plasmon resonance.

The differences in the source of extinction presented in a plasmonic NP may play different roles for different applications. For example, the absorption of light in metallic particles leads to a heating effect which may alter or even destroy the specific particle if the light power is sufficiently high. On the other hand, a large scattering efficiency will result in the dispersion of the incident light.

1.3.2.2 Aspect ratio effect dependence in the LSP

When a metallic NP is elongated or shortened along a certain axis it will exhibit two spectrally separated plasmon resonances which correspond to electronic oscillations along the major and minor axis. If the polarization of the incident light is parallel to the mayor axis we will be able to access to the longitudinal *plasmonic modes*, whereas for a perpendicularly polarized pump (parallel to the minor axis) only *transverse plasmonic modes* will be excited. Both resonances present significant features in their corresponding absorption and scattering spectra.

The longitudinal plasmonic modes substantial differ as the aspect ratio is modified. Similarly to increasing the size of a NP an increase in the aspect ratio, for a fixed value of one of the axis, leads to a red-shift of the spectral position of the longitudinal plasmon resonance, compared with the plasmon resonance of a sphere-like (aspect ratio = 1) particle of the same volume. The higher the value of the aspect ratio, the greater the red-shift [Wiley 2007].

1.3.2.3 Near-Field confinement in LSP

A fascinating property of LSPs is their ability to strongly concentrate and enhance electromagnetic fields near the metal-dielectric interface [Maier 2010]. The spatial field distribution in the surroundings of a plasmonic nanostructure, as well as its corresponding spectra (absorption, scattering, extinction...), can be described by solving the Maxwell's equations by different numerical methods, depending on the features presented by the plasmonic system, such as the geometry, distribution, size, etc...[Brongersma 2007]. Figure 3.5 shows an example of the electric field, calculated by the Finite difference time domain) method (FDTD, generated near a Ag NP under

resonant illumination. As can be observed, a strong intensification of the electric field is mainly localized along the polarization direction.

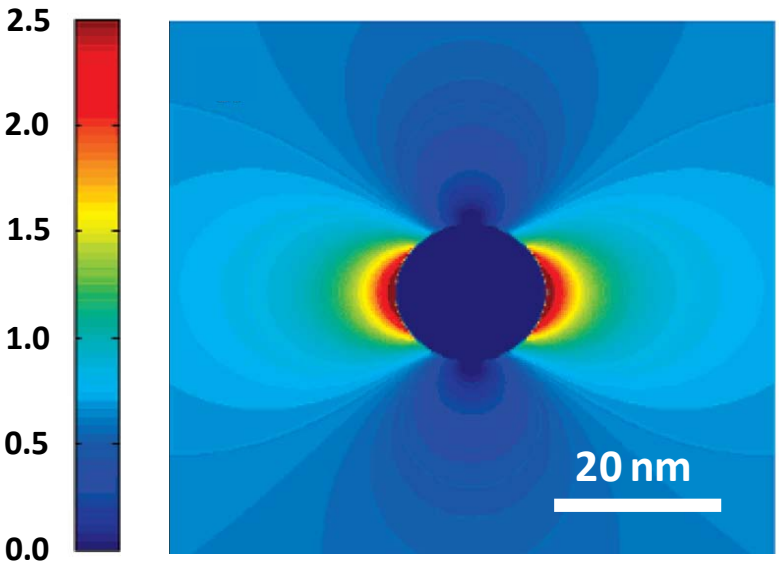

Figure 3.5: Electric field distribution near a silver NP under an incident light of 635 nm calculated by the FDTD model. The incident light is propagating along the *y*-axis, while the polarization is along the *x*-axis [Jian 2007].

In order to exploit this feature, metallic NPs and nanostructures can be designed to optimize the interaction between a localized source or receiver and the free-radiation field. This receiver/transmitter is ideally a quantum absorber/emitter, such as an atom, ion, molecule, quantum dot, or defect center in a solid. The strong local field enhancement induced by the LSP of metallic nanostructures can improve the quantum efficiency of the luminescence of these nearby emitters [Blanco 2004].

In this sense, metallic NPs can be considered as optical antennas since they can efficiently convert free-propagating light into localized energy confined in nanometric volumes, and then scattered back to the far field [Novotny 2011]. Actually, any field enhancement in a nano-plasmonic system is associated with a nano-antenna effect. This field enhancement at the plasmon frequency has also received a lot of attention in a broad range of applications such as surface-enhanced Raman scattering (SERS) [Kneipp 2002], photovoltaics [Atwater 2010], bio-sensing [Anker 2008], and SHG amplification [Sanchez-Garcia 2014, Yraola 2013].

1.3.2.4 Coupling between localized plasmons

Aggregates of metallic NPs in close proximity (separation distance < λ) can provide additional enhancement of electromagnetic fields exceeding those

corresponding to a single NP. Collective LSP modes may arise due to the coupling between adjacent particles. When excited they originate a region of strong EM field enhancement in inter-particle junction, commonly known as a "hot spot" [Maier 2010]. Thus, the inter-particle coupling distance plays an important role in the plasmonic properties of NP aggregates. The enhancement factors can vary, depending on the specific NPs arrangement and configuration, reaching values that in some cases can be orders of magnitude higher in the gap region between particles.

1.3.2.5 LSPs in linear arrays of metallic NPs

In an array of closely spaced NPs, the interacting particles can be described, in a first approximation, as an array of point dipoles interacting in the near-field. Using the simple approximation of a linear array of interacting point dipoles, the restoring force acting on the oscillating electrons of each particle will be either increased or decreased due to the charge distribution of the neighboring particles (Fig. 3.6). The response of a chain under linearly polarized light is strongly dependent on the orientation of the chain. Depending on the polarization direction of the exciting light, in general a blue-shift of the plasmon resonance will arise when exciting the transverse modes of the NPs chain (Figure 3.6 (a)). Besides, weaker interactions and less spatially-extended modes are observed under perpendicularly polarized excitation [Wang 2012]. On the contrary, a red-shift will take place for the longitudinal modes (Figure 3.6 (b)) [Maier 2010].

Additionally, if we increase the number of interacting particles in the linear array, the collective chain mode gradually red-shifts until it saturates above a certain number of particles [Tserkezis 2014].

On the other hand, in real-life experiments assembled NPs not always form perfectly arranged straight chains. Taking this into account, some authors have shown that the disorder degree presented in realistic metallic nanostructures make these systems to exhibit some relevant features [Esteban 2012, Tserkezis 2014].

Even so, in this work we considered 2D disordered configurations of Ag NPs as a distribution of short linear chains randomly oriented and separated an average distance. Therefore, we were able to distinguish the local excitation of short and long chain modes.

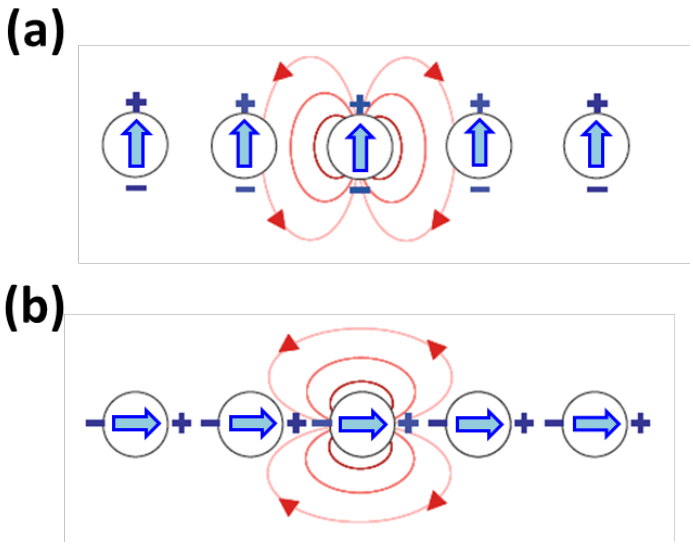

Figure 3.6: Schematics of the near-field coupling of electric dipoles in linear chains of metallic NPs [Maier 2010].

1.3.2.6 Interaction between LSP and RE^{3+} ions

One of the many emerging applications of optical nano-antennas is to enhance the fluorescence signal of single emitters and fluorophores placed in close proximity. As argued in the previous section, RE^{3+} ions are of both fundamental and technological interests because of their large Stokes shifts, narrow and thermally stable emission bandwidths, and long emission lifetimes. However, little work have been devoted to the interaction of light with RE^{3+} ions coupled with metallic NPs. Table 3.2 presents a summary of some studies in different NPs/RE^{3+} systems.

Some studies have experimentally observed that the addition of NPs in the emitter's environment results in a local increase of its quantum efficiency (η) and a decrease in its lifetime (τ) [Pillonnet 2012, Wu 2005]. The authors attributed these results to an energy transfer between RE^{3+} ions and the metallic NPs, arguing that the presence of metallic NPs modifies the local field around the emitters leading to an additional decay rate term.

On the contrary, other reports found increases in the intensities of RE^{3+} with no changes in the lifetime [Hayakawa 1999, Selvan 1999]. In these cases, the lack of energy transfer from the metallic NPs to RE^{3+} was attributed to the difference between the lifetime of the LSPs (10^{-14} s) and the fluorescence lifetime of the RE^{3+} (10^{-3} s). Thus, the enhancement in the fluorescence spectra was attributed to the local field enhancement around the RE^{3+} ions. However, an additional possibility is related to the increment of the excitation fields.

	NPs/RE^{3+} configuration	RE^{3+}	NPs size (nm)	Excitation wavelength (nm)	LSP peak wavelenght (nm)	Luminescence enhanced wavelenght (nm)	Enhancement factor	Ref.
Randomly distributed NPs	Ag/Y_2O_3/Eu:Y_2O_3/Y_2O_3/Ag multilayer	Eu^{3+}	diameter ~ 10	532	440	625	2	[Pillonnet 2012]
	Ag islands /Eu:SiO_2 gel	Eu^{3+}	diameter ~ 2	337	380	625	10	[Selvan 1999]
	Ag islands/Eu:Al_2O_3	Er^{3+}	diameter ~ 220	978	~ 600	520	220	[Aisaka 2008]
NPs arrays	Ag nanodisks arrays on Er:SiO_2 films	Er^{3+}	length ~ 400 height ~ 20	532	~ 1540	1540	2	[Mertens 2006]
	Au nanocylinders arrays on Er:SiN_x films	Er^{3+}	diameter ~ 200 height ~30	514	~ 1540	1540	3.6	[Gopinath 2010]

Table 3.2: Examples of emission enhancement in different NPs/RE^{3+} systems

1.3.3 Purcell effect

Although the physics of an optical emitter interacting with plasmons is a complex topic, the origin of the modification of spontaneous emission can be understood as the interaction of the emitter with its own secondary field, which is the field that arrives back at the atom's location after being scattered by the "new" local environment generated by the metallic NPs [Bharadwaj 2009].

This optical environment, characterized by the LSPR modes and the optical fields of the emitter, can be considered as a resonant nano-cavity. In this frame, this cavity will be characterized by the quality factor (Q) and the effective mode volume (V_{eff}) of the nanoscale plasmon cavitiy [Maier 2006]. These two parameters are related by the Purcell factor (F_P) defined as [Purcell 1946]:

$$F_P = \frac{3}{4\pi^2} \cdot \left(\frac{\lambda}{n}\right)^3 \cdot \left(\frac{Q}{V_{eff}}\right) \tag{3.5}$$

being λ the wavelength of light and *n* the refraction index inside the cavity.

In this sense, a resonant optical cavity presenting a high quality factor Q and a mode confined in an ultrasmall volume V enhances the density of photon states and increases the spontaneous emission rate of the emitter.

The design of optical cavities presenting high F_P constitutes a central target in solid-state physics. Actually, recent works have demonstrated nanoscale confinement presenting Purcell factors of the order of 10^3, which compete with other conventional dielectric cavities [Koenderink 2010].

In addition, several studies have combined the large Purcell effect of surface plasmons with different gain media in order to overcome the high absorption losses and obtain sub-diffraction laser confinement.

1.3.4 Plasmonic lasers

In 2003, Bergman and Stockman theoretically proposed a new class of optical amplification and laser action for charge density waves at the nanoscale, named plasmon lasers or spaser [Bergman 2003]. In contrast to classical lasers, plasmon lasers amplify light coupled to oscillating electrons, which adds momentum to light enabling their physical size and mode volume to shrink below the diffraction limit. By lasing into localized surface plasmons, a coherent light field can be generated directly at the nano-scale. This essentially allows focusing of optical energy beyond the diffraction limit in a much more efficient and compact way compared with that of passive nano-focusing. The minimum physical size of a plasmon laser can be just a few nanometers, limited only by a metal's inhomogeneity and non-locality length scale (1nm) [Ma 2013].

With the unprecedented small physical size and mode volume, new features in plasmonic lasers are evident. Firstly, the strong electromagnetic confinement in a plasmon cavity causes a drastic spatial redistribution of spontaneous emision: light can be inhibited into some modes and preferentially coupled to the plasmonic laser mode. This can significantly reduce the pump conditions for the onset of laser action, and will modify the threshold behavior. Additionally, due to the short lifetime of plasmons and the high Purcell factor, plasmon lasers can be potentially modulated at frequencies in the terahertz range [Genov 2011, Stockman 2010].

The highly focused near field of plasmon lasers could be useful for photolithography, enabling feature sizes beyond the limits of conventional lasers. They could also be useful for packing more data onto optical storage media. Moreover, the strong electric field confinement in plasmon lasers could be utilized to amplify very weak effects. This could be deployed for detecting single molecules, allowing for extremely sensitive bio-detection and in-situ nanoscale Raman and Fluorescence spectroscopy. Furthermore, owing to their small size and potentially fast operation speed, they are a promising light source for ultra-compact and fast photonic circuits. Plasmonic lasers thus offer the possibility of exploring extreme interactions between light and matter, opening up new avenues in the fields of active photonic circuits, bio-sensing and quantum information technology.

However, attempts to realize a plasmonic laser have proved to be a tough challenge due to absorption losses in metals, which are particularly strong at optical

frequencies. In this sense, optical gain from a gain medium adjacent to the metallic nanostructure has been shown to compensate losses and allow for loss-free operation, amplification in nanoscopic lasing. This suggestion of compensating losses by optical gain in localized or propagating surface plasmons has been recently implemented in various configurations.

In 2009 Hill and co-workers developed a plasmonic laser based on a metal-insulator-semiconductor-insulator-metal waveguide consisting in a InP/InGaAs/InP pillar surrounded by an insulating silicon nitride layer [Hill 2009]. The pillar was encapsulated in silver to provide feedback, and then electrically pumped to exhibit light emission after electron-hole recombination at 1500 nm (see Figure 3.7 (a)). Surface plasmons excited between the two metal planes were 1D-confined up to a few tens of nanometers due to the small index variation along the hetero-structure, leading to propagative wave. The end facets of the metalized structure completed a Fabry-Perot resonator. In the experiment, the laser light could escape through the bottom part of the device to be collected by a microscope objective placed underneath. Thus, this work demonstrated that a light mode could be confined to nano-sized scale in a hybrid SPs-semiconductor wave guide cavity and amplified to lasing action.

The same year Oulton and co-workers proposed another device [Oulton 2009]. The laser cavity consisted of a semiconductor nanowire of cadmium sulfide (CdS) lying on nano-sized insulating gap layer of magnesium floride, which separated the nanowire from a silver film placed underneath (Figure 3.7 (b)). A hybrid photonic-plasmonic mode was generated between the nanowire and the metal surface propagating along the wire's axis, and was hundreds of times smaller than the photonic mode. Similar to Hill's experiment, the feedback of the system was provided by the end facets of the nanowire, and multiple optical modes were confined between the metallic plane and the wire. The system was optically pumped to collect the main exciton emission line of CdS at 489 nm. The results revealed a broad-band enhancement of the nanowire's spontaneous emission rate by up to six times owing to the strong mode confinement.

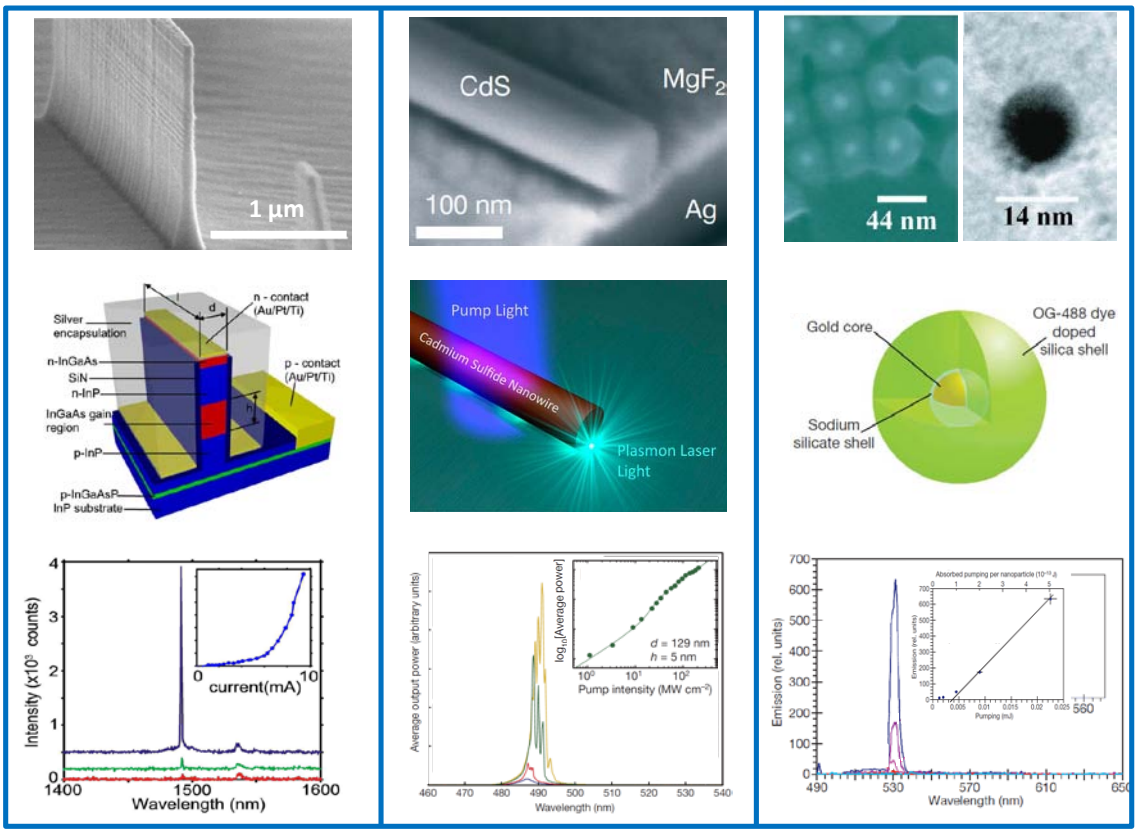

(a) **(b)** **(c)**

Figure 3.7: Nanolaser configurations presenting (a) 1D (b) 2D and (c) 3D sub-diffraction confinement.

These first two works presented similarities with conventional lasers since they use a Fabry-Perot cavity to generate feedback in the system. However, plasmons can overcome the need of a resonant cavity by exploiting the field amplification supported by metallic NPs and nanostructures. That was the case of Noginov [Noginov 2009], who reported lasing action from NPs with a gold core and dye-doped silica shell impregnated with OG-488 dye molecules that served as gain medium. A sketch of this system is presented in Figure 3.7 (c). Under strong optical excitation the gold core supported a dipole like plasmonic "cavity" mode which provided feedback for the stimulated emission.

These demonstrations showed clearly the principal advantages of plasmonic lasers: the threshold reduction and the delivery of coherent radiation in the nanoscale. However, in most cases cryogenic temperatures or high pump powers were required preventing them of easy applications. Since then, there has being a special interest in the use of gain materials combined with lattice plasmon modes of NPs arrays in order to develop loss-less laser systems at room temperature, with a better spatial and spectral control.

The research group of Odom proposed a design for a room-temperature nano-laser based on three-dimensional array of Au bowtie NPs supported by an organic gain material consisting of IR-140 molecules in polyurethane (see Figure 3.8 (a)) [Suh 2012]. In this study the system was optically pumped by fs-laser pulses and the emission was enhanced by the plasmonic cavities formed in the bowtie dimers. Consequently, the gain was increased by the Purcell factor well above threshold and the lasing of the system was possible at room temperature. Besides, when the pump beam was set parallel to the axis of the bowtie dimers the laser intensity was an order of magnitude higher than that for perpendicular polarization. In the following year Odom's group reported lasing action from band-edge lattice plasmons in two-dimensional arrays of Au NPs embedded in the same organic environment (see Figure 3.8 (b)) [Zhou 2013]. The system presented directional laser emission with narrow linewidth (< 1.3 nm) and small beam divergence (< 1.58^{o}).

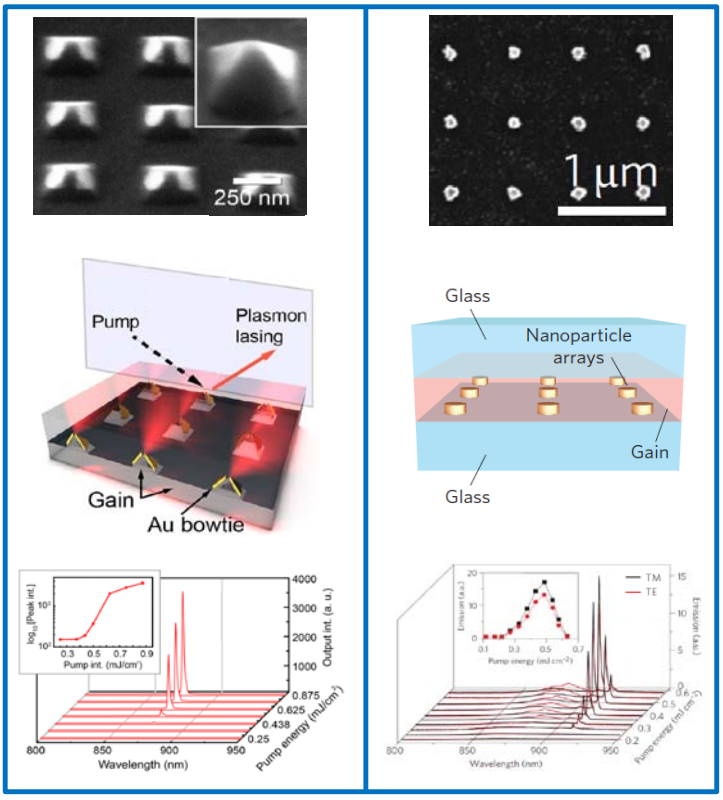

Figure 3.8: Nanolaser from a (a) 3D plasmonic bowtie laser array [Suh 2012], and (b) 2D NPs laser array [Zhou 2013].

Summarizing, all these demonstrations show the main advantages of plasmonic lasers, mainly based on organic dye molecules and semiconductors. However, plasmon-laser operation in other types of laser systems, as it is the case of SSLs,

remains unexplored. For this reason, achieving a plasmon-mediated solid state laser at the nanoscale constituted a primary goal in this work.

Section IV

Experimental methods

This section contains the description of the samples used in this work and the experimental methods.

1.4.1 Starting materials

The materials used in this work mainly consisted of Nd^{3+} doped periodically poled $LiNbO_3$ (PPLN) crystals. They were grown in the Crystal Growth Laboratory of the Physics of Materials Department of UAM by the off-centered Czochralski method along the x-axis. Nd^{3+} was incorporated by adding Nd_2O_3 to a congruent melt of $LiNbO_3$ [Li/Nb=0.94].

During the crystal growth the rotational axis was displaced 5 mm from the symmetry axis of the temperature field. This forces the crystal to grow in a thermal gradient able to generate alternating ferroelectric domains [Bermudez 1999]. The period length of the ferroelectric patterns was controlled by the rotation and pulling rates which were set at around 30 rpm and 1 mm/h respectively. This generated a duty cycle of alternating 180^o ferroelectric domains close to 50%. The ferroelectric patterns obtained by this technique exhibited homogeneous periodicities extended along areas of a few hundreds of square microns. The size of the ferroelectric domains used in these work was around 3 μm, being the total period of around 6 μm. An example of these ferroelectric PPLN structures is shown in Figure 4.1.

Nd^{3+} concentration in the crystals was determined by total-reflection X-ray fluorescence [Fernandez-Ruiz 2001], with a Rich & Seifert EXTRA-II spectrometer located at "Servicio Interdepartamental de Investigación (SIdI)" in the UAM. The obtained value was 0.1 at.%.

For the spectroscopic and laser gain studies plates around 1 cm^2 were cut with thicknesses ranging between 0.5 and 1 mm in two different crystallographic orientations: Z-cut with the ferroelectric axis perpendicular to the surface, and Y-cut

with the c-axis parallel to the surface. The samples were mechanically polished with different diamond pastes, up to 0.25 µm in grain size. Ferroelectric domain structures were revealed by chemical etching using a mixture of HF:HNO_3 (1:2 in volume) [Barry 1998]. Due to the atomic arrangement and the non-equivalence between the +z and -z, and the +y and –y directions it was possible to reveal the domain distributions in both Z-cut and Y-cut configurations [Brown 1985, Niizeki 1967].

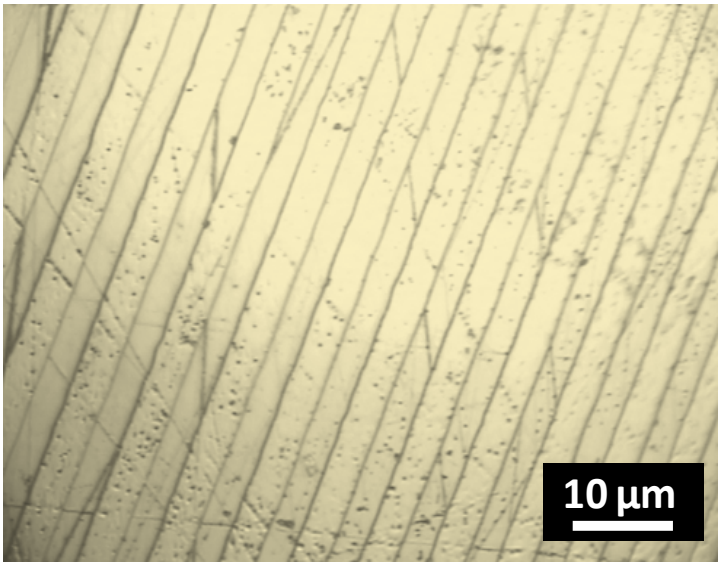

Figure 4.1: Optical image of the ferroelectric domain structure of (a) a Z-cut Nd^{3+}:PPLN sample grown by the off-centered Czochralski technique. The image was taken after chemical etching.

1.4.2 Photo-deposition of metallic nanostructures

Polar surfaces of ferroelectric materials, characterized by the presence of surface charges, offer a useful platform for polarization mediated chemistry enabling a low cost option for deposition of metallic nanoparticles (NPs) [Balobaid 2013, Carville 2012, Sun 2011, Sun 2011B].

A relatively novel photo-deposition technique, sometimes referred to as ferroelectric lithography [Kalinin 2004], has been employed for assembling metallic nanostructures on the surface of our ferroelectric crystals. This technique was previously demonstrated in different ferroelectrics obtaining, through domain specific chemical reactions, the assembly of metal nanoparticles, organic molecules, wires, etc [Haussmann 2009, Liu 2007, Riefer 2012].

As has been explained in Section II, ferroelectric domain structures in Nd^{3+}-doped $LiNbO_3$ crystals were used as templates for the self-assembly of Ag NPs. Illumination of ferroelectric domain-patterned $LiNbO_3$:Nd^{3+} crystals immersed in an $AgNO_3$ solution

with above-bandgap light at 254 nm induced the formation of Ag nanostructures on the different-polarity domain surfaces, as well as on the domain boundaries. Of the different metals to choose for the photochemical reduction silver was selected as it exhibits the lowest ohmic damping in visible and near IR regions.

Prior to the metallic photo-deposition on the PPLN crystals a second polished was performed in order to remove the surface reliefs generated during the chemical etching. After this treatment samples were cleaned in an ultrasonic bath of acetone for about 20 minutes. A scheme of the photo-chemical process for the ferroelectric lithography is depicted in Figure 4.2.

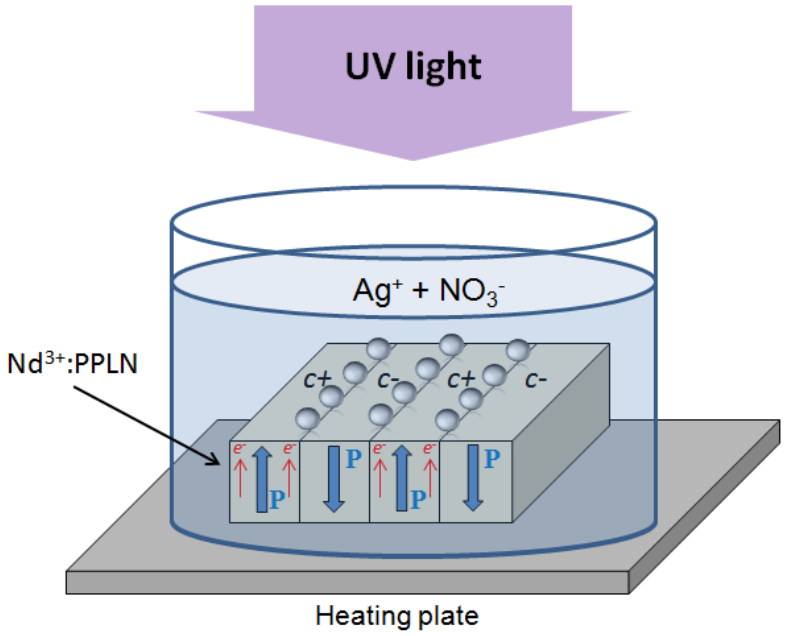

Figure 4.2: Schematic of the process used for the metallic NPs on the ferroelectric domain walls.

Samples were placed on a Petri dish containing an $AgNO_3$ solution (0.001 - 0.01 M) which provided the Ag^+ ions for the photo-deposition process. Then, samples were illuminated with above band gap light using a UV-mercury pen-lamp (UVP model 11SC-1) with its main line at 253.6 nm and emission power of 5400 µW/cm^2 at a distance of 1.9 cm. The photo-excited electrons move preferentially towards the surface where a reduction of the Ag^+ ions takes place as follows:

$$Ag^+ + e^- \rightarrow Ag^0 \quad (4.1)$$

It is well known that the rate of most chemical reactions increases with increasing temperature [Brown 2012]. Therefore, during the experiments samples were heated at 70 ± 5°C. To control this parameter a temperature controller (ASCON

M3) was used. Typical illumination time ranged from 1 to 20 minutes to control the nanoparticles deposition rate.

Immediately after the illumination, the samples were immersed in deionized water for about 1 minute and then blown dry with compressed air.

1.4.3 Microscopy techniques

The surfaces of the PPLN samples and the obtained metallic nanostructures were visualized by various microscopy techniques described below.

1.4.3.1 Differential interference contrast microscopy

The domain structures and the distributions of Ag NPs obtained in the Nd^{3+}:PPLN crystals where visualized using differential interference contrast microscopy, also called DIC or Nomarski microscopy, in reflectance operation mode. The system elements were integrated in an Olympus BX51 optical microscope. A schematic diagram of the key optical components of the DIC microscope is presented in Figure 4.3.

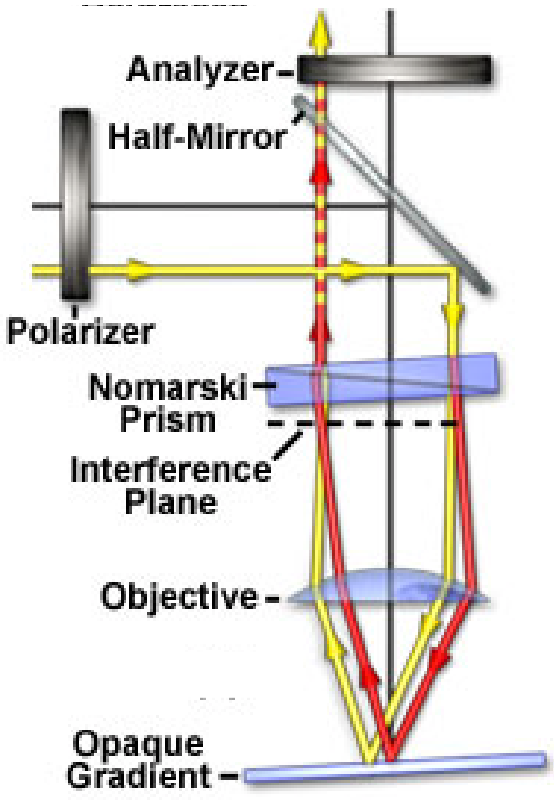

Figure 4.3: Scheme of the main elements of a Nomarski microscope.

This type of microscopy is used to increase the contrast in the light reflected from the surface of a sample. The slopes, valleys, and other discontinuities from the surface create optical path differences. These variations are collected and transformed by the DIC microscope into intensity variations that enhance the topographical profile of the image.

Illumination generated by a light source passes through a first linear polarizer. Then, the polarized light beam is reflected on half-mirror that makes it travel along the optical axis of the microscope, where the Nomarski prism and the objective lens are located. The Nomarski prism consists of two birefringent quartz slabs that are identical in shape, but their optical axes have different orientations. When the light passes through this element the beam is divided into two orthogonally polarized components (ordinary and extraordinary) with identical amplitudes. Besides, the two waves are deviated according to the geometry of the birefringent slabs. The microscope objective focuses both orthogonal wavefronts on the surface of the sample. Each wavefront reaches the surface at different positions, which could show different heights due topography variation on the sample. This has been represented in Figure 4.3 as an opaque gradient. Due to this, the optical paths followed by the two reflected waves differ, and a phase shift is induced between them. Later, the reflected beams are gathered on the interference plane of the Nomarski prism. The directional deviation that the light beam suffers when it crosses the Nomarski prism for the first time is corrected when the divided beams, on their way back, cross the prism for the second time. After exiting the Nomarski prism the superposed wavefronts travel through the half-mirror and encounter a second polarizer (analyzer) with its polar axis perpendicularly oriented to the axis of the first polarizer.

The components of the orthogonal wavefronts that are parallel to the analyzer transmission vector are able to pass through. Subsequently the resultant interferences generate amplitude fluctuations which form the Nomarski image. In other words, the formation of the final image is the result of the interference between the two distinct wavefronts that reach the image plane slightly out of phase with each other. Through an adjustable offset phase in the Nomarski prism we can vary the image contrast, as it is proportional to the path length gradient. The resultant image appears as a three-dimensional physical relief of the sample, emphasizing lines and edges.

The main advantages of this technique lie in its non-destructive character and in its easiness to obtain the images, allowing the visualization of ferroelectric domain boundaries and Ag NPs arrangements without requiring any previous sample preparation.

1.4.3.2 Dark field microscopy

Dark field microscopy (DFM) was used here to get experimental evidence of the radiative properties of the plasmonic modes supported by the arrangements of Ag NPs. In Figure 4.4 the components of the DFM are schematically presented.

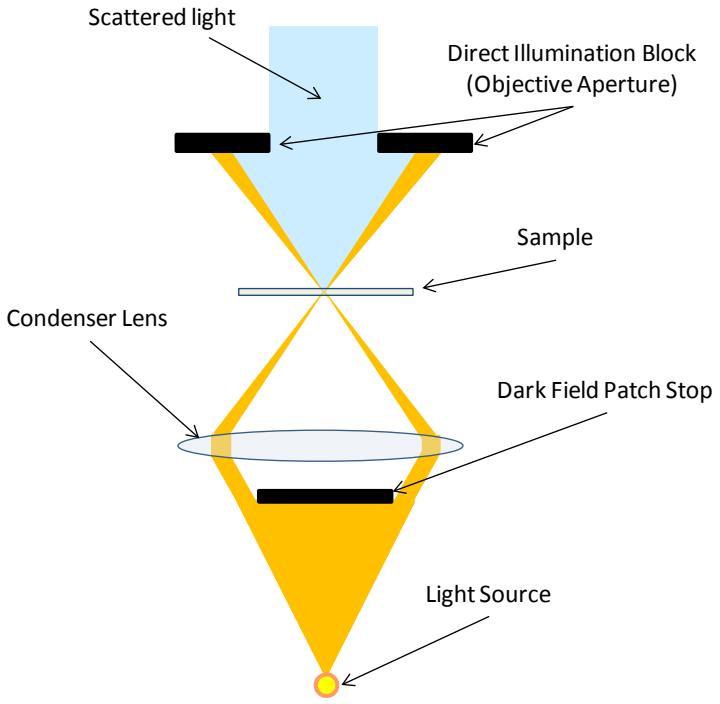

Figure 4.4: Scheme of the main elements that constitute a dark field microscope.

The configuration of the system allows that light collected from the sample corresponds mainly to scattered light instead of transmitted light. This microscopy technique uses a beam of light in the form of a hollowed cone focused by a condenser lens on the sample. The central region of the light cone generated from a source is blocked by an opaque patch. This patch is also coupled to a condenser lens (NA=0.8) that focuses the non-blocked light on the sample. By this illumination set up, only the oblique rays from the light source pass through the sample. Only scattered light from the sample is collected with the objective lens, while a direct illumination block prevents the directly transmitted light from reaching it. In our case this light blocking is achieved through the objectives numerical aperture which has to be smaller than that of the condenser lens.

Polarized images can also be recorded by placing a linear polarizer between the light source and the condenser. In our equipment all these elements were integrated in the Olympus BX51 optical microscope.

1.4.3.3 Atomic force microscopy

An atomic force microscope (AFM) Park Systems model XE-100 was used operating in non-contact mode to obtain topographic measurements over areas up to 1mm^2 from the PPLN surfaces. A scheme of this type of microscopy is shown in Figure 4.5.

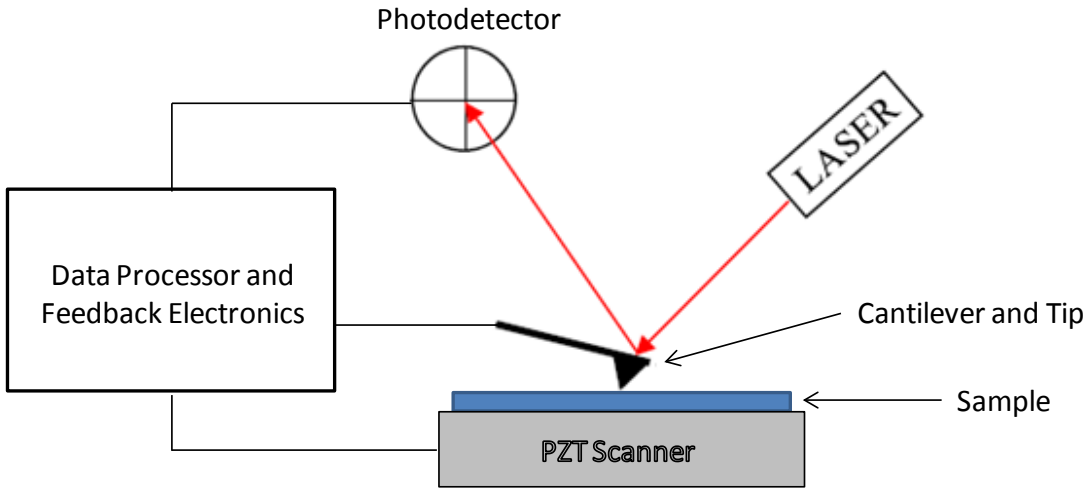

Figure 4.5: Diagram of an atomic force microscope.

The AFM consists of a silicon cantilever with a sharp tip at its end that is used to scan the sample surface. When the tip is brought into proximity of a sample surface forces between the tip and the sample lead to a displacement of the cantilever according to Hooke's law.

In non-contact mode the cantilever is above the sample at a distance of tens to hundreds of Angstroms. At this distance the tip is acting in the attractive force regime under force gradients from long-range Van der Waals and other electrostatic forces. The attractive forces are too small (10^{-9} - 10^{-11} N) to be measure just through bends of the cantilever. Instead an oscillating cantilever vibrating near its resonant frequency, in the range of 200 - 400 kHz, is used. The interacting forces tend to alter the resonance frequency of the cantilever and thus the phase and amplitude of the oscillation.

In order to keep the frequency of the vibration constant the tip-sample separation is adjusted by means of a feedback loop. A voltage is applied to a piezoelectric ceramic (PZT) below the sample in response to changes in the cantilever vibration. Therefore, the topographic image is generated from the feedback data of the PZT scanner. The oscillation of the cantilever is measured by detecting the deflections of a laser beam that is reflected from the back side of the cantilever as it

moves across the sample surface. The beam is detected with a position-sensitive photo-detector composed of four photodiodes. When the laser beam hits a photodiode a current is generated and a difference in intensity can be measured between the quadrants.

The principal advantage of this technique is that it has a Z-resolution on the order of fractions of a nanometer. Additionally, samples visualized by AFM do not need any special treatments that might change or damage the sample and does not typically suffer from any charging artifacts in the final image. This system was also used to obtain piezo-response force microscopy images.

1.4.3.4 Piezo-response force microscopy

A specific electrostatic force microscopy module incorporated in the previously described AFM system, set in contact mode, was used to obtain piezo-response force microscopy (PFM) images of the Y-cut Nd^{3+}:PPLN samples. PFM measurements were done in the Y-cut of the Nd^{3+}:PPLN samples. The principle of this technique is presented in Figure 4.6.

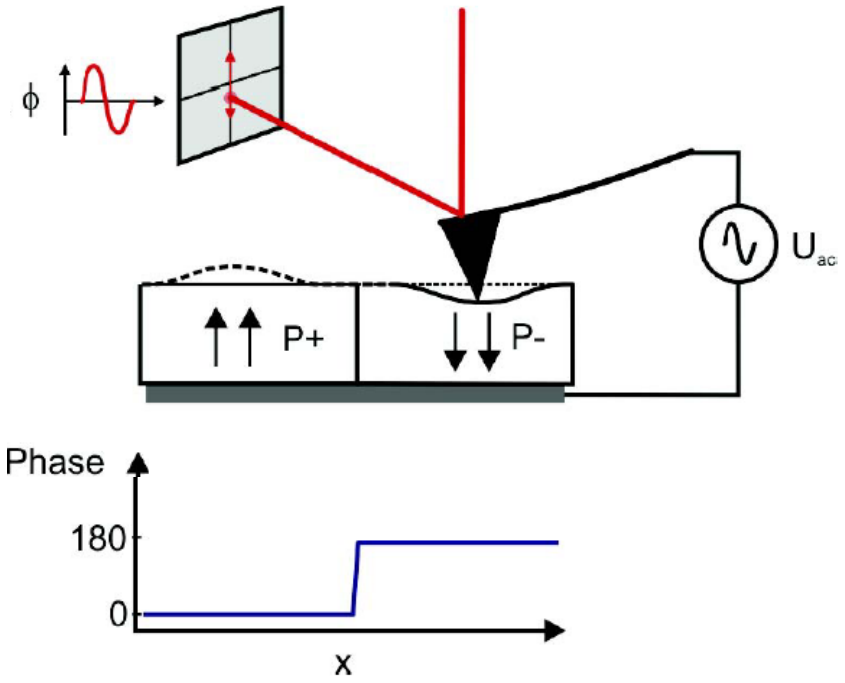

Figure 4.6: Schematics of the PFM system.

PFM has become one of the most commonly used microscopy technique for imaging ferroelectric domains due to its high resolution and relative ease of implementation.

An alternating bias voltage (±2 V) is applied to a metal-coated cantilever, in contact with the sample, in order to expand or contract the domains regarding their polarity due to the piezoelectric nature of the crystal. In the contact mode operation the electrically driven tip is acting predominantly in the repulsive force regime under short-range forces between the tip and the sample. This force is maintained by means of the feedback loop that applies a voltage to the piezoelectric scanner to adjusts the height between tip and sample.

When the bias voltage is applied the +z and -z surfaces give an in-phase or out-of-phase z-response respectively, relative to the modulated bias. Therefore, positive domains appear dark and negative domains appear bright in the PFM phase images. By recording this phase signal, through the feedback data of the PZT scanner, the piezoelectric response of ferroelectric domain surfaces can be imaged.

1.4.3.5 Scanning electron microscopy

To get high-resolution images of the Ag NPs structures we used a Philips XL30 S-FEG scanning electron microscope (SEM) located at the SIdI.

Due to the insulating character of the samples a thin film (around 5 nm) of metallic Chromium was deposited on the samples to evacuate the charges during the observation. High resolution images with spatial resolution near 1 nm were obtained.

1.4.4 Optical spectroscopy

The different systems based on $LiNbO_3$ crystals presenting metallic nanostructures on their surface were characterized by various spectroscopic techniques that are described below.

1.4.4.1 Absorption and extinction measurements

A PERKIN Elmer UV/VIS/NIR Lambda 1050 double-beam spectrophotometer was used to obtain the optical absorption of the Nd^{3+}:PPLN crystals and, when possible, the extinction spectra of the Ag NPs arrangements. A simple scheme of the operation mode is shown in Figure 4.7.

Two radiation sources, a deuterium lamp and a halogen lamp, cover the working wavelength range of the spectrophotometer. The generated light is spectrally selected by a monochromator. Then the light is separated into two beams through a beam splitter. One beam is used as the reference while the other beam passes through the

sample. Both signals are measured by a set of detectors that change automatically during the scan. A photomultiplier tube is used in the UV/VIS range between 175 - 860 nm, while an InGaAs or a lead sulfide detector can be selected for the NIR range between 860 - 1800 nm and 1800 - 3300 nm respectively.

The instrument was mainly used in transmittance mode to measure the intensity of light passing through a sample, and compare it to the intensity of light from the reference channel. To characterize the samples the absorption and extinction spectra were obtained.

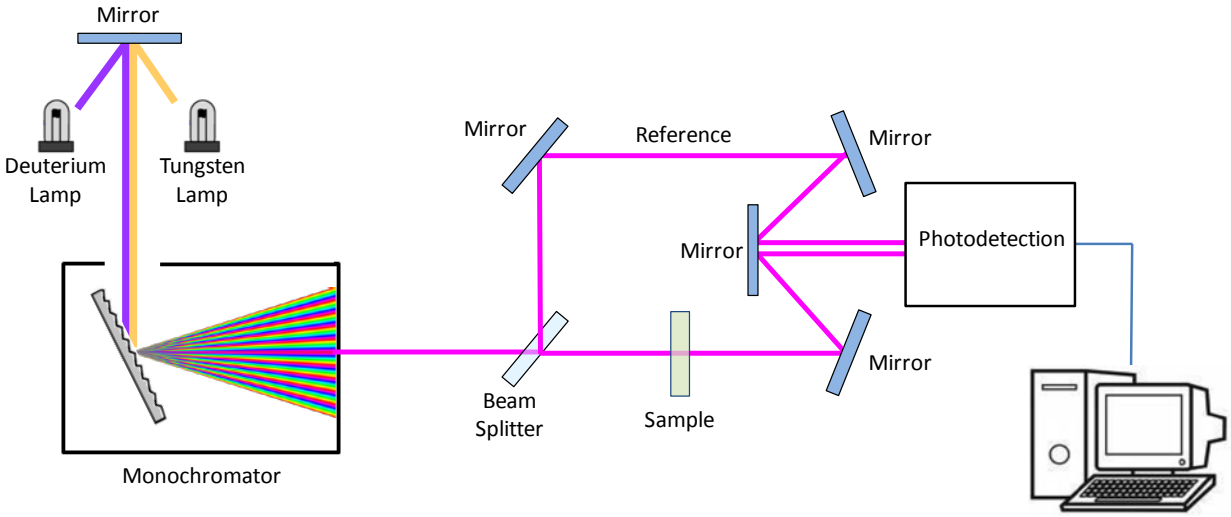

Figure 4.7: Schematics of an UV- visible spectrophotometer.

1.4.4.2 Micro-luminescence and SHG

In order to study the effect of the Ag NPs in the Nd^{3+} emission bands micro-fluorescence spatial maps were performed recording the emission spectra corresponding to the Stark lines of Nd^{3+} ions in the $LiNbO_3$ crystal.

Additionally, studies of the second harmonic generation (SHG) signal generated by the substrate were also obtained by the same experimental setup. A scheme of the experimental setup used for these measurements is illustrated in Figure 4.8.

As excitation sources we used an Ar^+ laser (Spectra Physics Model 177-Series) filtered to operate at 488 nm, or a tunable femtosecond Ti:Sapphire laser (3900S Tsunami Spectra Physics) set at 808 nm in continuous wave operation. The laser beam is guided by mirrors to the entrance of a Olympus BX41 microscope sketched in Figure 4.8. The magnification of the objectives ranged from 10X to 100X, being possible to focus the laser spot to a size less than 1µm. After focusing the beam on the sample the

emitted light goes backwards through the microscope objective following the same path as the excitation beam till it reaches a band-pass filter that blocks the excitation laser beam. The emitted light reaches a monochromator (HORIBA iHR 550). This device has a gratings of 950 grooves/mm that presents a blaze at 900 nm. The whole set has a spectral resolution of 0.02 nm and a dispersion of 1.6 nm/mm. The signal is finally detected with a CCD camera (Jobin Yvon Synapse) coupled to the output of the monochromator and electrically cooled by a Peltier (-70 °C). Samples were mounted on a motorized XY stage controlled by the LabSpec 5 software. The spatial and spectral resolution of the whole system was around 0.2 microns and 0.02 nm, respectively. A half-wave plate (λ/2) was placed before the entrance of the microscope to select the polarization orientation of the excitation beam. A polarizer was placed before the detection system to analyze the polarization of the emitted light.

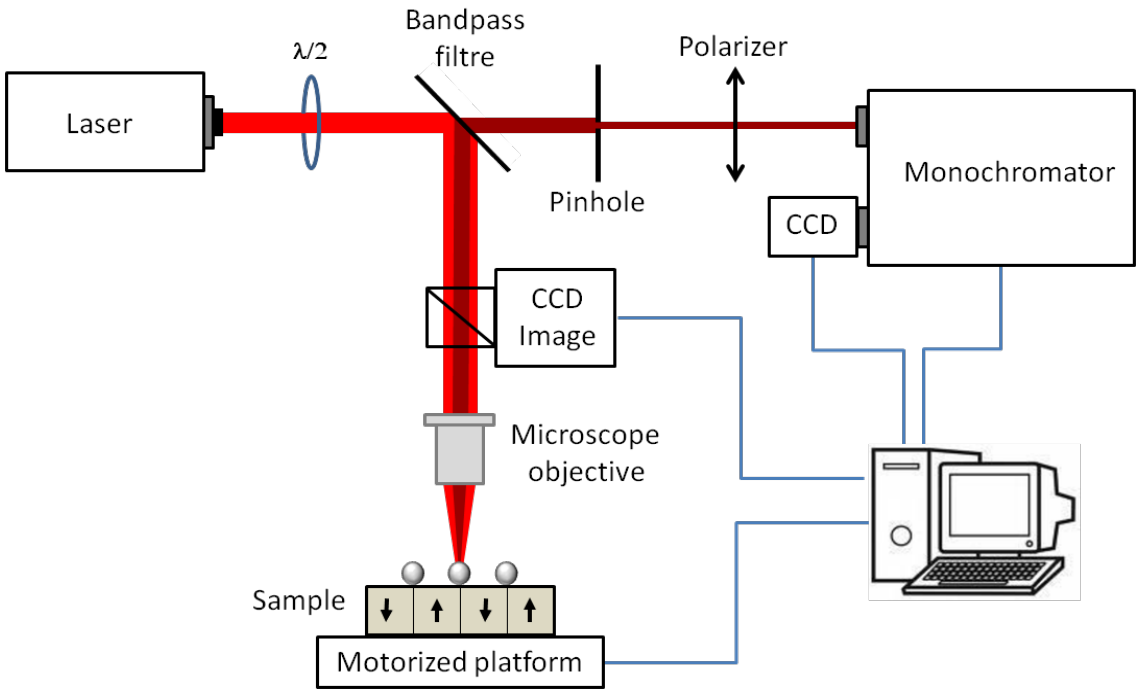

Figure 4.8: Experimental scheme of the setup used for the micro-luminescence measurements.

1.4.5 Laser oscillation measurements

For laser experiments, a c-cut 5x5 x0,8 mm (lenght x width x thickness) Nd^{3+}:PPLN plate was placed inside a Fabry–Pérot resonator formed by two plane-parallel mirrors (M1 and M2). M1 was coated for high reflection (R>99.8 %) at the laser wavelength (λ_{laser}=1093 nm) and for high transmittance (T>95%) at the pumping wavelength (λ_{pump} =808 nm), while M2 was coated for high reflection for both, the pump (R>99.8 %) and laser (R>97 %) wavelengths. The mirrors were separated at their edges by two 1 mm thick spacers to avoid the direct contact with the surface of the

sample. The whole system was positioned on the previously described microscope. As excitation source we used a cw Ti:sapphire laser (Spectra Physics) tuned at 808 nm. An objective lens (20X, numerical aperture 0.45) was used to focus the pump beam to a 2.2 mm-diameter spot onto the sample. The laser spectra were collected in backscattering geometry with the same objective. The polarization of the pump laser beam was selected by means of a λ/2 plate. All the experiments were carried out at room temperature.

Español

2 Resumen global

En este trabajo se demuestra por primera vez la posibilidad de obtener mediante la técnica de la litografía ferroeléctrica arreglos de nanopartículas (NPs) metálicas sobre un sustrato ferroeléctrico dopado con impurezas ópticas de tierras raras (RE^{3+}). En particular, se utiliza el patrón periódico de dominios ferroeléctricos alternos presente en un cristal de Nd^{3+}:PPLN como plantilla para la formación de NPs de Ag mediante el proceso fotoquímico descrito en la Sección IV. Como resultado, se obtienen alineamientos ordenados de NPs de Ag a lo largo de las paredes de dominio ferroeléctrico, así como distribuciones de NPs en posiciones aleatorias que crecen de manera selectiva sobre las superficies de los dominios con polarización espontanea alterna presentes en el substrato.

La obtención de este resultado constituye la base sobre la que se sustenta esta tesis y supone la validez de un método simple para la obtención de auténticos arreglos plasmónicos sobre un láser de estado sólido (SSL) constituido por un material ferroeléctrico. Merece la pena destacar que hasta el inicio de nuestro trabajo los resultados de la aplicación de la litografía ferroeléctrica no habían sido utilizados sobre materiales fotoluminiscentes, por lo que nuestra aproximación tiene un alto grado de originalidad.

La litografía ferroeléctrica ha demostrado ser una técnica “bottom-up” simple y de muy bajo coste para obtener arreglos metálicos (nanohilos) sobre superficies polares (corte Z) de cristales de $LiNbO_3$, fundamentalmente si se compara con los costosos y laboriosos métodos que requieren las aproximaciones del tipo “top-down”. La motivación fundamental de nuestro trabajo requería extender los relativamente escasos resultados previos sobre litografía ferroeléctrica al caso de un sustrato ferroeléctrico con ganancia óptica, en particular al caso del $LiNbO_3$ dopado con Nd^{3+}. El ion Nd^{3+} es el ión activo láser por excelencia cuya ganancia se obtiene, como se ha mencionado en la Sección II, a partir de un esquema de cuatro niveles. Este ión

muestra un buen número de bandas de absorción coincidentes con la región espectral en la que se producen las resonancias de plasmones localizados de metales nobles. Por otro lado su emisión, en la región del infrarrojo cercano (~1080 nm), se localiza en la zona donde puede extenderse la dispersión de determinados arreglos de NPs metálicas. A pesar de las excelentes cualidades como ion luminiscente y de la abundancia de trabajos existentes sobre dicho ion, la interacción del Nd^{3+} con las respuestas plasmónicas de nanoestructuras metálicas no ha sido objeto de estudio hasta la publicación de este trabajo, lo que aumenta el interés y el carácter original de la tesis doctoral.

Los primeros resultados experimentales obtenidos en esta tesis muestran por primera vez la formación de nanoestructuras metálicas sobre la superficie polar (corte Z) de un cristal PPLN dopado con Nd^{3+}. Entrando más en detalle, las estructuras metálicas obtenidas presentan dos tipos de distribuciones bien diferenciadas:

Por un lado, se observa la presencia de NPs de Ag que se distribuyen sobre la superficie de los dominios alternos del Nd^{3+}:PPLN. La formación de estas NPs tiene carácter selectivo ya que se obtiene claramente mayor densidad de partículas en las superficies de polaridad positiva que en la negativa. Los resultados se muestran en la Figura 1 del **artículo 1**. Se debe mencionar que la técnica de litografía ferroeléctrica admite un cierto grado de control en el tamaño de las NPs formadas sobre las superficies de dominio, habiéndose realizado en este trabajo estudios en muestras con partículas cuyos diámetros medios eran de 20 nm (**artículo 1**) y 50 nm (**artículo 4**).

Por otro lado, además de las distribuciones aleatorias de NPs sobre las superficies de los dominios, se obtuvieron cadenas de NPs sobre las paredes de dominio. Estas cadenas aparecen en nuestro sistema debido a la inhomogeneidad de campo eléctrico en la superficie del cristal PPLN, mostrando una fuerte componente en la dirección Z en las cercanías de la superficie de las paredes de dominio (ver Figura 1.9 en la Sección I). La presencia de estas cadenas de NPs obtenidas por litografía ferroeléctrica sobre un sustrato ferroeléctrico dopado con RE^{3+} fue observada por primera vez en nuestro trabajo, siendo estas estructuras de extrema utilidad en el contexto de esta tesis. Las partículas que forman las cadenas muestran diámetros medios mayores que los correspondientes a las NPs obtenidas sobre las superficies de dominio. En nuestro trabajo se han utilizado estructuras de cadenas cuyas partículas mostraban diámetros en el rango de 40-70 nm con separaciones entre sí inferiores a las longitudes de onda involucrada en nuestros experimentos (unos pocos nanometros). En condiciones extremas de preparación (tiempo de procesado fotoquímico en torno a 20 min) las NPs se juntaban entre sí formando nanohilos continuos de Ag que no eran de utilidad para explotar las propiedades ópticas del

material (ver **artículo 4**). Las imágenes de microscopía electrónica de barrido han permitido la observación y caracterización de estas cadenas de NPs de Ag.

En la Figura 1 del **artículo 1** se muestra una respuesta espectral típica de las estructuras metálicas obtenidas y su solape con las bandas de absorción y emisión del Nd^{3+}. Como puede observarse, el espectro de extinción del conjunto de NPs sobre la muestra de Nd^{3+}:PPLN se extiende desde la región visible hasta el infrarrojo, con un máximo en torno a 580 nm, solapando con gran parte de las transiciones electrónicas del Nd^{3+}. La presencia de diferentes tamaños y distribuciones de NPs de Ag sobre la superficie del cristal (cadenas de NPs y distribuciones alternas de NPs con posiciones aleatorias) hace que el espectro de extinción muestre la forma obtenida. Dicho espectro fue tomado mediante la utilización de un espectrofotómetro convencional de doble haz (Sección IV), cuya configuración no permite resolver la respuesta espectral asociada a las diferentes distribuciones de NPs. En un esfuerzo por obtener información sobre la respuesta específica de las diferentes distribuciones de Ag se llevó a cabo la puesta a punto de un sistema de microscopía de campo oscuro que ha sido descrito en la Sección IV. En el **artículo 3** se muestran los resultados obtenidos mediante esta técnica (Figura 3a y 3 b) con la que sí fue posible aislar la dispersión de la radiación producida por las cadenas lineales de NPs de Ag. Comparando los resultados obtenidos por las dos técnicas se puede concluir que el espectro de extinción obtenido tiene su origen preferentemente en la contribución de las cadenas de NPs, más que en las NPs distribuidas sobre las superficies de dominio.

El análisis de los efectos de las nanoestructuras de Ag sobre la luminiscencia del ion Nd^{3+} se llevó a cabo en nuestro trabajo mediante la técnica de microscopía de fluorescencia sobre el sistema NPs Ag/Nd^{3+}:PPLN. En particular se analizaron las emisiones en el IR en torno a 900 y 1084 nm del ion Nd^{3+}, correspondientes las transiciones $^4F_{3/2} \rightarrow {}^4I_{9/2}$ y $^4F_{3/2} \rightarrow {}^4I_{11/2}$ respectivamente, bombeando en el visible a 488 nm (**artículos 1-4**). En todos los casos y con el fin de obtener resultados sistemáticos se realizaron mapas espaciales integrando bajo diferentes condiciones la señal luminiscente proveniente de estas transiciones. La obtención de los mapas espaciales permitió el análisis de las respuestas ópticas de las diferentes nanoestructuras plasmónicas presentes en la superficie del cristal simultáneamente y en las mismas condiciones. Los detalles sobre la resolución espacial y espectral de la técnica se mencionaron en la Sección IV.

Entre los resultados más relevantes se destaca la observación por primera vez del efecto antena generado por las nanoestructuras plasmónicas sobre la luminiscencia de los iones Nd^{3+} en la proximidad de las NPs de Ag. Así, fue posible conseguir un incremento de aproximadamente el 80% en la emisión del Nd^{3+} en torno a 900 nm al excitar selectivamente los modos plasmónicos colectivos de las cadenas

lineales de NPs, las cuales generan mayor concentración de campo electromagnético en nuestro cristal (**artículo 1**). Se comprobó, como era de esperar, que el aumento de la luminiscencia es altamente sensible a la polarización de bombeo empleada en nuestros experimentos, debido a la geometría lineal de las cadenas plasmónicas. La configuración óptima corresponde a aquella en que la polarización de la radiación de excitación es paralela a la cadena de NPs metálicas. Polarizando la radiación de excitación en las direcciones paralela y perpendicular a las cadenas de NPs se obtienen diferentes respuestas ya que se excitan diferentes modos plasmónicos de las cadenas. Estos modos propios de las cadenas surgen de la interacción colectiva entre NPs individuales que actúan como dipolos eléctricos fuertemente acoplados y generan intensificaciones de campo mayores que cuando se consideran partículas aisladas.

Con el fin de entender con más profundidad las respuestas plasmónicas de las cadenas de NPs de Ag presentes en nuestro sistema, se colaboró con el grupo del profesor J. Aizpurua del Centro de Física CSIC-UPV-EHU quienes llevaron a cabo las simulaciones teóricas de las secciones eficaces de extinción y de absorción resolviendo las ecuaciones de Maxwell por el método de elementos de frontera (**artículos 3** y **4**). Los resultados pusieron de manifiesto el fuerte carácter radiativo de las oscilaciones de los modos de las cadenas de NPs que se excitan con luz polarizada paralelamente a las mismas (máximo alrededor de 600 nm), frente a las oscilaciones excitadas con radiación perpendicular que mostraban un fuerte carácter principalmente absorbente (máximo alrededor de 450 nm). Este hecho estaba en buen acuerdo con los resultados experimentales obtenidos a partir de las medidas de luminiscencia, y explicaba asimismo el espectro de extinción obtenido experimentalmente y cuya contribución mayoritaria se asocia por tanto a la presencia de los alineamientos de NPs. En lo que se refiere a este último espectro, las simulaciones explicaban bien su anchura espectral y posición (600 nm) considerando que la cadena contiene NPs con una distribución de tamaños centrada en 50 nm y separaciones medias de muy pocos nanómetros.

Una vez que se establece la posibilidad de obtener arreglos plasmónicos cuyas resonancias son aprovechadas para intensificar la fotoluminiscencia de los iones activos Nd^{3+}, pasamos a resumir aquí los estudios encaminados a analizar la posibilidad de controlar las propiedades ópticas de nuestro medio de ganancia mediante la utilización de diferentes orientaciones del cristal de $LiNbO_3$ y diferentes configuraciones de NPs de Ag.

Los experimentos de micro-fluorescencia mencionados con anterioridad fueron realizados analizando los efectos de las nanoestructuras plasmónicas sobre la superficie polar del cristal $LiNbO_3$:Nd^{3+} sobre el que estas fueron depositadas. De acuerdo con la estructura cristalina del $LiNbO_3$ y con el carácter dipolar eléctrico de las transiciones del ion Nd^{3+} en este cristal, en esta configuración (α) solo es posible

acceder a las líneas de emisión del ion Nd^{3+} con carácter σ. Sin embargo, tal y como se mostró en la Sección II, la transición láser $^4F_{3/2}(R_1)\rightarrow{}^4I_{11/2}(Y_2)$ se obtiene en configuración π cuando la polarización de luz es paralela al eje óptico (eje c) del cristal.

Con el fin de optimizar el sistema de ganancia, y conseguir intensificar la transición del Nd^{3+} que presenta mayor sección eficaz de emisión, se estudió la posibilidad disponer de cadenas de NPs paralelas al eje ferroeléctrico del cristal. Esto requería la utilización del corte Y del $LiNbO_3$ corte Z como plataforma para llevar a cabo el proceso de litografía ferroeléctrica. A pesar de que dicha superficie no es polar, la formación de cadenas de NPs se obtuvo con éxito sobre dicha cara. En el **artículo 2** se demuestra por primera vez la utilización del corte Y, no polar, del $LiNbO_3$ como plataforma alternativa al corte Z para la obtención de cadenas de NPs metálicas mediante el proceso de foto-reducción. Con este resultado se pudo establecer que la formación de las nanoestructuras metálicas está ligada a la presencia de carga superficial, más que a la polarización espontánea en sí. En nuestro caso dicha carga superficial está relacionada con presencia de piezoelectricidad a lo largo del eje Y del $LiNbO_3$ junto con la presencia de un intenso dipolo superficial. Con los resultados de esta tesis se pone de manifiesto la posibilidad de extender el proceso de fotoreducción a una gran variedad de materiales piezoeléctricos.

Por otra parte, y de acuerdo con el objetivo principal, la obtención de cadenas de NPs paralelas al eje *c* permite la presencia de resonancias plasmónicas que intensifican selectivamente las transiciones fotoluminiscentes (excitación y emisión) del ion Nd^{3+} con carácterπ (campo eléctrico de la luz paralelo al eje c del cristal). En particular, excitando los modos radiativos mediante una polarización paralela a las cadenas de NPs se origina la intensificación selectiva de las transición láser a alrededor de 1.08 μm, lo cual resulta de especial relevancia para el diseño de sistemas de ganancia óptica en la nanonoescala (**artículos 2 y 3**).

Como hemos mencionado, en la tesis se ha analizado también la posibilidad de controlar las propiedades ópticas de iones trivalentes de tierras raras en un medio de ganancia de estado sólido mediante la adecuada elección del arreglo plasmónico. En concreto, se han comparado los efectos que producen dos distribuciones diferentes de NPs de Ag sobre las propiedades ópticas del ion Nd^{3+}. Por un lado, una distribución bidimensional (2D) densa y desordenada de NPs y por otro, cadenas lineales (1D) de NPs de Ag (**artículo 4**). A partir de los experimentos de micro-fluorescencia se demostró que mientras que los arreglos 2D de NPs producían el bloqueo térmico de la fluorescencia de los iones Nd^{3+}, los arreglos 1D (cadenas) producían la intensificación de la emisión producida desde el nivel $^4F_{3/2}$. Las simulaciones teóricas de las resonancias plasmónicas fueron de gran valor para explicar los resultados experimentales obtenidos. Estos cálculos pusieron de manifiesto el diferente carácter

(óhmico o radiativo) de los modos plasmónicos localizados asociados a cada una de las dos distribuciones de NPs (2D y 1D, respectivamente) para la longitud de onda de excitación. Estos resultados son de relevancia por su utilidad para determinar la configuración óptima de los arreglos metálicos, y ponen de manifiesto el papel que juega la organización de las NPs metálicas a la hora de controlar las propiedades ópticas de los iones láser. En particular, su utilidad para eliminar el bloqueo térmico de la fluorescencia, un parámetro crucial que puede impedir la acción láser del sistema, y para producir la intensificación de la misma. El trabajo pone también de manifiesto la capacidad que tienen los iones ópticamente activos para actuar como sondas de campo cercano de las resonancias plasmónicas.

En el último trabajo compendiado (**artículo 5**) se demuestra la acción láser con confinamiento nanométrico en un medio de ganancia basado en Nd^{3+}. Con este artículo se alcanza el objetivo principal de la tesis: generar emisión de radiación coherente en la nanoescala empleando un laser de estado sólido, en concreto un cristal de $LiNbO_3$:Nd^{3+}. Aunque este tipo de amplificación haya sido reportada en pocos sistemas y configuraciones, esta es la primera vez que se consigue oscilación láser en la nanoescala en un láser de estado sólido. El confinamiento extraordinario del modo laser que presenta el $LiNbO_3$:Nd^{3+} a ~1,08 µm se consigue mediante las resonancias plasmónicas de las nanoestructuras metálicas dispuestas sobre este cristal de ganancia laser.

Para llevar a cabo este fin, se diseñó de una cavidad micrométrica y se realizaron medidas de ganancia láser bombeando y recogiendo la señal mediante técnicas de microscopia óptica. Se obtuvo por primera vez ganancia óptica en configuración nanométrica en un láser de estado sólido debido a la interacción entre los plasmones superficiales localizados en cadenas de NPs de Ag y las propiedades ópticas del ion activo Nd^{3+}. Se observó una reducción del 50% en la potencia umbral de bombeo para acción láser con respecto a la oscilación laser del mismo sistema en volumen, así como un incremento de la ganancia en un factor 15. Además, estos resultados fueron obtenidos a temperatura ambiente. La modelización de los resultados obtenidos se ha llevado a cabo en colaboración con J. Bravo Abad (UAM), quien realizó simulaciones tanto de las curvas de eficiencia laser de nuestro sistema como de las distribuciones de campo eléctrico en las cercanías de cadenas de NPs de Ag. Este último trabajo abre el camino para implementar el efecto de confinamiento nanoescala en otros SSLs con iones y matrices diferentes, a través de la correcta elección de la configuración y morfología de las nanoestructuras plasmónicas.

Como punto adicional queremos mencionar los resultados relacionados con la respuesta no lineal del $LiNbO_3$, en particular la generación de segundo harmónico (SHG). Entre los resultados obtenidos en la tesis se consiguió por primera

intensificación en la señal SHG producida por el cristal debido a la presencia de los plasmones superficiales localizados en cadenas de NPs de Ag. Los factores de amplificación obtenidos llegan a ser significativamente superiores a los correspondientes a la luminiscencia obteniendose un x20 de amplificación respecto a la zona del cristal que produce menos SHG. La diferencia en los factores de intensificación puede explicarse considerando el carácter no lineal del proceso de SHG que tiene una dependencia cuadrática con el campo eléctrico de la radiación fundamental. Así pues, este resultado vuelve a manifestar la relevancia de la intensificación de campo producido por las cadenas de NPs, demostrando además la multifuncionalidad del sistema.

A nuestro entender esta tesis constituye el primer trabajo sobre los efectos de las cadenas plasmónicas sobre un láser de estado sólido multifuncional. Este trabajo representa un enfoque alternativo en la búsqueda de láseres sub-micrométricos en los que se reduce el umbral y se mejora la ganancia óptica gracias a las resonancias plasmónicas de nanoestructuras metálicas. Los resultados obtenidos se pueden extender a la amplia variedad de sistemas SSLs utilizando en cada caso las técnicas de preparación y las nanoestructuras plasmónicas adecuadas.

Por otra parte, la decoración de estructuras de dominios en diferentes tipos de arreglos (1D, 2D...) puede permitir un aprovechamiento más eficaz de las propiedades no lineales, e incluso asociarlo a la ganancia laser, para generar fenómenos de autodoblado en frecuencia en la nanoescala. Además, a través de arreglos de nanoestructuras metálicas específicas se podrían conseguir resonancias colectivas del arreglo plasmónico completo sobre las estructuras no lineales o nanolaseres, poniendo de manifiesto la posible existencia de estados hibridos plasmónico-fotónico deslocalizados relacionados con acoplamiento difractivo o de modos guiados. En este sentido hay que destacar que el control de la polarización y direccionalidad de la emisión que se obtendría de estos sistemas es de importancia para el desarrollo de diferentes sistemas útiles en iluminación.

English

2 Overall summary

This work demonstrates for the first time the possibility to obtain arrangements of metallic nanoparticles (NPs) on a rare earth (RE^{3+}) doped ferroelectric substrate by means of ferroelectric lithography. In particular, a periodic pattern of alternating ferroelectric domains presented in a Nd^{3+}:PPLN crystal is used as a template for the deposition of Ag NPs by means of the photochemical process described in Section IV. As a result, ordered alignments of Ag NPs are obtained on the ferroelectric domain walls, as well as random distributions of Ag NPs selectively deposited on the domain surfaces of specific polarization.

This result is the basis of this thesis and validates a simple method to obtain real plasmonic arrays on a solid state laser (SSL) consisting of a RE^{3+} doped ferroelectric crystal. Until this work ferroelectric lithography had not been used in a photoluminescence material.

The ferroelectric lithography has been proved to be a very simple and low cost "bottom-up" technique to obtain metallic arrangements (nanowires) on the polar surfaces (Z-cut) of $LiNbO_3$ crystals, compared with more expensive and complex "top-down" approximations. The motivation of our work required to extend the relatively few results of ferroelectric lithography to the case of a ferroelectric gain medium, particularly, to Nd^{3+} doped $LiNbO_3$. As mentioned in Section II, Nd^{3+} is an outstanding laser ion whose optical gain arises from a four-level scheme. This ion presents a good number of absorption bands that overlap the spectral region where noble metals present their localized plasmon resonances. Besides, its main emission, in the near infrared (~1080 nm), is located in the spectral regions where the scattering of certain arrangements of metallic NPs is extended. Despite the excellent qualities of Nd^{3+} as a luminescent ion and the huge number of work dealing with its optical properties, this work constitutes the first time that the interaction of Nd^{3+} with the plasmonic response of metallic nanostructures is studied.

The first experimental results obtained in the frame of this thesis show for the first time the formation of metallic nanostructures on the polar surface (Z-cut) of a Nd^{3+} doped PPLN crystal. The metallic structures show two types of distributions:

On one hand, we obtained Ag NPs distributed on the surface of the alternating domains of the Nd^{3+}:PPLN. The formation of these NPs presents a selective character since a higher NPs density is observed on the surfaces of positive domains with respect to the negative ones. These results are shown in Figure 1 of **article 1**. It should be noted that the ferroelectric lithography technique allows, at a certain degree, to control the size of the NPs formed on the surfaces domain. The studies presented in this work have revealed average NPs diameters of 20 nm (**article 1**) and 50 nm (**article 4**).

On the other hand, in addition to the random distributions of NPs on the domains surfaces, chains of Ag NPs on the domain walls were obtained. The appearance of these chains is due to an electric field inhomogeneity at the surface of the PPLN crystal, which has a strong Z component in the vicinity of the domain walls (see Figure 1.9 in Section I). The presence of these chains were observed for the first time in our work and proved to be of extreme utility in the context of this thesis. The particles forming the chains showed higher diameters than the obtained on the domain surfaces. These particles had average diameters of about 40-70 nm, and inter-spacing distance values well below the wavelengths involved in our experiments (a few nanometers). Under extreme preparation conditions (photo-deposition time of 20 min) the NPs formed continuous Ag nanowires which were not useful to exploit the optical properties of the material (see **article 4**).

SEM images allowed the observation and the characterization of the morphology of these Ag NPs chains.

In Figure 1 of **article 1** a typical spectral response of the obtained metallic nanostructures is shown. As shown, the extinction spectrum of all NPs on the Nd^{3+}:PPLN sample extends from the visible to infrared region, with a maximum around 580 nm, overlapping many of the optical transitions of Nd^{3+}. The presence of different sizes and distributions of Ag NPs on the crystal surface (chains of NPs and NPs distributions with random positions) is responsible for the shape of the extinction spectrum. This spectrum was taken using a conventional double beam spectrophotometer (Section IV), whose configuration did not allow us to distinguish between the distinct spectral responses of the different NPs distributions. In an effort to obtain information about the specific response of the different Ag NPs distributions the setup of a dark field microscopy system was performed (previously described in Section IV). **Article 3** shows the results obtained with this technique (Figure 3a and 3b) from which it was possible to isolate the scattering produced by the linear Ag NPs

chains. Comparing the results obtained by these two techniques (transmittance and dark-field microscopy) it was possible to conclude that the obtained extinction spectrum was dominated from the contribution of the NPs chains.

The analysis of the effects produced by the Ag nanostructures on the Nd^{3+} luminescence was carried out by fluorescence microscopy. The Nd^{3+} NIR emissions around 900 and 1084 nm, corresponding to the $^4F_{3/2} \rightarrow {}^4I_{9/2}$ y $^4F_{3/2} \rightarrow {}^4I_{11/2}$ transitions, respectively, were analyzed under visible excitation at 488 nm (**articles 1**-**4**). In all cases spatial maps were performed by integrating the luminescence signal of these transitions under different conditions. These spatial maps enabled the analysis of the optical response of the different plasmonic nanostructures presented on our crystal simultaneously and under the same conditions. Details on the spatial and spectral resolution of this technique is mentioned in Section IV.

Among the most relevant results we highlight the observation for first time of the antenna effect generated by the plasmonic nanostructures on the Nd^{3+} luminescence in close proximity to the Ag NPs. According to this, it was possible to achieve an enhancement of approximately 80% in the Nd^{3+} emission at around 900 nm when the collective plasmon modes of the linear NPs chains were excited (**article 1**). As expected, we found that the luminescence enhancement is highly sensitive to the polarization of excitation light used in our experiments, due to the linear geometry of the plasmonic chains.

The optimal configuration corresponds to that in which the polarization of the excitation radiation is parallel to the metallic NPs chain. By polarizing the excitation radiation parallel and perpendicular to the chain axis direction we obtain different responses as different plasmonic modes are excited. These chain modes arise from the collective interactions between individual NPs which act as strongly coupled electric dipoles and generate higher field intensifications than the single particles.

In order to deeply understand the plasmonic response of the Ag NPs chains presented in our system, we collaborated with the group of Professor J. Aizpurua from the CSIC-UPV-EHU Physics Center who carried out theoretical simulations of the extinction and absorption cross sections of the NPs chains by solving Maxwell's equations using the boundary elements method (**articles 3** and **4**). The results demonstrated the strong radiative character of the plasmonic modes of the NPs chains, which are excited with light polarized parallel to the chains (maximum around 600 nm). Opposite to this case the modes excited under perpendicular polarization showed a strong absorptive component (maximum at around 450 nm). This fact is in good agreement with the experimental results obtained from the luminescence measurements, and also explained the experimental extinction spectrum whose main contribution was associated with the presence of the Ag NPs alignments. In fact this

extinction spectrum was consistent with those simulated for chains of NPs with average size around 50 and inter-spacing separations of a few nanometers.

Once we have established the possibility to obtain plasmonic arrangements, whose main resonances enhanced the photoluminescence of the Nd^{3+} ions, we summarize the studies directed towards controlling the optical properties of our gain medium by using i) different $LiNbO_3$ crystal orientations and ii) different Ag NPs configurations.

The previously mentioned micro-fluorescence experiments were performed in order to analyze the effects of plasmonic nanostructures deposited on to the polar surface of the $LiNbO_3$: Nd^{3+} crystal (Z-cut). According to the $LiNbO_3$ crystal structure and to the electric dipole character of the Nd^{3+} transitions in the crystal, only the σ polarized emission lines of Nd^{3+} are accessible in this α configuration. However, as shown in Section II, the $^4F_{3/2}(R_1) \rightarrow {}^4I_{11/2}(Y_2)$ laser transition is obtained in a π polarized line observed when the polarization of light is parallel to the optical axis (c axis) of the crystal.

In order to optimize the gain system, and enhance the Nd^{3+} transition presenting the highest emission cross section, we studied the possibility to obtain the Ag NPs chains parallel to the ferroelectric axis of the crystal. For this purpose a Y-cut of $LiNbO_3$ was required as platform to perform the ferroelectric lithography process. Although the Y-cut is nominally a non-polar surface, the Ag NPs chains were successfully obtained. The use of a non-polar Y-cut of $LiNbO_3$, as an alternative platform to the Z-cut surface to obtain metallic NPs chains by the photo-reduction process, is for the first time demonstrated (**article 2)**. This result established that the formation of metallic nanostructures is linked to the presence of surface charge, rather than to the spontaneous polarization itself. In our case this surface charge is related to the presence of piezoelectricity along the Y axis of $LiNbO_3$, together with the presence of a strong surface dipole. The possibility of extending the photoreduction process to the large variety of piezoelectric materials is therefore demonstrated.

Moreover, in accordance with the primary goal of the thesis, obtaining NPs chains parallel to the c axis allows to selectively enhance the Nd^{3+} photoluminescence transitions (excitation and emission) with π character (electric field of light parallel to the c axis of the crystal). Particularly, a selective intensification of the laser transition around 1.08 μm is observed when exciting the radiative modes of the NPs chains with light polarized parallel to the those chains. This result is of special relevance for the design of optical gain systems at the nanonoescale (**articles 2** and **3**).

As previously mentioned, we have also analyzed the possibility of controlling the optical properties of Nd^{3+} ions in a solid state gain medium by the appropriate selection of plasmonic arrangements. Specifically, we have compared the effects of two different Ag NPs distributions on the optical properties of Nd^{3+} ion: a two-dimensional (2D) high density and disordered Ag NP distribution and linear (1D) chains of Ag NPs (**article 4**). The micro-fluorescence experiments showed that while the 2D arrays produced thermal quenching of the Nd^{3+} fluorescence, the 1D arrangements (chains) produced intensification of the emission generated from the $^4F_{3/2}$ level. The theoretical simulations of the plasmonic resonances were determinant to explain the experimental results. These calculations showed the different character (ohmic or radiative) of the localized plasmon modes associated with each one of the two Ag NPs distributions (2D and 1D, respectively) at the specific excitation wavelength. These results are of particular relevance in order to determine the optimal configuration of the metallic arrangements and to evidence the role of these metallic NPs distributions on the optical properties of laser ions. Particularly, to eliminate the thermal quenching of the fluorescence, a crucial feature that can prevent laser action, or to produce the enhancement of the emission. The work also demonstrates the capability of optically active ions to probes the near field of the plasmonic resonances.

In the last work (**article 5**) lasing action with nanometric confinement is demonstrated in a Nd^{3+} based gain medium. Although this type of amplification has been reported in a few systems and configurations, this is the first time that laser oscillation is achieved at the nanoscale in a solid state laser. The extraordinary optical confinement of the laser mode of $LiNbO_3:Nd^{3+}$, presented at ~1,08 μm, is achieved by the presence of plasmonic resonance supported by the metallic nanostructures arranged on this laser crystal.

To accomplish it, a micrometric laser cavity was designed and gain measurements were performed by pumping and collecting the signal with optical microscopy techniques.

Plasmon mediated optical gain was obtained in our system by means of the localized surface plasmons supported by the Ag NPs chains. A 50% reduction of the pump power at threshold and a 15-fold improvement of the slope efficiency with respect to the bulk laser operation was obtained. These results were obtained at room temperature. The modeling of these results was carried out in collaboration with Dr. J. Bravo Abad (UAM), who performed simulations for both the laser efficiency curves of the system and the near-field distribution around the Ag NPs chains. This latter work opens the path to implement the effect of nanoscale confinement in other SSLs with different ions and matrices, by selecting the correct configuration and morphology of the plasmonic nanostructures.

Additionally, we would like to mention the results related to the nonlinear response of $LiNbO_3$ in the presence of the metallic nanostructures, particularly the second harmonic generation (SHG). An intensification of the SHG signal generated by the crystal was achieved for the first time through the interaction between localized surface plasmons of the Ag NPs chains and the $LiNbO_3$. The SHG enhancement took place at the domain walls following the periodicity of the metal arrangements. For this case the amplification factors become significantly higher: x20 factor with respect to the lowest SHG signal generated by crystal. The difference in the intensification factors can be explained taking into account that the SHG process presents a quadratic dependence with the electric field of the fundamental beam. Once more this result evidences the strong intensification of the electric fields in the Ag NPs chains, and thus demonstrates the multi-functionality of our system.

To the best of our knowledge, this thesis is the first study on the effects produced by plasmonic chains on a multifunctional solid state laser. This work represents an alternative approach in the search for sub-micrometric lasers in which the threshold is reduced and the optical gain is enhanced by the plasmonic resonances of metallic nanostructures. The results can be extended to the wide variety of SSL systems, using in each case the appropriate plasmonic nanostructures and the fabrication technique.

On the other hand, the metallic decoration of different types domain structures (1D, 2D) can allow a more efficient use of the nonlinear properties of the crystal, which can be even associated with the laser gain to generate self-frequency doubling at the nanoscale. In addition, through specific metallic nanostructures arrangements we could get collective plasmonic resonances revealing the possible existence of delocalized photonic-plasmonic modes related with diffractive couplings or the presence of guided modes. In this sense it is worth to mention that the control of polarization and directionality of the emission obtained from these systems is of special relevance for the development of different lighting systems.

3 Publications

Article 1

Spontaneous emission and nonlinear response enhancement by silver nanoparticles in a Nd^{3+} doped periodically poled $LiNbO_3$ laser crystal

E. Yraola, P. Molina, J. L. Plaza, M. O Ramírez, L. E. Bausá
Advanced Materials **25**, 910-915 (2013).

Inside Front Cover
Advanced Materials. **25**, 794 (2013).

Spontaneous Emission and Nonlinear Response Enhancement by Silver Nanoparticles in a Nd^{3+}-Doped Periodically Poled $LiNbO_3$ Laser Crystal

Eduardo Yraola, Pablo Molina, José L. Plaza, Mariola O. Ramírez, and Luisa E. Bausá*

Plasmonic nanostructures are attracting great interest because they can provide mechanisms for remarkable optical brightness enhancement and sub-wavelength light control, which are crucial features for a broad range of scientific and technological applications.[1,2] An extremely large variety of metal/dielectric combinations (types of materials and configurations) are currently the subject of intense studies, revealing new fundamental properties and leading to novel devices with improved performances, which in many cases has been possible owing to advances in complex synthesis and fabrication techniques.[3] However, little work has been devoted to studying the interaction between the optical response of ferroelectric crystals and localized surface plasmon (LSP) resonances supported by metallic nanostructures.[4] Ferroelectric materials commonly exhibit high values of their electro-optic, piezoelectric, pyroelectric, and nonlinear coefficients, so that they are often used in microelectronics and advanced photonics. Moreover, when activated with optically active ions they can exhibit laser action and self-frequency conversion processes, which substantially increase their multifunctionality in integrated photonics.[5–8] Additionally, ferroelectric polar surfaces offer a low-cost and simple alternative to the more complex and expensive top-down fabrication techniques usually employed for metallic nanostructure deposition. The capabilities of polarization-mediated chemistry can be exploited to obtain self-assembly of molecules and more complex nanostructures on the polar surfaces of ferroelectric materials.[9–14] Here we use a recently developed photochemical method[15,16] to demonstrate the possibility of metallic nanostructure deposition on a ferroelectric solid-state laser crystal in which a periodic pattern of 180° ferroelectric domains was used as a template for Ag nanoparticles (NPs). As a laser system we chose Nd^{3+}-doped $LiNbO_3$, for which laser action and coherent self-frequency conversion radiation have been reported.[17,18] In this optically active crystal we show the formation of chains of Ag NPs with interspacing distances well below the wavelength of visible light on the ferroelectric domain boundaries. These nanostructures allow periodic enhancement of the Nd^{3+} emission by around 80%. Moreover, given the nonlinear optical character of $LiNbO_3$, the excitation of the Ag NP LSP modes resonant with the generated second harmonic produces a remarkable periodic enhancement of the quadratic nonlinear response of the system by a factor greater than 20. The results constitute a required step in the study of the effects of periodic metallic nanostructures on optically active and nonlinear solid-state laser crystals, which could be promising candidates for sub-micrometer wavelength lasers[19] and gain-enhanced nanoplasmonic metamaterials.[20]

We used ferroelectric domain structures in Nd^{3+}-doped $LiNbO_3$ crystals as templates for the self-assembly of Ag NPs by means of a photoinduced deposition process previously used for undoped $LiNbO_3$ crystals.[15,16,21] Illumination of ferroelectric domain-patterned Nd^{3+}:$LiNbO_3$ crystals immersed in a $AgNO_3$ solution with above-bandgap light at 254 nm induced the formation of Ag nanostructures on the different-polarity domain surfaces, as well as on the domain boundaries. X-ray diffraction (XRD) spectra taken at glazing incidence showed the presence of metallic silver in the wurtzite phase, while no XRD peaks related to silver oxide phases were detected (Figure S1 in the Supporting Information). **Figure 1**a shows a scanning electron microscopy (SEM) image of the obtained distribution of Ag NPs on the *z*-cut of a Nd^{3+}-doped periodically poled $LiNbO_3$ (PPLN) crystal (see the Experimental Section). The possibility of selectively assembling spherical Ag NPs on optically active Nd^{3+}-doped ferroelectric crystals by photochemical methods is therefore demonstrated. As observed, the density of the Ag NPs formed on the c^+ positive domain surface is higher than on the c^- negative surface. Additionally, the preferential deposition on the ferroelectric domain boundaries, leading to Ag NP alignments, are also clearly observed. Figure 1b shows a view of the self-assembled Ag NP chain-like structure formed on a ferroelectric domain wall, as well as the different Ag NP density on the c^+ and c^- domain surfaces. The variation of deposition domain/boundary location is explained by considering the polarization screening mechanism (internal or external) and the resultant non-uniform electric field on the crystal surface (with a strong *z* component of the electric field *E* in the vicinity of the 180° domain boundaries), owing to the antiparallel ferroelectric domain structure.[15,16] The formation of Ag NPs on our optically active Nd^{3+}-doped system can be compared to that obtained for undoped PPLN crystals. Analogous average sizes of boundary NPs (diameter ranging from 40 to 70 nm) and particles on domain surfaces (diameter around 20 nm) are achieved for similar preparation conditions.[15] However, in Nd^{3+}-doped crystals the different density of nanoparticles on opposite-polarity domain surfaces differs from the case of undoped crystals, in which similar nanoparticle densities are obtained for both domains in comparable conditions. In our

E. Yraola, Dr. P. Molina, Dr. J. L. Plaza,
Dr. M. O. Ramírez, Prof. L. E. Bausá
Departamento de Física de Materiales
and Instituto Nicolás Cabrera
Universidad Autónoma de Madrid
Campus de Cantoblanco, 28049 Madrid, Spain
E-mail: pablo.molina@uam.es

DOI: 10.1002/adma.201203176

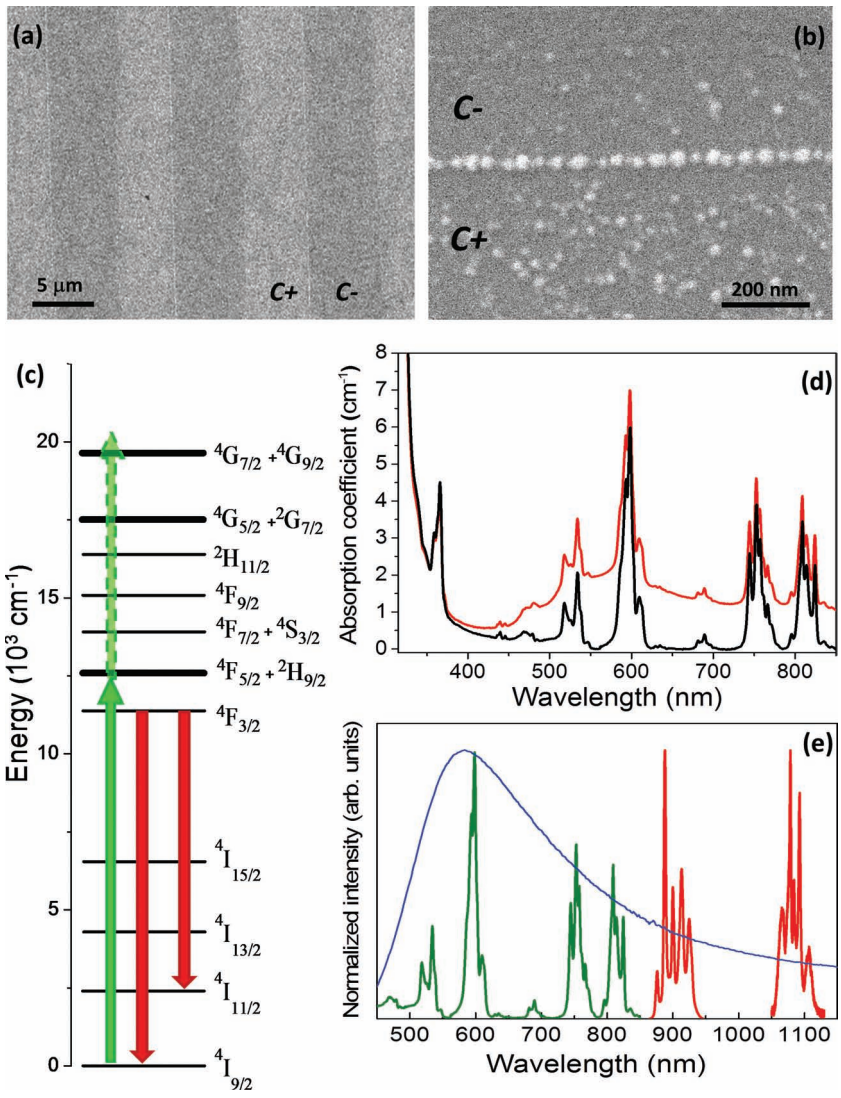

Figure 1. a) SEM image of the surface of a Nd^{3+}-doped PPLN crystal after selective photochemical deposition of Ag NPs; dark regions correspond to c^- domain surfaces with low Ag NP density; light regions are c^+ domain surfaces with higher density of Ag NPs. b) Higher resolution SEM image showing a domain boundary on which a chain of Ag NPs has formed. c) Nd^{3+} ion energy level scheme showing relevant electronic transitions. d) Absorption spectra of the Ag NPs/Nd^{3+}:PPLN system (red) and Nd^{3+}:PPLN crystal (black). e) Normalized Nd^{3+} absorption (green) and emission (red) bands overlapping the Ag NP spectrum (blue).

case, the enhanced contrast in the NPs' density on opposite domain surfaces could be related to the presence of Nd^{3+} ions as dopants. Nd^{3+} ions and related defects in the $LiNbO_3$ host crystal could act as charge defects, making internal screening, and therefore the electric field near the domain surface, more important. This could be responsible for the increase of the Ag deposition rate on the c^+ domains.[16] On the other hand, the formation of the Ag NP chains presents a slight asymmetry in the diameter of the constituent Ag NPs when two contiguous domain boundaries are compared (40 and 70 nm), indicating that the chain-like structure is formed preferentially on one of the two domain boundaries. This fact could be related to the asymmetric temperature field inherent to the off-center Czochralski growth process of the PPLN (see the Experimental Section), which could lead to additional charge-related defects and subsequently different electric field distribution between consecutive domain walls.

Once self-assembled Ag metallic nanostructures on optically active Nd^{3+}-doped $LiNbO_3$ had been demonstrated, we studied the effect of Ag NPs on the main optical properties of Nd^{3+}:$LiNbO_3$. Figure 1c presents an energy level scheme of the Nd^{3+} ion. A good variety of 4f–4f electronic transitions are available, some of the most important of which are marked on the figure. These include, in particular, some absorption bands lying in the visible and near-infrared (NIR) regions, useful for optical pumping, and relevant NIR emissions such as the main $^4F_{3/2} \rightarrow {}^4I_{11/2}$ laser channel (at around 1085 nm)[17] and the transition from the $^4F_{3/2}$ metastable state to the $^4I_{9/2}$ fundamental state (at around 900 nm). Figure 1d shows the absorption spectrum of the combined Ag NPs/Nd^{3+}:PPLN system in the UV-NIR spectral range. The spectrum of a different spatial region of the Nd^{3+}:PPLN crystal but without Ag NPs has also been included in the figure. The 4f–4f absorption bands of Nd^{3+} in $LiNbO_3$ are clearly observed in both cases. In the case of the Ag NPs/Nd^{3+}:PPLN system the Nd^{3+} transitions are superimposed on a broad band, which extends from the visible to the NIR spectral region. This band is isolated in Figure 1e after subtraction of the spectra in Figure 1d. It can be mainly attributed to excitation of dipole plasmon modes in the Ag nanostructures. As previously established, the spectral position and cross section of LSP resonances supported by metal nanostructures are dependent on size, shape, and surrounding environment.[22] In our case, the observed broad band can be related to the distribution of NPs on the PPLN crystal; it includes the contribution of the Ag NPs on the opposite domain surfaces and on the domain boundaries. Figure 1e also shows the visible and NIR absorption and emission bands of Nd^{3+} in $LiNbO_3$. As observed, most of the relevant Nd^{3+} absorption and emission bands match well the spectral region of the Ag NP absorption, including the Nd^{3+} absorption transitions in the visible and diode pumping region, and the emission transitions centered at 900 and 1085 nm. This fact supports possible resonances between the LSP modes of the metallic NPs and the transitions of the optically active Nd^{3+} ions in the substrate adjacent to the metallic structures. Therefore, Nd^{3+} excitation and radiative emission rates can be enhanced at the wavelengths where the LSP resonances are efficiently excited.

The effect of the Ag NPs on the luminescence of Nd^{3+} ions has been analyzed using microfluorescence spectroscopy on the Ag NPs/Nd^{3+}:PPLN system. **Figure 2**a shows a SEM image

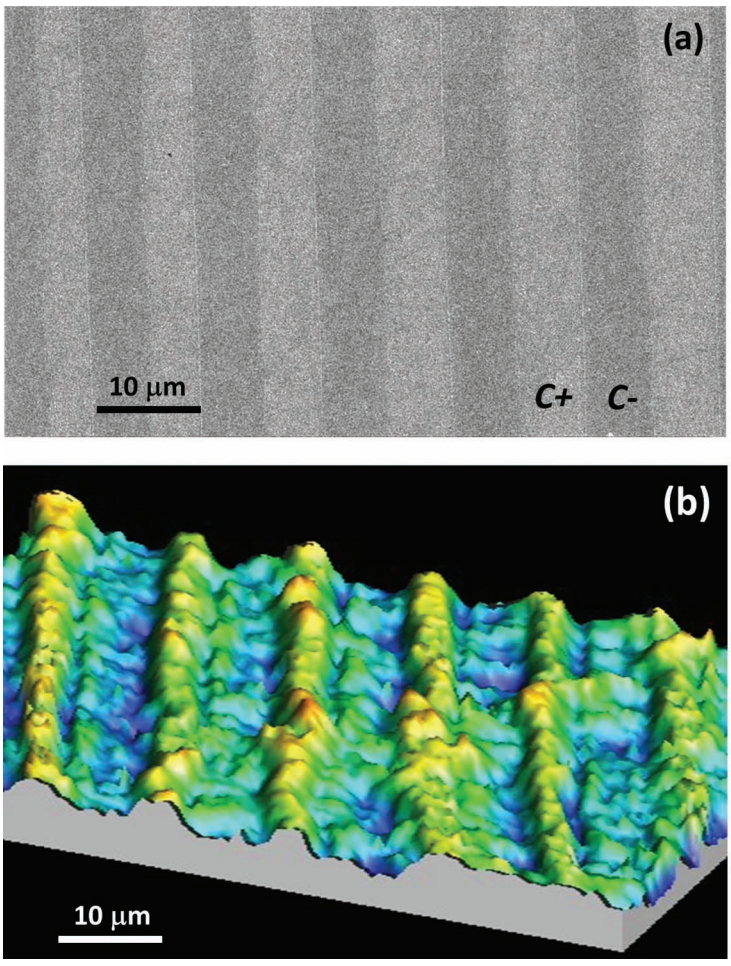

Figure 2. a) SEM image of the *z*-cut Nd^{3+}:PPLN crystal after selective deposition of Ag NPs. b) Corresponding microluminescence map obtained by integrating the $^4F_{3/2} \rightarrow {}^4I_{11/2}$ transition of Nd^{3+} ions.

of the PPLN polar surface, showing how the distribution of Ag NPs replicates the periodicity of the structure. Regions with different Ag NP densities and sizes, as well as the chain-like structures formed on alternate domain boundaries, can be observed. Figure 2b displays the microfluorescence map corresponding to the Nd^{3+} $^4F_{3/2} \rightarrow {}^4I_{11/2}$ integrated emission (1050–1130 nm spectral region), obtained under excitation at 488 nm. The corresponding spectrum is shown in Figure 1e. The integrated intensity image shows a peak–valley structure, which can be well correlated to the domain surfaces with higher and lower Ag NP concentration, respectively. A systematic periodic enhancement of the Nd^{3+}-emitted intensity from the regions with higher Ag NP density (positive domain surfaces) to those with lower Ag NP density (negative domain surfaces) is observed. It is important to mention that similar experiments were carried out on the same Nd^{3+}:PPLN crystal but without Ag deposition. In this case the Nd^{3+} emission intensity did not show significant variation, either with the type (positive or negative) of the polar domain surface or at the domain boundaries, which pointed out the homogeneity of the Nd^{3+} ion distribution in our PPLN crystal.

A point that should be addressed concerns the shape of the emission spectrum. As observed in Figure 1e, the Nd^{3+} $^4F_{3/2} \rightarrow {}^4I_{11/2}$ emission displays a clear structure arising from the Stark splitting of the involved states by the effect of the host crystal field. The number of Stark transitions and their intensity depend on the crystal configuration/polarization. In our case the spectra were taken in unpolarized α configuration, that is, the beam parallel to the crystallographic *c*-axis of $LiNbO_3$. Forced electric-dipole character has been confirmed for the Nd^{3+} Stark transitions, owing to the non-inversion C_3 local symmetry site of Nd^{3+} ions in $LiNbO_3$.[23] We confirmed that the shape of the Nd^{3+} emission spectrum was not affected by the Ag NP distribution, which indicates that in this α configuration the character of the Stark transitions was not altered by the interaction with the metallic nanostructures. A similar set of results — with regard to enhancement and behavior — was obtained for the Nd^{3+} $^4F_{3/2} \rightarrow {}^4I_{9/2}$ emission centered at a shorter wavelength, 900 nm. In both cases, the increase of the photoluminescence can be attributed to two possible mechanisms: On one hand, to the enhancement of the radiative emission rate owing to the excitation of surface plasmon modes in the Ag nanostructures, which are resonant with the Nd^{3+} $^4F_{3/2} \rightarrow {}^4I_{11/2}$ and $^4F_{3/2} \rightarrow {}^4I_{9/2}$ transition dipoles, and on the other, to the enhancement of the electric field of the incident light as a result of the coupling between the Nd^{3+} absorption transitions and the surface plasmon resonances supported by the Ag nanostructures (see Figure 1e).

To gain a deeper insight into the optical behavior of the Nd^{3+} emitter–Ag nanostructures, we analyzed the photoluminescence polarization dependence. We took advantage of the different types of Ag NP distributions on the PPLN crystal (lower density and smaller size nanoparticles randomly located on the alternate domain surfaces, and linear chains of bigger silver NPs on the domain boundaries) and their different responses to polarized light. The chain-like structures on the domain boundaries consist of aligned Ag NPs with average interspacing distances well below the wavelength of visible light (around 20 nm) (see Figure 1b). This type of Ag NP configuration supports the presence of strong near-field dipolar interaction between adjacent NPs, resulting in a strong polarization-dependent behavior.[24,25] The response of the Ag NP chains should clearly differ from that of the Ag NPs located on the domain surfaces.

Figure 3 displays the results related to the Nd^{3+} $^4F_{3/2} \rightarrow {}^4I_{9/2}$ emission from the Ag NPs/Nd^{3+}:PPLN system for different polarization configurations. Figures 3a and b show schemes of the experimental setup showing the excitation and emission polarization states (perpendicular and parallel to the NP chain axis, respectively). In the case of light polarized perpendicular

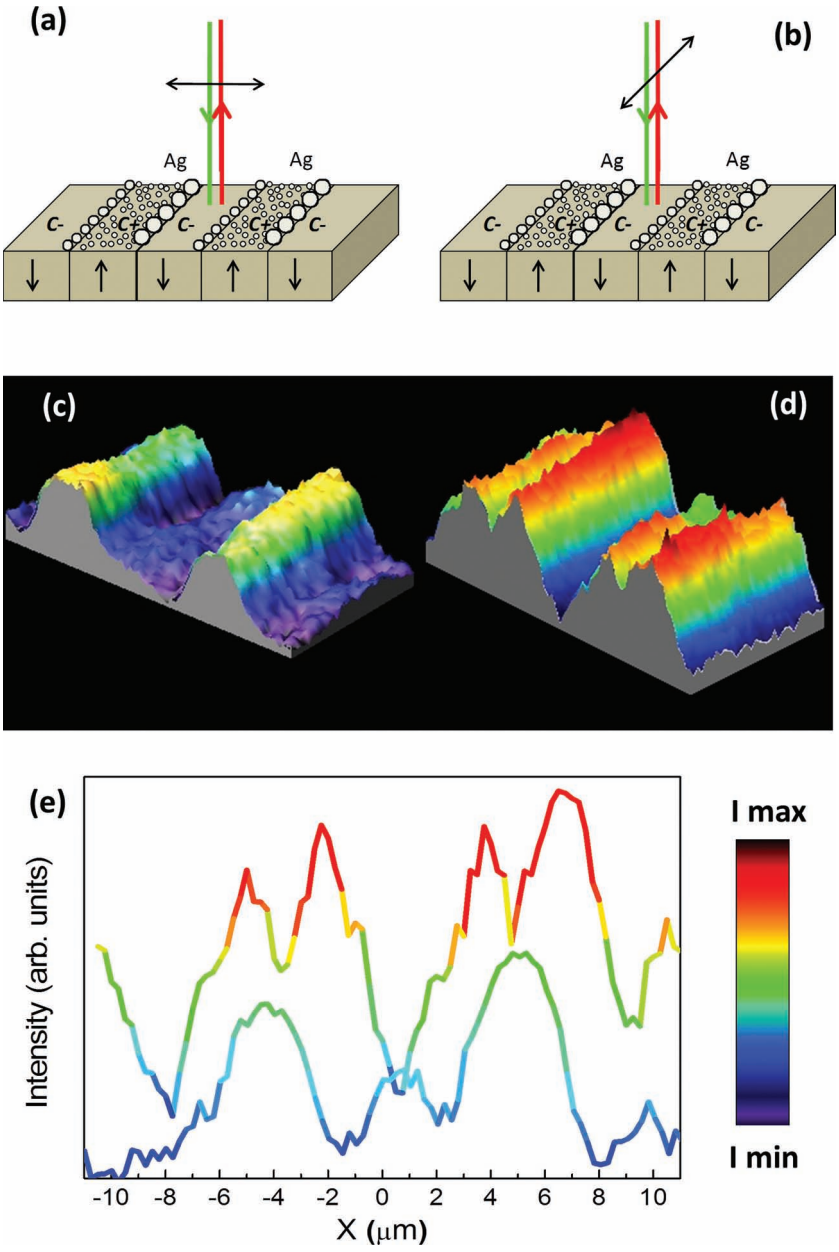

Figure 3. Effect of the Ag NP chains on the $^4F_{3/2} \rightarrow {}^4I_{9/2}$ Nd^{3+} emission. a,b) Experimental setup diagrams for excitation and emission polarizations perpendicular (a) and parallel (b) to the long axis of the Ag NPs chains. c,d) Polarized microluminescence maps obtained by integrating the emitted light in the polarization configurations shown in (a) and (b), respectively. e) Intensity profiles of the microluminescence intensity shown in (c) and (d) as a function of the spatial position on the sample surface.

to the NP chain, the recorded intensity map (Figure 3c) is very similar to that obtained in the unpolarized case (Figure 2b), where maxima of Nd^{3+} emission intensity are obtained from c^+ domain surfaces. However, when the excitation and emission beams are polarized parallel to the NP chain axis, the obtained map (Figure 3d) presents a more complex profile, showing maximum values of emitted intensity in the vicinity of the Ag NPs chains. For inner regions of the domain surfaces the emission exhibits a similar intensity to that observed for perpendicular polarization. These results can be more clearly seen in the intensity profiles (Figure 3e), where the variation of the integrated Nd^{3+} emitted intensity is represented as a function of spatial position on the PPLN surface. The highest emission values are obtained from the surroundings of the metallic chains, from where an enhancement of 80% is obtained relative to the case of negative domain surfaces. This increase is on the order of those observed for other trivalent rare earth emitter–metallic nanostructures.[26,27] Slightly different emission intensity is obtained from each one of the boundaries confining a positive domain surface, in agreement with the above-mentioned asymmetry of the nanostructures on consecutive domain boundaries. For inner regions between domain boundaries the emission intensity does not depend on the polarization direction, in accordance with the random location of the Ag NPs on domain surfaces where no preferential alignment exists.

The results can be interpreted by considering the distributions of Ag NPs as multiple optical antennas, their corresponding modes being responsible for the observed fluorescence enhancement. In the case of the chains of NPs, where the distance between particles is around 20 nm, a strong coupling between the antennas arms is possible, which results in an improved response of the Ag NP–Nd^{3+} emitter complex compared to the case of single Ag NPs or antennas with uncoupled arms, which are located on the domain surfaces. Therefore, out-coupling to the far field of the near field of Nd^{3+} emitters located adjacent to the metallic nanostructures is observed owing to the antenna effect.[20,28] To investigate separately the effects of the excitation and spontaneous emission on the increase of the fluorescence, we uncoupled the polarization of the emitted and excitation light. For polarization of the emitted light perpendicular to the axis of the chains while that of the excitation light was parallel, or vice versa (excitation light perpendicular and emitted light parallel), a decrease of the emitted intensity was observed compared to the case in which both excitation and emission polarization are parallel to the chains (see Figure S2 in the Supporting Information). These results indicate that the fluorescence intensity is related to both the emission properties of the antenna-coupled Nd^{3+} and the enhancement of the pump incident electric field. It should be mentioned here that, because of the α configuration used in the experiments (light beam parallel to the c optical axis of the crystal) and the forced electric-dipole character of the

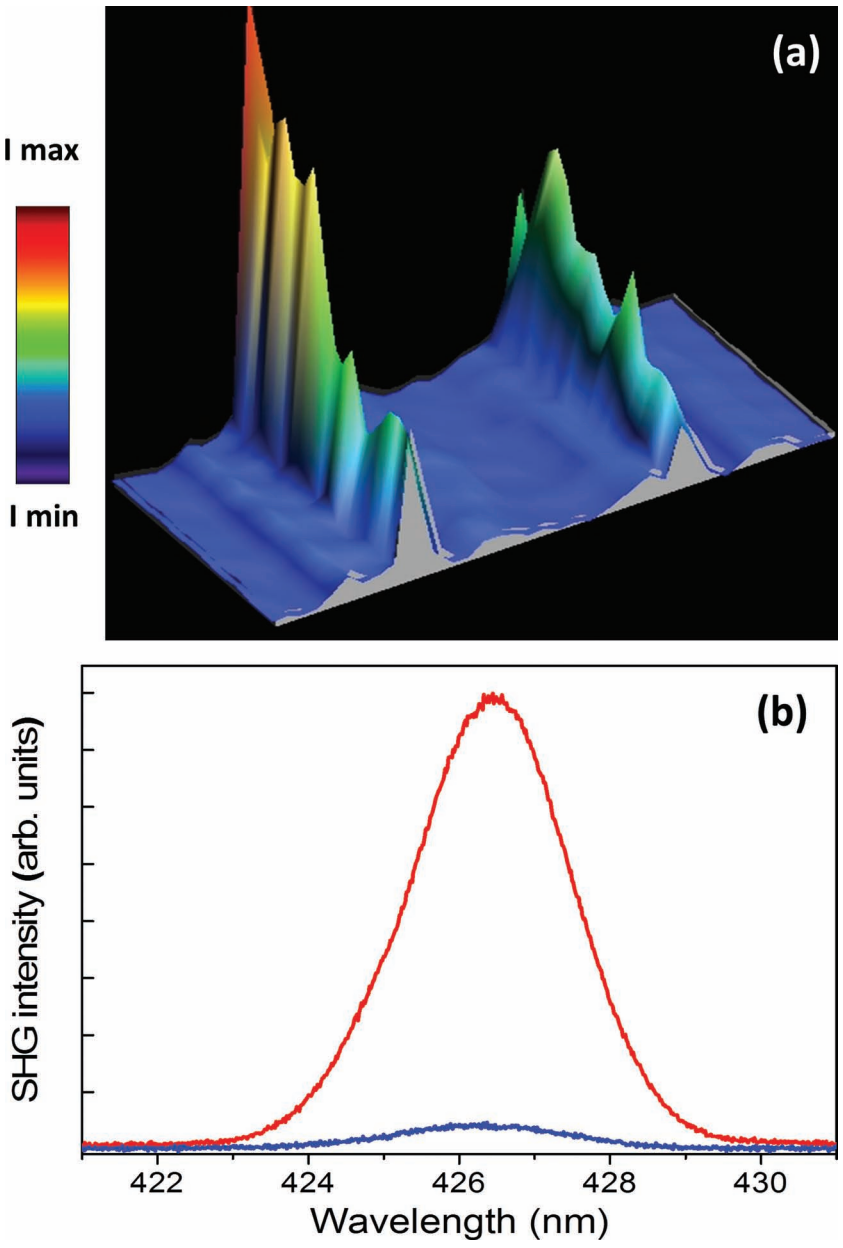

Figure 4. a) Spatial map of the integrated second harmonic obtained from the surface of the Ag NPs/PPLN:Nd^{3+}system. b) Second-harmonic spectra corresponding to the region of the Ag NPs chain (red); the negative domain surface with the lowest Ag nanoparticle density (blue). Pump wavelength was 852 nm.

Nd^{3+} transitions, no modification of the intensity of the Stark transitions takes place when the polarization is rotated around the *c* optical axis in an undoped $LiNbO_3$ crystal. Therefore, the observed changes with the two orthogonal polarization states are exclusively due to the presence of the metallic nanostructures, which produce not only an intensification of the Nd^{3+} fluorescence but also an optical anisotropy in the response of the system.

Finally, taking advantage of the high quadratic nonlinearity of the $LiNbO_3$ crystal,[29] we analyzed the effect of the Ag nanostructures on the second harmonic generation (SHG) at the surface of the Ag NPs/Nd^{3+}:$LiNbO_3$ system. In this case, the material was pumped with a femtosecond pulsed laser in the NIR region to obtain visible-light SHG. **Figure 4**a shows a map of the integrated second harmonic on the surface of the sample. As observed, the SHG is periodically intensified following the pattern of the Ag NP distribution. Maximum values are obtained from the regions of Ag NP chains and minima from the c^- domain surfaces. Figure 4b compares the second-harmonic spectra from two different zones of the PPLN. An enhancement in the SHG efficiency of 20 was obtained from the region of the Ag NP chain with respect the low density Ag nanoparticle regions. A much greater enhancement of SHG is obtained compared to the fluorescence intensity. Owing to the two-photon character of the process, the second-harmonic intensity is much more sensitive to the field intensity of the incident light than in the linear emission case. Accordingly, the observed second-harmonic intensification could be mainly related to the incident electromagnetic field enhancements in the vicinity of the NPs as a result of resonant excitation of plasmon modes. The SHG enhancement factor could seem moderate compared to other types of systems in which intensification of SHG has been reported.[30–32] However, the extremely importance of $LiNbO_3$ as electro-optic and nonlinear material in a large number of applications in integrated optics validates the interest of this first result, which, additionally, can be further improved by using different types of metallic structures.

In conclusion, by using a simple and low-cost photochemical technique we have prepared periodic arrays of metallic Ag NP chains on a Nd^{3+}-based ferroelectric solid-state laser using a one-dimensional (1D) periodic pattern of 180° ferroelectric domains as a template. By exploiting the unique features of plasmonic nanostructures to strongly concentrate electromagnetic fields, we have demonstrated a directional enhancement of Nd^{3+} luminescence, as well as a remarkable intensification of the quadratic nonlinear SHG response, which occurs with the periodicity of the metallic arrays. To our knowledge this constitutes the first report on the effects of metallic nanostructures on a multifunctional ferroelectric solid-state laser. The results can be easily extended to the 2D case to take advantage of the relevant nonlinear properties of different types of alternating ferroelectric domain structures on active materials,[33,34] which constitutes an alternative approach in the search for sub-micrometer wavelength lasers or gain-enhanced nanoplasmonic metamaterials.

Experimental Section

Nd^{3+} activated PPLN crystals were prepared by the off-center Czochralski method along the *a*-axis by adding Nd (1 mol%) in the form of oxide. During crystal growth the rotational axis was displaced 5 mm from the symmetry axis of the temperature field.[35] This produced a periodic temperature fluctuation able to create alternating ferroelectric domains. 5N congruent $LiNbO_3$ and 3N Nd_2O_3 powders were used as starting materials. The period length was controlled via rotation and pulling rates (30 rpm and 1 mm h^{-1}, respectively) to generate a 50% duty cycle of alternating domains with a period of 10 μm (single domain length of around 5 μm). The photoinduced silver deposition process was carried out by illuminating the surface of a 1 mm thick *z*-cut Nd^{3+}:PPLN crystal with UV light while the sample was immersed in $AgNO_3$ solution.[21] A mercury pen lamp (UVP model 11SC-1) with its main line at 253.6 nm was used. The emission power was 5400 μW cm^{-2} at a distance of 1.9 cm. The $AgNO_3$ solution (0.01 M) was illuminated between 1 and 10 min.

The absorption spectra were obtained with a UV/vis/NIR Lambda 1050 PerkinElmer spectrometer. The samples were measured in transmission configuration using a spot size of 5 mm^2. Micro-luminescence and SHG far-field experiments were performed in a laser scanning confocal microscope. An Ar^+ laser (Spectra Physics Model 177-Series) at 488 nm and a femtosecond Ti:sapphire laser (3900S Tsunami Spectra Physics) were used as excitation sources. The laser beam was focused onto the sample by a microscope objective (50× and 100× magnifications). The photoluminescence was collected in backscattering geometry with the same objective. Samples were placed on a two-axis *XY* motorized stage with 0.1 μm spatial resolution. For the visible excitation wavelength, the laser was focused to a spot size less than 1 μm.

Supporting Information

Supporting Information is available from the Wiley Online Library or from the author.

Acknowledgements

This work has been supported by the Spanish Government under project MAT2010-17443 and Comunidad de Madrid under grant S2009/1756.

Received: August 2, 2012
Published online: November 8, 2012

[1] W. L. Barnes, A. Dereux, T. W. Ebbesen, *Nature* **2003**, *424*, 824.
[2] L. Novotny, N. van Hulst, *Nat. Photonics* **2011**, *5*, 83.
[3] E. Hutter, J. H. Fendler, *Adv. Mater.* **2004**, *16*, 1685.
[4] D. Szwarcman, D. Vestler, G. Markovich, *ACS Nano* **2011**, *5*, 507.
[5] E. Lallier, J. P. Pocholle, M. Papuchon, M. de Micheli, M. J. Li, Q. He, D. B. Ostrowsky, C. Grezes-Besset, E. Pelletier, *Opt. Lett.* **1990**, *15*, 682.
[6] S. J. Field, D. C. Hanna, A. C. Large, D. P. Shepherd, A. C. Tropper, P. J. Chandler, P. D. Townsend, L. Zhang, *Opt. Lett.* **1992**, *17*, 52.
[7] P. Molina, M. D. Ramirez, L. E. Bausa, *Adv. Funct. Mater.* **2008**, *18*, 709.
[8] M. O. Ramirez, P. Molina, L. E. Bausa, *Opt. Mater.* **2012**, *34*, 524.
[9] S. V. Kalinin, D. A. Bonnell, T. Alvarez, X. J. Lei, Z. H. Hu, R. Shao, J. H. Ferris, *Adv. Mater.* **2004**, *16*, 795.
[10] G. I. Distler, V. P. Konstantinova, Y. M. Gerasimov, G. A. Tolmacheva, *Nature* **1968**, *218*, 762.
[11] S. Dunn, D. Cullen, E. Abad-Garcia, C. Bertoni, R. Carter, D. Howorth, R. W. Whatmore, *Appl. Phys. Lett.* **2004**, *85*, 3537.
[12] D. Ehre, E. Lavert, M. Lahav, I. Lubomirsky, *Science* **2010**, *327*, 672.
[13] S. Grilli, L. Miccio, V. Vespini, A. Finizio, S. De Nicola, P. Ferraro, *Opt. Express* **2008**, *16*, 8084.
[14] S. Habicht, R. J. Nemanich, A. Gruverman, *Nanotechnology* **2008**, *19*, 495303.
[15] Y. Sun, B. S. Eller, R. J. Nemanich, *J. Appl. Phys.* **2011**, *110*, 084303
[16] Y. Sun, R. J. Nemanich, *J. Appl. Phys.* **2011**, *109*, 104302.
[17] T. Y. Fan, A. Cordovaplaza, M. J. F. Digonnet, R. L. Byer, H. J. Shaw, *J. Opt. Soc. Am. B* **1986**, *3*, 140.
[18] J. Capmany, *Appl. Phys. Lett.* **2001**, *78*, 144.
[19] M. A. Noginov, G. Zhu, A. M. Belgrave, R. Bakker, V. M. Shalaev, E. E. Narimanov, S. Stout, E. Herz, T. Suteewong, U. Wiesner, *Nature* **2009**, *460*, 1110.
[20] O. Hess, J. B. Pendry, S. A. Maier, R. F. Oulton, J. M. Hamm, K. L. Tsakmakidis, *Nat. Mater.* **2012**, *11*, 573.
[21] X. Liu, K. Kitamura, K. Terabe, H. Hatano, N. Ohashi, *Appl. Phys. Lett.* **2007**, *91*, 044101.
[22] U. Kreibig, M. Vollmer, *Optical Properties of Metal Clusters*, Springer, Berlin **1995**.
[23] C. Bonardi, R. A. Carvalho, H. C. Basso, M. C. Terrile, G. K. Cruz, L. E. Bausa, J. G. Sole, *J. Chem. Phys.* **1999**, *111*, 6042.
[24] H. Tamaru, H. Kuwata, H. T. Miyazaki, K. Miyano, *Appl. Phys. Lett.* **2002**, *80*, 1826.
[25] S. A. Maier, H. A. Atwater, *J. Appl. Phys.* **2005**, *98*, 011101.
[26] J. Kalkman, L. Kuipers, A. Polman, H. Gersen, *Appl. Phys. Lett.* **2005**, *86*, 041113.
[27] Y. Lu, X. Chen, *Appl. Phys. Lett.* **2009**, *94*, 193110.
[28] O. L. Muskens, V. Giannini, J. A. Sánchez-Gil, J. Gómez Rivas, *Nano Lett.* **2007**, *7*, 2871.
[29] I. Shoji, T. Kondo, R. Ito, *Opt. Quantum Electron.* **2002**, *34*, 797.
[30] K. Chen, C. Durak, J. R. Heflin, H. D. Robinson, *Nano Lett.* **2007**, *7*, 254.
[31] W. Fan, S. Zhang, N. C. Panoiu, A. Abdenour, S. Krishna, R. M. Osgood, K. J. Malloy, S. R. J. Brueck, *Nano Lett.* **2006**, *6*, 1027.
[32] W. S. Cai, A. P. Vasudev, M. L. Brongersma, *Science* **2011**, *333*, 1720.
[33] A. Arie, N. Voloch, *Laser Photon. Rev.* **2010**, *4*, 355.
[34] P. Molina, M. O. Ramirez, B. J. Garcia, L. E. Bausa, *Appl. Phys. Lett.* **2010**, *96*, 261111.
[35] V. Bermudez, M. D. Serrano, E. Dieguez, *J. Cryst. Growth* **1999**, *200*, 185.

ADVANCED MATERIALS

Supporting Information

for *Adv. Mater.*, DOI: 10.1002/adma.201203176

Spontaneous Emission and Nonlinear Response Enhancement by Silver Nanoparticles in a Nd^{3+}-Doped Periodically Poled $LiNbO_3$ Laser Crystal

Eduardo Yraola, Pablo Molina, José L. Plaza, Mariola O. Ramírez, and Luisa E. Bausá*

Submitted to ADVANCED MATERIALS

Supplementary information: DOI: 10.1002/adma. 201203176

Spontaneous Emission and Nonlinear Response Enhancement by Silver Nanoparticles in Nd^{3+} doped Periodically Poled $LiNbO_3$ Laser Crystal

By *Eduardo Yraola, Pablo Molina*, José Luis Plaza, Mariola O Ramírez* and *Luisa E. Bausá*

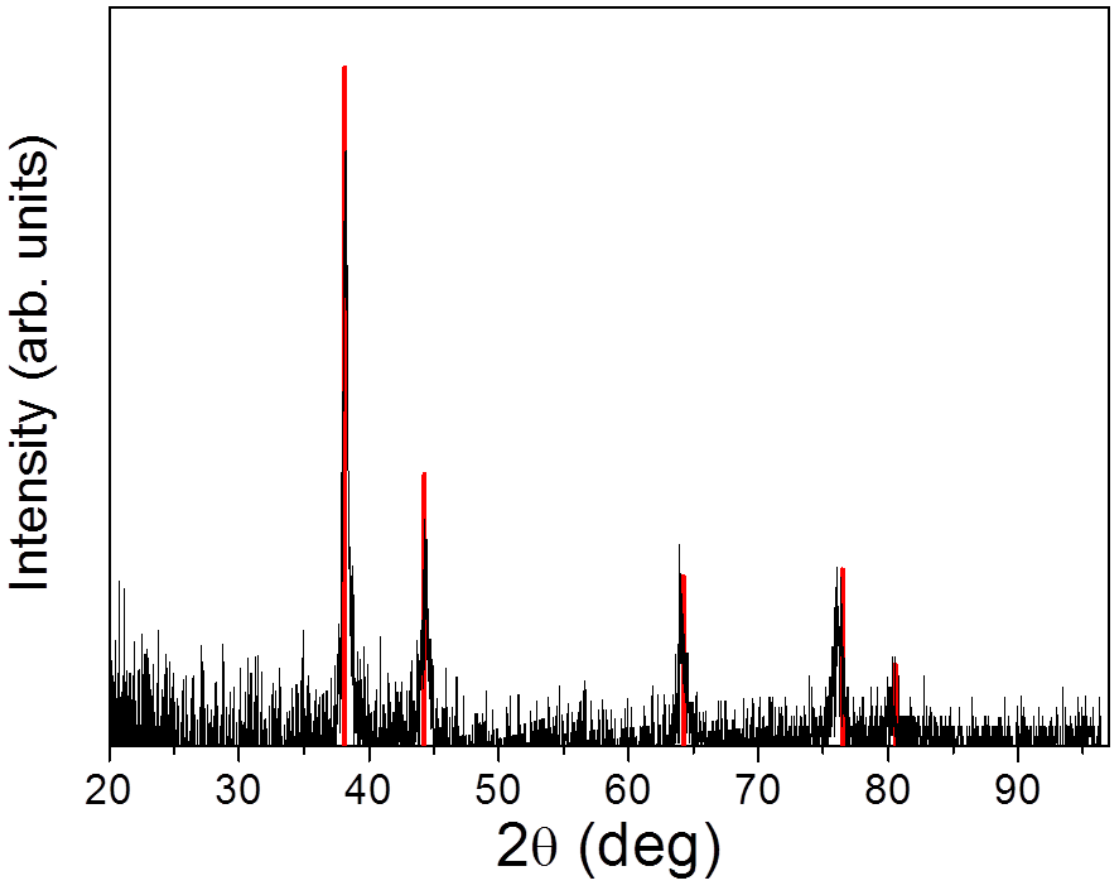

Figure S1. XRD spectra at glazing incidence showing the presence of metallic silver in wurtzite phase (red lines). No XRD peaks related to silver oxide phases are detected.

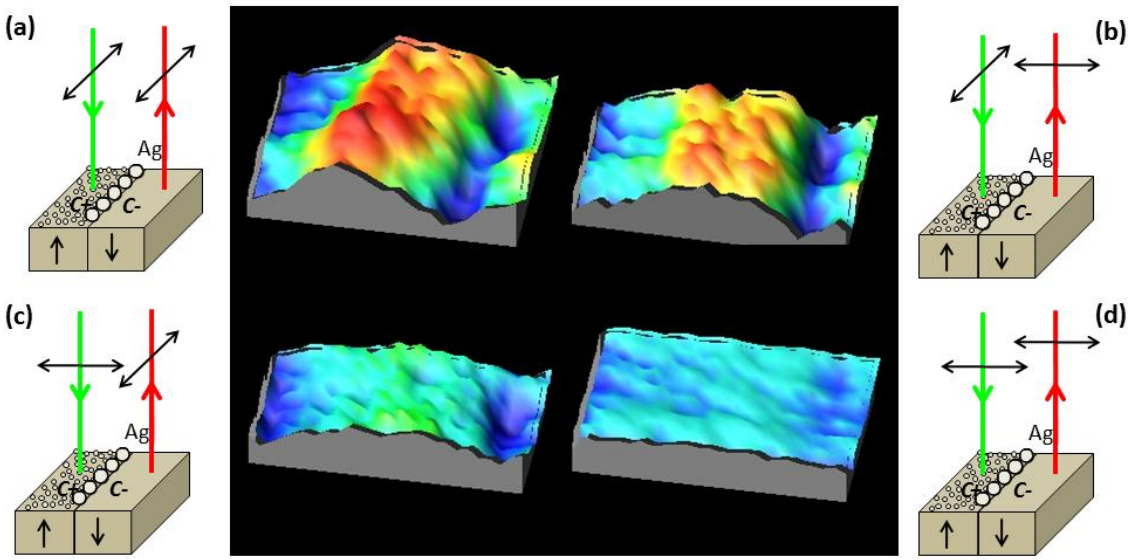

Figure S2. Effect of the excitation and emission polarization on the $^4F_{3/2} \rightarrow {}^4I_{9/2}$ luminescence. Experimental setup diagrams, and their corresponding spatial micro-luminescence maps. a) Excitation and emission parallel to the long axis of the Ag Nps chains. b) Excitation parallel and emission perpendicular. c) Excitation perpendicular and emission parallel. d) Excitation and emission perpendicular.

Vol. 25 • No. 6 • February 13 • 2013

D10488

www.advmat.de

ADVANCED MATERIALS

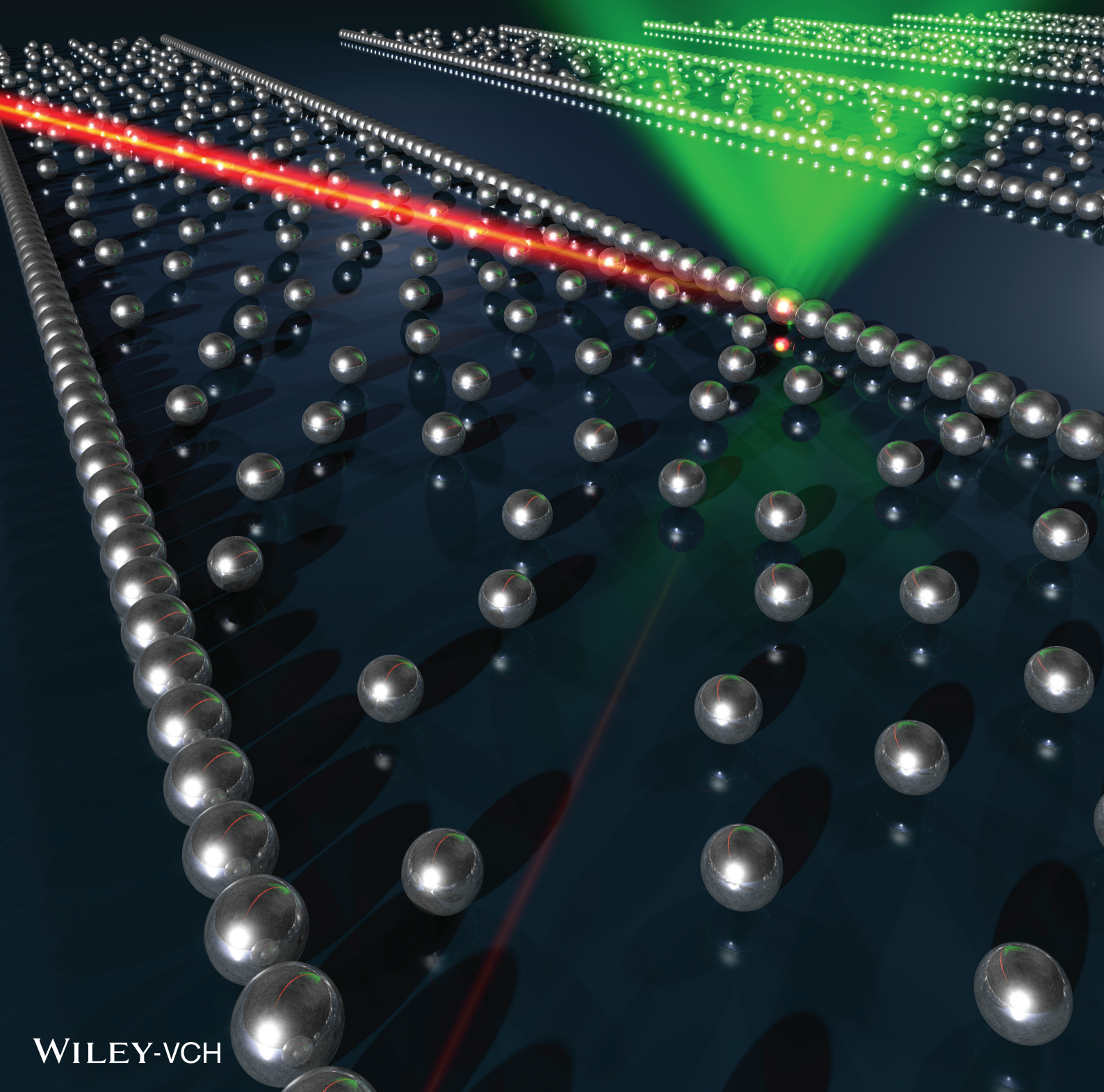

WILEY-VCH

Article 2

Selective plasmon enhancement of the 1.08 µm Nd^{3+} laser Stark transition by tailoring Ag nanoparticles chains on a PPLN Y‑cut.

P. Molina, E. Yraola, M. O Ramírez, J. L. Plaza, C. de las Heras, L. E. Bausá
Nano Letters. **13**, 4931 (2013).

NANO LETTERS

Letter

pubs.acs.org/NanoLett

Selective Plasmon Enhancement of the 1.08 μm Nd^{3+} Laser Stark Transition by Tailoring Ag Nanoparticles Chains on a PPLN *Y*-cut

Pablo Molina,* Eduardo Yraola, Mariola O Ramírez, José L. Plaza, Carmen de las Heras, and Luisa E. Bausá

Department of Física de Materiales and Instituto Nicolás Cabrera, Universidad Autónoma de Madrid, Campus de Cantoblanco, 28049 Madrid, Spain

Supporting Information

ABSTRACT: Selective photoluminescence enhancement of the specific Nd^{3+} Stark transition for which laser gain has been obtained in $Nd^{3+}/LiNbO_3$ is demonstrated by means of plasmonic resonances with the appropriate symmetry configuration. By using the nonpolar *Y*-cut of a periodically poled $LiNbO_3$ crystal as platform for photoreduction of metallic nanostructures, periodically distributed chains of Ag nanoparticles oriented parallel to the ferroelectric *c*-axis are obtained. This alternative metallic nanostructure configuration supports the resonance between the localized surface plasmon and exclusively the π-polarized Stark laser line of Nd^{3+} ions at 1.08 μm, while maintaining the remaining crystal field transitions unchanged. The work provides the experimental proof on how plasmonic-based optical antennas can be used to influence selectively rare earth optical Stark transitions to improve the performance of solid state laser gain media.

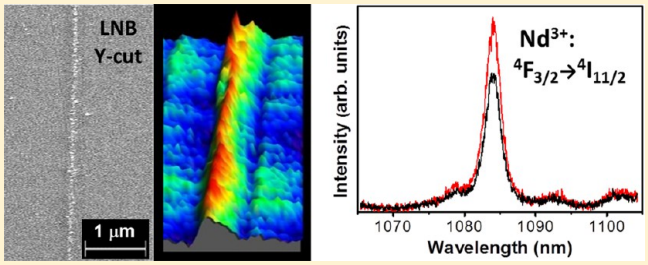

KEYWORDS: *Nd^{3+} emission, laser emission, $LiNbO_3$, ferroelectric domain pattern, Ag metallic nanoparticles, localized surface plasmon*

Noble metal nanoparticles exhibit an extraordinary capability to manipulate light at the nanometer scale. They get their unique optical properties from the ability to couple light with collective oscillations of their conduction-band electrons, known as localized surface plasmon (LSP) resonances.[1,2] Plasmonic nanostructures are currently the subject of intensive fundamental and technological studies and can be exploited to improve the performances of existing optical and optoelectronic devices, such as light-emitting systems,[3−6] biosensors,[7] solar cells,[8] or high-resolution fluorescence microscopes.[9] Additionally, the association of metallic nanostructures with different laser gain media has recently given rise to successful configurations such as nanolasers or lasing-spasers.[10,11] These applications relay in the unique features of plasmonic nanostructures for strongly concentrate electromagnetic fields in the vicinity of their physical boundaries, enhancing the interactions between optical species (atoms, QDs, organic fluorophores, and so forth) and far-field light. In this way, LSP can act as optical antennas bridging the size mismatch between the visible light and luminescent species and overcoming the diffraction-limit.[2,12] A large variety of systems, which combine different types of metallic nanostructures, optical species, and dielectric media are nowadays the subject of intense activity.[13] However, little work has been devoted to assess the usefulness of plasmonics on the emission of trivalent rare earth doped ferroelectric laser crystals.[14] These systems combine the relevant optical features provided by both ferroelectrics and trivalent rare earth ions as laser emitters. Ferroelectrics play an important role in photonics due to their suitable electro-optic and nonlinear properties for light control. Indeed, they are successfully used as high-speed light modulators, parametric oscillators, or nonlinear frequency converters, operating in a wide range of the optical spectrum.[15−18] The incorporation of optically active rare earth ions in nonlinear ferroelectric crystals extends the functionality of these systems to obtain compact devices, which can act as solid state lasers with added functions such as self-frequency conversion, self Q-switched, or even optical bistability.[19]

On the other side, polar surfaces of ferroelectrics materials, characterized by the presence of surface charges, offer a useful platform for polarization mediated chemistry enabling a low cost option for deposition of metallic nanoparticles.[20−23] Moreover, the progress achieved in micro- and nanoengineering of ferroelectric domains has allowed the fabrication of templates with regions of alternating surface charge on which domain-specific lithography has been demonstrated.[24−28]

Recently, the authors have shown the interest of combining the optical response of metallic nanostructures with optically active ferroelectric materials. Using a photochemical procedure, periodic distributions of silver nanoparticles (Ag Nps) were selectively assembled on the polar *Z*-cut of a Nd^{3+}-doped

Received: August 2, 2013
Revised: September 17, 2013
Published: September 25, 2013

   dx.doi.org/10.1021/nl4028999 | *Nano Lett.* 2013, 13, 4931−4936

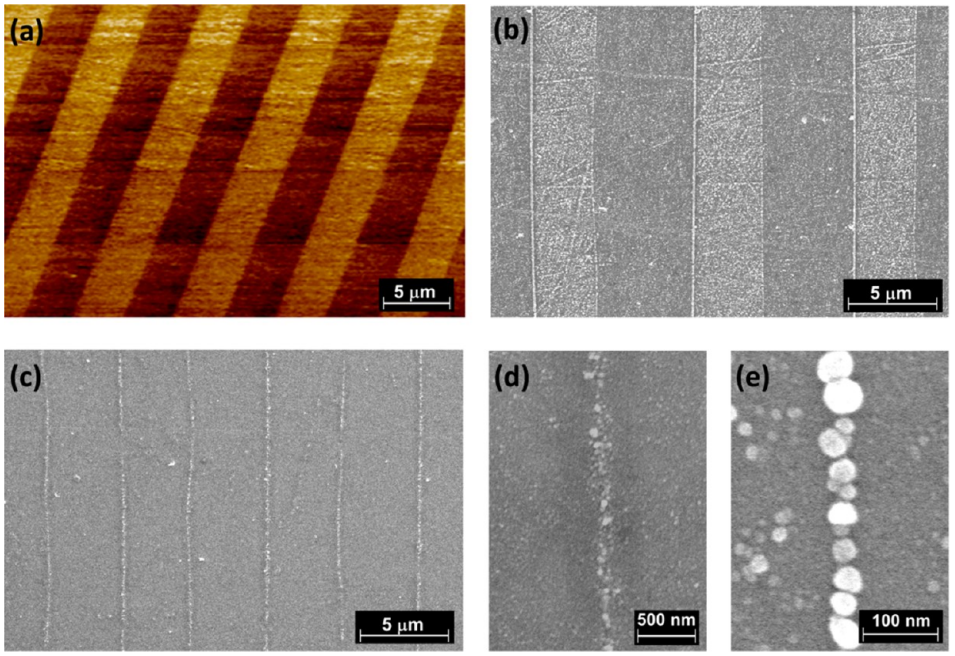

Figure 1. (a) PFM phase signal of Nd^{3+} doped PPLN *Y*-cut following the periodical surface charge distribution on that surface; (b,c) SEM images of two *Y*-cut surfaces after the selective photochemical deposition of Ag Nps on Nd^{3+} doped PPLN crystals for two different deposition time (20 and 3 min, respectively); (d,e) high-resolution SEM images showing the Ag Nps chainlike structures on the domain wall surfaces of Nd^{3+} doped PPLN *Y*-cuts. The average diameter of the Ag Nps was found to be around 40 nm.

periodically poled $LiNbO_3$ (PPLN) ferroelectric laser crystal. By exploiting the unique features of plasmonic nanostructures, an enhancement of Nd^{3+} luminescence, which took place with the periodicity of the metallic distribution, was demonstrated.[14] Photochemical assembling of Ag metallic Nps showed domain-specific deposition (the density of the Ag Nps formed on the c^+ positive domain surface was higher than on the c^- negative surface) as well a preferential deposition of chainlike structures of Ag Nps on the surface of the 180° ferroelectric domain boundaries.[20,21]

As has been demonstrated, these Ag Nps chains support the presence of strong near-field dipolar interaction between adjacent Nps,[29,30] resulting in a strong polarization dependent behavior of the photoluminescence of Nd^{3+} ions emitting in the vicinity of the Ag Nps. Specifically, when the excitation and emission beams are polarized parallel to the Ag Nps chains located on the domain boundary on the polar c surface, an enhancement of the photoluminescence is observed. A point that should be addressed concerns the shape of the emission spectra. As it is well-known, the $Nd^{3+}/{}^4F_{3/2} \rightarrow {}^4I_{11/2}$ and ${}^4F_{3/2} \rightarrow {}^4I_{9/2}$ emissions displays a clear structure arising from the Stark splitting of the involved states by the effect of the host crystal field. The number of Stark transitions and their intensity depend on the crystal configuration/polarization. In our previous work the spectra were taken in α configuration, that is, the excitation beam parallel to the crystallographic *c*-axis of $LiNbO_3$. In this α-configuration due to the C_3 symmetry of Nd^{3+} site and the forced electric-dipole character of the Nd^{3+} transitions, no modification of the shape or the intensity of the Stark transitions takes place when the polarization is rotated around the C_3 optical axis.[31] Therefore, the intensification of the ${}^4F_{3/2} \rightarrow {}^4I_{11/2}$ and ${}^4F_{3/2} \rightarrow {}^4I_{9/2}$ emission spectra affects the whole transitions without any change in the relative intensity of the different Stark lines composing the spectra. That is, the shape of the Nd^{3+} emission spectra is not modified by the Ag Nps distribution, which indicates that in that configuration, the electric dipole character of the Nd^{3+} Stark transitions is not altered by the interaction with the metallic nanostructure.

Here we investigate an alternative metallic nanoparticle configuration, which could selectively affects a particular Stark transition of Nd^{3+} ions. That is, we show selective photoluminescence enhancement of a specific Stark line for which laser gain has been demonstrated in $Nd^{3+}/LiNbO_3$ system, while maintaining the remaining crystal field transitions unchanged. Such enhancement was made feasible by using the technologically relevant nonpolar *Y*-cut of $LiNbO_3$, as an alternative platform for photoreduction of metallic nanoparticles which could support LSPs with the appropriate symmetry configuration. According to the electric dipole selection rules and the C_3 symmetry site for Nd^{3+} ions in $LiNbO_3$, the 1085 nm laser line presents π-character, that is, it is allowed for polarized light with the electric field parallel to the crystallographic *c*-axis (in contrast with σ character in which the electric field oscillates perpendicular to the crystallographic *c*-axis).[32,33] Therefore, chains of Ag Nps on the $LiNbO_3$ *Y*-cut oriented parallel to the ferroelectric *c*-axis could support resonances between the LSP of the metallic chainlike structure and the π-character Stark lines of Nd^{3+} ions. To the best of our knowledge, this is the first time that periodical arrays of metallic Nps are obtained via photoreduction method on a nonpolar surface, which enables new metal/active substrate configurations in uniaxial nonlinear photonic structures without crystallographic restrictions. By this means, the optical performance of the Ag Nps/Nd^{3+}/PPLN system has been optimized in a way that goes beyond the global enhancement of the emission and/or absorption by means of a selective plasmon intensification of the Nd^{3+} laser line. This selectivity provides the proof of concept on how plasmonic-based optical antennas can be used to influence rare earths optical transitions to improve the performance of crystalline gain media.

dx.doi.org/10.1021/nl4028999 | *Nano Lett.* 2013, 13, 4931−4936

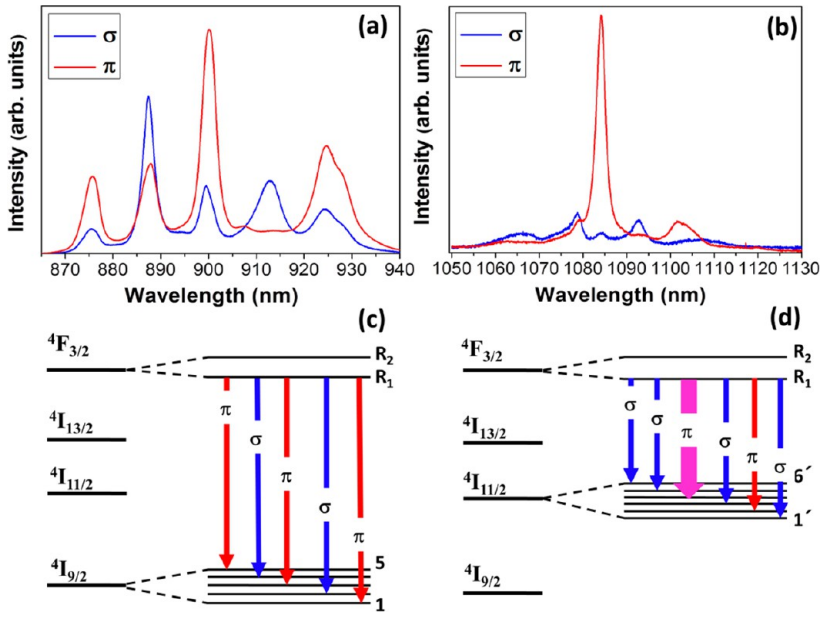

Figure 2. (a,b) Polarized emission spectra corresponding to the $^4F_{3/2}\rightarrow{}^4I_{9/2}$ and $^4F_{3/2}\rightarrow{}^4I_{11/2}$ transitions of Nd^{3+}, respectively. (c,d) Energy level scheme showing relevant Stark transitions of Nd^{3+} in $LiNbO_3$ and their σ- and π-polarization character.[32,33] The Stark transition for which laser gain has been demonstrated ($R_1\rightarrow 4'$) has been highlighted.

In $LiNbO_3$, it is well established that the reversal of the spontaneous polarization is a consequence of the displacement of the Li^+ cations along the ferroelectric *z*-axis.[34] After electric poling along the polar axis, the cationic reorder along *z*-axis also reverses the cationic sequence along the *y*-axis. Accordingly, domain reversal in $LiNbO_3$ leads not only to the inversion of the *z*-axis ($+z \rightarrow -z$), but also to the inversion of the *y* axis of the crystal ($+y \rightarrow -y$).[35] This *y*-axis is nominally nonpolar. However, as previously pointed out, piezoelectricity along this axis, together with the presence of a strong surface dipole, leads to surface charge on the *Y*-cut.[36]

As a first step in our study, a *Y*-cut slab of a Nd^{3+} doped PPLN sample was cut and polished from a crystal grown by the off-center Czochralski method (see Supporting Information). Figure 1a shows the phase signal of the piezoelectric response obtained from the *Y*-cut surface of the Nd^{3+} doped PPLN crystal. The piezoelectricity of the $LiNbO_3$ *y*-axis, together with the axis inversion, $+y \rightarrow -y$, which follows the polarization reversal, has a major effect in the sign of the surface charge distribution and therefore, in the piezoelectric response. Therefore, the observed periodic pattern can be correlated to the antiparallel domain structure in the PPLN crystal. The periodic distribution of surface charge on the nonpolar *Y*-cut in our Nd^{3+} doped $LiNbO_3$ crystals is going to play a crucial role allowing the photochemical reduction processes for assembling metallic structures. Following a previously described procedure,[14,20,21,37] the formation of Ag nanopatterns on the alternate charge surfaces, as well as on domain boundaries of the Nd^{3+} doped PPLN crystal, is demonstrated. Figure 1b,c shows SEM images of the *Y*-cut surfaces after the deposition processes for two different times. As observed, a domain selective deposition is obtained leading to different density of Ag Nps on the y^+ and y^- surfaces in a similar way to the previous results obtained for c^+ and c^- polar surfaces in a Nd^{3+}/PPLN *Z*-cut.[14] Additionally, the dominant formation of metallic Ag Nps chainlike structures on the domain wall surfaces is observed. The Ag NP chainlike structure is formed preferentially on one of the two domain boundaries. A similar behavior has been previously reported by the authors for the case of photoreduction process on the *Z*-cut and related to the asymmetric temperature gradient inherent to the off-center Czochralski growth process of the PPLN.[14] SEM images with higher magnification are shown in Figure 1d,e, where the presence of Ag Nps chainlike structures on the domain walls of a Nd^{3+} doped PPLN *Y*-cut surface is demonstrated. The average diameter size of the Ag Nps is in the range 20−70 nm depending on the selected deposition conditions (illumination time, $AgNO_3$ concentration, and UV photon flux). At this point, it is important to recall the presence of surface charge on the piezoelectric and nonpolar *Y*-cut of $LiNbO_3$ single crystal. This surface charge is a consequence of a strong surface dipole introduced by the stable termination of the surface which is interconnected with the piezoelectric response of $LiNbO_3$ along the *y*-axis.[36] The variation of deposition, domain/boundary can be explained in a similar way to that of the *Z*-cut, by means of the surface charge and the nonuniform electric field on the crystal surface, which shows a strong component in the vicinity of the 180° domain boundaries.[20,21] On the other hand, the magnitude of the surface charge on the *Y*-cut is approximately one-third of the one on the polar *Z*-cut surface.[36] This explains the comparable metallic deposition rates obtained on both *Y*- and *Z*-cut surfaces.

Once the assembling of Ag metallic Nps on optically active Nd^{3+} doped $LiNbO_3$ is demonstrated on the nonpolar *Y*-cut, the effect of Ag Nps chains on the optical properties of Nd^{3+}/PPLN is analyzed using polarized microfluorescence spectroscopy. As a starting point, Figure 2a,b shows the σ- (blue line) and π- (red line) polarized emission spectra corresponding to the $^4F_{3/2}\rightarrow{}^4I_{9/2}$ and $^4F_{3/2}\rightarrow{}^4I_{11/2}$ transitions centered at around 900 and 1085 nm, respectively. The σ/π spectrum corresponds to the configurations in which the electric field of the emitted light is perpendicular/parallel to the crystallographic *c*-axis (*z*-axis) of $LiNbO_3$. The spectra display a clear structure due to the Stark splitting of the states by the effect of the host crystal field.

dx.doi.org/10.1021/nl4028999 | *Nano Lett.* 2013, 13, 4931−4936

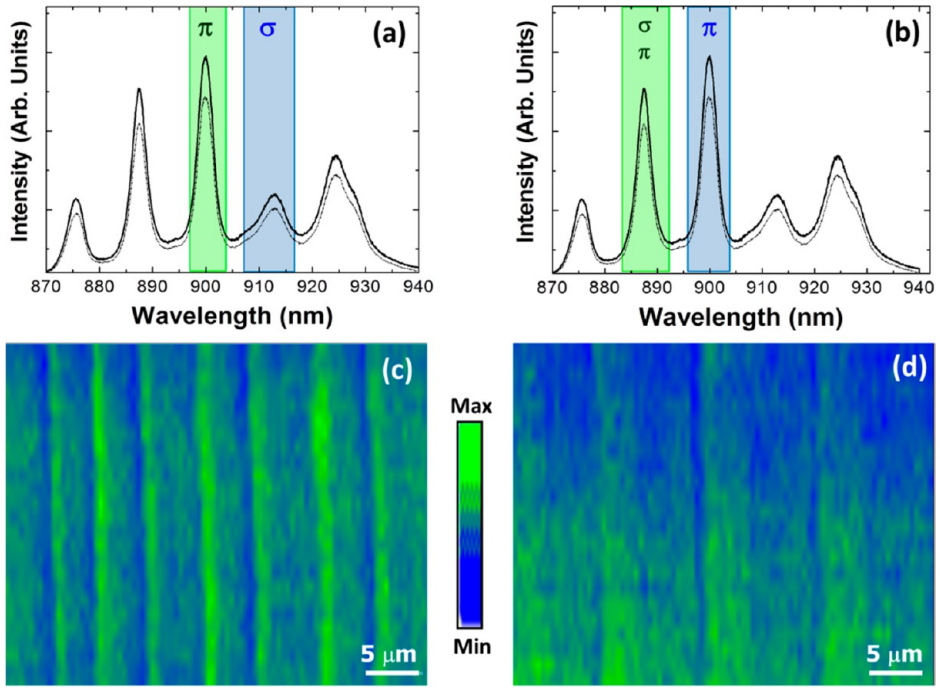

Figure 3. (a,b) Unpolarized microfluorescence spectra from the PPLN *Y*-cut corresponding to the $Nd^{3+}/{}^4F_{3/2}\rightarrow{}^4I_{9/2}$ transition taken on the vicinity Ag Nps chains on the domain wall surfaces (solid line) and from the inner domain surfaces (dashed lines); (c) microfluorescence spatial map representing the intensity ratio between the π- and σ-Stark transitions marked in panel (a) as green and blue shaded regions, respectively; (d) microfluorescence spatial map representing the intensity ratio between the (σ,π) and π-Stark lines marked in panel (b) as green and blue shaded zones, respectively.

The number of Stark transitions and their relative intensity depend on the crystal configuration and polarization and they are in agreement with the forced electric-dipole character of the Nd^{3+} Stark transitions and the noninversion C_3 local symmetry site of Nd^{3+} ions in $LiNbO_3$.[33] Figure 2c,d sketch the assignments of the Stark transitions. Only the main emission lines from the lower Stark level of the ${}^4F_{3/2}$ state (R_1) are shown for shake of clarity. In the ${}^4F_{3/2}\rightarrow{}^4I_{11/2}$ spectrum the Stark transition at around 1085 nm, which dominates the π-polarized spectrum, corresponds to the line for which laser action has been demonstrated.[38]

Figure 3 shows the results from confocal microfluorescence on the *Y*-cut of Nd^{3+}/PPLN obtained to analyze the contribution of the π polarized emitted light to the total spectrum when the Ag Nps are deposited on the *Y*-cut. For that purpose, the ${}^4F_{3/2}\rightarrow{}^4I_{9/2}$ unpolarized emission spectra obtained from the vicinity of Ag Nps chains (solid lines in Figure 3) are compared to those from the inner domain surfaces (dashed lines in Figure 3). The results correspond to the chainlike metallic nanostructures array shown in Figure 1c, which displays a Nps average diameter of around 40 nm. Two main features can be observed: First, the total emission of the unpolarized ${}^4F_{3/2}\rightarrow{}^4I_{9/2}$ optical transition of Nd^{3+} ions is enhanced in the vicinities of the Ag Nps chains (solid lines) with respect to the emission obtained from the domain surfaces (dashed lines). Second, the microfluorescence map corresponding to the intensity ratio between the π-and σ-Stark transitions shaded in Figure 3a shows a remarkable increase in the vicinity of the chainlike Nps (See Figure 3c.) That is, a selective increase of the photoluminescence associated with the π-character contribution is taking place. As a further confirmation, Figure 3d shows the microfluorescence map showing the spatial evolution of the intensity ratio $(\sigma,\pi)/\pi$ marked in Figure 3b. Again differences in the emission intensity ratio are observed on the surroundings of the metallic chains. In particular, a systematic decrease in the fluorescence intensity ratio when approaching the Ag Nps chains is obtained, indicating the relative diminution of the σ-polarization to the π-one. Hence, the selective enhancement of the Nd^{3+} π-laser emission is not related to the randomly distributed NPs around the Ag chainlike structures but to the specific arrangement of the Ag Nps forming chains parallel to the *c*-axis of the $LiNbO_3$ crystal and to their interspace distances.

The effect of the Ag Nps on the luminescence polarization character of Nd^{3+} ions was also analyzed on the ${}^4F_{3/2}\rightarrow{}^4I_{11/2}$ laser transition. Figure 4a displays the unpolarized microfluorescence spatial map corresponding to the ${}^4F_{3/2}\rightarrow{}^4I_{11/2}$ integrated emission intensity in the 1050−1130 nm spectral region. The image shows a systematic periodic exaltation of the Nd^{3+} emitted intensity coming from the domain boundaries surfaces, where the chainlike Ag Nps structures are assembled. The spectra corresponding to two different regions of the PPLN (on the Ag Nps chain and on domain surfaces) are compared in Figure 4b. This emission enhancement can be related to the coupling between the plamonic resonances supported by the chainlike structures and the optical Stark transitions of the active ion. In fact, the chains of Ag Nps support the presence of strong near-field dipolar interaction between adjacent Nps, resulting in a strong polarization-dependent behavior of the photoluminescence of Nd^{3+} ions in the vicinity of the Ag Nps. To confirm this fact, the polarized microfluorescence was studied. Figure 4c displays a microfluorescence map obtained when both the excitation and emission beams are polarized perpendicular to the Ag Nps chains. When compared to the unpolarized map, an almost flat contour map is obtained in this case revealing only a very

dx.doi.org/10.1021/nl4028999 | *Nano Lett.* 2013, 13, 4931−4936

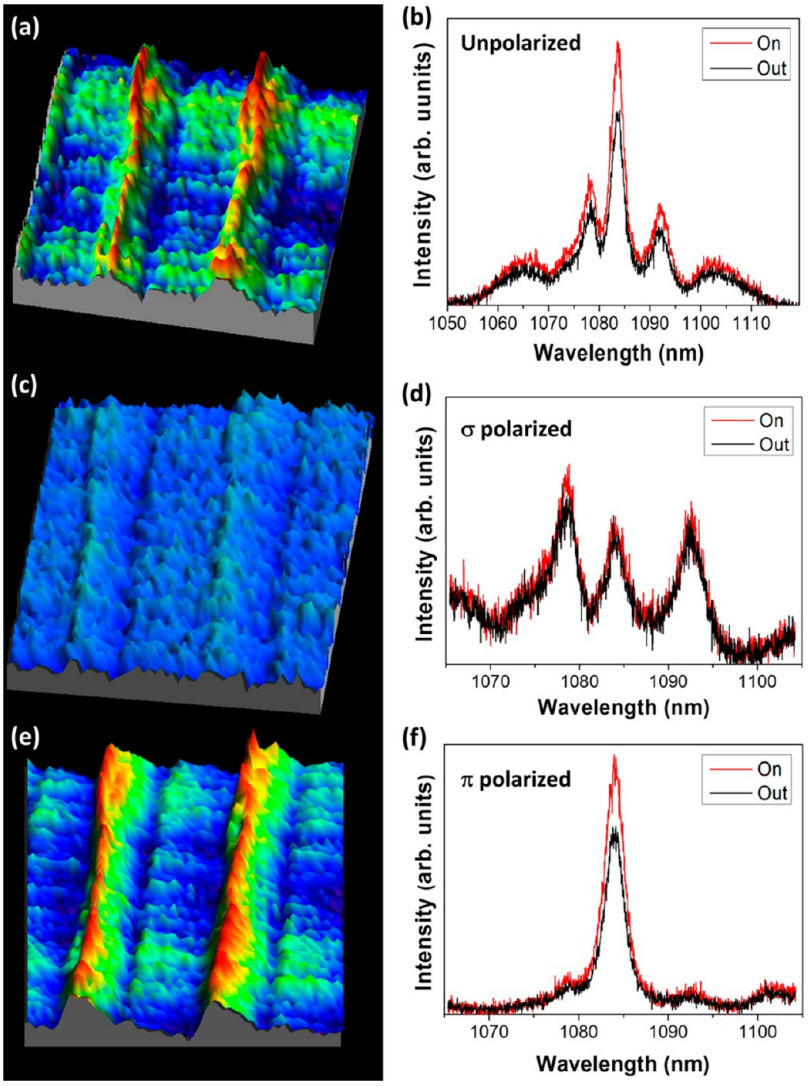

Figure 4. (a) Unpolarized, (c) σ-polarized, and (e) π-polarized spatial maps of the $Nd^{3+}/^4F_{3/2} \rightarrow {}^4I_{11/2}$ integrated emission obtained from the *Y*-cut surface of the Ag-PPLN:Nd^{3+} crystal. (b) Unpolarized, (d) σ-polarized, and (f) π-polarized representative spectra obtained from the vicinity of the Ag Nps chain (red) and from domain surfaces regions (black). Pump wavelength was fixed at 488 nm.

slightly periodic enhancement of the Nd^{3+} emission on the regions where the Ag Nps chainlike structures are formed. The corresponding polarized spectra are associated with the σ-configuration spectra of Nd^{3+} ions, since the electric field of the light is perpendicular to the *c*-symmetry axis of the crystal. Figure 4d shows two representative details of the σ-luminescence spectra obtained on the Ag Nps chains and on domain surfaces. As observed, they display the same intensity and spectral shape. It is important to remark that for this specific polarization configuration (electric field perpendicular to the Ag Nps chains) the collective resonances supported by the chainlike structure are not excited. Accordingly, the Nd^{3+} photoluminescence enhancement observed with respect to the case in which no Ag is deposited must be assigned to LSP resonances of individual Ag Nps which are not sensitive to the polarization state of light. Finally, Figure 4e shows the π-polarized microfluorescence map in which both excitation and emission beams are polarized parallel to the to the c-symmetry axis of the crystal and therefore, to the Ag Nps chains. As seen, in contrast to the σ-polarized Stark lines of Nd^{3+} ions in $LiNbO_3$, the π-type fluorescence lines do couple to the chainlike Ag Nps array, resulting in a clear and systematic periodical enhancement of the laser line. Two illustrative spectra collected on the Ag Nps chains and on the inner domain surface are displayed in Figure 4f. They exhibit a main line centered at 1085 nm, which corresponds to the laser emission of Nd^{3+} in this system with a π-character. As observed the maximum values of emitted intensity are obtained for the 1085 laser line in the vicinity of the Ag Nps chainlike structures. However, for inner regions between domain boundaries, the emission intensity does not depend on the polarization direction, in accordance with the shape and random location of the Ag Nps on domain surfaces where no preferential alignment exists.

The observed luminescence enhancement is in the order of 30%, equivalent to those observed for other trivalent rare earth emitter−metallic nanostructures[39,40] with the additional advantage of being produced on a multifunctional ferroelectric laser host. A slightly different emission intensity from each one of the boundaries confining a positive domain surface is in agreement with the aforementioned asymmetry of the

dx.doi.org/10.1021/nl4028999 | *Nano Lett.* 2013, 13, 4931−4936

nanostructures formed on consecutive domain boundaries due to the crystal growth procedure.[41]

Summarizing, we have experimentally shown the proof of concept of a selective coupling of forced electric dipole transitions of trivalent Nd^{3+} laser ions with the localized surface plasmon resonances supported by aligned arrays of metallic Ag Nps. As a result, directional enhancement of a single Stark line, particularly the π-polarized Nd^{3+} laser line at 1085 nm, is demonstrated in a material of technological interest such as $LiNbO_3$. The observed enhancement of the Nd^{3+} Stark laser transition exhibits a micrometric spatial periodicity provided by the formation of metallic Ag Nps chainlike structures on the nonpolar *Y*-cut surface of the PPLN structure. The possibility of photoreduction of metallic nanostructures on the nonpolar *Y*-cut establishes that the metallic nanostructure formation is linked to the presence of surface charge rather than to the presence of a spontaneous polarization. As a result, the easy-to-apply method of assembling Ag Nps via photochemical procedure can be extended to a large number of piezoelectric materials that show stable surface charge termination interconnected with the piezoelectric response.

■ ASSOCIATED CONTENT

Ⓢ Supporting Information

Materials and methods. This material is available free of charge via the Internet at http://pubs.acs.org.

■ AUTHOR INFORMATION

Corresponding Author

*E-mail: pablo.molina@uam.es.

Author Contributions

The manuscript was written through contributions of all authors. All authors have given approval to the final version of the manuscript.

Notes

The authors declare no competing financial interest.

■ ACKNOWLEDGMENTS

This work has been supported by the Spanish Government under project MAT2010-17443 and Comunidad de Madrid under grant S2009/1756.

■ REFERENCES

(1) Barnes, W. L.; Dereux, A.; Ebbesen, T. W. *Nature* **2003**, *424*, 824−830.

(2) Novotny, L.; van Hulst, N. *Nat. Photonics* **2011**, *5*, 83−90.

(3) Debasu, M. L.; Ananias, D.; Pastoriza-Santos, I.; Liz-Marzán, L. M.; Rocha, J.; Carlos, L. D. *Adv. Mater.* **2013**, DOI: 10.1002/adma.201300892.

(4) Elvira, D.; Braive, R.; Beaudoin, G.; Sagnes, I.; Hugonin, J.-P.; Abram, I.; Robert-Philip, I.; Lalanne, P.; Beveratos, A. *Appl. Phys. Lett.* **2013**, *103*, 061113−061116.

(5) Zhou, W.; Dridi, M.; Suh, J. Y.; Kim, C. H.; Co, D. T.; Wasielewski, M. R.; Schatz, G. C.; Odom, T. W. *Nat. Nanotechnol.* **2013**, *8*, 506−511.

(6) Lozano, G.; Louwers, D. J.; Rodríguez, S. R.; Murai, S.; Jansen, O. T.; Verschuuren, M. A.; Rivas, J. G. *Light: Sci. Appl.* **2013**, *2*, e66.

(7) Hutter, E.; Fendler, J. H. *Adv. Mater.* **2004**, *16*, 1685−1706.

(8) Atwater, H. A.; Polman, A. *Nat. Mater.* **2010**, *9*, 205−213.

(9) Maier, S. A.; Kik, P. G.; Atwater, H. A.; Meltzer, S.; Harel, E.; Koel, B. E.; Requicha, A. A. G. *Nat. Mater.* **2003**, *2*, 229−232.

(10) Noginov, M. A.; Zhu, G.; Belgrave, A. M.; Bakker, R.; Shalaev, V. M.; Narimanov, E. E.; Stout, S.; Herz, E.; Suteewong, T.; Wiesner, U. *Nature* **2009**, *460*, 1110−U68.

(11) Hess, O.; Pendry, J. B.; Maier, S. A.; Oulton, R. F.; Hamm, J. M.; Tsakmakidis, K. L. *Nat. Mater.* **2012**, *11*, 573−584.

(12) Muskens, O. L.; Giannini, V.; Sanchez-Gil, J. A.; Rivas, J. G. *Nano Lett.* **2007**, *7*, 2871−2875.

(13) Garcia, M. A. *J. Phys. D: Appl. Phys.* **2011**, *44*, 283001.

(14) Yraola, E.; Molina, P.; Plaza, J. L.; Ramirez, M. O.; Bausa, L. E. *Adv. Mater.* **2013**, *25*, 910−915.

(15) Myers, L. E.; Miller, G. D.; Eckardt, R. C.; Fejer, M. M.; Byer, R. L. *Opt. Lett.* **1995**, *20*, 52−54.

(16) Levenius, M.; Pasiskevicius, V.; Laurell, F.; Gallo, K. *Opt. Express* **2011**, *19*, 4121−4128.

(17) Molina, P.; Ramirez, M. O.; Bausa, L. E. *Adv. Funct. Mater.* **2008**, *18*, 709−715.

(18) Mateos, L.; Molina, P.; Galisteo, J.; Lopez, C.; Bausa, L. E.; Ramirez, M. O. *Opt. Express* **2012**, *20*, 29940−29948.

(19) Ramírez, M. O.; Molina, P.; Bausá, L. E. *Opt. Mater.* **2012**, *34*, 524−535.

(20) Sun, Y.; Eller, B. S.; Nemanich, R. J. *J. Appl. Phys.* **2011**, *110*, 084303.

(21) Sun, Y.; Nemanich, R. J. *J. Appl. Phys.* **2011**, *109*, 104302.

(22) Carville, N. C.; Manzo, M.; Damm, S.; Castiella, M.; Collins, L.; Denning, D.; Weber, S. A. L.; Gallo, K.; Rice, J. H.; Rodriguez, B. J. *ACS Nano* **2012**, *6*, 7373−7380.

(23) Balobaid, L.; Carville, N. C.; Manzo, M.; Gallo, K.; Rodriguez, B. J. *Appl. Phys. Lett.* **2013**, *102*, 042908.

(24) Kalinin, S. V.; Bonnell, D. A.; Alvarez, T.; Lei, X. J.; Hu, Z. H.; Shao, R.; Ferris, J. H. *Adv. Mater.* **2004**, *16*, 795.

(25) Dunn, S.; Cullen, D.; Abad-Garcia, E.; Bertoni, C.; Carter, R.; Howorth, D.; Whatmore, R. W. *Appl. Phys. Lett.* **2004**, *85*, 3537−3539.

(26) Ehre, D.; Lavert, E.; Lahav, M.; Lubomirsky, I. *Science* **2010**, *327*, 672−675.

(27) Grilli, S.; Miccio, L.; Vespini, V.; Finizio, A.; De Nicola, S.; Ferraro, P. *Opt. Express* **2008**, *16*, 8084−8093.

(28) Damm, S.; Carville, N. C.; Rodriguez, B. J.; Manzo, M.; Gallo, K.; Rice, J. H. *J. Phys. Chem. C* **2012**, *116*, 26543−26550.

(29) Tamaru, H.; Kuwata, H.; Miyazaki, H. T.; Miyano, K. *Appl. Phys. Lett.* **2002**, *80*, 1826−1828.

(30) Maier, S. A.; Atwater, H. A. *J. Appl. Phys.* **2005**, *98*, 011101.

(31) Loro, H.; Voda, M.; Jaque, F.; Sole, J. G.; Santiuste, J. E. M. *J. Appl. Phys.* **1995**, *77*, 5929−5935.

(32) Lifante, G.; Cusso, F.; Jaque, F.; Sanz Garcia, J. A.; Monteil, A.; Varrel, B.; Boulon, G.; Garcia Sole, J. *Chem. Phys. Lett.* **1991**, *176*, 482−488.

(33) Burlot, R.; Moncorge, R.; Manaa, H.; Boulon, G.; Guyot, Y.; Sole, J. G.; Cochet, M., D. *Opt. Mater.* **1996**, *6*, 313−330.

(34) Gopalan, V.; Dierolf, V.; Scrymgeour, D. A. *Annu. Rev. Mater. Res.* **2007**, *37*, 449−489.

(35) Sono, T. J.; Scott, J. G.; Sones, C. L.; Valdivia, C. E.; Mailis, S.; Eason, R. W.; Frey, J. G.; Danos, L. *Phys. Rev.B* **2006**, *74*, 205424.

(36) Sanna, S.; Schmidt, W. G. *Phys. Rev. B* **2010**, *81*, 214116.

(37) Liu, X.; Kitamura, K.; Terabe, K.; Hatano, H.; Ohashi, N. *Appl. Phys. Lett.* **2007**, *91*, 044101.

(38) Fan, T. Y.; Cordova Plaza, A.; Digonnet, M. J. F.; Byer, R. L.; Shaw, H. J. *J. Opt. Soc. Am. B* **1986**, *3*, 140−148.

(39) Kalkman, J.; Kuipers, L.; Polman, A.; Gersen, H. *Appl. Phys. Lett.* **2005**, *86*, 041113.

(40) Lu, Y.; Chen, X. *Appl. Phys. Lett.* **2009**, *94*, 193110.

(41) Bermudez, V.; Serrano, M. D.; Dieguez, E. *J. Cryst. Growth* **1999**, *200*, 185−190.

Materials and methods

Nd^{3+} activated PPLN crystals were prepared by the off-centered Czochralski method along the x-axis by adding the Nd (1 mol%) in the form of oxide. During crystal growth the rotational axis was displaced 5 mm away from the symmetry axis of the temperature gradient. This produced a periodic temperature fluctuation able to create alternating ferroelectric domains. 5N congruent $LiNbO_3$ and 3N Nd_2O_3 powders were used as starting materials. The period length was controlled via rotation and pulling rates (30 rpm and 1 mm/h, respectively) to generate a close to 50% duty cycle of alternating domains with a period of 6 μm (single domain length of around 3 μm). The photoinduced silver deposition process was carried out by illuminating the surface of 1 mm thick Y-cut and Z-cut Nd^{3+}:PPLN crystal with UV-light while the samples were immersed in $AgNO_3$ solution. A Mercury pen-lamp with its main line at 253.6 nm was used as light source in the photo-induced Ag Nps deposition. The emission power was 5400 $\mu W/cm^2$ at a distance of 3 cm. The $AgNO_3$ solution (0,01 M) was illuminated during 3 min.

Far-field polarized micro-luminescence experiments were performed in a laser scanning confocal microscope. An Ar^+ laser (Spectra Physics Model 177-Series) at 488 nm and a tunable femtosecond Ti:Sapphire laser (3900S Tsunami Spectra Physics) were used as excitation sources. The laser beam was focused onto the sample by a microscope objective (50x and 100x magnifications). The photoluminescence was collected in backscattering geometry with the same objective. Samples were placed on a two-axis XY motorized stage with 0.2μm spatial resolution. For the visible excitation wavelength, the laser was focused to a spot size less than1μm.

Piezorresponse force microscopy characterization was obtained by using an AFM (Parksystems XE-100) provided with a specific Electrostatic Force Microscopy module.

Article 3

Controlling solid state gain media by deposition of silver nanoparticles: from thermally-quenched to plasmon-enhanced Nd^{3+} luminescence.

E. Yraola, L. Sánchez-García, C. Tserkezis, P. Molina, M. O Ramírez, J. L. Plaza, J. Aizpurua, L. E. Bausá
Optics Express **23**, 15670 (2015).

Controlling solid state gain media by deposition of silver nanoparticles: from thermally-quenched to plasmon-enhanced Nd^{3+} luminescence

Eduardo Yraola,[1] Laura Sánchez-García,[1] Christos Tserkezis,[2] Pablo Molina,[1] Mariola O Ramírez,[1] Jose Luis Plaza,[1] Javier Aizpurua[2] and Luisa E. Bausá[1,*]

[1]*Dpto. Física de Materiales and Instituto Nicolás Cabrera, Universidad Autónoma de Madrid, Madrid, 28049, Spain*
[2]*Center for Materials Physics (CSIC-UPV/EHU) and Donostia International Physics Center (DIPC), Paseo Manuel Lardizabal 4, Donostia-San Sebastián 20018, Spain*
[*]*luisa.bausa@uam.es*

Abstract: We show the possibility of controlling the optical properties of Nd^{3+} laser ions by using different configurations of metallic nanoparticles (NPs) deposited on a solid state gain medium. In particular, we analyze the effect of two different silver NP arrangements on the optical properties of Nd^{3+} ions in $LiNbO_3$: a two-dimensional (2D) high density and disordered Ag NP distribution and a one-dimensional (1D) long single chain of Ag NPs. We demonstrate that while the 2D disordered distribution produces a thermal quenching of the Nd^{3+} luminescence, the 1D single chain leads to the enhancement of the fluorescence from the $^4F_{3/2}$ metastable state. The experimental data are theoretically interpreted by taking into account the different character, radiative or non-radiative, of the localized surface plasmonic modes supported by the Ag nanoparticle distributions at the excitation wavelength. The results point out the capabilities of rare earth ions as optical tools to probe the local plasmonic fields and are relevant to determine the optimal configuration of metallic arrays to improve the performance of potential rare earth ion based sub-micrometer lasers.

OCIS codes: (160.5690) Rare-earth-doped materials; (300.6280) Spectroscopy, fluorescence and luminescence; (160.3380) Laser materials; (250.5403) Plasmonics; (140.3530) Lasers, neodymium.

References and links

1. R. M. Ma, R. F. Oulton, V. J. Sorger, and X. Zhang, "Plasmon lasers: coherent light source at molecular scales," Laser Photon. Rev. **7**(1), 1–21 (2013).
2. O. Hess, J. B. Pendry, S. A. Maier, R. F. Oulton, J. M. Hamm, and K. L. Tsakmakidis, "Active nanoplasmonic metamaterials," Nat. Mater. **11**(7), 573–584 (2012).
3. M. A. Noginov, G. Zhu, A. M. Belgrave, R. Bakker, V. M. Shalaev, E. E. Narimanov, S. Stout, E. Herz, T. Suteewong, and U. Wiesner, "Demonstration of a spaser-based nanolaser," Nature **460**(7259), 1110–1112 (2009).
4. R. F. Oulton, V. J. Sorger, T. Zentgraf, R. M. Ma, C. Gladden, L. Dai, G. Bartal, and X. Zhang, "Plasmon lasers at deep subwavelength scale," Nature **461**(7264), 629–632 (2009).
5. W. Zhou, M. Dridi, J. Y. Suh, C. H. Kim, D. T. Co, M. R. Wasielewski, G. C. Schatz, and T. W. Odom, "Lasing action in strongly coupled plasmonic nanocavity arrays," Nat. Nanotechnol. **8**(7), 506–511 (2013).
6. E. Yraola, P. Molina, J. L. Plaza, M. O. Ramírez, and L. E. Bausá, "Spontaneous emission and nonlinear response enhancement by silver nanoparticles in a Nd^{3+}-doped periodically poled $LiNbO_3$ laser crystal," Adv. Mater. **25**(6), 910–915 (2013).
7. T. Y. Fan, A. Cordova-plaza, M. J. F. Digonnet, R. L. Byer, and H. J. Shaw, "Nd:MgO:$LiNbO_3$ spectroscopy and laser devices," J. Opt. Soc. Am. B **3**(1), 140–148 (1986).
8. S. V. Kalinin, D. A. Bonnell, T. Alvarez, X. J. Lei, Z. H. Hu, R. Shao, and J. H. Ferris, "Ferroelectric lithography of multicomponent nanostructures," Adv. Mater. **16**(910), 795–799 (2004).

#237088 - $15.00 USD Received 27 Mar 2015; revised 24 May 2015; accepted 28 May 2015; published 4 Jun 2015

9. P. Molina, E. Yraola, M. O. Ramírez, J. L. Plaza, C. de las Heras, and L. E. Bausá, "Selective plasmon enhancement of the 1.08 μm Nd^{3+} laser Stark transition by tailoring Ag nanoparticles chains on a PPLN Y-cut," Nano Lett. **13**(10), 4931–4936 (2013).
10. V. Bermudez, M. D. Serrano, and E. Dieguez, "Bulk periodic poled lithium niobate crystals doped with Er and Yb," J. Cryst. Growth **200**(1-2), 185–190 (1999).
11. Y. Sun, B. S. Eller, and R. J. Nemanich, "Photo-induced Ag deposition on periodically poled lithium niobate: Concentration and intensity dependence," J. Appl. Phys. **110**(8), 084303 (2011).
12. Y. Sun and R. J. Nemanich, "Photoinduced Ag deposition on periodically poled lithium niobate: Wavelength and polarization screening dependence," J. Appl. Phys. **109**(10), 104302 (2011).
13. F. J. García de Abajo and J. Aizpurua, "Numerical simulation of electron energy loss near inhomogeneous dielectrics," Phys. Rev. B **56**(24), 15873–15884 (1997).
14. F. J. G. de Abajo and A. Howie, "Retarded field calculation of electron energy loss in inhomogeneous dielectrics," Phys. Rev. B **65**, 17 (2002).
15. S. V. Kalinin and D. A. Bonnell, "Local potential and polarization screening on ferroelectric surfaces," Phys. Rev. B **63**(12), 125411 (2001).
16. H. Loro, M. Voda, F. Jaque, J. G. Sole, and J. E. M. Santiuste, "Polarized absorption of Nd^{3+} in $LiNbO_3$: efect of MgO codoping," J. Appl. Phys. **77**(11), 5929–5935 (1995).
17. A. O. Govorov and H. H. Richardson, "Generating heat with metal nanoparticles," Nano Today **2**(1), 30–38 (2007).
18. D. V. Guzatov, S. V. Vaschenko, V. V. Stankevich, A. Y. Lunevich, Y. F. Glukhov, and S. V. Gaponenko, "Plasmonic enhancement of molecular fluorescence near silver nanoparticles: theory, modeling, and experiment," J. Phys. Chem. C **116**(19), 10723–10733 (2012).
19. K. Lau, I. Staude, Y. Liu, H. Chen, Z. R. Li, and D. N. Neshev, "Ferroelectric domain engineered photochemical deposition for area-selectable broadband enhancement of quantum dot photoluminescence," Adv. Opt. Mater. **1**(10), 720–723 (2013).
20. E. Yraola, L. Sánchez-García, C. Tserkezis, P. Molina, M. O. Ramírez, J. Aizpurua, and L. E. Bausá, "Polarization-selective enhancement of Nd^{3+} photoluminescence assisted by linear chains of silver nanoparticles," J. Lumin., doi:10.1016/j.jlumin.2014.12.053i.
21. R. Esteban, R. W. Taylor, J. J. Baumberg, and J. Aizpurua, "How chain plasmons govern the optical response in strongly interacting self-assembled metallic clusters of nanoparticles," Langmuir **28**(24), 8881–8890 (2012).
22. C. Tserkezis, R. W. Taylor, J. Beitner, R. Esteban, J. J. Baumberg, and J. Aizpurua, "Optical response of metallic nanoparticle heteroaggregates with subnanometric gaps," Part. Part. Syst. Charact. **31**(1), 152–160 (2014).
23. Z. B. Wang, B. S. Luk'yanchuk, W. Guo, S. P. Edwardson, D. J. Whitehead, L. Li, Z. Liu, and K. G. Watkins, "The influences of particle number on hot spots in strongly coupled metal nanoparticles chain," J. Chem. Phys. **128**(9), 094705 (2008).

1. Introduction

A large variety of systems which combine different types of metallic nanostructures, optical emitters, and dielectric media are nowadays the subject of intense activity. In particular, the association of metallic nanostructures with different gain media, has recently given rise to successful configurations such as nanolasers [1,2] from which high energy density can be supplied due to sub-diffraction confinement. Organic dyes and semiconductor based media in association with metallic nanostructures have shown coherent radiation at the nanoscale [3–5]. However, the reports studying the influence of localized surface plasmons (LSPs) on the optical response of trivalent rare earth doped solid state lasers are scarce. Recently, some of the authors have demonstrated the possibility of a remarkable intensification of the spontaneous emission of a Nd^{3+} based solid state laser due to the large local electric fields associated with the LSP from arrays of silver NPs in the proximity of the optically active ions [6]. As a host matrix for the Nd^{3+} active ions, $LiNbO_3$ was chosen, a ferroelectric crystal in which laser action and self-frequency conversion processes have been demonstrated [7].

Due to the polar character of this crystal and taking advantage of the presence of surface charges, metallic silver nanoparticles were photochemically assembled on the $LiNbO_3$ surface by means of ferroelectric lithography [8]. A domain selective deposition was obtained, with the density of the Ag NPs formed on the positive domain surface being much higher than on the negative domain surface. Additionally, a preferential deposition of Ag NPs forming chains on the surface of the antiparallel ferroelectric domain boundaries was also achieved. The LSP resonances supported by those chains of Ag NPs on the ferroelectric domain walls produced an intensification and a strong polarization dependence of the photoluminescence of Nd^{3+} emitting ions in the vicinity of the Ag NPs [6]. This result is of particular interest when the Ag

#237088 - $15.00 USD Received 27 Mar 2015; revised 24 May 2015; accepted 28 May 2015; published 4 Jun 2015

NP chains are distributed parallel to the ferroelectric c-axis of the crystal, on a periodically poled $LiNbO_3$ (PPLN) Y-cut crystal, since the Nd^{3+} laser line at 1.08 μm ($^4F_{3/2}$ $(R_1)\rightarrow$ $^4I_{11/2}(Y_2)$ Stark transition) can be selectively enhanced by exciting with light polarized parallel to the Ag NP chains [9].

Here we compare the effect of two different Ag NP arrangements on the optical properties of Nd^{3+} ions: a 2D high density and disordered Ag NP distribution on positive domain surfaces and a 1D single, long chain of Ag NPs on domain boundaries, both deposited on the relevant Y-cut surface of a Nd^{3+} doped PPLN. While for the 1D distribution an enhancement of the fluorescence is achieved, for the 2D distribution a thermal quenching of the Nd^{3+} luminescence from the $^4F_{3/2}$ metastable state is observed. The results are interpreted taking into account the plasmonic modes supported by finite linear chains of Ag NPs with different number of interacting Ag spheres (from 2 to 15), and considering the 2D configuration as a distribution of short chains randomly oriented, which, as shown later, describes well our experimental NP arrangement. At the visible excitation wavelength used in this work (488 nm) the short-chain plasmonic modes (low number of Ag interacting nanospheres) are characterized by a much larger absorption than that corresponding to a long- chain mode (15 nanoparticles) which, in turn, shows a stronger radiative character. The larger absorption of the 2D Ag NP distribution leads to the presence of heating due to ohmic losses and consequently to the luminescence thermal quenching of Nd^{3+} ion, which could prevent laser action. On the contrary, the lower absorption and the stronger radiative character associated with the 1D distribution of Ag NPs explains the intensification provided by a long single linear chain of Ag NPs. The results show both experimentally and theoretically how by spatially organizing Ag NPs from a 2D disordered configuration to a 1D chain it is possible not only to eliminate the thermal fluorescence quenching, but also to enhance the fluorescence from the Nd^{3+} laser ions. This work is relevant to determine the optimal configuration of metallic arrays to improve the performance of possible rare earth ion based sub-micrometer lasers. Additionally, the results show the potential of optically active ions as tools to investigate the effects of metallic plasmon resonances. In this sense, trivalent rare earth ions provide a great number of crystal field transitions with different character and spectral location suitable to probe the local fields of a variety of metallic configurations.

2. Experimental

Nd^{3+} doped PPLN crystals were grown by the off-centered Czochralski method along the x-axis by adding Nd (1 mol %) in the form of Nd_2O_3. Details on the crystal growth procedure can be found elsewhere [10]. 1 mm thick plates were cut and polished with their main faces oriented parallel to the ferroelectric c-axis (Y-cut).

Photochemical deposition of Ag NPs was achieved by means of ferroelectric lithography following the previously reported procedure [6,11,12]. The crystal surface was illuminated with a UV Mercury pen-lamp (main line at 253.6 nm) while the samples were immersed in a 0,01M $AgNO_3$ at 70 °C. By modifying the time of the process we obtained a 2D high density and random distribution of Ag NPs on positive domain surfaces (20 minutes) or 1D chains of Ag NPs located on the domain wall surfaces (2 min).

Micro-luminescence experiments were carried out with a laser scanning confocal microscope provided with a two-axis XY motorized platform with 0.1μm spatial resolution. An Ar^+ laser at 488 nm was used as excitation source. The laser beam was focused to a spot size less than 1μm, on the surface of the sample and the photoluminescence signal from the samples was collected in backscattering geometry with the same objective. The polarization of the excitation laser beam was parallel to the ferroelectric c-axis of the crystal.

Extinction and absorption spectra were calculated by solving Maxwell's equations with use of the boundary-element method (BEM) [13,14]. Within the BEM, the different inhomogeneous media are described by abrupt interfaces that separate different media characterized by local dielectric functions. The surface charges and currents induced at the

#237088 - $15.00 USD Received 27 Mar 2015; revised 24 May 2015; accepted 28 May 2015; published 4 Jun 2015

interfaces are solved self consistently through a discretization of the boundaries and subsequent solution of the resulting matrix equations. Electromagnetic fields are then calculated in terms of these induced charges and currents. In our systems, full convergence of the results was achieved with use of 2 discretization points per nm at each interface between different materials.

3. Results and discussion

Figure 1(a) shows a SEM image of the selective domain distribution of Ag NPs on the alternating polarity surfaces of a Nd^{3+} doped PPLN-Ycut crystal deposited by the above described photochemical procedure. A 2D high density and disordered distribution of Ag NPs with average size of 50 nm was obtained on the positive polar surfaces. A higher resolution image (see inset) reveals a detail of the Ag NP distribution on the positive domain surfaces as well as the presence of a continuous Ag nanowire on the domain boundary surface. The variation of deposition between domain and boundary has been previously explained considering the polarization screening mechanism and the resultant non-uniform electric field on the crystal surface, which shows a strong component of the electric field in the vicinity of the antiparallel domain boundaries [15]. A very low density distribution of smaller Ag NPs (~20 nm size) on the negative polar surfaces was also observed.

Figure 1(b) shows the unpolarized emission spectra corresponding to the $^4F_{3/2} \rightarrow {}^4I_{11/2}$ transition of Nd^{3+} ions under excitation at 488 nm from the PPLN-Y-cut surface shown in Fig. 1(a). The spectra obtained from the positive domains with high density of Ag NPs and from the negative domains with very low Ag density are plotted in red and blue, respectively. Both spectra display the structure associated with the Stark splitting of the involved $^4F_{3/2}$ and $^4I_{11/2}$ electronic states by the effect of the host crystal field. The number of the observed Stark transitions and their intensity depend on the crystal configuration and polarization, and are in agreement with the non-inversion C_3 local symmetry site of Nd^{3+} ions in $LiNbO_3$ and with the forced electric-dipole character of the Nd^{3+} Stark transitions in this crystal [16]. A comparison between the two emission spectra reveals intensity variations in the relative contribution of some of their bands. Specifically, when the emission spectrum is collected from the surfaces of the 2D high density distribution of Ag NPs, a systematic increase of the high energy bands -shaded region I in Fig. 1(b), accompanied by a decrease of the intensity of the main Nd^{3+} emission line at 1084 nm (region II) is observed. The effect is even more evident when comparing the micro-fluorescence spatial maps from the surface of the Ag deposited PPLN by integrating the Nd^{3+} emission intensity from 1050 to 1070 nm (spectral region I) and by integrating the spectra from 1082 to 1087 nm (spectral region II). These maps are depicted in Figs. 1(c) and 1(d), respectively, and are in agreement with the periodicity observed in the SEM image of the surface. A systematic and periodical increase of the high energy side of the spectrum (region I) arising from areas with a high density of NPs [Fig. 1(c)] is observed. Simultaneously, the map obtained by integrating the intensity of the Nd^{3+} laser transition centred at 1084 nm (region II) results into the negative image, i.e when the density of Ag NPs is high, the main line emission decreases. Furthermore, the total emission area of the $^4F_{3/2} \rightarrow {}^4I_{11/2}$ transition (from 1050 nm to 1120 nm) decreases at the surfaces with high density of Ag NPs, giving rise to a micro-fluorescence map similar to that displayed in Fig. 1(d).

#237088 - $15.00 USD Received 27 Mar 2015; revised 24 May 2015; accepted 28 May 2015; published 4 Jun 2015

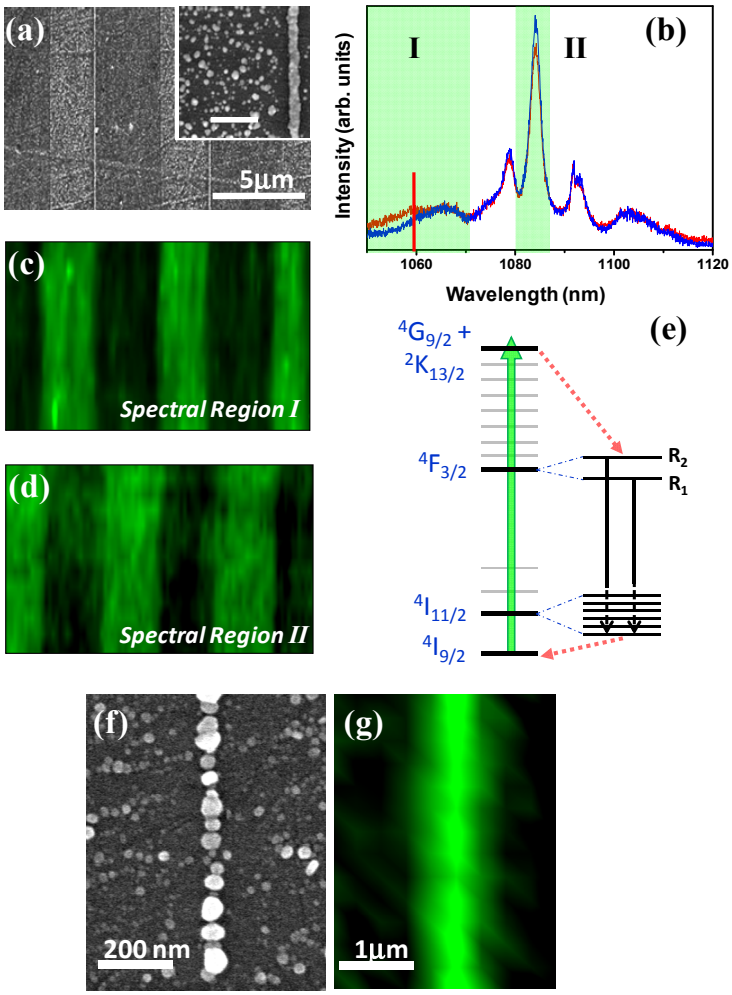

Fig. 1. (a). SEM image of the domain selective distribution of Ag NPs obtained on a Nd^{3+} doped PPLN-Y cut crystal after 20 minutes of UV illumination. A 2D disordered distribution of Ag NPs is preferentially deposited on the positive polar face. (Inset) High resolution image showing a detail of the Ag NP distribution on domain surfaces and the presence of an Ag nanowire parallel to the ferroelectric c-axis of the crystal on a domain wall. The white scale bar corresponds to 500 nm. (b) Unpolarized emission spectra corresponding to the $^4F_{3/2} \rightarrow {}^4I_{11/2}$ laser transition of Nd^{3+} ions collected from regions of low (blue) and high (red) density of Ag NPs. The vertical red line indicates the $^4F_{3/2}$ (R_2) $\rightarrow {}^4I_{11/2}$ (Y_1) thermal transition of Nd^{3+} ions in $LiNbO_3$. (c,d) Micro-fluorescence spatial maps of the integrated Nd^{3+} emission intensity from 1050 to 1070 nm (spectral region I) and from 1082 to 1087 nm (spectral region II), respectively. (e) Schematics of the energy level diagram of Nd^{3+} ions showing the relevant transitions and the crystal field splitting of the $^4F_{3/2}$ and the $^4I_{11/2}$ states. (f) SEM image of one isolated Ag NP chain deposited on the domain wall surface after 2 minutes of UV illumination. (g) Micro-fluorescence spatial map of a single Ag NP chain integrating the $^4F_{3/2} \rightarrow {}^4I_{11/2}$ emission spectrum.

The results can be understood by taking into account that absorption losses of plasmonic nanostructures can efficiently generate heat in the presence of electromagnetic radiation, particularly under the plasmon resonance condition [17]. In fact, the intensity decrease of both the main Nd^{3+} emission line at 1084 nm and the overall $^4F_{3/2} \rightarrow {}^4I_{11/2}$ emission can be attributed to a fluorescence thermal quenching driven by the 2D high density distribution of Ag NPs. This is further supported by the observed increase of the emission at the high energy

#237088 - $15.00 USD Received 27 Mar 2015; revised 24 May 2015; accepted 28 May 2015; published 4 Jun 2015

side of the Nd^{3+} spectrum, which is related to thermal transitions, as explained below. To better illustrate the heating process, Fig. 1(e) shows the Nd^{3+} energy level scheme with the relevant transitions. In $LiNbO_3$, the C_3 crystal field symmetry splits the Nd^{3+} free ion energy states into (2J + 1)/2 Stark crystal field levels. The $^4F_{3/2}$ metastable state splits into two, $^4F_{3/2}(R_1)$ and $^4F_{3/2}(R_2)$, and the $^4I_{11/2}$ state into six ($Y_{1,...,}Y_6$ in order of increasing energy). The relatively small energy gap between the R_1 and R_2 levels (180 cm^{-1} in $LiNbO_3$) [16], makes the $^4F_{3/2}$ (R_2) state especially sensitive to thermal variations so that a moderate increase in temperature produces an increase in the population of the excited Stark component (R_2) of the $^4F_{3/2}$ metastable state and the subsequent intensification of thermal bands. At room temperature most of the transitions from the R_2 level are masked by the dominant emissions coming from the R_1 level with the exception of the $^4F_{3/2}$ (R_2) $\rightarrow ^4I_{11/2}$ (Y_1) which is well isolated at the high energy side of the spectra. The location of this transition is marked on the emission spectra with a vertical red line. Thus, the systematic increase in the intensity of the high energy side of the spectrum (region I) from the high density Ag NP distribution reveals the increase of the thermal population of the $^4F_{3/2}(R_2)$ level. This confirms the presence of heating, which not only modifies the population distribution between the R_1 and R_2 levels, but also produces the activation of non-radiative channels responsible for the observed thermal fluorescence quenching of Nd^{3+} ions. In this respect, it should be taken into account that plasmonic nanostructures could promote fluorescence quenching by processes different than those associated with heating. However, in such a case the spectral shape of Nd^{3+} ions would not be modified. Here, the observed spectral changes in the emission shape of Nd^{3+} ions reflect the thermal origin of the luminescence quenching.

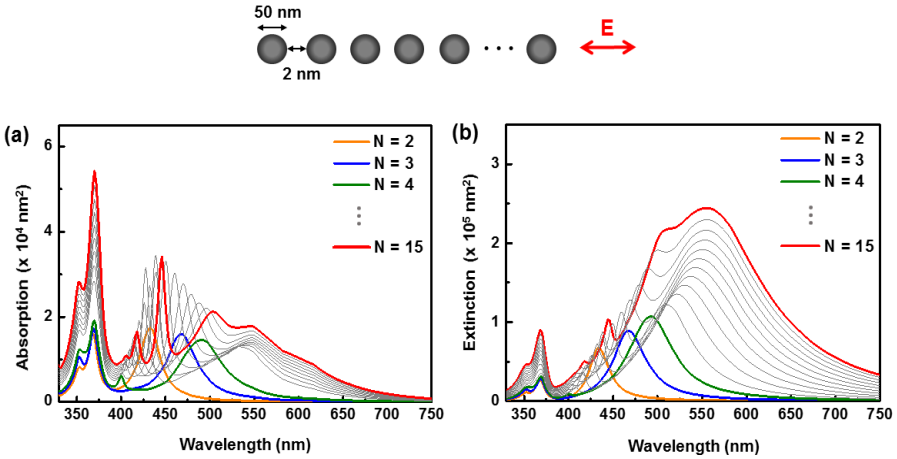

Fig. 2. (a) Absorption and (b) extinction cross section spectra of straight chains of N 50 nm Ag NPs separated by 2 nm gaps calculated for incident light polarized along the chains. Relevant spectra for N = 2, 3 4 and 15 are shown in color. The different order of magnitude between the absorption and the extinction spectra shows the radiative character of the long-wavelength mode for a single long chain of 15 NPs. A scheme of the NP chains and the polarization of the electric field, E, is represented on top.

By modifying the parameters which govern the photochemical deposition a 1D Ag NP arrangement distributed parallel to the ferroelectric c-axis on the domain wall surfaces was obtained [see Fig. 1(f)]. The average size of the NPs forming the chain-like structure is around 50 nm and their separation ranges from 2 to 10 nm. The shape of the Nd^{3+} emission spectrum in the proximity of the chain (obtained under excitation with a beam polarized parallel to the Ag chain) is similar to that shown in Fig. 1(b) (blue). In fact, it coincides with that obtained at room temperature for Nd^{3+} doped $LiNbO_3$ without metallic deposition, and no signs of thermal quenching associated with Ag nanostructures are observed. Moreover, the emitted

#237088 - $15.00 USD Received 27 Mar 2015; revised 24 May 2015; accepted 28 May 2015; published 4 Jun 2015

intensity shows an enhancement in the region of the Ag NP chain. Figure 1(g) shows the corresponding micro-luminescence spatial map illustrating the $^4F_{3/2} \rightarrow {}^4I_{11/2}$ integrated emission spectra in the proximity of the long chain of NPs where an intensification of around 30% is observed [9], in agreement with previous results in fluorophore/Ag NP combinations [18]. These results point out the key role of the Ag NP assembly on the hybrid metal-ferroelectric heterostructures to control the optical properties of laser ions. While the 2D disordered distribution of Ag NPs produces a thermal quenching of the Nd^{3+} spontaneous emission, the 1D distribution of Ag NPs in isolated and long chains supports the enhancement of the fluorescence. Additionally, an area-selectable enhancement of luminescence is also possible as reported for our system as well as for other emitters [6, 19].

To get further insight into the role of the different Ag NP configurations on the spectroscopic properties of Nd^{3+} ions we have analyzed the spectral differences of plasmonic modes associated with silver nanospheres distributed both in short and long linear chains. For that purpose the absorption and extinction cross section spectra of chains formed by different number, N, of Ag NPs have been calculated. Figures 2(a) and 2(b) show the results for N ranging from 2 up to 15. In all cases, the calculations were performed considering spherical Ag NPs with an average size of 50 nm and interspacing distances of 2 nm forming a perfectly straight chain. The polarization of the incident plane wave was chosen parallel to the chain. Here it is important to mention that mixing spheres of different sizes leads to modes at intermediate wavelengths, so that the final result is equivalent to studying a chain of spheres with a size corresponding to the average size of the distribution. Therefore, the deposited metallic structures can be well modeled by chains of spheres with a size corresponding to that average size, 50 nm in our case. The specific distribution size as well as the effect of the particle size, and the effect of mixing NPs with different sizes on the extinction cross section spectra of chains of Ag NPs on $LiNbO_3$ can be found elsewhere [20].

On the other hand, as shown in previous works, the spectra for moderately disordered chains remain remarkably close to the results of the perfectly straight chains [21, 22]. For illustrative purposes the spectra associated with N = 2, 3, 4 and 15 nanoparticles are plotted with different colors in Fig. 2. The absorption spectra in Fig. 2(a) can be divided into two different spectral ranges: the high (λ = 325 - 400 nm) and the low energy region (λ > 400 nm). The high energy region is governed by the contribution of the single plasmon resonance of 50 nm Ag NPs, and increases with N while maintaining both the spectral shape and the energy position. The low energy region accounts for the coupling between the Ag NPs forming the chains and depends strongly on the number of interacting NPs [21]. Moreover, as N increases there is a red shift accompanied by a broadening of the absorption bands due to the presence of higher order collective interactions supported by the chains. Additionally, there is also a significant dependence of sharp resonances (absorption bands), associated with higher-order modes, within the 400-500 nm spectral range. This spectral region is of particular interest in the context of our work since it contains the excitation wavelength (λ = 488 nm) used for the photoluminescence experiments.

The extinction cross section spectra are shown in Fig. 2(b). Similarly to the absorption, the intensity of the single plasmon resonances at 370 nm increases with N. Additionally, the dimers and short-chain modes (N = 2, 3 and 4) display broad resonances centered at 432 nm, 467 and 493 nm, respectively. For larger N values, the main mode broadens and shifts to longer wavelengths. A convergence of the position of the main mode at around 580 nm is obtained for chains of about 15 NPs. Indeed, increasing the number of interacting NPs above N~10 does not substantially change the spectral shape of the extinction spectrum, but only its intensity. It is important to note that the extinction values for the long-wavelength mode are one order of magnitude larger the values obtained for the absorption at similar wavelengths pointing out the strong radiative nature of the long-chain mode compared to those of single Ag NPs or short chains, in agreement with previous works predicting the influences of particle number in strongly coupled metal NP chains [23]. Once the plasmonic modes

#237088 - $15.00 USD Received 27 Mar 2015; revised 24 May 2015; accepted 28 May 2015; published 4 Jun 2015

supported by linear chains of N Ag NPs have been analyzed, the plasmon enhanced Nd^{3+} emission related to the 1D long single chain [Fig. 1(g)], and the Nd^{3+} luminescence thermal quenching associated with the 2D distribution of Ag NPs [Fig. 1(d)] can be explained. In this latter case the 2D disordered configuration of Ag NPs [Fig. 3(a)] can be interpreted as a distribution of short linear chains randomly oriented [Fig. 3(b)], and can be compared to the 1D system illustrated in Fig. 3(c).

Figure 3(d) shows a SEM image with a detail of the 2D distribution of Ag NPs formed on the domain surfaces. For illustrative purposes, some short chains have been marked with colored boxes. The SEM image of the long chain of Ag NPs formed on the domain boundary surfaces is shown in Fig. 3(e).

By using different high resolution SEM images we first performed a statistical analysis in 5x5 μm^2 spatial regions to determine: i) the average size of the NPs, which was found to be close to 50 nm, ii) the percentage of short chains among the total distribution that was composed by dimers (36%) and short N-chains with N = 3 (37%) and N = 4 (22%), and iii) their orientation with respect to the axis of polarization of the incoming light, which strongly governs the optical response of a given linear chain. The distribution of short chains was used to estimate an effective average absorption coefficient $\alpha_{eff}(\lambda)$ by:

$$\alpha_{eff}(\lambda) = \sum_{N} \frac{1}{A_N} \chi_N \cos\theta_N Abs_N(\lambda) \quad (1)$$

where N is the number of NPs in a considered N-chain, A_N its area calculated as N times the area of a single NP, χ_N is the fraction of the N-chain contributing to the optical response, $<\cos\theta_N>$ accounts for the orientation of the chains (projecting the absorption on the direction of the polarization of the excitation beam) and $Abs_N(\lambda)$ the theoretically calculated absorption cross-section spectrum of a single N-chain from Fig. 2(a). For the sake of comparison, for the 1D distribution (formed by 15 NPs), the cross section obtained from the calculations was divided by its area, considered as 15 times the area of a single sphere. The results of the effective absorption coefficient corresponding to each configuration are shown in Fig. 3(f). As observed, for the excitation wavelength used in our experiments (488 nm) the effective absorption of the disordered 2D configuration is around twice the absorption obtained for the single long chain. This results into a considerable heating effect (absorption losses) in the proximity of the NPs, hence limiting the final operation of the 2D hybrid metal-ferroelectric heterostructure. These results are consistent with scanning confocal photoluminescence experiments which show a thermal quenching of the luminescence from the $^4F_{3/2}$ metastable state at the spatial regions with high density 2D distribution of Ag NPs. On the contrary, the lower absorption and the stronger radiative character associated with the 1D single chain explains the intensification provided by the long linear chains of Ag NPs.

#237088 - $15.00 USD Received 27 Mar 2015; revised 24 May 2015; accepted 28 May 2015; published 4 Jun 2015

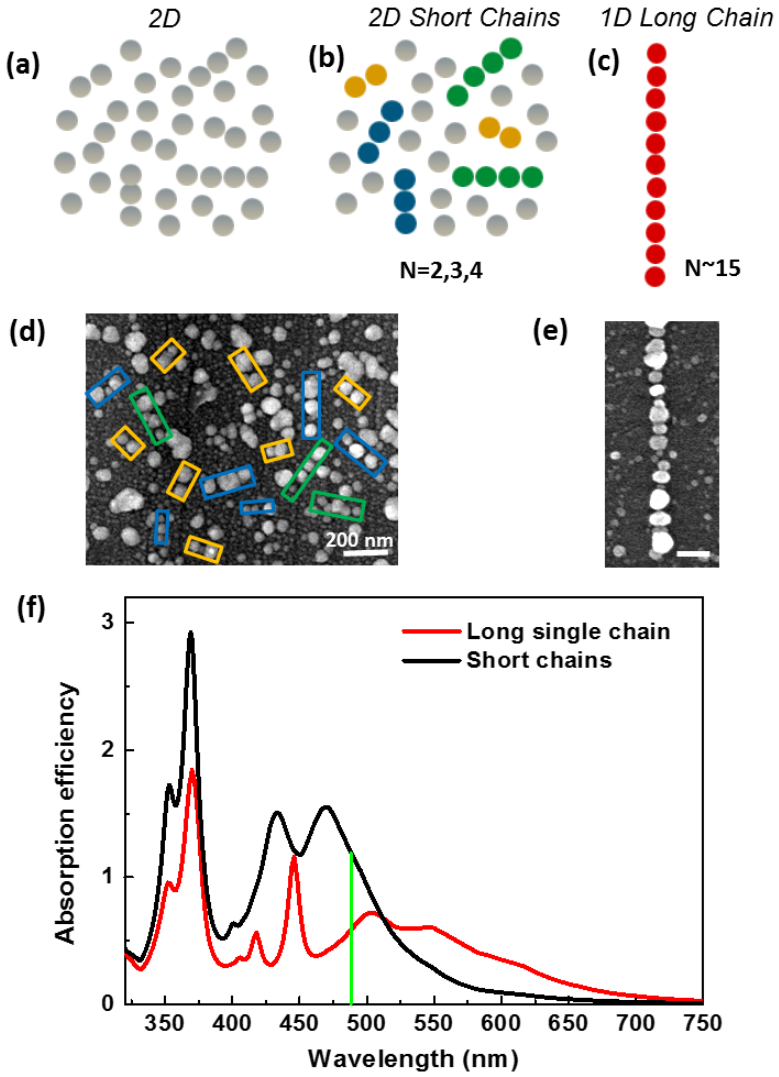

Fig. 3. (a-c) Schematics of the analyzed Ag NP arrangements. As illustrated in panel (b) the 2D disordered distribution of Ag NPs can be interpreted as a distribution of short linear chains randomly oriented (colored in yellow, blue and green for N = 2, 3 and 4, respectively. (d) SEM image of 2D disordered distribution of Ag NPs. Silver NPs are grouped as short chains with colored boxes. (e) SEM image of a single 1D long chain. White bar corresponds to a 100nm length. (f) Effective average absorption calculated for the 2D disordered Ag Np distribution (black spectrum) and for the long single chain (red spectrum). The incident wavelength (488 nm, coinciding with the $^4I_{9/2} \rightarrow {}^4G_{9/2} + {}^2K_{13/2}$ transition of Nd^{3+} ions) is marked by a green vertical line.

4. Summary

In conclusion, the possibility of controlling the properties of optically active rare earth ions by different arrays of metallic nanoparticles is demonstrated. By organizing silver NPs from a 2D disordered configuration to a 1D single chain it is possible not only to eliminate the thermal fluorescence quenching, a crucial feature that could prevent laser action, but also to enhance the fluorescence from the Nd^{3+} laser ions. The results are relevant to determine the optimal configuration of arrays of silver NPs which improve the performance of solid state gain media

#237088 - $15.00 USD Received 27 Mar 2015; revised 24 May 2015; accepted 28 May 2015; published 4 Jun 2015

and constitute a necessary step to study the interaction between metal nanostructures and optically-active ions, which is of interest in the field of solid state based sub-micrometric lasers or gain-enhanced metamaterials.

Acknowledgments

This work has been supported by the Spanish Ministry of Economy and Competitiveness (MINECO) under projects MAT2010-17443 and MAT2013-43301-R and Comunidad de Madrid under grant S2013/MIT-2740. CT and JA acknowledge financial support from Project FIS2013-41184-P of the Spanish MINECO, project ETORTEK NANOGUNE'14 of the Department of Industry of the Basque Government, and from the Department of Education of the Basque Government, IT756-13 of consolidated groups. MOR acknowledges Ramon y Cajal Contract from Spanish MINECO. LSG acknowledges FPU13/02476 grant from the Spanish Ministry of Education.

#237088 - $15.00 USD Received 27 Mar 2015; revised 24 May 2015; accepted 28 May 2015; published 4 Jun 2015

Article 4

Polarization-selective enhancement of Nd^{3+} photoluminescence assisted by linear chains of silver nanoparticles.

E. Yraola, L. Sánchez-García, C. Tserkezis, P. Molina, M. O Ramírez, J. Aizpurua, L. E. Bausá

Journal of Luminescence (2015). doi:10.1016/j.jlumin.2014.12.053

Journal of Luminescence ∎ (∎∎∎∎) ∎∎∎–∎∎∎

Contents lists available at ScienceDirect

Journal of Luminescence

journal homepage: www.elsevier.com/locate/jlumin

Polarization-selective enhancement of Nd^{3+} photoluminescence assisted by linear chains of silver nanoparticles

E. Yraola [a], L. Sánchez-García [a], C. Tserkezis [b], P. Molina [a], M.O Ramírez [a], J. Aizpurua [b], L.E. Bausá [a,*]

[a] Departamento Física de Materiales and Instituto Nicolás Cabrera, Universidad Autónoma de Madrid, 28049 Madrid, Spain
[b] Center for Materials Physics (CSIC-UPV/EHU) and Donostia International Physics Center (DIPC), Paseo Manuel Lardizabal 4, 20018 Donostia/San Sebastián, Spain

ARTICLE INFO

Article history:
Received 22 November 2014
Accepted 23 December 2014

Keywords:
Luminescence enhancement
Nd^{3+} emission
Linear chain of metal nanoparticles
Localized surface plasmons
Boundary-element calculation

ABSTRACT

A control of the emission of Nd^{3+} ions by polarization-dependent plasmon modes, supported by chains of silver nanoparticles deposited on the surface of a Nd^{3+}:$LiNbO_3$ crystal, is demonstrated. By combining micro-fluorescence measurements with theoretical calculations based on the boundary-element method, we explain how the energy splitting between the longitudinal and transverse modes of silver nanoparticle chains produces a selective enhancement of the Nd^{3+} emission Stark lines: exciting radiative modes of silver nanoparticle chains with light polarized parallel to their axis produces a spectral-selective intensification of the π-character Stark transitions of Nd^{3+} located in the vicinity of the silver nanoparticles. The results are relevant to the design of devices for coherent generation at the nanoscale based on rare earth solid state gain media.

1. Introduction

The manipulation of light-matter interaction phenomena at the nanoscale by means of plasmonic nanostructures is currently a subject of an intense activity from both fundamental and technological points of view [1,2]. Noble metal nanostructures exhibit the capability to couple light with the collective oscillations of their conduction-band electrons, which can result into a strong confinement of the electromagnetic field in the vicinity of the metallic physical boundaries. This can be used to enhance the interactions between far-field light and optical emitters placed in close proximity with the metallic nanostructures [1,3].

Recently, some of the authors have shown the interest of combining the optical response of metallic nanostructures with optically active ferroelectric materials. Using a photochemical procedure, periodic distributions of silver nanoparticles (Ag NPs) were selectively assembled on polar and non-polar surfaces (Z- and Y-cut, respectively) of a Nd^{3+}-doped periodically-poled $LiNbO_3$ (PPLN) ferroelectric laser crystal in which laser action and coherent self-frequency converted radiation were demonstrated [4]. Photochemical assembly of Ag metallic NPs showed domain-specific deposition as well as a preferential formation of chains of Ag NPs on the surface of the 180° ferroelectric domain boundaries [5,6]. By exploiting the unique features of plasmonic nanostructures, an enhancement of both the second harmonic generation and the luminescence of Nd^{3+} ions took place when the metallic NPs were deposited on a Nd^{3+} doped PPLN crystal [7]. In addition, due to the linear character of the Ag NPs arrangement, a strong polarization dependence of the photoluminescence of Nd^{3+} ions emitting in the vicinity of the Ag NPs, was observed [8].

Here, we get deeper insight into the analysis of the polarization-selective enhancement of the photoluminescence of Nd^{3+} ions around the chains of Ag NPs. By combining spatially resolved spectroscopic measurements with theoretical calculations based on the boundary-element method (BEM), we show and explain the relationship between the polarization-sensitive radiative plasmonic modes supported by finite chains of silver NPs and the selective enhancement of the π polarized Nd^{3+} emission in the uniaxial $LiNbO_3$ crystal.

The manuscript is structured as follows. First, the polarized spectra of the collective plasmonic modes associated with Ag NPs distributed in long linear chains are calculated taking into account both the NP size and the separation distance distributions in our crystal. Second, the results from dark field microscopy are related to the calculated scattering cross-section spectra of the chains of Ag NPs. The polarized absorption spectra of Nd^{3+} ions are experimentally obtained in the spectral region overlapping the main mode of the Ag NPs. Finally, the influence of the polarization of the plasmon resonance supported by linear chains of Ag NPs on the optical properties of Nd^{3+} ions in this solid state gain medium is analyzed by means of the $^4F_{3/2} \rightarrow {}^4I_{11/2}$ emission of Nd^{3+} ions. As

* Corresponding author.
E-mail address: luisa.bausa@uam.es (L.E. Bausá).

http://dx.doi.org/10.1016/j.jlumin.2014.12.053
0022-2313/

will be shown, exciting the chain of NPs with light polarized parallel to its axis produces a spectral selection of the π-character Stark transitions of Nd^{3+} ions located in the vicinity of the Ag NPs. The results are of interest in the search for efficient subwavelength confinement and active control of light at nanoscale dimensions in rare earth based solid state gain media.

2. Materials and methods

2.1. Materials and synthesis

Nd^{3+} doped PPLN crystals were grown by the off-centered Czochralski method along the *x*-axis by adding Nd (1 mol %) in the form of Nd_2O_3. A 1 mm thick plate was cut and polished with its main faces oriented parallel to the ferroelectric *c*-axis (Y-cut).

The photoinduced silver deposition process was carried out by illuminating the surface of the Y-cut PPLN crystal with above-band gap light provided by a mercury lamp (main line at 253.6 nm) while the crystal was immersed in a 0.01 M $AgNO_3$ solution at 70 °C. The power of the lamp was 5400 μW cm^{-2} at a distance of 3 cm. The illumination time was 10 min. Further details on the experimental procedure can be found elsewhere [5,6]. A scanning electron microscope (SEM) model Philips XL30 SFEG was used to obtain the nanometric-scaled images of the metallic nanoparticles.

2.2. Optical measurements

Dark field microscopy was performed in transmission configuration by using an Olympus BX51 microscope equipped with a dark-field condenser.

Far-field micro-luminescence experiments were performed with a laser scanning confocal microscope provided with a two-axis XY motorized platform with 0.1 μm spatial resolution controlled by software. An Ar^{+} laser (Spectra Physics Model 177-Series) with a filtered emission at 488 nm was used as excitation source. The laser

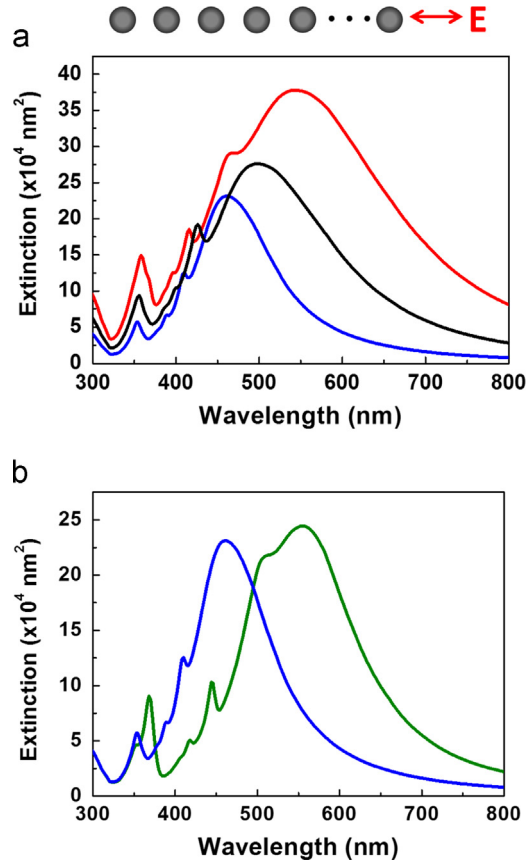

Fig. 2. Calculated extinction cross-section spectra of different linear chains of 15 Ag NPs for a plane wave polarized along the chain axis; (a) Effect of the nanoparticle size: (blue) 50 nm diameter, (red) 70 nm diameter, (black) mixed chain with 6 NPs of 70 nm and 9 NPs of 50 nm. (b) Effect of the inter-particle distance: (blue) 5 nm, (green) 2 nm. For interpretation of the references to color in this figure legend, the reader is referred to the web version of this article.

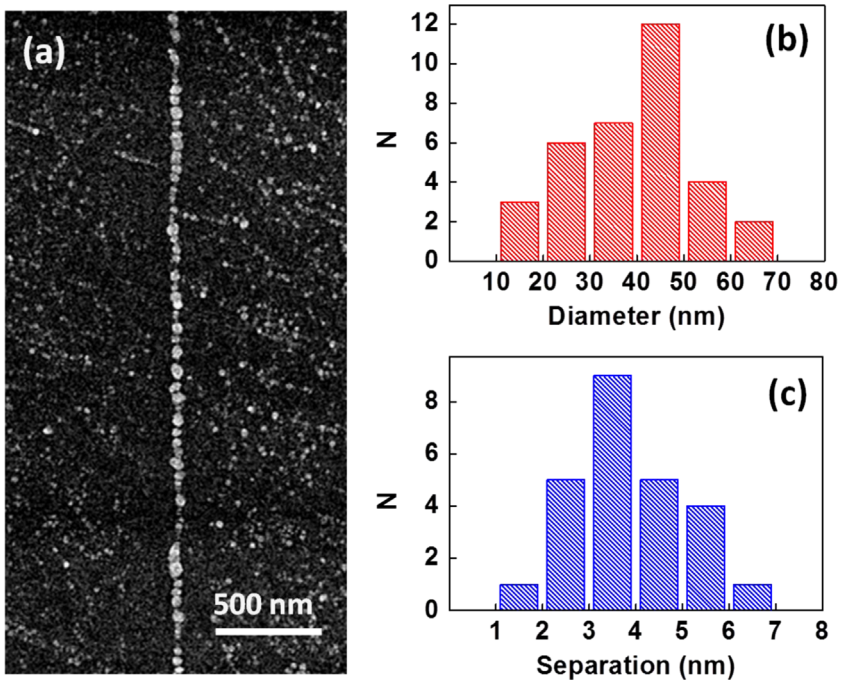

Fig. 1. (a) SEM image of the Y-cut surface of a Nd^{3+} doped PPLN showing a chain of Ag NPs obtained by photochemical procedure on a domain wall surface. (b) Distribution of the NP sizes and (c) inter-particle distances, *N* being the number of particles.

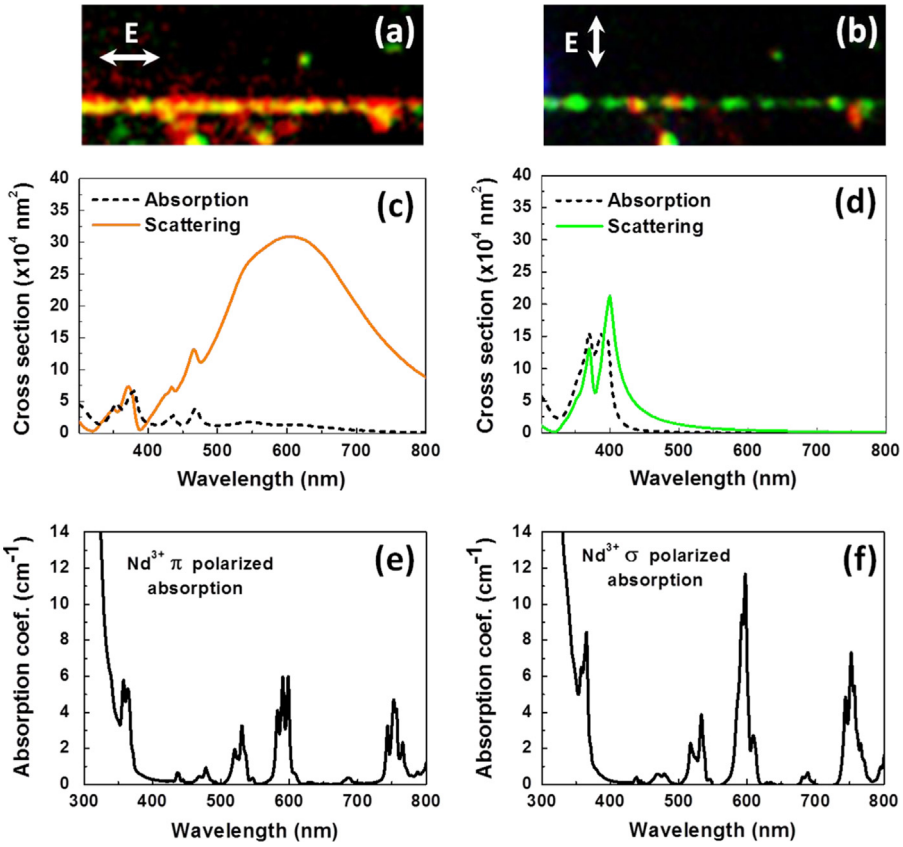

Fig. 3. Dark-field images obtained from a single Ag NP chain for light polarized (a) parallel and (b) perpendicular to the chain axis. Calculated scattering (continuous line) and absorption (dashed line) cross-section spectra of a chain of 15 Ag NPs of 50 nm separated 2 nm for (c) a plane wave polarized parallel to the chain axis and (d) a plane wave polarized perpendicular to the chain axis. (e) and (f) Nd^{3+} absorption spectra corresponding to the π and σ polarized configurations, respectively.

beam was focused to a spot size less than 1 μm, on the surface of the sample by the objectives from the microscope (100× magnification), and the photoluminescence signal from the samples was collected in backscattering geometry with the same objective. The absorption spectra of the Nd^{3+}:$LiNbO_3$ crystals were obtained with a Lambda 1050 Perkin Elmer spectrophotometer.

2.3. Calculations

Far-field extinction and absorption spectra have been calculated by solving the Maxwell's equations with use of the boundary-element method (BEM) [9,10]. Within the BEM the different inhomogeneous media are described by abrupt interfaces that separate different media characterized by local dielectric functions. The surface charges and currents induced at the interfaces are solved self consistently through a discretization of the boundaries and subsequent solution of the resulting matrix equations. Electromagnetic field is then calculated in terms of these induced charges and currents. In our systems, full convergence of the results was achieved with use of 2 discretization points per nm at each interface between different materials.

3. Results and discussion

Fig. 1(a) shows a SEM image of the selective deposition of Ag metallic nanoparticles on the surface of a Nd^{3+} doped PPLN-Y cut crystal obtained under the experimental conditions described above. The metallic Ag NPs were preferentially deposited on the surfaces of the 180° ferroelectric domain walls forming linear chains [8]. Due to the bottom-up character of the photochemical technique, the chains of NPs display a certain degree of disorder. Fig. 1(b) shows the size distribution of the NPs in the chains. As seen, the NPs size ranges from 10 to 70 nm with a maximum at around 40–50 nm. On the other hand, the inter-particle separation varies from 1 to 7 nm showing the most frequent values at around 3–4 nm (Fig. 1(c)).

Varying the number of interacting particles, their average size or their inter-particle separation may affect the localized surface plasmon resonances [11–13]. Therefore, the effects of the particle size distribution and separation distances have been analyzed for our particular system. Fig. 2(a) shows the far field extinction cross-section spectra calculated for different finite chains formed by 15 Ag NPs with particle size of 50 nm (blue line), 15 Ag NPs with particle size of 70 nm (red line) and a mixed chain formed by 6 NPs of 70 nm and 9 NPs of 50 nm (black). The calculations were performed by considering spherical Ag NPs with interspacing distances of 5 nm, as representative values for the interaction. The polarization of the plane wave was parallel to the chain. The position of the main mode converges for chains of about 15 particles, therefore the calculation was limited to that number of particles. The obtained results reveal a red shift of the plasmonic resonance when the size of the silver NPs is increased. In particular, the main mode shifts from 460 nm to 560 nm when the size is increased from 50 nm to 70 nm. On the other hand, mixing NPs of different sizes results into modes located at intermediate wavelengths. Therefore, the size dispersion effects found in our system can be well modeled by simply considering a chain of spheres with a size corresponding to the average size of the distribution (~50 nm). The effect of varying the distance between interacting silver NPs is displayed in Fig. 2(b). As observed, decreasing the interspace distance between metallic NPs in a linear chain shifts the maximum of the extinction towards

longer wavelengths due to the increased inter-particle capacitive coupling as the separation distance decreases [14].

To get experimental evidence of the radiative properties of the plasmonic modes supported by the linear chains of Ag NPs deposited on the domain wall surfaces of Nd^{3+}:$LiNbO_3$ system dark field microscopy has been used. Fig. 3(a) and (b) show the images corresponding to the visible scattered light obtained from a single chain of Ag NPs for longitudinal and transverse polarizations, respectively. A dominant orange-yellowish color is obtained for light polarized parallel to the chain (Fig. 3(a)). On the other hand, at the same spatial location the scattered radiation switches to green color for light polarized perpendicular to the chain (Fig. 3(b)). These results are compared with the calculated scattering cross-section spectra. Fig. 3(c) and (d) show the polarization of the modes calculated for a finite chain of 15 Ag nanospheres with mixed sizes and 2 nm inter-space distance, as representative values of the inter-particle interactions. As observed, the spectral differences obtained for the longitudinal and transverse configurations are in good agreement with the experimental dark field images. Specifically, an intense and broad mode with a dominant radiative character is obtained in the range of 500–700 nm for the parallel configuration (Fig. 3(c)), being the corresponding absorption (dashed black spectrum) considerably smaller. For the perpendicular configuration, a small contribution dominates the scattering spectrum in the 450–550 nm range associated with the excitation of the transverse modes of the individual particles, which explains the green scattering seen in the dark field image for this configuration. Here it is important to note that the camera sensitivity favors the green spectral contribution.

Once the spectral features related to the metal Ag NP distribution have been analyzed we consider the effect of the polarization on the spectroscopic properties of Nd^{3+} ions in $LiNbO_3$. As known, $LiNbO_3$ is

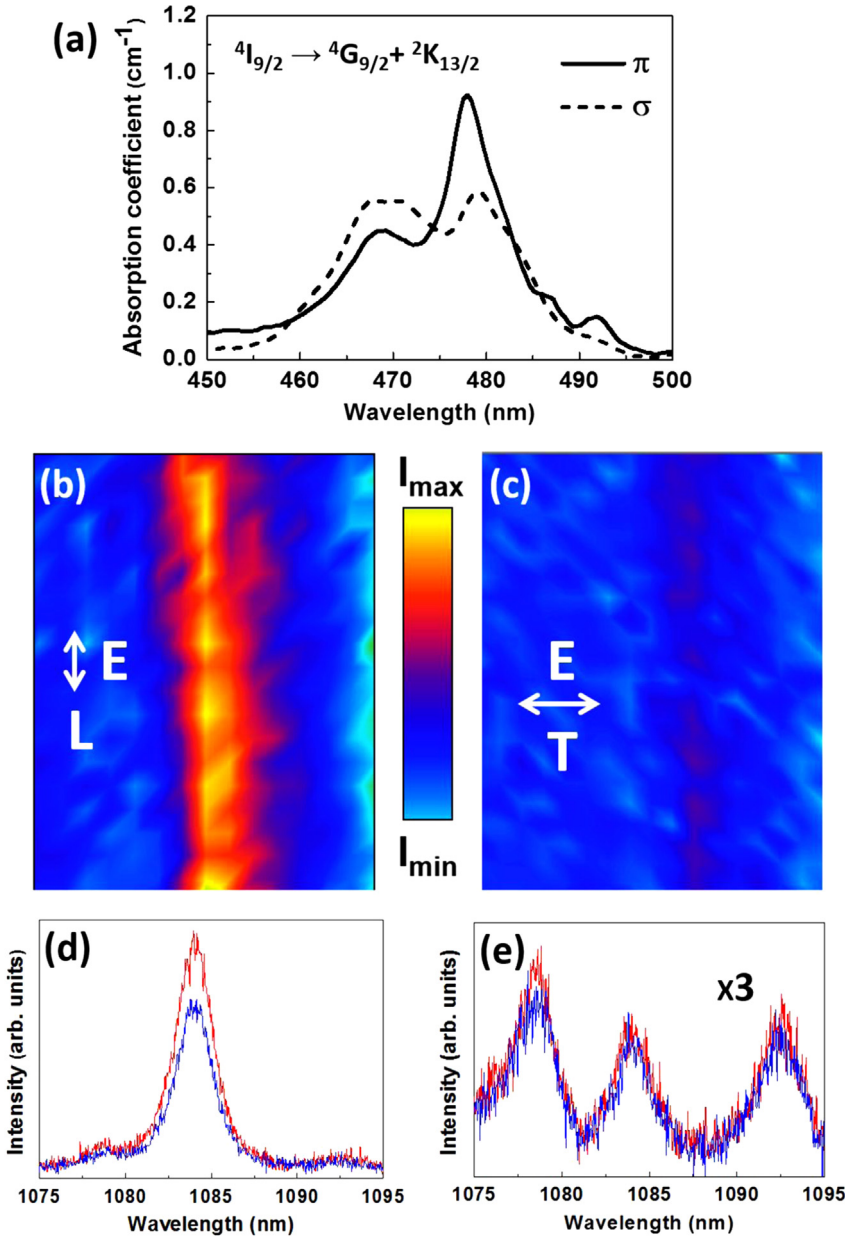

Fig. 4. (a) Absorption spectra of the $^4I_{9/2} \rightarrow {}^4G_{9/2} + {}^2K_{13/2}$ transition of Nd^{3+} for π-polarized (continuous) and σ-polarized (dashed) configurations. (b) Micro-fluorescence spatial map of the π-polarized $^4F_{3/2} \rightarrow {}^4I_{11/2}$ integrated emission and (c) σ-polarized $^4F_{3/2} \rightarrow {}^4I_{11/2}$ emission. (d) π-polarized, and (e) σ-polarized representative emission spectra obtained from the vicinity of the silver nanoparticles chain (red) and from the domain surfaces regions (blue). For interpretation of the references to color in this figure legend, the reader is referred to the web version of this article.

Please cite this article as: E. Yraola, et al., J. Lumin. (2015), http://dx.doi.org/10.1016/j.jlumin.2014.12.053

an uniaxial crystal, the symmetry axis being the ferroelectric *c*-axis. For the Y-cut configuration employed in this work, the ferroelectric *c*-axis coincides with the axis of the linear chains of Ag NPs. On the other hand, according to the C_3 symmetry site for Nd^{3+} ions in this crystal and to the forced electric-dipole character of the inter-Stark transitions of Nd^{3+} ions in $LiNbO_3$ [15,16], different spectra related to different polarization configurations are obtained. Fig. 3(e) and (f) show the π and σ polarized absorption spectra of Nd^{3+} ions in $LiNbO_3$ in the UV–VIS spectral range obtained before the metallic photo-deposition process. The π (σ) spectrum corresponds to the configuration in which the electric field of the incident light is parallel (perpendicular) to the crystallographic *c*-axis of $LiNbO_3$. Both spectra display the optical transitions from the $^4I_{9/2}$ ground state to the different ^4G_J, ^2K_J, $^2P_{1/2}$ and ^4D_J excited states of the 4f configuration of Nd^{3+} ions [17]. The relative contribution observed for the different transitions is in agreement with the polarization-dependent character of the Stark transitions of Nd^{3+} in $LiNbO_3$. The comparison between the polarized absorption spectra of Nd^{3+} ions and the scattering cross-section spectra of the Ag NPs chains (Fig. 3(c) and (d)) reveals a large spectral overlap for light polarized parallel to the linear Ag NP chains which are distributed along the ferroelectric *c*-axis of the crystal. This overlap provides an exceptional support for the assessment of the optical properties of the hybrid metal-gain media under different pumping conditions. In addition, exciting the chain with light polarized parallel or perpendicular to its axis could involve a spectral selection of the π or σ character of the Stark transitions of Nd^{3+} ions located in the vicinity of the Ag NPs.

Finally, the influence of the polarization of the plasmon resonance supported by linear chains on the optical properties of Nd^{3+} ions in this solid state gain medium is analyzed. The specific $^4F_{3/2}\rightarrow{}^4I_{11/2}$ emission of Nd^{3+} ions was studied using two different polarization configurations: i) both excitation and emission polarized with the electric field parallel to Ag NPs chain axis, which corresponds to π configuration for Nd^{3+} spectra and ii) both excitation and emission polarized with the electric field perpendicular, σ character of Nd^{3+} spectra. The excitation has been carried out at the $^4I_{9/2}\rightarrow{}^4G_{9/2}+{}^2K_{13/2}$ absorption of Nd^{3+} ions. For this particular transition the absorption coefficient of Nd^{3+} at the excitation wavelength (488 nm) presents almost identical values for both π and σ configurations (see Fig. 4(a)).

Fig. 4(b) displays the micro-fluorescence spatial map obtained around a single chain of Ag NPs by integrating the obtained π spectra related to the $^4F_{3/2}\rightarrow{}^4I_{11/2}$ transition of Nd^{3+} ions when both the excitation and emission beams are polarized parallel to the chain axis. As seen, a clear enhancement of the Nd^{3+} fluorescence is observed around the Ag NPs chain. For the same spatial region, the micro-fluorescence map obtained by integrating the σ spectra for excitation and emission beams polarized perpendicular to the Ag NPs chains is shown in Fig. 4(c). In this case the fluorescence map reveals a very slight enhancement of the Nd^{3+} emission in the vicinity of the Ag NPs. Representative emission spectra collected in and out the vicinity of the Ag NPs chains are displayed in Fig. 4(d) and (e) for the π and σ configurations, respectively. The spectra display a clear structure due to the Stark splitting of the spin-orbit states by the effect of the host crystal field. The number of Stark transitions and their relative intensity are in agreement with the electric-dipole character of the Nd^{3+} Stark transitions and the noninversion C_3 local symmetry site of Nd^{3+} ions in $LiNbO_3$. Moreover, the shape of the Nd^{3+} emission spectra is not modified by the Ag NPs distribution, which indicates that the electric dipole character of the involved Nd^{3+} Stark transitions is not altered by the interaction with the metallic nanostructure. As observed, the dominant effect of the Ag NPs chains consists on the selective enhancement of the specific π main emission line centered at 1085 nm ($R_1\rightarrow Y_2$) for which laser action has been reported [4]. According to the results of the calculations shown in Fig. 3, the overlap between the Nd^{3+} absorption transitions and the large main mode of the Ag NPs chains in the longitudinal configuration is a cause responsible for the polarization-selective enhancement of the Nd^{3+} emission. Thus, the near field confinement originated due to the radiative character of the chain mode for light polarized parallel to the chain axis produces the intensification of the absorbed light, and therefore, of the emitted light. Due to the crystal symmetry of the $LiNbO_3$ and to the electric dipole selection rules affecting the $^4F_{3/2}\rightarrow{}^4I_{11/2}$ inter-Stark transitions, the intensification of the absorbed light produces, in addition, a spectral selective enhancement of the main laser Stark transition at 1085 nm.

4. Conclusions

We have shown and analyzed the possibility of controlling the optical properties of Nd^{3+} ions by using the polarization features of plasmon modes supported by linear chains of Ag NPs deposited on anisotropic host crystals. In the particular case of Nd^{3+} doped $LiNbO_3$, exciting radiative modes of silver NPs chains with light polarized parallel to their axis produces a spectral-selective intensification of the π-character Stark transitions of Nd^{3+} located in the vicinity of the Ag NPs. The results are relevant to the design of devices for coherent generation at the nanoscale based on rare earth solid state gain media.

Acknowledgments

This work has been supported by the Spanish Ministry of Economy and Competitiveness (MINECO) under projects MAT2010-17443 and MAT2013-43301-R and Comunidad Autónoma de Madrid under project S2013/MIT-2740. MOR acknowledges Ramon y Cajal Contract from Spanish MINECO. LSG acknowledges FPU13/02476 grant from the Spanish Ministry of Education. CT and JA acknowledge financial support from Project FIS2013-41184-P of the Spanish Ministry of Economy and Competitiveness (MINECO), project ETORTEK 2014-15 of the Department of Industry of the Basque Government, and from the Department of Education of the Basque Government, IT756-13 of consolidated groups.

References

[1] L. Novotny, N. van Hulst, Nat. Photonics 5 (2011) 83.
[2] D.K. Gramotnev, S.I. Bozhevolnyi, Nat. Photonics 4 (2010) 83.
[3] M.L. Debasu, D. Ananias, I. Pastoriza-Santos, L.M. Liz-Marzan, J. Rocha, L.D. Carlos, Adv. Mater. 25 (2013) 4868.
[4] T.Y. Fan, A. Cordova-Plaza, M.J.F. Digonnet, R.L. Byer, H.J. Shaw, J. Opt. Soc. Am. B-Opt. Phys. 3 (1986) 140.
[5] Y. Sun, B.S. Eller, R.J. Nemanich, J. Appl. Phys. 110 (2011) 084303.
[6] Y. Sun, R.J. Nemanich, J. Appl. Phys. 109 (2011) 104302.
[7] E. Yraola, P. Molina, J.L. Plaza, M.O. Ramirez, L.E. Bausa, Adv. Mater. 25 (2013) 910.
[8] P. Molina, E. Yraola, M.O. Ramirez, J.L. Plaza, C. de las Heras, L.E. Bausa, Nano Lett. 13 (2013) 4931.
[9] F.J.G. de Abajo, J. Aizpurua, Phys. Rev. B 56 (1997) 15873.
[10] F.J. Garcia de Abajo, A. Howie, Phys. Rev. Lett. 80 (1998) 5180.
[11] R. Esteban, R.W. Taylor, J.J. Baumberg, J. Aizpurua, Langmuir 28 (2012) 888.
[12] C. Tserkezis, R.W. Taylor, J. Beitner, R. Esteban, J.J. Baumberg, J. Aizpurua, Part. Part. Syst. Charact. 31 (2014) 152.
[13] S.T. Jones, R.W. Taylor, R. Esteban, E.K. Abo-Hamed, P.H.H. Bomans, N.A.J. M. Sommerdijk, J. Aizpurua, J.J. Baumberg, O.A. Scherman, Small 10 (2014) 4298.
[14] I. Romero, J. Aizpurua, G.W. Bryant, F.J. Garcia de Abajo, Opt. Express 14 (2006) 9988.
[15] G. Lifante, F. Cusso, F. Jaque, J.A. Sanz-Garcia, A. Monteil, B. Varrel, G. Boulon, J. Garcia Sole, Chem. Phys. Lett. 176 (1991) 482.
[16] R. Burlot, R. Moncorge, H. Manaa, G. Boulon, Y. Guyot, J.G. Sole, D. Cochet Muchy, Opt. Mater. 6 (1996) 313.
[17] H. Loro, M. Voda, F. Jaque, J.G. Sole, J.E.M. Santiuste, J. Appl. Phys. 77 (1995) 5929.

Article 5

Plasmon assisted Nd^{3+} based solid-state nanolaser.

P. Molina, E. Yraola, M. O. Ramírez, C. Tserkezis, J. L. Plaza, J.Aizpurua, J. Bravo-Abad, L.E. Bausá.
Nano Letters (under revision).

Plasmon assisted Nd^{3+} based solid-state nanolaser

Pablo Molina,[1] Eduardo Yraola,[1] Mariola O. Ramírez,[1] Christos Tserkezis,[2] José L. Plaza,[1] Javier Aizpurua,[2] Jorge Bravo-Abad[3] and Luisa E. Bausá[1]*

[1]Dept. Física de Materiales and Instituto Nicolás Cabrera, Universidad Autónoma de Madrid, 28049-Madrid, Spain

[2]Center for Materials Physics (CSIC-UPV/EHU) and Donostia International Physics Center (DIPC), Paseo Manuel Lardizabal 4, 20018-Donostia-San Sebastián, Spain

[3]Dept. Física Teórica de la Materia Condensada and Condensed Matter Physics Center (IFIMAC), Universidad Autónoma de Madrid, 28049-Madrid, Spain

ABSTRACT - Solid-state lasers constitute essential tools in a variety of scientific and technological areas, being available in many different designs. However, although nanolasing has been successfully achieved for dyes and semiconductor gain media associated with plasmonic structures, the operation of solid-state lasers beyond the diffraction limit has not been reported yet. Here we demonstrate room temperature laser action with sub-wavelength confinement in a Nd^{3+}-based solid-state laser by means of the localized surface plasmon resonances supported by chains of metallic nanoparticles. We show a 50% reduction of the pump power at threshold and a remarkable 15-fold improvement of the slope efficiency with respect to the bulk laser operation. The results can be extended to the large diversity of solid-state lasers with the subsequent impact on their applications.

KEYWORDS: Nd^{3+}, plasmonic nanolaser, solid-state laser, chains of Ag nanoparticles

Since the first experimental demonstration of the ruby laser in 1960,[1] the development of solid-state lasers (SSLs) has led to an enormous variety of systems capable of generating laser action with characteristics relevant for applications in research, industry, medicine or optical communications.[2] Their versatile performance includes the possibility of operating in continuous-wave or ultra-short pulsed regimes, as well as single line or tunable sources,[3-5] being accessible in very different configurations comprising from large devices delivering high power to fibers or compact microchip lasers for integrated optics.[6-8] In this class of lasers, the laser transition usually takes place between localized crystal-field levels of rare-earth or transition-metal ions incorporated as optically active impurities in insulating crystals, glasses or ceramics.[9] Additionally, an external optical resonator containing the gain medium is generally employed to provide the optical feedback. Among the different optically active ions, trivalent neodymium (Nd^{3+}) is by far the most widely employed laser ion due to its excellent properties. Namely, it shows a four-level operation in pulsed or continuous-wave (cw) mode, presents a metastable laser level of high quantum efficiency, and has numerous absorption bands throughout the visible and the near-infrared (NIR) spectral regions to ensure efficient pumping.[9]

In the last years, nanoscale laser action with sub-diffraction confinement has been reported for a certain number of configurations combining different gain media (mainly organic dye molecules or semiconductors) with plasmonic nanostructures.[10-18] However, although plentiful devices allow shaping the spatial, temporal and spectral profile of SSLs, laser operation from these systems remains a challenge.

Here we report on the first demonstration of a SSL operating at the subwavelength scale. The system operates at room temperature with a laser emission wavelength close to 1 μm. As gain

medium we have used a Nd^{3+} doped periodically poled $LiNbO_3$ (Nd^{3+}:PPLN) laser crystal,[19] on which long chains of closely spaced silver interacting nanoparticles (NPs) have been deposited (Figure 1a). These chains were assembled on the ferroelectric domain boundary surfaces of the PPLN laser crystal following a simple and low-cost photochemical procedure.[20] The average size of the silver NPs was about 50 nm and the inter-particle distance close to 2 nm (See supporting information and Figure 1b). The metallic nanostructures support broad radiative plasmonic modes which extend from the visible up to the NIR matching the relevant optical transitions of Nd^{3+} ions.[21] Indeed, the possibility to boost the Nd^{3+} photoluminescence in this class of system has been recently reported.[21,22]

To evaluate the effect of the Ag NP chains on the laser performance of our system, we carried out spatially resolved scanning confocal laser gain microscopy experiments (Figure 1a). We pump the device along the *c*-optical axis of the crystal by means of a cw Ti:sapphire laser tuned at 808 nm, where the maximum of the $^4I_{9/2} \rightarrow {}^4F_{5/2}$ absorption of Nd^{3+} ions in $LiNbO_3$ takes place.[23] After a fast non radiative decay to the $^4F_{3/2}$ upper metastable state, radiative transitions to the lower lying states take place. Out of these transitions, free running laser occurs in a four level scheme at the $^4F_{3/2} \rightarrow {}^4I_{11/2}$ (~1μm) transition (Figure 1c).

For a pump beam polarized parallel to the Ag NP chains (with powers in the 125-300 mW range), full laser oscillation occurs only at the immediate surroundings of the metallic nanostructures. The stimulated emission takes place for the individual $^4F_{3/2}(R_1) \rightarrow {}^4I_{9/2}(Y_3)$ Stark transition at λ_e=1093 nm, the spectral linewidth being 0.6 cm^{-1}, which corresponds to the limit of our experimental set-up (green curve in Figure 2a). A two dimensional spatial map of the integrated laser intensity is depicted in Figure 2b. The image replicates the periodicity of the

plasmonic arrays (Figure 2c) and is consistent with a nanoscale confinement driven by the localized surface plasmon (LSP) resonances supported by the metallic NP chains. This sub-wavelength confinement can be achieved all along the chain. The spatial distribution of lasing confirms the nanoscopic character of the laser action around the plasmonic nanostructures and reveals a significant threshold reduction with respect to the bare Nd^{3+}:$LiNbO_3$ regions.

Figure 3b shows the input-output gain curves obtained from the laser light emitted in the vicinity of the metallic nanostructures for two polarization states of the pump beam, parallel and perpendicular to the chains (Figure 3a). As expected, they display the pronounced threshold behavior characteristic of SSLs. Depending on the polarization of the pump beam, we observe two different threshold values, the lowest being obtained when the pump beam is polarized parallel to the NPs chains. The laser slope efficiency is similar for both pump polarizations, parallel and perpendicular. According to the C_3 symmetry site of Nd^{3+} ions in $LiNbO_3$ and to the forced electric-dipole character of the Stark transitions in this system,[24] the intensity of the optical transitions of Nd^{3+} ions does not vary when rotating the polarization around the *c*-optical axis of the crystal. The significant threshold reduction when pumping parallel to the chains can thus be accounted for in terms of the nanophotonic properties of the metallic NP chains as will be discussed below.

On the other hand, the laser preferentially oscillates perpendicularly to the domain walls on which the metallic NPs are deposited. This also occurs in the absence of NPs, and relates to the effect of light diffraction at the ferroelectric domain boundaries, which affects more intensely to the light polarized parallel to the boundaries.[25] As a result, the cavity losses increase preventing

laser oscillation with this polarization. Note that although laser action occurs at the nanoscale, the emitted radiation travels in the resonator through the whole thickness of the medium.

The observed plasmon-mediated lasing process at the nanoscale can be well compared with the conventional bulk laser operation obtained in the same Nd^{3+}:$LiNbO_3$ gain medium in the absence of metallic NP chains and under the same experimental configuration. In this case the laser exhibits a pump power at threshold two times larger than that observed for lasing around the plasmonic chains (parallel pump beam). We also observe a remarkable deterioration of the laser slope efficiency (by a factor of 15) as a result of the bulk photorefractive effect in $LiNbO_3$.[19] Conversely, the sub-wavelength mode confinement produced by the plasmonic chains counteracts the photorefractive beam distortion leading to an extraordinary improvement of the laser performance.

To obtain further physical insight into the experimental observations, we carried out full-wave simulations of the near-field response of the metallic NP chain deposited on top of a Nd^{3+}:PPLN laser crystal (see supporting information). Figure 3c displays cross sections of the electric-field distribution at the NP midplane computed at the pump wavevelength λ_a=808 nm, as obtained for an incident plane wave polarized along the direction of the metallic NP chain (top) and perpendicularly to it (bottom). Similar mode profiles were obtained at the laser emission wavelength λ_e=1093 nm (not shown). For incident polarization parallel to the chain, the optical pump excites a plasmonic resonance characterized by a large electric-field enhancement (of about a factor 100) in the air gap in-between the NPs.[26] This enhancement is significantly reduced (to a factor of approximately 5) when the system is illuminated by a pump perpendicularly polarized with respect to the chain. To reveal the effect of the plasmonic local

fields on the lasing action, we develop a simple semi-analytical model.[27,28] Within this approach, the lasing threshold (R_p^{th}) and slope efficiency (G_e), derived from the dependence of the photon-number on the external pump rate, can be written as $R_p^{th} = V_a / (Q_e \Gamma \zeta)$ and $G_e = Q_e / \omega_e$. V_a stands for the volume of the laser medium, whereas the parameter ζ includes the details of the laser transition (see supporting information). The photonic temporal and spatial confinement properties of the system at the lasing frequency are accounted for by the corresponding quality factor (Q_e) and energy confinement factor (Γ), respectively. Taking into account that the laser photons generated by both polarizations of the pump are stored in the same lasing mode (the plasmonic mode that starts lasing first), the laser slope efficiency is independent of the polarization of the pump field, and governed by the product (Figure 3d). This result agrees well with the fact that similar slope efficiencies are obtained experimentally for the two polarizations of the pump beam (Figure 3b). On the other hand, from our numerical calculations we obtained quality factors of $Q_a \approx 4$ and $Q_a \approx 1$ for the modes excited at λ_a=808 nm with parallel and perpendicular pump polarizations, respectively. Thus, the larger photon-lifetime associated with the plasmonic mode excited at by the parallel polarization (note that $\tau_a = Q_a \lambda_a / 2\pi c$) leads to a reduction of the corresponding value of R_p^{th} with respect to the perpendicular polarization. From this argument it follows that the parallel polarization is expected to feature a lasing threshold approximately a factor of 4 smaller than that corresponding to the perpendicular polarization (Figure 3d), consistent with the values found in the experimental observations. Therefore, the tendencies and values derived from our theoretical analysis support the mechanism of plasmonic light-trapping as the mediator of the nanoscale lasing action in our system.

In summary, we have demonstrated room temperature laser operation of a Nd^{3+} based SSL at the nanoscale by exploiting the capability of LSPs from linear chains of metallic NPs. Our results unambiguously show that laser action occurs in a nanometric region of the system in which the pump power at threshold features a dramatic reduction compared to the conventional bulk laser operation in the same system. These findings open up the fascinating possibility of extending the approach reported here to the extremely vast list of solid state gain media, constituted by hundreds of host-ion combinations. This novel class of plasmonic lasers could cover a broad spectral range from the ultraviolet to the mid-infrared, with the inherent advantages of compactness, chemical and thermal frequency stability distinctive of SSLs, and with the subsequent significant impact for the development of a wide variety of devices and applications.

AUTHOR INFORMATION

Corresponding Author

*Email: luisa.bausa@uam.es

Author Contributions

P.M., E.Y, M.O.R. and L.E.B. were in charge of the experimental results. C.T., J.A. and J.B.-A. worked on the theoretical analysis. J.L.P. performed the crystal growth. M.O.R., J.B.-A. and L.E.B. wrote the manuscript. L.E.B. conceived the project and supervised the work. All authors contributed to the scientific discussion.

ACKNOWLEDGMENT

This work has been supported by the Spanish Ministry of Economy and Competitiveness (MINECO) under projects MAT2013-43301-R and FIS2013-41184-P and Comunidad de Madrid under grant S2013/MIT-2740.

REFERENCES

(1) Maiman, T. H. *Nature* **1960**, 187, 493-494.

(2) Denker, B., Shklovsky, E. Eds.; *Handbook of Solid-State Lasers: Materials, Systems and Applications*; Woodhead Publishing, Cambridge, 2013.

(3) Sennaroglu, A. *Handbook of Solid-State Lasers and Applications*; CRC Press, Boca Raton, 2007.

(4) Keller, U. *Nature* **2003**, 424, 831-838.

(5) Kaminskii, A. A. *Laser Crystals: Their Physics and Properties*; Springer Verlag, Berlin, 1990.

(6) Perry, M. D.; Mourou, G. *Science* **1994**, 264, 917-924.

(7) Jackson, S. D. *Nature Photon*. **2012**, 6, 423-431.

(8) Zayhowski, J. J.; Mooradian, A. *Opt. Lett.* **1989**, 14, 24-26.

(9) Huber, G.; Krankel, C.; Petermann, K. *J. Opt. Soc. Am. B* **2010**, 27, 93-105.

(10) Oulton, R.F.; Sorger, V.J. ; Zentgraf, T.; Ma, R.M.; Gladden, C.; Dai, L.; Bartal, G.; Zhang, X. *Nature* **2009**, 461, 629-632.

(11) Hill, M.T.; Marell, M.; Leong, E.S.P.; Smalbrugge, B.; Zhu, Y.C.; Sun, M.H.; van Veldhoven, P.J.; Geluk, E.J.; Karouta, F.; Oei, Y.S. *Opt. Express* **2009**, 17, 11107-11112.

(12) Noginov, M. A.; Zhu, G.; Belgrave, A. M.; Bakker, R.; Shalaev, V. M.; Narimanov, E. E.; Stout, S.; Herz, E.; Suteewong, T.; Wiesner, U. *Nature* **2009**, 460, 1110.

(13) Ma, R.M.; Oulton, R.F.; Sorger, V.J.; Bartal, G.; Zhang, X.A. *Nature Mater.* **2011**, 10, 110-113.

(14) Lu, Y. J.; Kim, J.; Chen, H.-Y.; Wu, C.; Dabidian, N.; Sanders, C. E.; Wang, C. Y.; Lu, M.-Y.; Li, B. H.; Qiu, X.; Chang, W.-H.; Chen, L. J.; Shvets, G.; Shih, C. K.; Gwo, S. *Science* **2012**, 337, 450−453.

(15) Wu, X. ; Xiao, Y.; Meng, C.; Zhang, X. ; Yu, S.; Wang, Y.; Yang, C.; Guo, X.; Ning, C. Z.; Tong, L. *Nano Lett.* **2013**, 13, 5654–5659.

(16) Zhou, W.; Dridi, M.; Suh, J. Y.; Kim, C. H.; Co, D. T.; Wasielewski, M. R.; Schatz, G. C.; Odom, T. W. *Nat. Nanotechnol.* **2013**, 8, 506−511.

(17) Lu, Y. J.; Wang, C. Y.; Kim, J.; Chen, H. Y.; Lu, M. Y.; Chen, Y. C. l; Chang, W. H.; Chen, L. J.; Stockman, M. I.; Shih, C. K.; Gwo, S. *Nano Lett.* **2014**, 14, 4381-4388.

(18) Sidiropoulos, T.P.H.; Roder, R.; Geburt, S.; Hess, O.; Maier, S.A.; Ronning, C.; Oulton, R.F. *Nature Phys.* **2014**, 10, 870-876.

(19) Fan, T. Y.; Cordova-Plaza, A.; Digonnet, M. J. F.; Byer, R. L.; Shaw, H. J. *J. Opt. Soc. Am. B* **1986**, 3, 140-148.

(20) Kalinin, S. V.; Bonnell, D. A.; Alvarez, T.; Lei, X. J.; Hu, Z. H.; Shao, R.; Ferris, J. H. *Adv. Mater*. **2004**, 16, 795.

(21) Yraola, E.; Molina, P.; Plaza, J. L.; Ramirez, M. O.; Bausa, L. E. *Adv. Mater.* **2013**, 25, 910-915.

(22) Molina, P.; Yraola, E.; Ramirez, M. O.; Plaza, J. L.; De las Heras, C.; Bausa, L. E. *Nano Lett.* **2013**, 13, 4931-4936.

(23) Burlot, R.; Moncorge, R.; Manaa, H.; Boulon, G.; Guyot, Y.; Sole, J. G.; Cochet, M., D. *Opt. Mater.* **1996**, 6, 313−330.

(24) Bonardi, C; Carvalho, R.A.; Basso, H.C.; Terrile, M.C.; Cruz, G.K.; Bausa, L.E.; Sole, J.G. *J. Chem. Phys.* **1999**, 111, 6042-6046.

(25) Müller, M., Soergel, E., Wengler, M.C.; Buse, K. **2004**, 78, 367-370.

(26) Maier, S. A. *Plasmonics: Fundamentals and Applications*; Springer, New York, 2007.

(27) Chang, S. W.; Chuang, S. L. *IEEE J. Quantum Electron.* **2009**, 45, 1004-1013.

(28) Cuerda, J., Ruting, F., Garcia-Vidal, F. J.; Bravo-Abad, J. *Phys. Rev. B* **2015**, 91, 5.

Figure 1

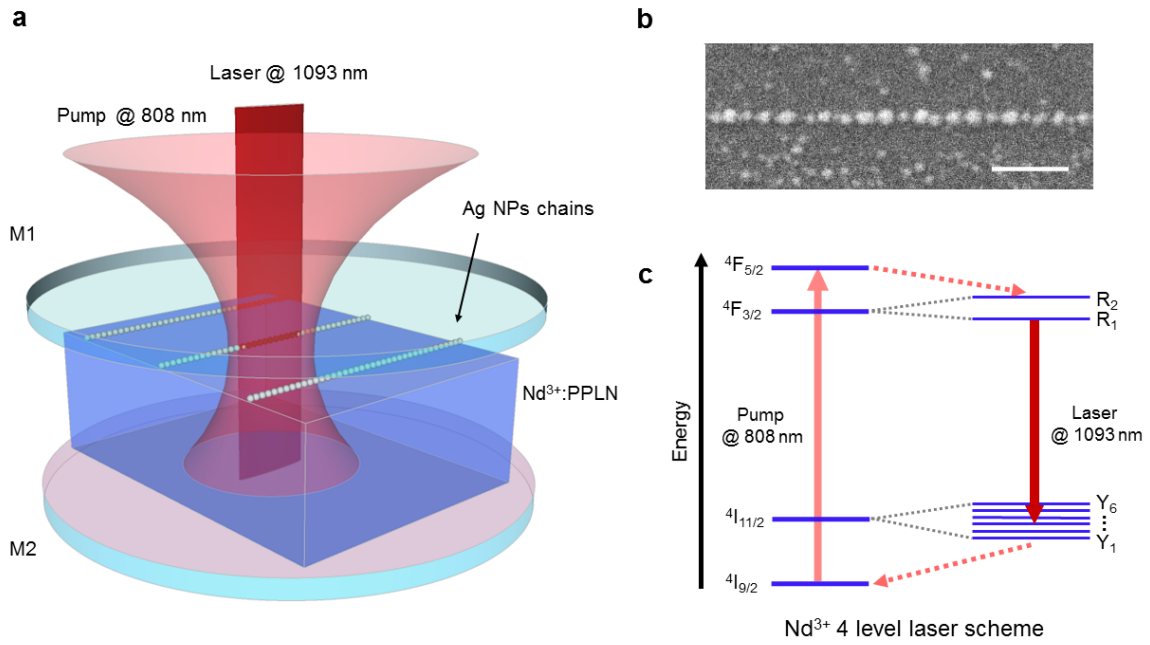

Figure 1. (a) Schematics of the optically pumped Nd^{3+} based solid-state nanolaser. A Nd^{3+}:PPLN solid-state gain medium with periodical arrays of Ag NP chains deposited on it is placed between two plane-parallel mirrors (Fabry-Pérot resonator). The system is optically pumped at λ_a=808 nm with a 20x microscope objective, and the generated laser radiation at λ_e=1093 nm is collected by the same objective in backscattering geometry. (b) SEM image showing a portion of a chain of Ag NPs deposited onto the domain wall surface of the crystal. Scale bar corresponds to 200 nm. (c) Energy level diagram of Nd^{3+} displaying the pump and laser transitions and the crystal field splitting of the relevant $^4F_{3/2}$ and the $^4I_{11/2}$ states. The Stark transition for which laser action is obtained in this work ($R_1 \rightarrow Y_3$) has been highlighted by a thick arrow.

Figure 2

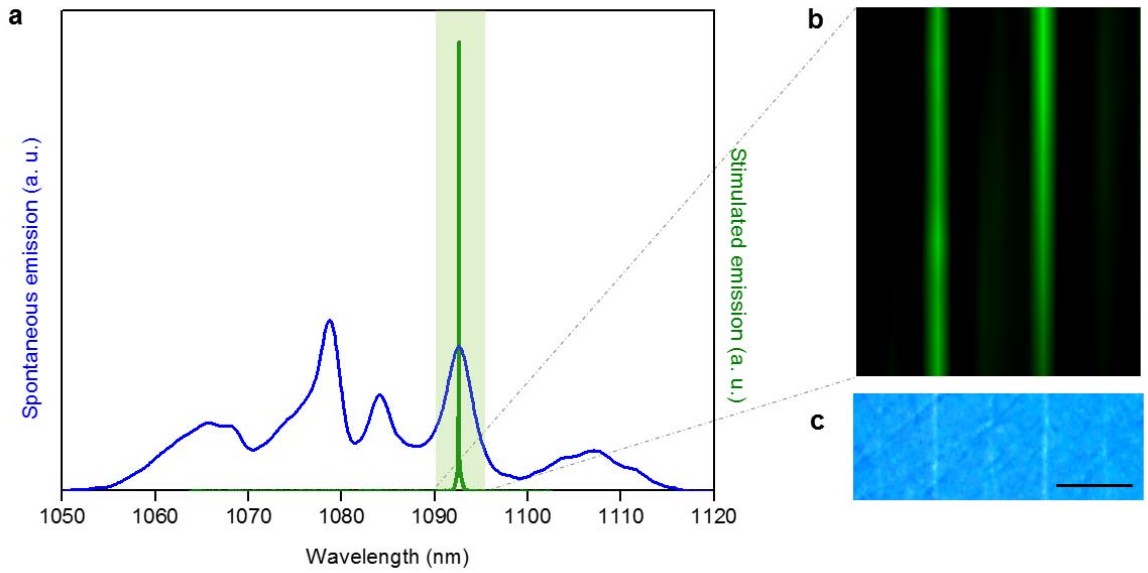

Figure 2. (a) Spontaneous and stimulated emission spectra corresponding to the $^4F_{3/2} \rightarrow {}^4I_{11/2}$ transition of Nd^{3+} in $LiNbO_3$. The spontaneous emission spectrum shows a clear structure due to the Stark splitting of the involved states by the effect of the crystal field (blue line). The stimulated emission spectrum corresponds to the individual $^4F_{3/2}(R_1) \rightarrow {}^4I_{11/2}(Y_3)$ Stark transition at λ_e=1093 nm (green line). (b) Spatially resolved confocal laser gain image obtained by integrating the laser intensity when the pump radiation (fixed at a power of 230 mW) is scanned on a macroscopic area containing several chains. (c) Detailed view of an optical micrograph of the crystal surface around the Ag NP chains. Scale bar corresponds to 5 μm. Laser oscillation takes place in the vicinity of the chains while it is absent in the remaining areas.

Figure 3

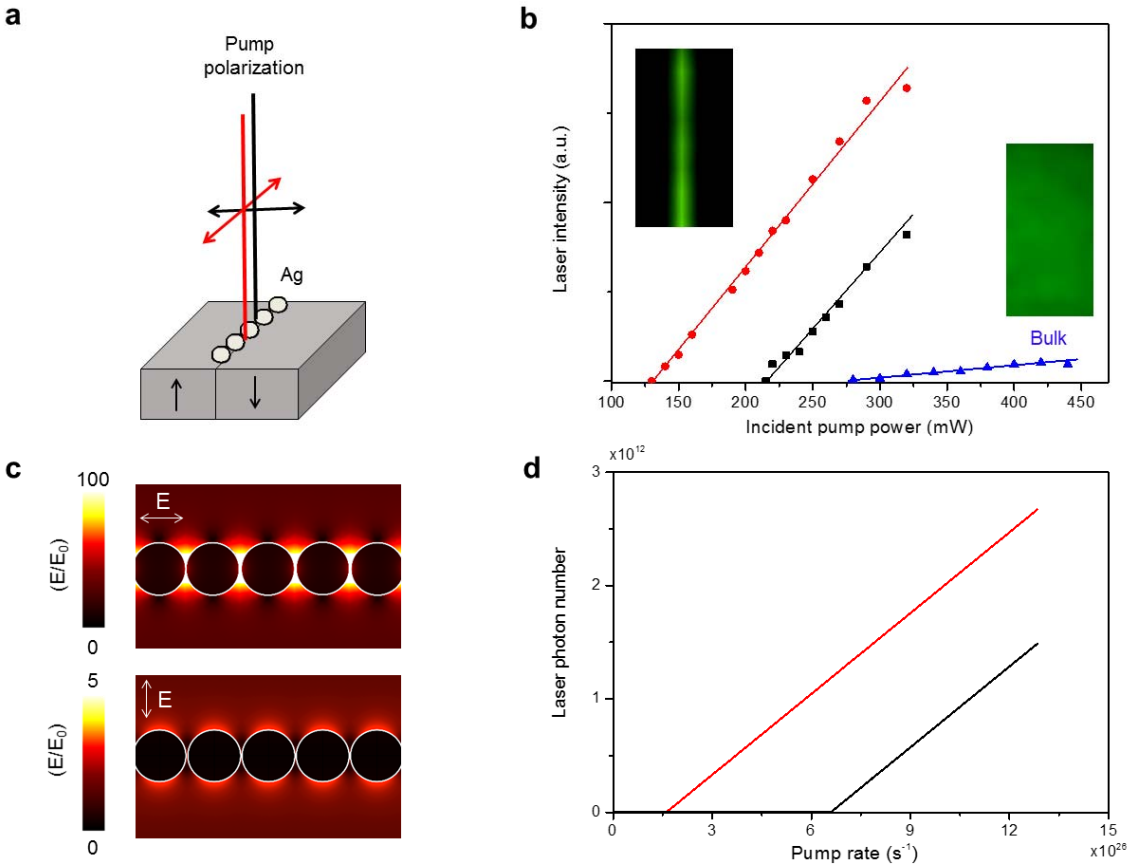

Figure 3. (a) Schematics of the pump configuration of the plasmon mediated Nd^{3+}:PPLN laser crystal (b) Input-output laser gain curves at the vicinity of the Ag NP chains when the pump beam is polarized parallel (red) and perpendicular to the chains (black). The lowest threshold value is obtained when the pump beam is polarized parallel to the chains. The laser performance of the same Nd^{3+}:PPLN crystal after removing the chains (bulk behavior) is shown in blue. In this case the spatial distribution of the laser intensity presents a homogeneous distribution (right inset) in contrast to the well-defined line pattern obtained around the metallic nanostructures (left inset). For illustrative purposes the image from the non-plasmonic part of the gain medium has

been multiplied by a factor of 15. (c) Calculated electric-field amplitudes of the plasmonic resonances excited at λ_a=808 nm using parallel and perpendicular incident polarizations (top and bottom panels, respectively). In both cases, the displayed cross-section corresponds to a xy plane (parallel to the $LiNbO_3$ surface) passing through the center of the Ag NP chain. (d) Calculated steady-state values of the laser photon-number as a function of the pump rate for the case of parallel (red line) and perpendicular (black line) pump polarizations.

Supporting information

Sample preparation

Nd^{3+}:PPLN laser crystal was grown by the off-centered Czochralski technique along the *x*-axis.[1] The period length was controlled via rotation and pulling rates (30 rpm and 1 mm/h, respectively) to generate a closely 50% duty cycle of alternating antiparallel ferroelectric domains with a periodicity close to 7 μm. The Nd^{3+} concentration was found to be 0.1 at % relative to Nb as determined by total-reflection X-ray fluorescence.

The photoinduced silver deposition process was carried out by illuminating during 5 min an optical grade polished surface of a 0.8 mm thick *c*-cut Nd^{3+}:PPLN crystal with a UV Mercury pen-lamp (UVP model 11SC-1, its main line at 253.6 nm) while the sample was immersed in 0,01 M $AgNO_3$ solution at 70 ºC. The size and distribution of the silver NP chains were analyzed by means of scanning electron microscopy (SEM) using a Philips XL30 Schottky field emission gun electron microscope. Optical micrographs were obtained with an Olympus BX51 microscope equipped with crossed polarizers and a Nomarski modified Wollaston prism.

Laser experiments

For laser experiments, a *c*-cut 5 x 5 x 0,8 mm (L x W x T) Nd^{3+}:PPLN plate was placed inside a Fabry–Pérot resonator formed by two plane-parallel mirrors (M1 and M2). M1 was coated for high reflection (R>99.8 %) at the laser wavelength (λ_e=1093 nm) and for high transmittance (T>95%) at the pumping wavelength (λ_a=808 nm), while M2 was coated for high reflection for both, the pump (R>99.8 %) and laser (R>97 %) wavelengths. The mirrors were separated at their edges by two 1 mm thick spacers to avoid the direct contact with the surface of the sample. The whole system was positioned on a customized scanning confocal microscope (Olympus BX41) provided with a two-

axis XY motorized platform (0.2 μm spatial resolution) driven by Labspec software. As excitation source we used a cw Ti:sapphire laser (Spectra Physics) tuned at 808 nm. An objective lens (20X, numerical aperture 0.45) was used to focus the pump beam to a 2.2 μm-diameter spot onto the sample. The laser spectra were collected in backscattering geometry with the same objective, and directed by an optical fiber to a Peltier-cooled Horiba Synapse CCD attached to a Horiba iHR 550 monocromator. The polarization of the pump laser beam was selected by means of a λ/2 plate. The input-output laser curves were also obtained in confocal geometry recording two dimensional spatial maps by integrating the laser intensity for different values of the pump power. All the experiments were carried out at room temperature.

Numerical calculations

Full-wave three-dimensional (3D) simulations of the considered chain of silver metallic NPs lying on top of a laser crystal were performed using both a finite-difference time-domain (FDTD) approach (Lumerical Inc.) and a finite-element method (FEM; COMSOL Multiphysics package). Open space in both types of simulations was mimicked by using perfectly matched layers or/and scattering boundary conditions. Periodic boundary conditions were used to simulate the optical response of an infinitely periodic chain of metallic NPs. The dielectric permittivity of silver metallic NPs was modeled following Ref. (2). A Sellmeier formula was used to model the refractive index of the laser crystal.[3] The discretization grids in the simulations were refined until a relative numerical error of less than 1% is achieved in all reported results. No additional approximations, apart from the one introduced by the spatial discretization of the dielectric constant (inherent to any FDTD or FEM implementation) were introduced in the simulations, and no fitting parameters to experimental data were assumed in the calculations.

Semi-analytical laser model

We used a semi-analytical theoretical approach based on a simple formulation of the Maxwell-Bloch equations.[4,5] This model allows us to obtain compact expressions of the main lasing characteristics of the system in terms of a small number of effective parameters (which, in turn, can be obtained from the full-wave simulations described above). Specifically, assuming a conventional four-level description of the emitters forming the lasing medium and solving for steady-state photon- and electron-population numbers, we obtained the following analytical expressions for the lasing threshold (R_p^{th}) and slope efficiency (G_e), $R_p^{th} = V_a / (Q_e \Gamma \zeta)$ and $G_e = Q_e / \omega_e$. Here V_a is the volume of the laser medium and Q_e is the quality factor of the plasmonic resonance. Γ represents the energy confinement factor at the lasing frequency, $\Gamma = \int_{V_a} d\mathbf{r}\, u(\mathbf{r},t) / \int dr\, u(\mathbf{r},t)$ (with $u(\mathbf{r},t)$ being the time-average over one optical period of the density of electromagnetic energy). The parameter ζ is defined as $\zeta = v_g \sigma_e \tau_{21} N_0 / \omega_e$, where v_g is the material group velocity of the active medium, σ_e (5 x 10^{-20} cm^2) is the emission cross-section of the laser emitters, N_0 is the total number of emitters, and τ_{21} (100 μs) is the spontaneous emission lifetime of the considered laser transition.

REFERENCES

(1) Ming, N. B., Hong, J. F.; Feng D. *J. Mater. Sci.* **1982**, 17, 1663-1670.

(2) Johnson, P. B.; Christy, R. W. *Phys. Rev. B* **1972**, 6, 4370-4379.

(3) Zelmon, D.E., Small, D.L.; Jundt, D. *J. Opt. Soc. Am. B* **1997**, 14, 3319–3322.

(4) Chang, S. W.; Chuang, S. L. *IEEE J. Quantum Electron.* **2009**, 45, 1004-1013.

(5) Cuerda, J., Ruting, F., Garcia-Vidal, F. J.; Bravo-Abad, J. *Phys. Rev. B* **2015**, 91, 5.

Español

4 Conclusiones

A continuación se presentan las conclusiones más relevantes obtenidas en este trabajo.

1. *Foto-deposición de arreglos de nanopartículas de plata metálica sobre cristales de $LiNbO_3$ dopados con Nd^{3+}*

Mediante la técnica de deposición fotoquímica denominada litografía ferroeléctrica se ha demostrado por primera vez la posibilidad de obtener diferentes arreglos de NPs de plata sobre las superficies de un cristal con ganancia láser, el $LiNbO_3$:Nd^{3+}. Utilizando como plataforma cristales de $LiNbO_3$:Nd^{3+} con estructura mono-dimensional de dominios ferroeléctricos se han obtenido fundamentalmente dos tipos de arreglos periódicos de NPs: (a) cadenas lineales de NPs distribuidas sobre las superficies de las paredes de dominios ferroeléctricos y (b) NPs distribuidas desordenadamente cubriendo las superficies de los dominios. Dichas distribuciones se han obtenido tanto en corte Z (superficie polar del $LiNbO_3$) como en corte Y, demostrando por primera vez la validez de utilizar de una superficie no polar como plataforma para el proceso de litografía ferroeléctrica. Las NPs de plata se han obtenido a través de un procedimiento del tipo abajo-arriba ("bottom-up") muy sencillo y barato frente a las costosas y complejas técnicas nanolitográficas tipo arriba-abajo ("top-down")

2. *Intensificación de la luminiscencia del $LiNbO_3$:Nd^{3+}*

Se ha demostrado que las NPs de Ag distribuidas en cadenas sobre las fronteras de dominios alternos, y separadas entre sí distancias inferiores a las longitudes de onda visible, producen una intensificación de la emisión de los iones Nd^{3+} alrededor de un 80%. Los valores de intensificación más altos se producen al excitar los modos plasmónicos con luz polarizada paralelamente a las cadenas de NPs. La

intensificación se produce mediante efecto antena tanto para la radiación de excitación como para la emisión, siendo más eficiente en el primer caso.

3. *Efectos del ordenamiento de las NPs de Ag en la luminiscencia del sistema $LiNbO_3:Nd^{3+}$*

Se han estudiado los efectos de dos arreglos de NPs de plata mencionadas en la emisión del sistema $LiNbO_3:Nd^{3+}$. Mientras que las distribuciones desordenadas de NPs distribuidas sobre las superficies de los dominios pueden producir un bloqueo térmico de la fluorescencia del ion Nd^{3+}, las distribuciones de NPs alineadas en cadenas rectilíneas producen la intensificación de la luminiscencia de dicho ion. El resultado se ha explicado atendiendo al carácter radiativo dominante de los modos NPs asociados a la cadena lineal en contraposición con el carácter absorbente de los arreglos desordenados. Dado que un bloqueo térmico de la fluorescencia puede impedir la acción láser, la conclusión obtenida es de relevancia a la hora de desarrollar sistemas SSL en la nanoescala.

4. *Control selectivo de la intensificación de transiciones luminiscentes en el $LiNbO_3:Nd^{3+}$*

Se ha demostrado la posibilidad de intensificar selectivamente la emisión procedente de transiciones Stark del Nd^{3+} con polarización específica mediante la excitación de resonancias plasmónicas de simetría apropiada. Mediante la preparación de cadenas de NPs de Ag dispuestas paralelamente al eje polar (corte Y) se ha demostrado la intensificación selectiva de la línea Stark $^4F_{3/2}$ $(R_1) \rightarrow {}^4I_{11/2}$ (Y_2) (línea láser), con carácter π gracias a la excitación de los modos con luz polarizada paralelamente a dichas cadenas. El trabajo demuestra como mediante el uso apropiado de antenas ópticas de simetría específica se pueden intensificar selectivamente las transiciones de iones de tierras raras y así modificar las propiedades espectroscópicas en la nanoescala con respecto al volumen.

5. *Acción laser en la nanoescala*

Se ha demostrado por primera vez acción láser confinada en regiones espaciales inferiores al límite de difracción a partir de un medio de ganancia de estado sólido activado con iones Nd^{3+} gracias a la presencia de plasmones localizados superficiales suministrados por cadenas de NPs metálicas. Los resultados obtenidos se pueden comparar con la acción láser del mismo sistema en configuración volumétrica, obteniéndose una reducción del umbral de bombeo del 50% y una mejora de la eficiencia láser en un factor 15. La acción láser en la

nanoescala tiene lugar a temperatura ambiente, preservándose las características de los láseres de estado sólido. Los resultados abren la vía para la operación en la nanoescala de la gran diversidad de láseres de estado sólido existentes en la actualidad.

English

4 Conclusions

The most relevant conclusions of this work are presented below.

1. Photo-deposition of metallic arrangements of silver nanoparticles on Nd^{3+} doped $LiNbO_3$ crystals.

By means of a photochemical deposition technique called ferroelectric lithography we have demonstrated for the first time the possibility to obtain different arrangements of silver NPs on the surfaces of a laser crystal, the $LiNbO_3:Nd^{3+}$. Using the mono-dimensional ferroelectric structure presented in the $LiNbO_3:Nd^{3+}$ crystals as a template for the photo-deposition process, we have mainly obtained two types of periodic NPs arrays: (a) linear chains of NPs distributed on the surfaces of the ferroelectric domain walls and (b) disorderly distributed NPs covering the domain surfaces. Such distributions were obtained on both Z-cut (polar surface of $LiNbO_3$) and Y-cut, demonstrating for the first time the validity to use of a non-polar surface as a platform for ferroelectric lithography processes. Silver NPs were obtained by a very simple and low-cost bottom-up process, compared with the more expensive and complex top-down nanolithography techniques.

2. Enhancement of the $LiNbO_3:Nd^{3+}$ luminescence

We have shown that the chain-like Ag NPs, distributed on the domain boundary surfaces with separations lower than the visible wavelength of light, produce an enhancement of around 80% in the Nd^{3+} emission. The highest intensification occurs when exciting with light parallel to the NPs chains. The intensification takes place by means of an antenna effect for both the excitation and the emission radiation, being more efficient in the first case.

3. Order effects of the Ag NPs in the $LiNbO_3:Nd^{3+}$ luminescence

We have studied the effects of two different silver NPs distributions on the $LiNbO_3:Nd^{3+}$ emission. While disordered distributions of Ag NPs on the domain surfaces can produce a thermal quenching of the Nd^{3+} ion fluorescence, linear NPs chains produce the intensification of the Nd^{3+} signal. This result has been explained by taking into account the dominant radiative nature of the plasmonic modes associated with the straight chains, in contrast with the ohmic character of the disorder arrangements. Since the thermal quenching of the fluorescence can prevent lasing action, the obtained result is relevant for the development of a SSL at the nanoscale.

4. Selective intensification of specific luminescent transitions in $LiNbO_3:Nd^{3+}$

With the appropriate symmetry configuration we have experimentally demonstrated the possibility to selectively enhance emissions with specific polarization by exciting the appropriate plasmonic resonances. Arranging the Ag NPs chains parallel to the polar axis (Y-cut surface) we have demonstrated a selective enhancement of the π polarized $^4F_{3/2}$ (R_1) → $^4I_{11/2}$ (Y_2) laser line, through the excitation with light polarized parallel to the linear chains. This work demonstrates how optical antennas of specific symmetry can be exploited to selectively enhance the optical transitions of rare earth ions, and even to modify the spectroscopic properties at the nanoscale with respect to the bulk.

5. Laser action at the nanoscale

We demonstrated room temperature laser action with sub-wavelength confinement in a Nd^{3+}-based solid-state laser by means of the localized surface plasmon resonances supported by chains of metallic nanoparticles. The obtained results can be compared with the bulk laser operation in the same system, exhibiting a pump threshold reduction of 50% and a 15-fold improvement of laser efficiency. The nano-lasing occurs at room temperature, and preserves the SSL characteristics. These results open the path for the laser operation at the nanoscale in a large variety of SSL systems at the present time.

5 References

[Aisaka 2008] T. Aisaka, M. Fujii, S. Hayashi, *Applied Physics Letters*, **92**, 132105 (2008).

[Anker 2008] J.N. Anker, W.P. Hall, O. Lyandres, N.C. Shah, J. Zhao, R.P. Van Duyne, *Nature Materials*, **7**, 442 (2008).

[Arizmendi 2004] L. Arizmendi, *Physica Status Solidi a-Applied Research*, **201**, 253 (2004).

[Atwater 2010] H.A. Atwater, A. Polman, *Nature Materials*, **9**, 205 (2010).

[Auciello 1998] O. Auciello, J.F. Scott, R. Ramesh, *Physics Today*, **51**, 22 (1998).

[Balobaid 2013] L. Balobaid, N.C. Carville, M. Manzo, L. Collins, K. Gallo, B.J. Rodriguez, *Applied Physics Letters*, **103**, 182904 (2013).

[Ballman 1965] A.A. Ballman, *Journal of the American Ceramic Society*, **48**, 112 (1965).

[Barnes 2003] W.L. Barnes, A. Dereux, T.W. Ebbesen, *Nature*, **424**, 824 (2003).

[Barry 1998] I.E. Barry, G.W. Ross, P.G.R. Smith, R.W. Eason, G. Cook, *Materials Letters*, **37**, 246 (1998).

[Belabaev 1975] K.G. Belabaev, A.A. Kaminskii, S.E. Sarkisov, *Physica Status Solidi (a)*, **28**, K17 (1975).

[Bergman 2003] D.J. Bergman, M.I. Stockman, *Physical Review Letters*, **90**, 027402 (2003).

[Bergman 1968] J.G. Bergman, A. Ashkin, A.A. Ballman, J.M. Dziedzic, Levinste.Hj, R.G. Smith, *Applied Physics Letters*, **12**, 92 (1968).

[Bermudez 1999] V. Bermudez, M.D. Serrano, E. Dieguez, *Journal of Crystal Growth*, **200**, 185 (1999).

[Bharadwaj 2009] P. Bharadwaj, B. Deutsch, L. Novotny, *Advances in Optics and Photonics*, **1**, 438 (2009).

[Blanco 2004] L.A. Blanco, F.J.G. de Abajo, *Journal of Quantitative Spectroscopy & Radiative Transfer*, **89**, 37 (2004).

[Bohren 1983] C.F. Bohren, D.R. Huffman, *Absorption and scattering of light by small particles*, Wiley, (1983).

[Bordui 1991] P.F. Bordui, R.G. Norwood, C.D. Bird, G.D. Calvert, *Journal of Crystal Growth*, **113**, 61 (1991).

[Brongersma 2007] M.L. Brongersma, P.G. Kik, *Surface Plasmon Nanophotonics*, Springer Netherlands, (2007).

[Brown 1985] I.D. Brown, D. Altermatt, *Acta Crystallographica, Section B (Structural Science)*, **B41**, 244 (1985).

[Brown 2012] T.L. Brown, *Chemistry : the central science*, Prentice Hall, Boston (2012).

[Burlot 1996] R. Burlot, R. Moncorge, H. Manaa, G. Boulon, Y. Guyot, J.G. Sole, D. CochetMuchy, *Optical Materials*, **6**, 313 (1996).

[Carville 2012] N.C. Carville, M. Manzo, S. Damm, M. Castiella, L. Collins, D. Denning, S.A.L. Weber, K. Gallo, J.H. Rice, B.J. Rodriguez, *Acs Nano*, **6**, 7373 (2012).

[Cordovaplaza 1988] A. Cordovaplaza, T.Y. Fan, M.J.F. Digonnet, R.L. Byer, H.J. Shaw, *Optics Letters*, **13**, 209 (1988).

[Chen 2012] Y.H. Chen, W.K. Chang, N. Hsu, C.Y. Chen, J.W. Chang, *Optics Letters*, **37**, 2814 (2012).

[Chow 1974] K. Chow, H.G. McKnight, L.R. Rothrock, *Materials Research Bulletin*, **9**, 1067 (1974).

[Dawber 2005] M. Dawber, K.M. Rabe, J.F. Scott, *Reviews of Modern Physics*, **77**, 1083 (2005).

[Di Paolo 2001] R.E. Di Paolo, E. Cantelar, P.L. Pernas, G. Lifante, F. Cusso, *Applied Physics Letters*, **79**, 4088 (2001).

[Dieke 1968] G.H. Dieke, H.M. Crosswhite, H. Crosswhite, *Spectra and energy levels of rare earth ions in crystals*, Interscience Publishers, (1968).

[Drude 1902] P. Drude, *Annalen Der Physik*, **7**, 687 (1902).

[Dunn 2007] S. Dunn, P.M. Jones, D.E. Gallardo, *Journal of the American Chemical Society*, **129**, 8724 (2007).

[Esteban 2012] R. Esteban, R.W. Taylor, J.J. Baumberg, J. Aizpurua, *Langmuir*, **28**, 8881 (2012).

[Evanoff 2004] D.D. Evanoff, G. Chumanov, *Journal of Physical Chemistry B*, **108**, 13957 (2004).

[Evlanova 1967] N.F. Evlanova, A.S. Kovalev, V.A. Koptsik, Kornienk.Ls, Prokhoro.Am, Rashkovi.Ln, *Jetp Letters-Ussr*, **5**, 291 (1967).

[Fan 1986] T.Y. Fan, A. Cordovaplaza, M.J.F. Digonnet, R.L. Byer, H.J. Shaw, *Journal of the Optical Society of America B-Optical Physics*, **3**, 140 (1986).

[Fedulov 1965] S.A. Fedulov, Z.I. Shapiro, Ladyzhin.Pb, *Soviet Physics Crystallography, Ussr*, **10**, 218 (1965).

[Fernandez-Ruiz 2001] R. Fernandez-Ruiz, J. Capmany, *Journal of Analytical Atomic Spectrometry*, **16**, 867 (2001).

[Foldvari 1984] I. Foldvari, K. Polgar, R. Voszka, R.N. Balasanyan, *Crystal Research and Technology*, **19**, 1659 (1984).

[Forget 2013] S. Forget, S. Chénais, *Organic Solid-State Lasers*, Springer Berlin Heidelberg, (2013).

[Freestone 2007] I. Freestone, N. Meeks, M. Sax, C. Higgitt, *Gold Bulletin*, **40**, 270 (2007).

[Fridkin 1980] V.M. Fridkin, *Ferroelectric semiconductors*, Consultants Bur., (1980).

[Ganesamoorthy 2005] S. Ganesamoorthy, M. Nakamura, S. Takekawa, S. Kumaragurubaran, K. Terabe, K. Kitamura, *Materials Science and Engineering B-Solid State Materials for Advanced Technology*, **120**, 125 (2005).

[Garcia 2012] M.A. Garcia, *Journal of Physics D-Applied Physics*, **44**, 283001 (2012).

[Genov 2011] D.A. Genov, R.F. Oulton, G. Bartal, X. Zhang, *Physical Review B*, **83**, G245312 (2011).

[Giocondi 2001] J.L. Giocondi, G.S. Rohrer, *Journal of Physical Chemistry B*, **105**, 8275 (2001).

[Gopalan 1998] V. Gopalan, T.E. Mitchell, Y. Furukawa, K. Kitamura, *Applied Physics Letters*, **72**, 1981 (1998).

[Gopalan 2007] V. Gopalan, V. Dierolf, D.A. Scrymgeour, *Annual Review of Materials Research*, **37**, 449 (2007).

[Gopinath 2010] A. Gopinath, S.V. Boriskina, S. Yerci, R. Li, L. Dal Negro, *Applied Physics Letters*, **96**, 071113 (2010).

[Gupta 2006] M.C. Gupta, J. Ballato, *The Handbook of Photonics, Second Edition*, CRC Press, (2006).

[Guy 1998] S. Guy, C.L. Bonner, D.P. Shepherd, D.C. Hanna, A.C. Tropper, *Ieee Journal of Quantum Electronics*, **34**, 900 (1998).

[Hanson 2006] J.N. Hanson, B.J. Rodriguez, R.J. Nemanich, A. Gruverman, *Nanotechnology*, **17**, 4946 (2006).

[Haussmann 2009] A. Haussmann, P. Milde, C. Erler, L.M. Eng, *Nano Letters*, **9**, 763 (2009).

[Hayakawa 1999] T. Hayakawa, S.T. Selvan, M. Nogami, *Applied Physics Letters*, **74**, 1513 (1999).

[Haynes 2005] C.L. Haynes, A.D. McFarland, R.P. Van Duyne, *Analytical Chemistry*, **77**, 338A (2005).

[Heine 2007] V. Heine, *Group Theory in Quantum Mechanics: An Introduction to Its Present Usage*, Dover Publications, (2007).

[Henderson 2006] B. Henderson, G.F. Imbusch, *Optical Spectroscopy of Inorganic Solids*, Clarendon Press, (2006).

[Hill 2009] M.T. Hill, M. Marell, E.S.P. Leong, B. Smalbrugge, Y. Zhu, M. Sun, P.J. van Veldhoven, E.J. Geluk, F. Karouta, Y.-S. Oei, R. Notzel, C.-Z. Ning, M.K. Smit, *Optics Express*, **17**, 11107 (2009).

[Hu 2006] M. Hu, J. Chen, Z.-Y. Li, L. Au, G.V. Hartland, X. Li, M. Marquez, Y. Xia, *Chemical Society Reviews*, **35**, 1084 (2006).

[Hu 2010] M. Hu, A. Ghoshal, M. Marquez, P.G. Kik, *Journal of Physical Chemistry C*, **114**, 7509 (2010).

[Huignard 1989] J.P. Huignard, P. Gunter, *Topics in Applied Physics*, **62**, 1 (1989).

[Ishibashi 1996] S. Ishibashi, H. Itoh, T. Kaino, I. Yokohama, K. Kubodera, *Optics Communications*, **125**, 177 (1996).

[Iyi 1992] N. Iyi, K. Kitamura, F. Izumi, J.K. Yamamoto, T. Hayashi, H. Asano, S. Kimura, *Journal of Solid State Chemistry*, **101**, 340 (1992).

[Jackson 2012] S.D. Jackson, *Nature Photonics*, **6**, 423 (2012).

[Jaque 1999] D. Jaque, J. Capmany, J.A.S. Garcia, A. Brenier, G. Boulon, J.G. Sole, *Optical Materials*, **13**, 147 (1999).

[Jian 2007] Z. Jian, F. Yi, M.H. Chowdhury, J.R. Lakowicz, *Nano Letters*, **7**, 2101 (2007).

[Johnson 1972] P.B. Johnson, R.W. Christy, *Physical Review B*, **6**, 4370 (1972).

[Jona 1962] F. Jona, G. Shirane, *Ferroelectric crystals*, Pergamon Press, (1962).

[Jones 2009] P.M. Jones, S. Dunn, *Journal of Physics D-Applied Physics*, **42**, 065408 (2009).

[Kalinin 2001] S.V. Kalinin, D.A. Bonnell, *Physical Review B*, **63**, 125411 (2001).

[Kalinin 2004] S.V. Kalinin, D.A. Bonnell, T. Alvarez, X.J. Lei, Z.H. Hu, R. Shao, J.H. Ferris, *Advanced Materials*, **16**, 795 (2004).

[Kaminow 1975] I.P. Kaminow, L.W. Stulz, *Ieee Journal of Quantum Electronics*, **QE11**, 306 (1975).

[Kaminskii 1968] A.A. Kaminskii, *Soviet Physics Jetp-Ussr*, **27**, 388 (1968).

[Kaminskii 1972] A.A. Kaminskii, *Soviet Physics - Crystallography*, **17**, 194 (1972).

[Kaminskii 1990] A.A. Kaminskii, *Laser crystals*, Springer, (1990).

[Keller 2003] U. Keller, *Nature*, **424**, 831 (2003).

[Kitaeva 1998] G.K. Kitaeva, Naumova, II, A.A. Mikhailovsky, P.S. Losevsky, A.N. Penin, *Applied Physics B-Lasers and Optics*, **66**, 201 (1998).

[Kneipp 2002] K. Kneipp, H. Kneipp, I. Itzkan, R.R. Dasari, M.S. Feld, *Journal of Physics-Condensed Matter*, **14**, R597 (2002).

[Koenderink 2010] A.F. Koenderink, *Optics Letters*, **35**, 4208 (2010).

[Kreibig 1995] U. Kreibig, M. Vollmer, *Optical properties of metal clusters*, Springer, (1995).

[Lallier 1990] E. Lallier, J.P. Pocholle, M. Papuchon, M. Demicheli, M.J. Li, Q. He, D.B. Ostrowsky, C. Grezesbesset, E. Pelletier, *Optics Letters*, **15**, 682 (1990).

[Lallier 1992] E. Lallier, *Applied Optics*, **31**, 5276 (1992).

[Lines 1977] M.E. Lines, A.M. Glass, *Principles and applications of ferroelectrics and related materials*, OUP Oxford, (1977).

[Liu 2007] X. Liu, K. Kitamura, K. Terabe, H. Hatano, N. Ohashi, *Applied Physics Letters*, **91**, 044101 (2007).

[Lorenzo 1997] A. Lorenzo, H. Loro, J.E. Muñoz Santiuste, M.C. Terrile, G. Boulon, L.E. Bausá, J. García Solé, *Optical Materials*, **8**, 55 (1997).

[Loro 1995] M. Loro, M. Voda, F. Jaque, J. Garcia Sole, J.E. Munoz Santiuste, *Journal of Applied Physics*, **77**, 5929 (1995).

[Ma 2013] R.-M. Ma, R.F. Oulton, V.J. Sorger, X. Zhang, *Laser & Photonics Reviews*, **7**, 1 (2013).

[Maier 2003] S.A. Maier, P.G. Kik, H.A. Atwater, S. Meltzer, E. Harel, B.E. Koel, A.A.G. Requicha, *Nature Materials*, **2**, 229 (2003).

[Maier 2005] S.A. Maier, H.A. Atwater, *Journal of Applied Physics*, **98**, 011101 (2005).

[Maier 2006] S.A. Maier, *Optical and Quantum Electronics*, **38**, 257 (2006).

[Maier 2010] S.A. Maier, *Plasmonics: Fundamentals and Applications*, Springer US, (2010).

[Maiman 1960] T.H. Maiman, *Nature*, **187**, 493 (1960).

[Matthias 1948] B. Matthias, A. Vonhippel, *Physical Review*, **73**, 1378 (1948).

[Matthias 1949] B.T. Matthias, *Physical Review*, **75**, 1771 (1949).

[Matthias 1949.B] B.T. Matthias, J.P. Remeika, *Physical Review*, **76**, 1886 (1949).

[Matthias 1951] B.T. Matthias, J.P. Remeika, *Physical Review*, **82**, 727 (1951).

[McMillen 1998] D.K. McMillen, T.D. Hudson, J. Wagner, J. Singleton, *Optics Express*, **2**, 491 (1998).

[Megaw 1954] H.D. Megaw, *Acta Crystallographica*, **7**, 187 (1954).

[Mertens 2006] H. Mertens, A. Polman, *Applied Physics Letters*, **89**, 211107 (2006).

[Meyer 2002] B. Meyer, D. Vanderbilt, *Physical Review B*, **65**, 104111 (2002).

[Mie 1908] G. Mie, *Annalen Der Physik*, **25**, 377 (1908).

[Munoz 1998] J.A. Munoz, J.O. Tocho, F. Cusso, *Europhysics Letters*, **43**, 159 (1998).

[Nai-Ben 1982] M. Nai-Ben, H. Jing-Fen, F. Duan, *Journal of Materials Science*, **17**, 1663 (1982).

[Nassau 1966] K. Nassau, Levinste.Hj, G.M. Loiacono, *Journal of Physics and Chemistry of Solids*, **27**, 983 (1966).

[Niizeki 1967] N. Niizeki, T. Yamada, H. Toyoda, *Japanese Journal of Applied Physics*, **6**, 318 (1967).

[Noginov 2009] M.A. Noginov, G. Zhu, A.M. Belgrave, R. Bakker, V.M. Shalaev, E.E. Narimanov, S. Stout, E. Herz, T. Suteewong, U. Wiesner, *Nature*, **460**, 1110 (2009).

[Novotny 2011] L. Novotny, N. van Hulst, *Nature Photonics*, **5**, 83 (2011).

[Novotny 2012] L. Novotny, B. Hecht, *Principles of nano-optics*, Cambridge University Press, (2012).

[Oulton 2009] R.F. Oulton, V.J. Sorger, T. Zentgraf, R.-M. Ma, C. Gladden, L. Dai, G. Bartal, X. Zhang, *Nature*, **461**, 629 (2009).

[Ozbay 2006] E. Ozbay, *Science*, **311**, 189 (2006).

[Padilla 1996] J. Padilla, W. Zhong, D. Vanderbilt, *Physical Review B*, **53**, R5969 (1996).

[Perry 1994] M.D. Perry, G. Mourou, *Science*, **264**, 917 (1994).

[Pillonnet 2012] A. Pillonnet, A. Berthelot, A. Pereira, O. Benamara, S. Derom, G.C. des Francs, A.M. Jurdyc, *Applied Physics Letters*, **100**, 153115 (2012).

[Pinchuk 2004] A. Pinchuk, A. Hilger, G. von Plessen, U. Kreibig, *Nanotechnology*, **15**, 1890 (2004).

[Poykko 1999] S. Poykko, D.J. Chadi, *Applied Physics Letters*, **75**, 2830 (1999).

[Purcell 1946] E.M. Purcell, *Physical Review*, **69**, 681 (1946).

[Rankin 2007] C. Rankin, C.-H. Chou, D. Conklin, D.A. Bonnell, *Acs Nano*, **1**, 234 (2007).

[Riefer 2012] A. Riefer, S. Sanna, W.G. Schmidt, *Physical Review B*, **86**, 125410 (2012).

[Sanchez-Garcia 2014] L. Sanchez-Garcia, M.O. Ramirez, P. Molina, F. Gallego-Gomez, L. Mateos, E. Yraola, J.J. Carvajal, M. Aguilo, F. Diaz, C. de las Heras, L.E. Bausa, *Advanced Materials*, **26**, 6447 (2014).

[Sanna 2010] S. Sanna, W.G. Schmidt, *Physical Review B*, **81**, 214116 (2010).

[Scott 2007] J.F. Scott, *Science*, **315**, 954 (2007).

[Scott 2008] J.F. Scott, *Journal of Physics-Condensed Matter*, **20**, 021001 (2008).

[Selvan 1999] S.T. Selvan, T. Hayakawa, M. Nogami, *Journal of Physical Chemistry B*, **103**, 7064 (1999).

[Sennaroglu 2006] A. Sennaroglu, *Solid-State Lasers and Applications*, CRC Press, (2006).

[Shirane 1950] G. Shirane, S. Hoshino, K. Suzuki, *Physical Review*, **80**, 1105 (1950).

[Sole 1993] J.G. Sole, T. Petit, H. Jaffrezic, G. Boulon, *Europhysics Letters*, **24**, 719 (1993).

[Stockman 2010] M.I. Stockman, *Journal of Optics*, **12**, 024004 (2010).

[Suh 2012] J.Y. Suh, C.H. Kim, W. Zhou, M.D. Huntington, D.T. Co, M.R. Wasielewski, T.W. Odom, *Nano Letters*, **12**, 5769 (2012).

[Sun 2011] Y. Sun, B.S. Eller, R.J. Nemanich, *Journal of Applied Physics*, **110**, 084303 (2011).

[Sun 2011B] Y. Sun, R.J. Nemanich, *Journal of Applied Physics*, **109**, 104302 (2011).

[Tian 2004] L. Tian, V. Gopalan, L. Galambos, *Applied Physics Letters*, **85**, 4445 (2004).

[Tinkham 2003] M. Tinkham, *Group Theory and Quantum Mechanics*, Dover Publications, (2003).

[Tserkezis 2014] C. Tserkezis, R.W. Taylor, J. Beitner, R. Esteban, J.J. Baumberg, J. Aizpurua, *Particle & Particle Systems Characterization*, **31**, 152 (2014).

[Uchino 2000] K. Uchino, *Ferroelectric Devices*, Taylor & Francis, (2000).

[Valasek 1921] J. Valasek, *Physical Review*, **17**, 475 (1921).

[Volk 1996] T. Volk, M. Woehlecke, N. Rubinina, A. Reichert, N. Razumovski, *Ferroelectrics*, **183**, 291 (1996).

[Wang 2012] X. Wang, P. Gogol, E. Cambril, B. Palpant, *Journal of Physical Chemistry C*, **116**, 24741 (2012).

[Weis 1985] R.S. Weis, T.K. Gaylord, *Applied Physics a-Materials Science & Processing*, **37**, 191 (1985).

[Wiley 2007] B.J. Wiley, Y. Chen, J.M. McLellan, Y. Xiong, Z.-Y. Li, D. Ginger, Y. Xia, *Nano Letters*, **7**, 1032 (2007).

[Wolf 2014] S. Wolf, J. Rensberg, H. Stoecker, B. Abendroth, W. Wesch, C. Ronning, *Nanotechnology*, **25**, 135611 (2014).

[Wong 2002] K.K. Wong, I.o.E. Engineers, INSPEC, *Properties of Lithium Niobate*, INSPEC/Institution of Electrical Engineers, (2002).

[Wu 2005] M. Wu, J.R. Lakowicz, C.D. Geddes, *Journal of Fluorescence*, **15**, 53 (2005).

[Xiaojun 2005] L. Xiaojun, L. Dongbo, S. Rui, D.A. Bonnel, *Journal of Materials Research*, **20**, 712 (2005).

[Xu 2013] Y. Xu, *Ferroelectric Materials and Their Applications*, Elsevier Science, (2013).

[Yang 2004] W.C. Yang, B.J. Rodriguez, A. Gruverman, R.J. Nemanich, *Applied Physics Letters*, **85**, 2316 (2004).

[Yraola 2013] E. Yraola, P. Molina, J.L. Plaza, M.O. Ramirez, L.E. Bausa, *Advanced Materials*, **25**, 910 (2013).

[Zayhowski 1989] J.J. Zayhowski, A. Mooradian, *Optics Letters*, **14**, 24 (1989).

[Zhang 2015] D.L. Zhang, C.X. Qiu, W.-J. Du, W.H. Wong, E.Y.-B. Pun, *Journal of the American Ceramic Society*, **98**, 567 (2015).

[Zhang 1996] K.S. Zhang, C.D. Xie, R.X. Guo, J.M. Wang, K.C. Peng, *Applied Optics*, **35**, 3200 (1996).

[Zhou 2013] W. Zhou, M. Dridi, J.Y. Suh, C.H. Kim, D.T. Co, M.R. Wasielewski, G.C. Schatz, T.W. Odom, *Nature Nanotechnology*, **8**, 506 (2013).

[Zotov 1994] N. Zotov, H. Boysen, F. Frey, T. Metzger, E. Born, *Journal of Physics and Chemistry of Solids*, **55**, 145 (1994).